LEABHARLANN CHOLÁISTE NA TRÍONÓIDE, BAILE ÁTHA CLIATH | TRINITY COLLEGE LIBRARY DUBLIN
Ollscoil Átha Cliath | The University of Dublin

Terms and Conditions of Use of Digitised Theses from Trinity College Library Dublin

Copyright statement

All material supplied by Trinity College Library is protected by copyright (under the Copyright and Related Rights Act, 2000 as amended) and other relevant Intellectual Property Rights. By accessing and using a Digitised Thesis from Trinity College Library you acknowledge that all Intellectual Property Rights in any Works supplied are the sole and exclusive property of the copyright and/or other IPR holder. Specific copyright holders may not be explicitly identified. Use of materials from other sources within a thesis should not be construed as a claim over them.

A non-exclusive, non-transferable licence is hereby granted to those using or reproducing, in whole or in part, the material for valid purposes, providing the copyright owners are acknowledged using the normal conventions. Where specific permission to use material is required, this is identified and such permission must be sought from the copyright holder or agency cited.

Liability statement

By using a Digitised Thesis, I accept that Trinity College Dublin bears no legal responsibility for the accuracy, legality or comprehensiveness of materials contained within the thesis, and that Trinity College Dublin accepts no liability for indirect, consequential, or incidental, damages or losses arising from use of the thesis for whatever reason. Information located in a thesis may be subject to specific use constraints, details of which may not be explicitly described. It is the responsibility of potential and actual users to be aware of such constraints and to abide by them. By making use of material from a digitised thesis, you accept these copyright and disclaimer provisions. Where it is brought to the attention of Trinity College Library that there may be a breach of copyright or other restraint, it is the policy to withdraw or take down access to a thesis while the issue is being resolved.

Access Agreement

By using a Digitised Thesis from Trinity College Library you are bound by the following Terms & Conditions. Please read them carefully.

I have read and I understand the following statement: All material supplied via a Digitised Thesis from Trinity College Library is protected by copyright and other intellectual property rights, and duplication or sale of all or part of any of a thesis is not permitted, except that material may be duplicated by you for your research use or for educational purposes in electronic or print form providing the copyright owners are acknowledged using the normal conventions. You must obtain permission for any other use. Electronic or print copies may not be offered, whether for sale or otherwise to anyone. This copy has been supplied on the understanding that it is copyright material and that no quotation from the thesis may be published without proper acknowledgement.

Development, Modelling and Characterization of Metal Micro-Textured Thermal Interface Materials

by

Roger Kempers

A thesis submitted to the University of Dublin for the degree of Doctor of Philosophy,
Department of Mechanical & Manufacturing Engineering, Trinity College, Dublin 2.

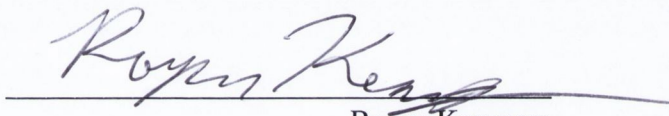
March 2010

TRINITY COLLEGE
12 MAY 2012
LIBRARY DUBLIN
9487

Declaration

I, Roger Kempers, declare that the present work has not been previously submitted as an exercise for a degree at any other university. It consists of entirely my own work, except where references indicate otherwise.

The library of Trinity College Dublin may lend or copy of this thesis on request.



Roger Kempers
March 2010

Abstract

A metal micro-textured thermal interface material (MMT-TIM) has been developed to address the shortcomings of conventional TIMs. In the present study, the MMT-TIMs consist of silver foils with raised, small-scale, hollow features. Upon compression between two solids, these features plastically deform, conforming to the asperities of the contacting surfaces thereby achieving intimate contact in the contact regions and a high conductivity bondline.

An experimental apparatus for characterizing TIMs having unprecedented precision and accuracy was developed to quantify the thermal and mechanical response of MMT-TIMs. A robust and conservative uncertainty analysis provides quantitative assessments of all results. Additionally, the simultaneous measurements of thermal and electrical resistance allowed for the indirect estimation of thermal contact resistance of the MMT-TIMs investigated in the present study.

A combined thermal-mechanical model was developed to simultaneously predict the mechanical and thermal response of MMT-TIMs as they undergo large plastic compressive deformations for the purposes of serving as a design tool to optimize MMT-TIM geometry.

The mechanical response of this model was improved by reconstructing actual MMT-TIMs geometries using SEM images of MMT-TIM features and 3D surface reconstruction software. Model results based on this approach demonstrated significant improvement over conventional geometry representation techniques

The thermal response of the model was improved by developing two different approaches to characterizing the MMT-TIM thermal contact resistance. The first approach relied on mechanical model predictions for local contact pressures and an empirical correlation for thermal contact conductance developed using silver tubes. This approach yielded a more realistic prediction of MMT-TIM total thermal response, however tended to over predict the contact resistance of the MMT-TIMs.

In the second approach, an additional electrical resistance measurement was used to develop a direct correlation between electrical and thermal contact resistance for MMT-TIMs. Subsequent experimental results demonstrated this approach well predicted the contact resistance of the silver MMT-TIMs studied here.

Based on this work, recommendations for further work on this technology are presented and discussed.

Acknowledgements

The author gratefully acknowledges the assistance and guidance of Dr. Alan Lyons and Dr. Anthony Robinson. Their advice and support throughout this project were invaluable.

I also wish to acknowledge Rich La Grotta from Alcatel-Lucent for agreeing to fund both my studies and the experimental apparatus constructed herein.

Many thanks go to Dr. Paul Kolodner for sharing his expertise on precision resistance thermometry (among other things) and Mr. Paul Ahern for his time and effort spent imaging MMT-TIMs.

I'm also grateful to my colleagues at Trinity's Thermodynamics Lab and at Alcatel-Lucent for their support and assistance.

Finally, I wish to thank my family and friends for their support, encouragement and prayers throughout.

Table of Contents

Abstract..... iii

Acknowledgments..... iv

Table of Contents.....v

List of Figures.....viii

List of Tables.....xiv

Nomenclature..... xv

Chapter 1 Introduction.....1

1.1 Background & Motivation.....1

1.2 Research Objectives.....1

Chapter 2 Literature Review & Background.....3

2.1 Thermal Contact Resistance..... 3

2.2 Thermal Contact Conductance Modelling.....6

2.2.1 Constriction Resistance.....6

2.2.2 Contact Conductance Modelling.....8

2.3 Mitigation of Thermal Contact Resistance.....9

2.3.1 Conventional Thermal Interface Materials.....9

2.4 Metal Micro-Textured Thermal Interface Materials.....13

2.4.1 Prototype MMT-TIM Fabrication.....14

2.5 Summary.....16

References.....17

Chapter 3 Model Development.....19

3.1 Analytical Thermal Model.....19

3.1.1 Analytical Thermal Model Formulation..... 19

3.1.2 Analytical Thermal Model Results.....22

3.2 Simultaneous Numerical Thermal-Mechanical Model.....24

3.2.1 Numerical Model Formulation..... 24

3.2.2 Comparison between Numerical and Analytical Models..... 29

3.2.3 Initial Comparison to Experimental Results.....29

3.3 Accurate Characterization of MMT-TIM Geometry.....35

3.3.1 Background & Literature Review.....35

3.3.2 Image Acquisition.....37

3.3.3 Surface Reconstruction.....38

3.3.4 Data Processing and Generation of Solid Geometry..... 38

3.4 Characterization of MMT-TIM Thermal Contact Resistance.....42
3.4.1 Literature Review.....43
3.4.2 Proposed Approach.....44
3.5 Summary.....45
References.....46
Chapter 4 Experimental Apparatus.....49
4.1 Introduction.....49
4.2 Apparatus Design.....56
4.2.1 Meter Bars, Thermal Instrumentation & Calibration.....58
4.2.2 Electrical Contact Resistance Measurement.....60
4.2.3. *In-Situ* Sample Thickness Measurement.....60
4.2.4 Load Application & Measurement.....61
4.3 Uncertainty Analysis.....62
4.3.1 Calculated Quantities.....62
4.3.2 Comparison to Previous Apparatuses.....66
4.4 Results & Discussion.....68
4.5 Summary.....74
References.....75
Chapter 5 Results & Discussion.....81
5.1 Baseline Experimental Results.....81
5.2 Model Predictions: Mechanical Response.....87
5.2.1 Influence of Geometrical Reconstruction.....87
5.2.2 Sensitivity Analysis of Reconstructed Geometry.....96
5.2.3 Numerical Convergence.....98
5.2.4 Summary of Mechanical Results.....100
5.3 Model Predictions: Thermal Response.....101
5.3.1 Thermal Contact Resistance in MMT-TIMs.....102
5.3.2 Development of an Expression for $h_c(P)$.....105
5.3.3 Implementation of h_c Correlation.....113
5.3.4 Summary.....115
5.4 Thermal and Electrical Contact Resistance Relationship.....116
5.4.1 Flat Foil Tests.....117
5.4.2 Silver Tube Tests.....117
5.4.3 Correlation derived from Silver MMT-TIMs.....120
5.4.4 Summary.....122

5.5 Additional MMT-TIM Geometries: Results & Model Comparisons..... 124
5.5.1 MMT-TIM Sample F..... 124
5.5.2 MMT-TIM Sample K..... 128
5.5.3 Summary..... 132
5.6 Summary..... 134
References..... 135
Chapter 6 Conclusions & Recommendations..... 137
6.1 Summary & Conclusions..... 137
6.2 Recommendations & Future Outlook..... 140

Appendix A – Material Property Testing..... 141
Appendix B – DEFORM Data Extraction and Heat Transfer Calculations..... 145
Appendix C – 3D Surface Data Processing..... 151
Appendix D – Photographs of Experimental Apparatus..... 153
Appendix E – Experimental Apparatus Data Acquisition and Control Software..... 159
Appendix F – Additional MMT-TIM Experimental Results..... 169

List of Figures

Fig. 2.1: Constriction of heat flux lines through a joint..... 4
Fig. 2.2: a) Two surfaces in apparent contact, b) temperature drop at their interface.....4
Fig. 2.3: a) Cluster of contact spots on a given area, b) Semi-infinite cylinder representing a single contact spot.....7
Fig. 2.4: Conventional Thermal Interface Material.....10
Fig. 2.5: Graphite TIM used in a mobile telecommunications radio power amplifier....11
Fig. 2.6: Metallic micro-textured thermal interface material (MMT-TIM) concept.....13
Fig. 2.7: Prototype MMT-TIM fabrication process.....14
Fig. 2.8: Textured silver foil as an embodiment of a MMT-TIM.....14

Fig. 3.1: a) Unit cell for simplified MMT-TIM thermal model, and b) an array of unit cells.....20
Fig. 3.2: Incorporation of constriction resistance.....21
Fig 3.3: Idealized compression of cylinders.....22
Fig. 3.4: Change in effective thermal conductivity with decreasing cylinder height.....23
Fig. 3.5: Unit cell model for an arbitrary MMT-TIM geometry and the equivalent thermal circuit.....25
Fig. 3.6: Typical meshed MMT-TIM unit cell showing conical MMT-TIM geometry..28
Fig. 3.7: Comparison between the analytical and numerical (FE) models for the variation of thermal resistance for a silver cylinder with force during compression..... 30
Fig. 3.8: a) 3D view of nominal MMT-TIM geometry, b) 3D cross-section, c) Schematic of cross-section with key dimensions labelled.....31
Fig. 3.9: Comparison of effective thermal conductivity of MMT-TIM during compression with initial model results.....32
Fig. 3.10: Comparison of applied pressure during MMT-TIM compression with initial model results.....32
Fig 3.11: Model prediction of MMT-TIM unit cell undergoing deformation corresponding to Fig. 3.10.....33
Fig. 3.12: An SEM images of a single conical MMT-TIM feature from a) above and b) obliquely.....34
Fig. 3.13: a) Side view of SEM setup for imaging MMT-TIMs for 3D surface reconstruction, b) eucentric tilting of an individual MMT-TIM unit cell.....37

Fig. 3.14: The 3D surface of a MMT-TIM generated using stereoscopic imaging with MeX.....39
Fig. 3.15: a) Original MeX output data set, b) surface data cropped to the specified unit cell size.....39
Fig. 3.16: Effect of edge condition of a thickened surface for, a) raw edge surface data resulting in a non-uniform perimeter surface, b) equalized edge z-coordinates resulting in a uniform vertical surface at the boundary.....41
Fig. 3.17: Cross-sectioned prototype plated MMT-TIM demonstrating uniform plating thickness.....41

Fig. 4.1: Meter Bar implementation of ASTM D5470-06.....53
Fig. 4.2: Rendering of experimental facility developed in the present study.....57
Fig. 4.3: Schematic of instrumentation and control of experimental facility.....57
Figure 4.4: Variation of specific thermal resistance uncertainty, U_{RA}, with thermal sensor uncertainty, U_T, for a common set of experimental parameters.....67
Fig. 4.5: Low-heat-flux meter-bar temperature distribution during self-contact.....68
Fig. 4.6: Energy balance between upper and lower meter bars for a range of powers...69
Fig. 4.7: Change in Specific Thermal Resistance and Electrical Contact Resistance with Pressure for Dry Self-Contact, $Q \approx 4.4$ W.....70
Fig. 4.8: Specific thermal resistance as a function of heat flux for dry and wet self contact.....71
Fig 4.9: Change in specific thermal resistance and electrical contact resistance with applied pressure for a graphite.....72
Fig 4.10: Change in effective thermal conductivity with applied pressure for a graphite TIM during three tests.....73

Fig. 5.1: Nominal feature geometry for baseline MMT-TIM Sample B.....81
Fig. 5.2: Photograph of MMT-TIM Sample B prior to testing.....81
Fig 5.3: Mechanical response of Sample B during compressive deformation.....82
Fig. 5.4: Effective thermal conductivity of Sample B during compressive deformation.....83
Fig 5.5: Variation of specific thermal resistance with pressure for MMT-TIM Sample B, t=36 μm and a flat silver foil 35 μm thick.....84
Fig. 5.6: Variation of effective thermal conductivity with pressure for MMT-TIM Sample B, t=36 μm and a flat silver foil 35 μm thick.....85

Fig. 5.7: Comparison between a) idealized geometry of MMT-TIM Sample B, t=36 μm unit-cell, b) reconstructed geometry of MMT-TIM Sample B, t=36 μm unit-cell...88
Fig. 5.8: SEM Image of MMT-TIM Sample B, t=36 μm unit-cell.....88
Fig. 5.9: Model prediction of compressive deformation of idealized MMT-TIM Sample B geometry.....90
Fig. 5.10: Model prediction of compressive deformation of reconstructed MMT-TIM Sample B geometry.....91
Fig. 5.11: SEM Image of the final shape of a single feature of MMT-TIM Sample B, 36 μm.....93
Fig. 5.12: SEM Image of the final shape of a several features of MMT-TIM Sample B, 36 μm.....93
Fig. 5.13a: Comparison between model predictions for compressive pressure based on idealized and reconstructed geometries and the experimental results for MMT-TIM Sample B, t=36 μm.....94
Fig. 5.13b: Comparison between model predictions for compressive pressure based on idealized and reconstructed geometries and the experimental results for MMT-TIM Sample B, t=28 μm..... 94
Fig. 5.14: Accuracy comparison between model responses based on idealized and reconstructed geometries for MMT-TIM Sample B.....95
Fig. 5.15: Comparison of model predictions of mechanical response for several independently imaged and reconstructed geometries of MMT-TIM Sample B, t=36 μm.....97
Fig. 5.16: Reconstructed Geometries before and after simulated compression to 3 MPa: a-b) Reconstructed Geometry 1, c-d) Reconstructed Geometry 2, e-f) Reconstructed Geometry 3..... 98
Fig. 5.17: Comparison of model predictions of mechanical response for several simulations with varying numbers of elements demonstrating numerical convergence.99
Fig. 5.18: Specific thermal resistance of MMT-TIM Sample B during deformation compared to model predictions neglecting contact resistance.....101
Fig. 5.19: Effective thermal conductivity of MMT-TIM Sample B during deformation compared to model predictions with contact resistance neglected.....102
Fig. 5.20: Estimated average local contact pressures for MMT-TIM Sample B, t=36 μm based on model results.....104
Fig. 5.21: Estimated local contact areas for MMT-TIM Sample B, t=36 μm based on model results.....104

Fig. 5.22: a) Rendering of Ag tube test (upper meter-bar not shown), b) cross-section of Ag tube.....106
Fig. 5.23: Overall compressive pressure required to deform Ag tubes.....107
Fig. 5.24: Model prediction of the cross-sectional shape of the Ag tubes, showing apparent contact regions, during compressive deformation.....108
Fig. 5.25: Model prediction local contact pressure of tubes during deformation.....109
Fig. 5.26: Model prediction of apparent contact area of tubes during deformation.....110
Fig. 5.27: Comparison of between experimentally measured and model-predicted thermal resistance of Ag tubes during deformation.....110
Fig. 5.28: Thermal contact conductance as a function of mean local contact pressure.112
Fig. 5.29: Predicted effective thermal conductivity of Ag tubes based on different values of h_c.....112
Fig. 5.30: Predicted effective thermal conductivity of MMT-TIM Sample B, t=36 μm based on different values of h_c.....114
Fig. 5.31: Predicted effective thermal conductivity of MMT-TIM Sample B, t=28 μm based on different values of h_c.....114
Fig. 5.32: Specific electrical resistance of MMT-TIM Sample B during deformation..116
Fig. 5.33: Specific electrical resistance of Ag tubes during deformation.....118
Fig. 5.34: Relationship between estimated specific thermal resistance and measured specific electrical resistance for Ag tubes.....119
Fig 5.35: Prediction of effective thermal conductivity of Ag tubes based on various contact resistance models.....119
Fig. 5.36: Relationship between estimated specific thermal resistance and measured specific electrical resistance for MMT-TIM Sample B and Ag tubes.....120
Fig. 5.37: Model predictions of effective thermal conductivity of MMT-TIM Sample B, t=36 μm.....121
Fig. 5.38: Model predictions of effective thermal conductivity of MMT-TIM Sample B, t=28 μm.....122
Fig. 5.39: SEM Image and nominal outer dimensions of MMT-TIM Sample F.....124
Fig. 5.40: Model prediction of compressive deformation of reconstructed MMT-TIM Sample F, t=36 μm geometry.....125
Fig. 5.41: Comparison of model predictions of mechanical response for MMT-TIM Sample F.....126
Fig. 5.42: Model predictions of effective thermal conductivity of MMT-TIM Sample F, t=36 μm.....127

Fig. 5.43: Model predictions of effective thermal conductivity of MMT-TIM Sample F, t=28 μm.....127
Fig. 5.44: SEM Image of MMT-TIM Sample K.....129
Fig. 5.45: Reconstructed geometry of a unit-cell of MMT-TIM Sample K.....129
Fig. 5.46: Model prediction of compressive deformation of MMT-TIM Sample K....130
Fig. 5.47: Experimental and model-predicted of mechanical response for MMT-TIM Sample K during deformation.....131
Fig. 5.48: Model predictions of effective thermal conductivity of MMT-TIM Sample K during deformation.....132
Fig. 5.49: Comparison between various model predictions and measured values of effective thermal conductivity for MMT-TIM Samples F and K.....133

Fig. A.1: Instron 5589 Material Tester used for compressive upsetting tests.....142
Fig. A.2: Sample setup for upsetting test.....142
Fig. A.3: Deformation of a cylindrical specimen during compressive upsetting test...143
Fig. A.4: Summary of stress-strain data obtained from compressive upsetting tests...144

Fig. D.1: Experimental Apparatus.....153
Fig. D.2: Experimental Apparatus.....154
Fig. D.3: Close-up of Meter-Bars.....155
Fig. D.4: Die Set and Lower Platen.....156
Fig. D.5: Meter-bars configured for calibration.....157
Fig. D.6: Meter-bar calibration can.....158

Fig. F.1: Cross-section of hollow conical MMT-TIM geometry.....169
Fig. F.2: Nominal feature geometries and measured dimensions of MMT-TIMs.....170
Fig. F.3: Variation of compressive pressure with strain for MMT-TIMs of different heights, outer dimensions and metal thicknesses.....171
Fig. F.4: Variation of effective thermal conductivity with pressure for MMT-TIMs of different heights, outer dimensions and metal thicknesses.....172
Fig. F.5: Variation of compressive pressure with strain for MMT-TIMs of different pitches.....173
Fig. F.6: Variation of effective thermal conductivity and specific thermal resistance with pressure for MMT-TIMs of two different pitches.....173

Fig. F.7: Variation of compressive pressure with strain for two conical and pyramidal MMT-TIM geometries of similar dimensions.....174
Fig. F.8: Variation of effective thermal conductivity with pressure for conical and pyramidal MMT-TIMs.....175
Fig. F.9: Variation of specific thermal resistance with pressure at 50% strain for each MMT-TIM.....176

List of Tables

Table 4.1: Uncertainty of Measured Quantities..... 62

A.1: Annealing conditions.....141

Nomenclature

Symbol

A	Area, m^2
d	Diameter, m
F	Force, N
h	Height, m
h_c	Thermal Contact Conductance, W/m^2K
k	Thermal Conductivity, W/m·K
L	Length, m
m	Temperature Gradient, K/m
p	Pitch, m
P	Pressure, MPa
Q	Heat Transfer Rate, W
r	Radius , m
R	Thermal Resistance, K/W
R_e	Electrical Resistance, Ω
RA	Specific Thermal Resistance, m^2K/W
R_eA	Specific Electrical Resistance, $m^2\Omega$
S	Surface
t	Thickness, m
T	Temperature, °C or K
U	Uncertainty
v	Velocity, mm/s
V	Volume, m^3

α	Fraction of Mechanical Energy Converted to Heat
ε	Porosity
$\bar{\varepsilon}$	Effective Strain
$\dot{\bar{\varepsilon}}$	Effective Strain rate, s^{-1}
$\dot{\varepsilon}_V$	Volumetric Strain Rate, s^{-1}
$\bar{\sigma}$	Effective Stress, MPa
ρ	density, kg/m^3

Subscript

a	surface A or dimension A
b	surface B or dimension B
c	contact or specific heat
const	constriction
e	electrical
eff	effective
l	lower
mb	meter-bar
meas	measured
u	upper
uc	unit-cell
z	measured quantity

Chapter 1

Introduction

1.1 Background & Motivation

Thermal contact resistance is an important issue in conduction heat transfer. In many systems where heat dissipation or transport is critical, contact resistance can play an important, and sometimes dominant role, in overall system performance.

Often the most effective and feasible method for mitigating thermal contact resistance is through the use of Thermal Interface Materials (TIMs). These materials are designed to conform to the roughness and surface asperities of the contacting surfaces, displacing any interfacial air, thereby providing an improved path for heat transfer across the interface. Conventional TIMs come in many forms, depending on the specific application and interface conditions required to interface. While these TIMs can demonstrate an improvement over bare surface-surface contact, the interface thermal resistance can still remain a severe bottleneck in many heat dissipating applications due to their relatively low effective thermal conductivity.

1.2 Objectives

The overall goal of this research is to develop a high performance thermal interface material to address the limitations of conventional TIMs while remaining manufacturable and cost-effective compared with the state-of-the-art. The solution conceived here is presented as a Metal Micro-Textured Thermal Interface Material (MMT-TIM). In this concept, the TIM consists of an array of raised, small-scale metal features based upon a thin metal substrate. When compressed between two solids, these features plastically deform and conform to the asperities of the contacting surfaces thereby achieving intimate contact between the mating regions resulting in a highly conductivity bondline.

To accomplish this goal, a number of objectives, or engineering challenges, must be overcome. The first is to demonstrate the feasibility of MMT-TIMs themselves. This will require the development of unique fabrication methods in order to create the requisite metal geometries. A second goal is to develop the high resolution measurement apparatus necessary to quantify and characterize the performance of MMT-TIMs.

Another key objective of this research is to develop accurate and innovative modelling techniques that are able to capture the underlying physics of this complex thermo-mechanical problem in order to predict the mechanical and thermal performance of these materials as they undergo the large-scale plastic deformations during compression. These models will ultimately serve as design tools in order to design and optimize MMT-TIMs for a variety of practical applications constrained by thermo-mechanical and cost considerations.

With the concept proven and the experimental and analytical tools in place, MMT-TIMs can then be designed and developed to serve as solutions in practical industrial settings.

Chapter 2

Literature Review & Background

The phenomenon of thermal contact resistance is an important consideration in conduction heat transfer for situations in which two solid bodies are meant to be in thermal communication with one another. This chapter details the underlying issue of thermal contact resistance, gives an overview relevant modelling techniques and presents mitigation strategies with an emphasis on thermal interface materials. Finally, the concept of a Metal Micro-Textured Thermal Interface Material (MMT-TIM) is introduced as an alternative to conventional TIM technologies.

2.1 Thermal Contact Resistance

Surface irregularities are present in nearly all solid surfaces. When two surfaces are brought into contact with each other, these asperities limit the amount of actual contact area between the two objects. The amount of actual contact area depends on the topology of the mating surfaces, the contact pressure and the material properties. For many engineering surfaces, this area can be as little as 2% of the apparent contact area [1]. At the macroscopic level, surface issues such as waviness and co-planarity also contribute to the amount of area in actual contact.

Heat transfer between two solid bodies can consist of conduction, convection and radiation. For contacting bodies however, the length scales of the interstitial gaps are typically too small for convection currents to be established. In air at atmospheric pressure, convective heat transfer is negligible up to gap widths of approximately 6 mm [2]. Additionally, radiation heat transfer can usually be neglected for temperatures below 300 °C [3]. Thus, heat transfer between the two mating bodies is dominated by conduction through the actual contact spots as well as conduction across the interstitial medium occupying the voids.

If the thermal conductivity of the interstitial medium is low compared with that of the contacting solids, then heat preferably flows through the contact points. This is the case even though an additional resistance, due to the constriction of the heat flow lines illustrated in Fig. 2.1, contributes to the overall thermal contact resistance.

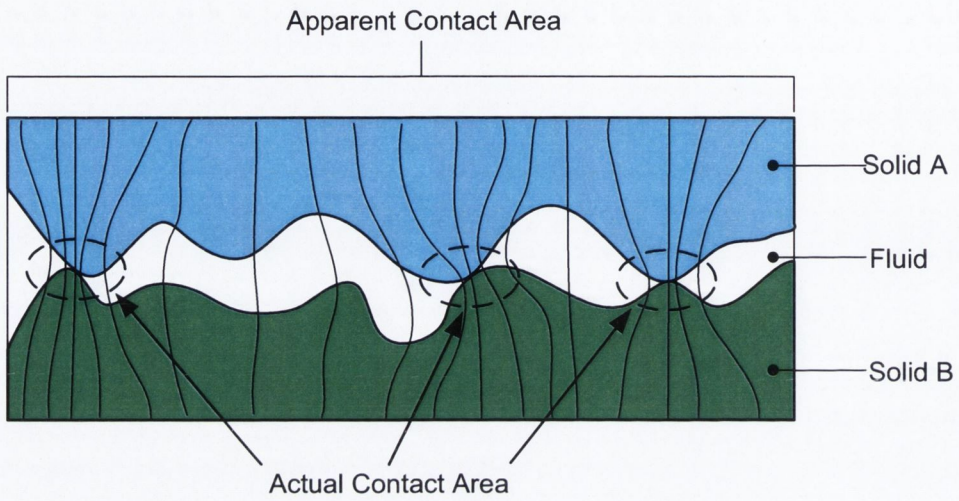


Fig. 2.1: Constriction of heat flux lines through a joint

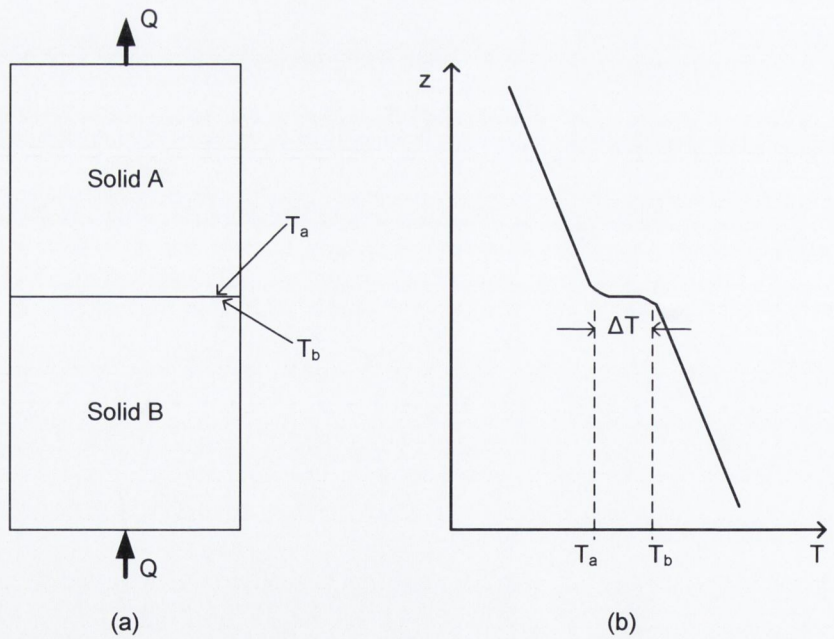


Fig. 2.2: a) Two surfaces in apparent contact, b) temperature drop at their interface

In many practical applications the contacting solids are metals ($k \approx 100$ to 400 W/m·K) and the interstitial fluid is air ($k \approx 0.025$ W/m·K), resulting in approximately four orders of magnitude difference between the respective thermal conductivities. As a result, the exact temperature distribution near the joint is complex and three-dimensional. These

constrictions and expansions in the heat flux lines manifest themselves as a sudden temperature drop between contacting solids at their mating surfaces as illustrated in Fig. 2.2.

The approximation of a surface averaged "temperature jump" across the interface is adequate for most practical purposes. For this situation the thermal contact resistance is simply defined in terms of the conventional definition of thermal resistance which is the temperature drop which can be expected per unit of heat throughput;

$$R_c = \frac{\Delta T}{Q} = \frac{(T_a - T_b)}{Q} \tag{2.1}$$

where Q is the rate of heat transfer, T_a is the temperature at surface A and T_b is the temperature at surface B. The contact thermal resistance can be expressed in terms of the product of the nominal contact area and is deemed the specific thermal resistance (often referred to as thermal impedance) which is defined as,

$$RA = \frac{A\Delta T}{Q} \tag{2.2}$$

where A is the apparent or nominal contact area. Alternatively, the specific thermal contact resistance can be expressed as thermal contact conductance or contact heat transfer coefficient in the form,

$$h_c = \frac{Q}{A\Delta T} = \frac{1}{RA} \tag{2.3}$$

which is simply the reciprocal of the specific thermal resistance.

2.2 Thermal Contact Conductance Modelling

Much effort has been put forth in order to predict h_c for a variety of contacting surfaces. Madhusudana [4] and Yovanovich [5] provide excellent reviews of the work done in the area of thermal contact resistance and conductance modelling as well as experimental characterization of thermal properties. Thermal contact conductance (or resistance) is typically calculated by analytically modelling the thermal constriction resistance of a single contact spot. The size and number of contact spots for a given interface is then approximated using various mechanical and statistical models. This section examines the first aspect of this modelling due to its particular relevance to the thermal modelling detailed in the following chapter.

2.2.1 Constriction Resistance

As discussed in Sec. 2.1, thermal contact resistance is due to both the difference between apparent and actual contact area and the constriction resistance as the heat flux lines are constrained to pass through the actual contact points: particularly if the thermal conductivity of the interstitial medium is low compared with that of the contacting solids. Constriction resistance is a measure of the additional temperature drop associated with a single constriction given by,

$$R_c = \frac{T - T_0}{Q} \tag{2.4}$$

where T_0 is the temperature difference required for a heat rate of Q with no constriction and T is the temperature difference required when the constriction is present [4].

In a real joint, there are numerous contact spots. Consider the illustration in Fig. 2.3a where each actual contact spot of radius a_i would serve as a constriction point for heat being fed from a larger cylinder having radius b_i. Each contact spot could then be modelled as a semi-infinite cylinder as shown in Fig. 2.3b [4].

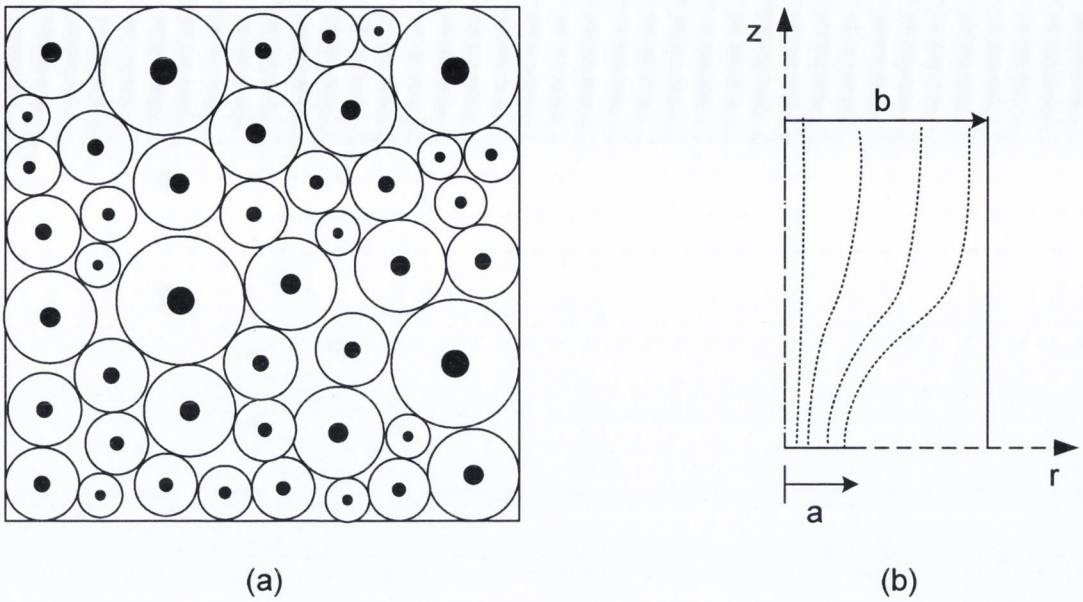


Fig. 2.3: a) Cluster of contact spots on a given area, b) Semi-infinite cylinder representing a single contact spot

If it is assumed that there is no thermal communication between adjacent cylinders and between the gaps of adjacent contact spots then the boundary conditions for this simplified scenario are

$$\text{T} = \text{constant};\ z = 0,\ 0 < r \le a \tag{2.5a}$$

$$-k\frac{\partial T}{\partial z} = 0\ ;\ z = 0,\ r > a \tag{2.5b}$$

$$-k\frac{\partial T}{\partial z} = \frac{Q}{\pi b^2}\ ;\ z \to \infty \tag{2.5c}$$

$$-k\frac{\partial T}{\partial z} = 0\ ;\ r = b \tag{2.5d}$$

$$-k\frac{\partial T}{\partial z} = 0\ ;\ r = 0 \tag{2.5e}$$

The solution to this problem as posed by Mikic & Rohsenow [6] and Cooper *et al.* [7] is presented in Madhusudana [4]. The constriction resistance is given as,

$$R_c = \frac{1}{4ka}F(a/b) \tag{2.6}$$

Where F(a/b) is the constriction alleviation factor which was evaluated by Negus & Yovanovich [8] as

$$F(a/b) = 1 - 1.4098(a/b) + 0.3441(a/b)^3 + 0.0435(a/b)^5 + \ldots \tag{2.7}$$

This solution assumes a uniform temperature distribution at the constriction and that the thicknesses of the upper and lower surfaces were sufficiently thick that the heat flux lines are parallel at the extents (i.e. uniform temperature at the extents). This solution also predicts the constriction resistance under the assumption that no heat is transferred through the interstitial medium.

2.2.2 Contact Conductance Modelling

Madhusudana [4] goes on to consider both sides of the constriction and the sum total of all of the constrictions of a given contacting surface. Assuming there are n contact spots with a mean contact spot radius of a_m and by neglecting the variation in F, the contact conductance of an interface can be written as,

$$h = \frac{2na_m k}{F} \tag{2.8}$$

where

$$k = \frac{2k_1 k_2}{k_1 + k_2} \tag{2.9}$$

and k_1 and k_2 are the conductivities of the contacting surfaces [4]. The number of contact spots, n, and the mean contact spot radius, a_m, are then modelled using statistical surface characterizations and mechanical deformation analysis. A number of approaches are reviewed and detailed in [4] and [5] and generally produce reasonable predictions of thermal contact conductance for a range of engineering surfaces.

2.3 Mitigation of Thermal Contact Resistance

In many applications such as heat exchangers, manufacturing process and electronics cooling, it is desirable to minimize the amount of thermal contact resistance between mating components in order to increase heat transfer rates. This is particularly relevant to electronics thermal management which continues to experience rapid increases in both overall output power and power density of hardware devices.

Thermal contact resistance can be reduced in three ways: The first is to reduce the roughness and waviness of the mating surfaces before assembly. Surface finish can be improved through grinding and polishing techniques. However, achieving the surface finish necessary for significant reductions in contact resistance is not trivial and is generally prohibitively expensive with respect to the required price point of the component being manufactured. A further aspect that needs to be ensured is the co-planarity of the mating surfaces at larger length scales.

Another method employed to lower thermal contact resistance is to increase the contact pressure which has the effect of increasing actual contact area through deformation of the micro-roughness peaks or by deflection of the larger scale waviness of the mating surfaces. Again, this option has practical limitations, particularly in electronics applications where interfacing components are often fragile.

Finally, the most feasible and popular option remains the employment of a thermal interface material (TIM) which is an interstitial medium sandwiched between two solid surfaces meant to improve the thermal communication between them.

2.3.1 Conventional Thermal Interface Materials

The mitigation of thermal contact resistance is essential to the performance of conduction-based electronic thermal management solutions. Typically the most feasible strategy to reduce thermal contact resistance is to insert a thermal interface material (TIM) of higher thermal conductivity between the mating surfaces to conform to the contacting surface asperities and displace any micro and macroscopic air voids, thereby providing a path of improved heat conduction.

To work effectively, TIMs must physically conform to the mating surfaces under reasonable assembly pressures and exhibit low contact resistance with adequate bulk thermal conductivity. The bond-line thickness values are kept to a minimum to help reduce bulk thermal resistance; however the thickness must be sufficiently large to enable the TIM to comply with surface irregularities and non-planarities. For assembly of microprocessors, where surfaces are relatively smooth and flat, TIMs are thin (typically 5-

50 μm thick). However for other demanding applications, such as the assembly of high powered wireless amplifiers where surfaces can be rough and undulating, relatively thick (0.1 – 5 mm thick) TIMs are required to ensure good contact across the entire surface. Many different TIMs are commercially available that attempt to meet these requirements in different ways. These include a range of adhesives, greases, elastomeric pads and various phase-change materials [9].

The main weakness of many commercially available TIMs is their relatively poor thermal performance. Often the TIM consists of a low-conductivity organic phase, such as silicone grease, interspersed with higher conductivity metal (e.g. silver, copper) or ceramic particles (e.g. aluminium oxide, zinc oxide or boron nitride) to boost the overall effective thermal conductivity of the material. The end result is a material whose effective thermal conductivity is limited by multiple point-to-point contacts between adjacent particles. Despite using extremely high conductivity filler materials, such as silver ($k \approx 420$ W/m·K), the effective thermal conductivity of the best commercially available TIMs is on the order of 5 to 10 W/m·K, which is considerably lower than the thermal conductivities of typical mating components. In addition, dispensing and flow of the particle-matrix composite results in voids being trapped within the bond.

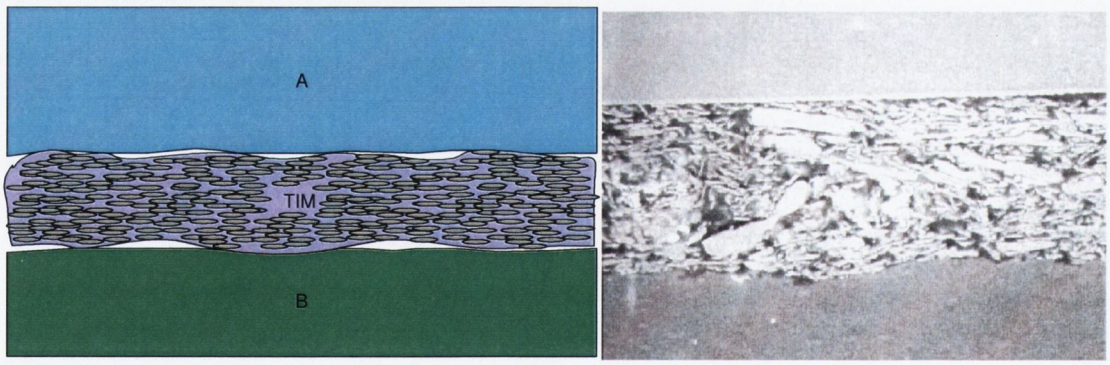


Fig. 2.4: Conventional Thermal Interface Material

Indeed in many high thermal energy dissipating systems, the TIMs can account for up to 50% of the available thermal budget of the package [10]. With the inevitable implementation of high performance liquid cooling strategies, this percentage will become even greater. If the thermal management of an electronic device is inadequate, unacceptable temperature levels may be reached which can adversely affect device performance, reliability and lifespan [10]. These thermal issues have spawned a global effort towards the development of novel TIMs with complex formulations [11-13].

Another often used type of thermal interface material are graphite pads. Graphite flakes are exfoliated by thermally vaporizing an intercalant ion inserted between its layers, generating an internal pressure that causes the intercalated graphite to expand in the direction perpendicular to the layers. The expanded graphite flakes are then mechanically consolidated together with a matrix into a cohesive sheet of flexible graphitic material [14, 15]. The results is a flexible sheet that has a reasonable through-plane thermal conductivity (3-5 W/m·K) [14]. However, due to the highly anisotropic nature of the structure, the in-plane conductivity is significantly higher, ranging from 140 to 500 W/m·K according to Smalc *et al.* [15]. As a result, they are a viable option for heat spreading applications [15]. An example of a graphite pad used in a commercial implementation is shown in Fig. 2.5.

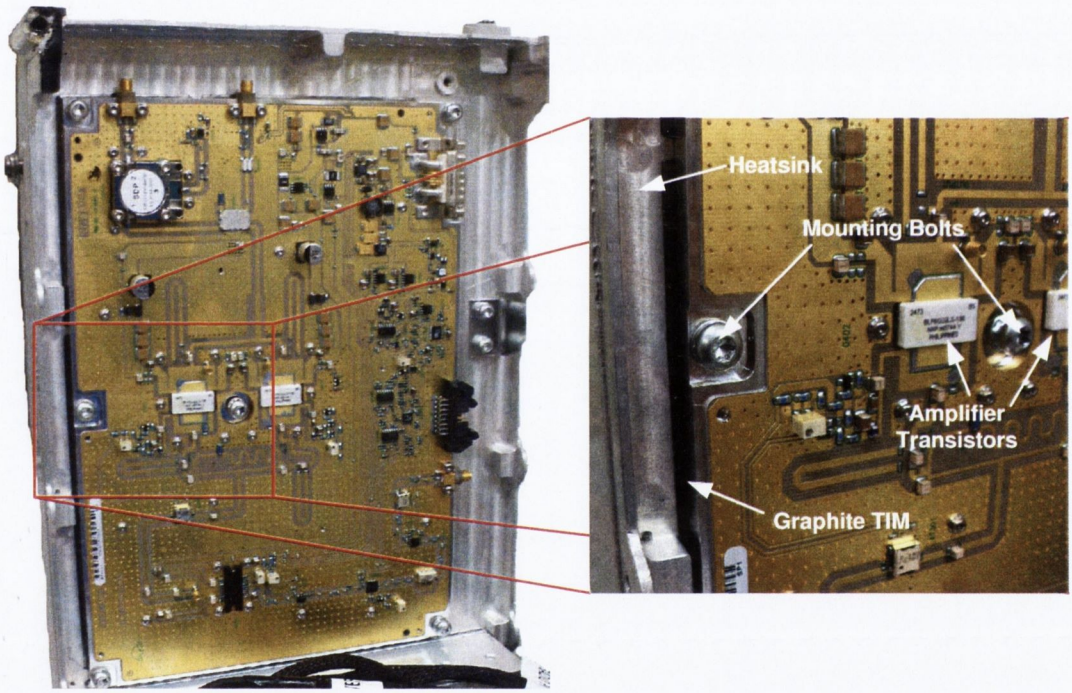


Fig. 2.5: Graphite TIM (t=0.125 mm) used in a mobile telecommunications radio power amplifier (application area ≈ 200 mm × 300 mm)

Here, the graphite pad (nominally 0.125 mm thick) serves as the thermal interface material between a relatively large RF power amplifier and a cast aluminium heat sink. The power amplifier, which measures approximately 200 mm × 300 mm, is bolted to the heat sink at four corners and centrally. Here, not only does the TIM need to accommodate the microscopic surface roughness associated with the mating components, it must also comply with the larger overall errors in form such as waviness or non-planarity. In this application, qualitative measurements with pressure sensitive film demonstrated that intimate contact between the amplifier and heat sink occurs only in the regions

immediately next to the bolted joints. As a result, there remains a major resistance due to an insulating interstitial air layer trapped between TIM and PWB and/or TIM and aluminium heat sink. This application serves to illustrate one of the major shortcomings of graphite TIMs: despite being a flexible sheet, graphite pads exhibit very little compliance as they are compressed normally. Even at compressive pressures of 1 MPa, graphite pads exhibit only approximately 5% strain [14].

2.4 Metal Micro-Textured Thermal Interface Materials

To address these issues, a novel TIMs have been developed called metal micro-textured thermal interface materials (MMT-TIMs). These materials consist of an array of small-scaled raised metal features on a thin metallic substrate. When this structure is compressed between two mating surfaces, the features plastically deform and conform to the contacting bodies as illustrated in Fig. 2.6. This approach reverses the conventional TIM paradigm by creating two interpenetrating continuous phases – one of high-conductivity plastically deformable metal features and a second of an optional organic compound which flows around these features.

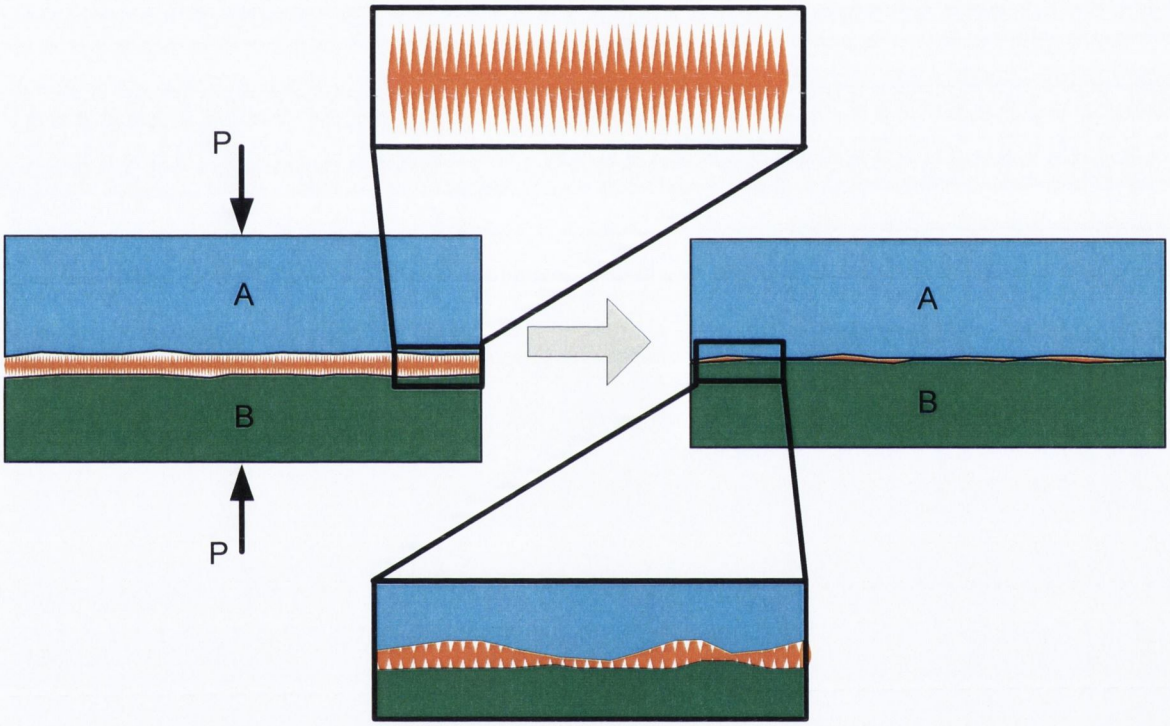


Fig. 2.6: Metallic micro-textured thermal interface material (MMT-TIM) concept

The constraint on thermal conductivity imposed by multiple point-to-point contacts in conventional TIMs is thus eliminated. In addition, the possibility of void formation is significantly reduced since these micro-textured contact points are fixed in an array. Air voids, which may become entrapped in the organic phase, will not affect metal contact density. The result is an array of conformable, yet continuous solid metal features of high effective thermal conductivity that are in intimate contact with the mating surfaces due to the plastic deformation of the raised features. Furthermore, by employing pure metals such as copper, silver or aluminium, the features of the MMT-TIM are both good thermal conductors and relatively compliant.

2.4.1 Prototype MMT-TIM Fabrication

The process used to create the MMT-TIMs investigated in the present study is depicted in Fig. 2.7. First, the 3D geometry of the desired surface-negative was created using a conventional CAD package (PTC ProEngineer). This form or template was then built from wax directly using a 3D Systems CPX-3000 3D printer in high-resolution mode. Metal was electroplated onto the wax template to a desired thickness and the wax subsequently removed. Finally, the metal structured was appropriately annealed in order to promote grain growth and remove any internal stresses. This annealing step not only softens the MMT-TIM, but ensures the metal has known and reproducible mechanical properties that allow for its systematic modelling. Details regarding the annealing process are presented in Appendix A.

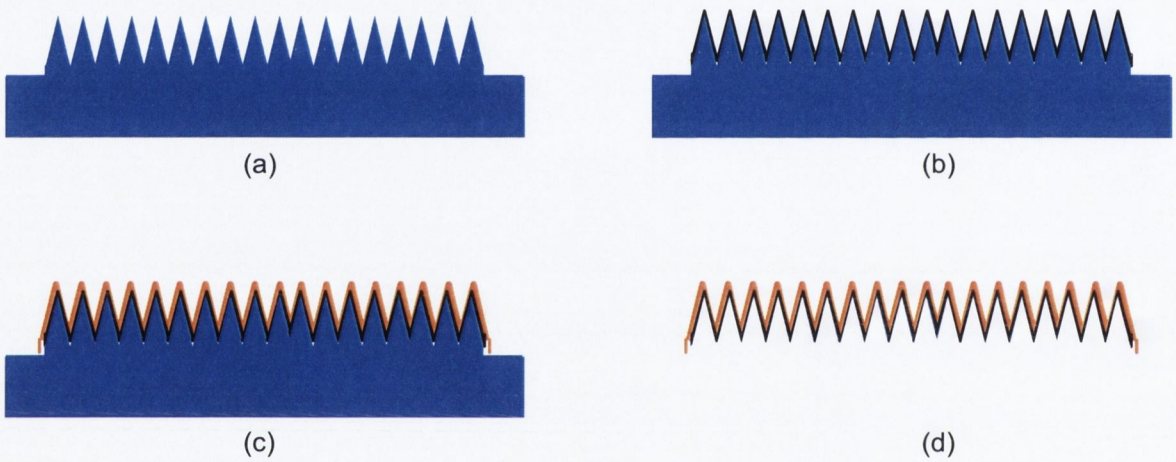


Fig. 2.7: Prototype MMT-TIM fabrication process: a) wax template printed using a wax 3D printer, b) seed layer coated onto wax template, c) metal electroplated to desired thickness, d) wax subsequently removed leaving textured metal foil

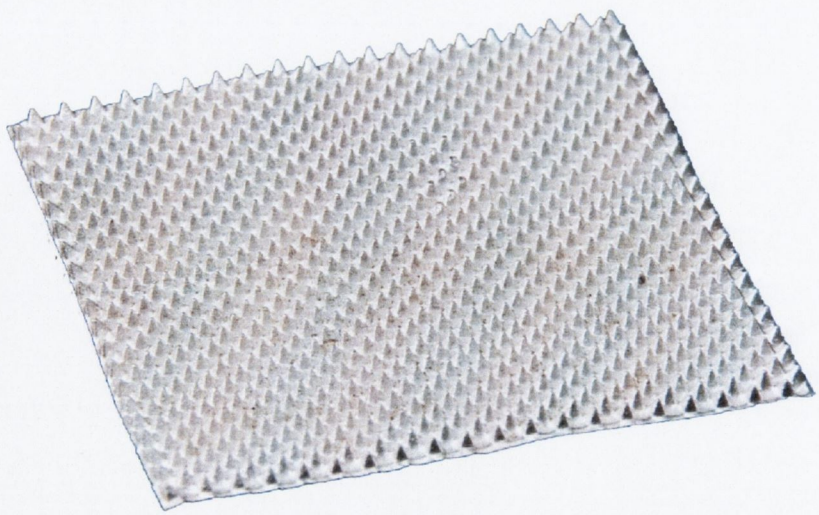


Fig. 2.8: Textured silver foil as an embodiment of a MMT-TIM

The resulting MMT-TIM structure consists of an array of hollow metal features and can be described as a textured metal foil. An example the resultant foil is shown in Fig. 2.8

This process allows for the creation of a wide range of relatively detailed geometries rendering it well suited for the study of geometrical effect on the mechanical and thermal performance of the MMT-TIMs. Furthermore, these hollow geometries potentially lend themselves to low-cost, high-volume manufacturing techniques such as micro-stamping or embossing, making this an attractive option for a low-cost TIM. Details regarding the specific geometries studied in the present work are discussed in Chapter 5.

2.5 Summary

The mitigation of thermal contact resistance is essential to improving the effectiveness of conduction-based heat transfer between contacting bodies. Conventional thermal interface materials accomplish this by displacing any interstitial air with a conformable material of higher thermal conductivity. Despite this, the interface bondline can remain a significant thermal resistance due to the low bulk thermal conductivity of TIMs, the high thermal contact resistance between TIM and substrate and the numerous voids trapped in the interface. To address these issues, a novel approach of using an array of metal micro-textured foils which plastically deform and conform to the contacting surfaces has been developed. Prototype manufacturing techniques allow for the creation of a range of geometries in order to develop an understanding of how a given MMT-TIM design will perform as it is compressed.

In order to demonstrate the feasibility of this concept, the mechanical and thermal response of prototype MMT-TIMs will be characterized experimentally. Additionally, models will be required to predict the mechanical and thermal response of MMT-TIMs during compression on order to optimize and design MMT-TIMs for a specific application. The remainder of this work addresses these issues.

References

1. Bowden, F.P. & Tabor, D., The Friction and Lubrication of Solids, Oxford University Press, London, 1950.

2. Lang, P.M., 1962, "Calculating Heat Transfer Across Small Gas-Filled Gaps", Nucleonics, 20 (1), pp 62 - 63.

3. Incropera & DeWitt, Introduction to Heat Transfer, 3rd Edition, John Wiley & Sons, New York, 1996.

4. Madhusudana, C.V., Thermal Contact Conductance, Springer-Verlag, New York, (1996).

5. Yovanovich, M.M., 2005, "Four Decades of Research on Thermal Contact, Gap, and Joint Resistance in Microelectronics", IEEE Transactions on Components and Packaging Technologies, **28**, pp. 182-206.

6. Mikic, B.B. & Rohsenow, W.M., 1966, "Thermal Contact Resistance", Mech. Eng. Depart Report No. DSR 74542-41, MIT, Cambridge, MA.

7. Cooper, M.G., Mikic, B.B. & Yovanovich, M.M., 1969, "Thermal Contact Conductance", Int. J. Heat Mass Transfer, **12**, pp. 279-300.

8. Negus, K.J & Yovanovich, M.M., 1984, "Constriction Resistance of Circular Flux Tubes with Mixed Boundary Conditions by Superposition of Neumann Solutions", ASME Paper 84-HT-84, 6pp., ASME, New York.

9. Liu, J., Michel, B., Rencz, M., Tantolin, C, Sarno, C., Miessner, R., Schuett, K-V., Tang, X., Demoustier, S. & Ziaei, A., "Recent Progress of Thermal Interface Material Research—An Overview", Proceedings of the 14th Workshop on Thermal Issues in ICs and Systems (THERMINIC), Rome, Italy, September 24-26, 2008

10. Smith B., Brunschwiler, T., & Michel, B. "Comparison of transient and static test methods for chip-to-sink thermal interface characterization". *Microelectron. J.*, doi:10.1016/j.mejo.2008.06.079 (2008).

11. Linderman, R., Brunschwiler, T., Smith B., and Michel, B. "High performance thermal interface technology overview". Proceedings of the 13th Workshop on Thermal Issues in ICs and Systems (THERMINIC), pp. 129-134 (2007).

12. Ziaei, A. & Demoustier, S., "NANOPACK – Nano Packaging Technology for Interconnect and Heat Dissipation". Proceedings of the 14th Workshop on Thermal Issues in ICs and Systems (THERMINIC), Rome, Italy, September 24-26, 2008.

13. Liu, J., Michel, B., Rencz, M., Tantolin, C., Sarno, C., Miessner, R., Schuett, K. V., Tang, X., Demoustier, S. & Ziaei, A. "Recent Progress of Thermal Interface Material Research – An Overview". Proceedings of the 14th Workshop on Thermal Issues in ICs and Systems (THERMINIC), Rome, Italy, September 24-26, 2008.

14. Smalc, M., Norley, J., Reynolds, R.A., Pachuta, R. & Krassowski, D.W., "Advanced Thermal Interface Materials Using Natural Graphite". Proceedings of the International Electronic Packaging Technical Conference and Exhibition (InterPACK 2003), Maui, USA, July 6-11, 2003.

15. Smalc, M., Shives, G., Chen, G., Guggari, S., Norley, J. & Reynolds, R.A., "Thermal Performance of Natural Graphite Heat Spreaders". Proceedings of the International Electronic Packaging Technical Conference and Exhibition (InterPACK 2005), San Francisco, USA, July 17-22, 2005.

Chapter 3

Model Development

In Chapter 2 the concept of a Metal Micro-Textured Thermal Interface Material (MMT-TIM) was introduced. These MMT-TIMs consist of an array of small-scale metal features that plastically deform under an applied pressure between two contacting surfaces resulting in a high-conductivity TIM that is in intimate contact with both surfaces. The performance of a MMT-TIM is dependent upon a number of factors, including feature size, feature geometry, array density and material properties. Models were developed to capture the necessary physics in order to understand how these factors contribute to the thermal-mechanical properties of a MMT-TIM and to ultimately serve as a design tool for MMT-TIMs given a set of criteria such as assembly pressure and desired bondline thickness. This chapter details the development of models to predict and characterize MMT-TIM performance.

3.1 Analytical Thermal Model

Initially, a simple analytical thermal model was created to estimate the effective thermal conductivity of a simple micro-structure and to approximate the array density necessary to demonstrate improvement in effective thermal conductivity over conventional TIM technologies.

3.1.1 Analytical Thermal Model Formulation

Since MMT-TIMs consist of arrays of identical repeating features, the model can be simplified by considering a single unit-cell of the larger array. Consider the simple case of a unit-cell consisting of a single cylinder of metal between two mating surfaces, as shown in Fig. 3.1.

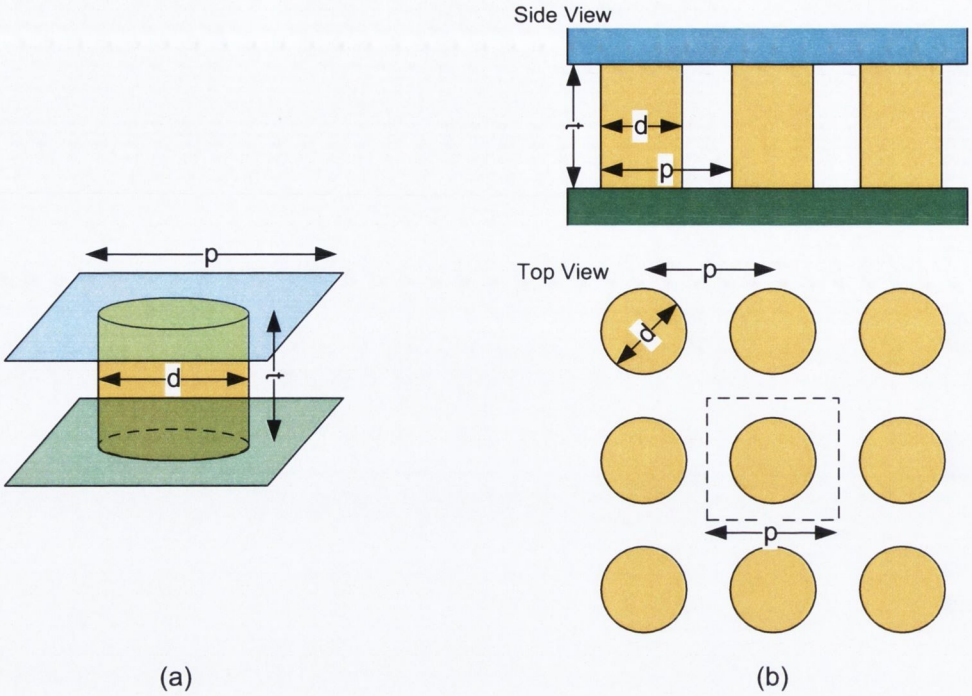


Fig. 3.1: a) Unit cell for simplified MMT-TIM thermal model, and b) an array of unit cells where d is the cylinder diameter, p is the pitch and t is the bondline thickness.

Assuming one-dimensional heat flow, the thermal resistance of this unit-cell can be modelled as two resistances in parallel and is given by:

$$\frac{1}{R_{total}} = \frac{1}{R_{fluid}} + \frac{1}{R_{solid}} \tag{3.1}$$

where

$$R_{solid} = \frac{t}{k_{solid} A_{solid}} \tag{3.2}$$

and

$$R_{fluid} = \frac{t}{k_{fluid} A_{fluid}} \tag{3.3}$$

Thus, the effective conductivity of the micro-textured thermal interface material can be written as

$$k_{eff} = \frac{A_{fluid} k_{fluid} + A_{solid} k_{solid}}{A_{fluid} + A_{solid}} \tag{3.4}$$

Written another way, the effective thermal conductivity, k_{eff}, of this structure can be represented as

$$k_{eff} = \varepsilon k_{fluid} + (1-\varepsilon) k_{solid} \tag{3.5}$$

where ε is the porosity or void fraction of the structure. This formulation is the most simplified case in that it only calculates the thermal resistance of the cylinders alone and neglects the constriction resistance associated with the sudden change of area that occurs at the interface between the mating surfaces. To include this additional effect, the unit cell with constriction resistance, as illustrated in Fig. 3.2, must be considered.

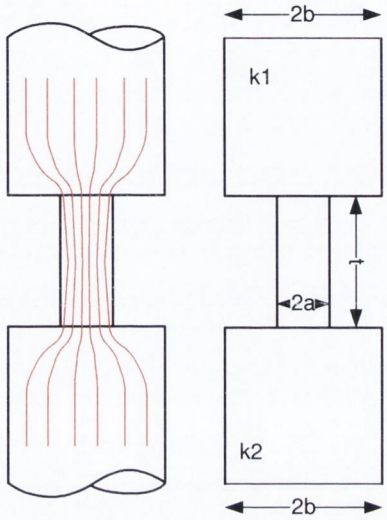


Fig. 3.2: Incorporation of constriction resistance.

These macroscopic constriction resistances can be calculated using a similar approach to that outlined in Chapter 2, Sec. 2.2.1.

Another element of the analytical thermal model is a characterization of the effect of the change in shape of the cylinders as they are compressed. If it is assumed that the cylinders remain roughly cylindrical as they are compressed, as illustrated in Fig. 3.3, the diameter ratio between initial and final states can be computed as

$$\frac{d_f}{d_i} = \sqrt{\frac{t_i}{t_f}} \tag{3.6}$$

For cases where the coefficient of friction is low, this assumption is valid [1]. Thus, the effective thermal conductivity of a unit cell containing a cylinder can be computed as a function of the bondline thickness as the structure is deformed.

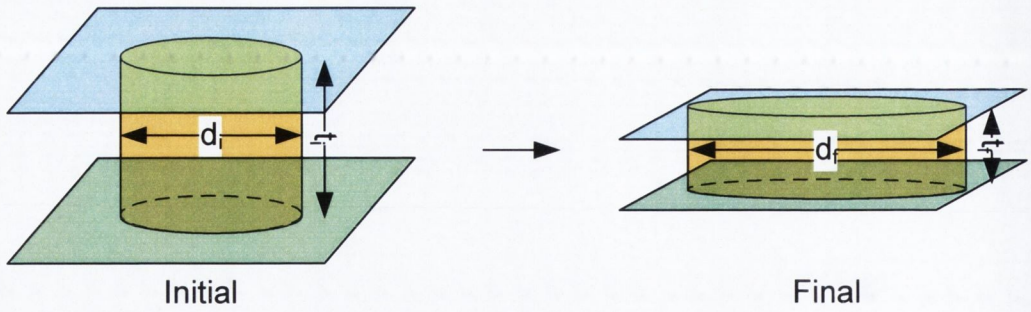


Fig. 3.3: Idealized compression of cylinders

Assuming that the top and bottom of the cylinders are in intimate contact with the mating surfaces, the total thermal resistance of the bondline unit cell can be calculated as

$$R_{unitcell} = \frac{t}{A_{fluid}k_{fluid} + A_{solid}k_{solid}} + 2R_{const} \tag{3.7}$$

resulting in the effective thermal conductivity given by

$$k_{eff} = \frac{t}{\left(\frac{t}{A_{fluid}k_{fluid} + A_{solid}k_{solid}} + 2R_{const}\right)\left(A_{fluid} + A_{solid}\right)}. \tag{3.8}$$

3.1.2 Analytical Thermal Model Results

A representative case was examined based upon arrays of gold cylinders, which could be potentially fabricated using wire bonding techniques. The cylinders were initially 50 μm in diameter and 50 μm tall and on a 200 μm pitch. Thermal conductivity of the gold cylinders was assumed to be 297 W/m·K. Perfect contact between the cylinder surfaces was assumed, whilst constriction resistance and heat transfer through the interstitial fluid were ignored. The resulting estimation for bondline effective thermal conductivity as the cylinders are compressed was calculated using Eq. 3.8 and is shown in Fig. 3.4.

The result shown in Figure 3.4 indicates that an effective thermal conductivity of >20 W/m·K could be achieved with a material that occupied only 5% of the initial contact area. As the cylinder compresses, the effective conductivity increases due to increasing contact area with the mating surfaces as the cylinder deforms. The thermal model predictions for the simple cylinder case represent a significant potential for improvement over conventional thermal interface materials whose effective thermal conductivity is generally less than 5 to 10 W/m·K.

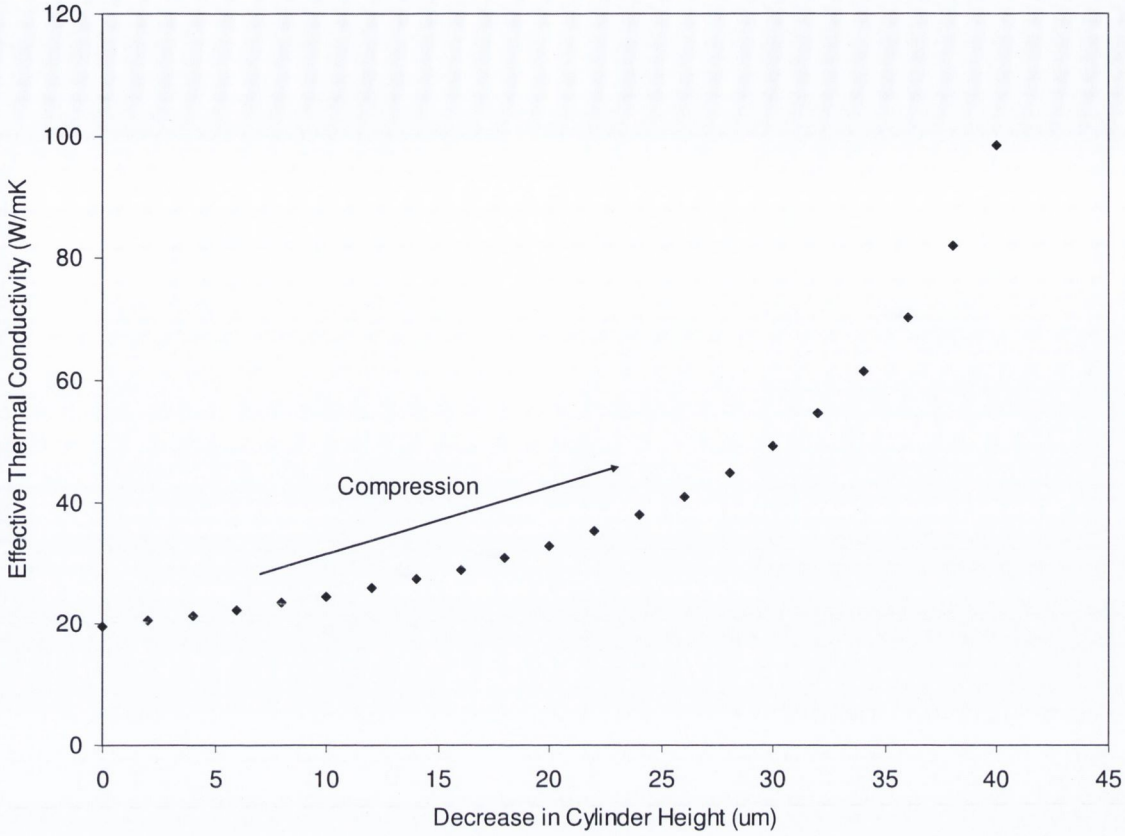


Fig. 3.4: Change in effective thermal conductivity with decreasing cylinder height.

While this simple model demonstrates the feasibility of the basic concept of a MMT-TIM from a thermal standpoint, it reveals nothing about the mechanical properties of the material, particularly the amount of pressure required to deform these structures. Intuitively, solid cylinders require relatively high assembly pressure to undergo significant deformation and thus represent a sub-optimal geometry for most practical applications. As described in section 3.2.2, we demonstrate how it proves advantageous to design MMT-TIM structures that take advantage of buckling, shearing and bending mechanisms to lower the amount of force required for deformation. To implement this approach, a numerically based hybrid thermal-mechanical model was developed to not only characterize the large plastic deformations in more complex MMT-TIM structures, but to also simultaneously model the thermal and mechanical properties as they undergo significant changes in geometry.

3.2 Simultaneous Numerical Thermal-Mechanical Model

The objective of the combined thermal-mechanical model was to simultaneously characterize both the thermal and mechanical response of a given MMT-TIM geometry as it undergoes large compressive deformation. Ultimately, the goal of the model is that it would be used as a design tool to optimize a given MMT-TIM geometry for maximum effective thermal conductivity within a desired assembly pressure and bondline thickness.

3.2.1 Numerical Model Formulation

As a MMT-TIM is compressed, the raised features undergo significant strains as they conform to the mating surfaces. Depending on the MMT-TIM geometry, several possible modes of large plastic deformation such as bending, shearing and bucking can occur that change the geometry to such a degree that it influences the overall effective thermal conductivity of the material. From a design standpoint, it is important to characterize the compressive force required to deform a MMT-TIM to a given extent. The pressure that can be applied to an assembly is generally limited to avoid damaging the underlying device. For example assembly pressures must not exceed approximately 100 psi for the case of microprocessor ICs. Furthermore, since the topography of these features can undergo significant changes, the influence of contact area and self-contact (where portions of the MMT-TIM structure come into contact with other initially non-contacting parts) during compression on the effective thermal conductivity of the MMT-TIMs must also be characterized. To accomplish this, a commercial finite element (FE) package called DEFORM (Scientific Forming Technologies Corporation) was used to simultaneously model the large plastic deformations as well as the bulk thermal response of the MMT-TIMs as they undergo large topographic changes during compression. This package was designed for modelling high-strain operations such as forging, rolling and extrusion and thus is well suited towards modelling the large plastic deformations inherent to this study [2-4].

Similar to the method employed in the simple analytical model presented in the previous section, symmetry was used to simplify the numerical model to a unit-cell consisting of a single MMT-TIM feature with the appropriate boundary conditions. A representation of a MMT-TIM unit cell bounded by the two contacting surfaces is shown in Fig. 3.5.

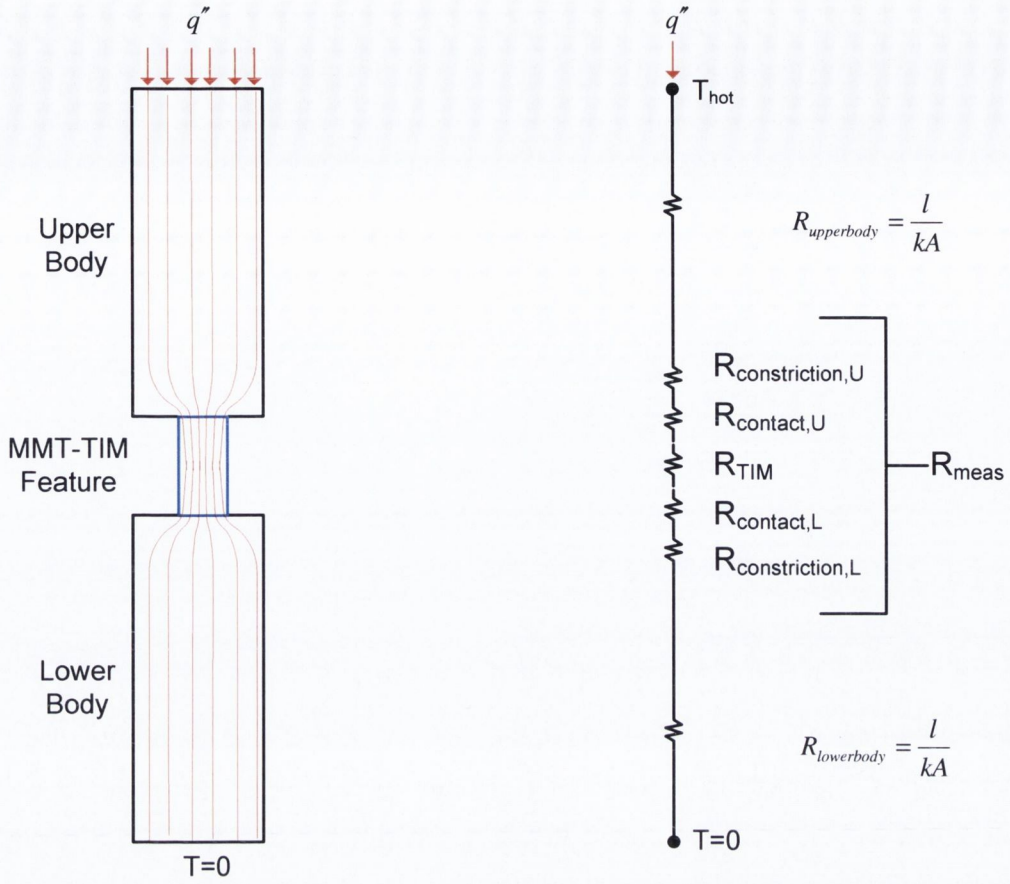


Fig. 3.5: Unit cell model for an arbitrary MMT-TIM geometry and the equivalent thermal circuit

From a mechanical standpoint, a rigid-viscoplastic material model is used. This material model behaves rigidly below a certain strain rate, after which it deforms plastically. It is often used to simulate forming operations due to its simplicity and fast convergence when used with iterative solution schemes [2]. The basic equations that are satisfied are the equilibrium condition, the incompressibility condition, boundary conditions and constitutive relations [2, 3]. These field equations can be expressed in variational form as

$$\delta\phi(v,P) = \int_V \bar{\sigma}\delta\dot{\bar{\varepsilon}}dV + \int_V P\delta\dot{\varepsilon}_V dV + \int_V \dot{\varepsilon}_V dP - \int_S F_i\delta v_i dS = 0 \qquad (3.9)$$

where v is velocity, P is pressure $\dot{\varepsilon}_V$ is the volumetric strain rate, $\bar{\sigma}$ is the effective stress, $\bar{\varepsilon}$ is the effective strain, $\dot{\bar{\varepsilon}}$ is the effective strain rate and V and S are the volume and surface of the deforming MMT-TIM, respectively [1, 2]. This equation is then converted into a set of algebraic equations using standard FEM discretization methods, and solved

iteratively using either direct methods or the Newton-Raphson method [3]. Symmetric boundary conditions were imposed at the sides of the unit-cell domain.

The accuracy of the solution depends strongly on the material properties employed by the model [4]. As a result, data for the true stress-true stain (flow stress) relationships for the materials studied here were measured experimentally using traditional compressive upsetting tests on annealed cylindrical specimens [5, 6]. Details and data regarding these tests are detailed in Appendix A.

From a thermal standpoint, by imposing a temperature/heat flux boundary condition on the system and assuming adiabatic conditions on the side surfaces, the system can be represented by the one-dimensional thermal resistance network shown in Fig. 3.5. Here the thermal resistance due to the MMT-TIM consists of its bulk resistance, R_{TIM}, the contact resistances that occur where it touches the upper and lower bodies, $R_{contact}$, and the constriction resistance that occurs in the contacting bodies themselves due to difference in contact area with the MMT-TIM, $R_{constriction}$. Thus, the apparent or measured thermal resistance of the MMT-TIM, R_{meas}, can be calculated as the sum of these five resistances in series. Numerically, the three-dimensional temperature field is calculated throughout the contacting bodies and the TIM, and the one-dimensional bulk resistances of the upper and lower contacting bodies, $R_{upperbody}$ and $R_{lowerbody}$, are subtracted from the end-to-end thermal resistance to render R_{meas}.

The temperature distribution in the MMT-TIM and upper and lower bodies is obtained by solving the energy balance equation, written here using the weighted residual method, as

$$\int_V kT_j \delta T_j dV + \int_V \rho c \dot{T} \delta T dV - \int \alpha \bar{\sigma} \dot{\bar{\varepsilon}} \delta T dV = \int_S q_n \delta T dS \tag{3.10}$$

where k is the thermal conductivity, T is the temperature, ρ is the density, c is the specific heat, α is the fraction of mechanical energy that is converted into heat, and q_n is the heat flux normal to the surface [2]. For the purposes of the simulations carried out here, α is set equal to zero since the quantity of generated heat is irrelevant over time in comparison to the measurements obtained from the larger steady-state thermal solution. As illustrated in Fig. 3.5, a uniform heat flux boundary condition was imposed on the top-most surface of the upper body, while a uniform temperature was imposed on the bottom surface of the lower body. An adiabatic (symmetrical) boundary condition was imposed on the sides of the unit cell domain. Similar to the mechanical formulation, standard discretization methods were used to convert Eq. 3.10 into a set of algebraic equations.

For most typical simulations designed to be carried out by DEFORM and other multi-physics packages, the simultaneous solution of the temperature fields are relevant in order to accurately calculate any temperature dependent material properties that may affect the mechanical solution. For the present study, however, this approach is reversed. Here, the primary interest is the influence of overall MMT-TIM geometry and contact conditions on the thermal solution. While capable of carrying out temperature dependent simulations, this aspect was not considered, nor was it necessary in the present models since the corresponding experiments were carried out at a relatively constant room temperature.

The geometry of the MMT-TIM unit cells and contacting bodies were discretized using a sufficient number of tetrahedral elements, and the deformation of the structures was calculated using an updated Lagrangian finite element formulation [2]. An example mesh for a conical MMT-TIM feature is shown in Fig. 3.6. The structure was loaded by controlling the downward displacement of the upper surface, while the lower surface remained stationary. The total deformation of the moving die was applied in small steps to maintain the accuracy of the solution. The self-contact algorithm of DEFORM was employed to ensure the collapsing MMT-TIMs did not intersect themselves and give physically unrealistic solutions. In problems involving large deformations, the quality of the mesh in many simpler FE packages can quickly degrade, causing poor predictions of element stresses and possible numerical instabilities. This issue is handled automatically in DEFORM by remeshing areas of the geometry where excessive element distortion has been detected. The software constructs an optimum mesh in these areas, based upon the curvature of the area and its previous solution behaviour [3]. This local remeshing tool avoids the need to remesh the entire structure, thus maintaining simulation accuracy while being computationally efficient.

During the deformation analysis, the changing geometry leads to different levels of contact within the model for a given step. As the number of nodes in contact is constantly changing, unsteady thermal solutions would be predicted. Since it is desirable to extract only steady-state temperatures for accurate comparison with experimental results, the mechanical simulation was run to completion first. The resultant geometries, boundary and contact conditions from the mechanical simulation were then imported into the multiple operations environment in DEFORM where the subsequent heat transfer computations were carried out at the desired deformation steps. The time over which the heat transfer calculations were conducted was set to be sufficiently large to ensure a steady-state solution was reached; typically, this was on the order of 20×10^3 seconds for each deformation step.

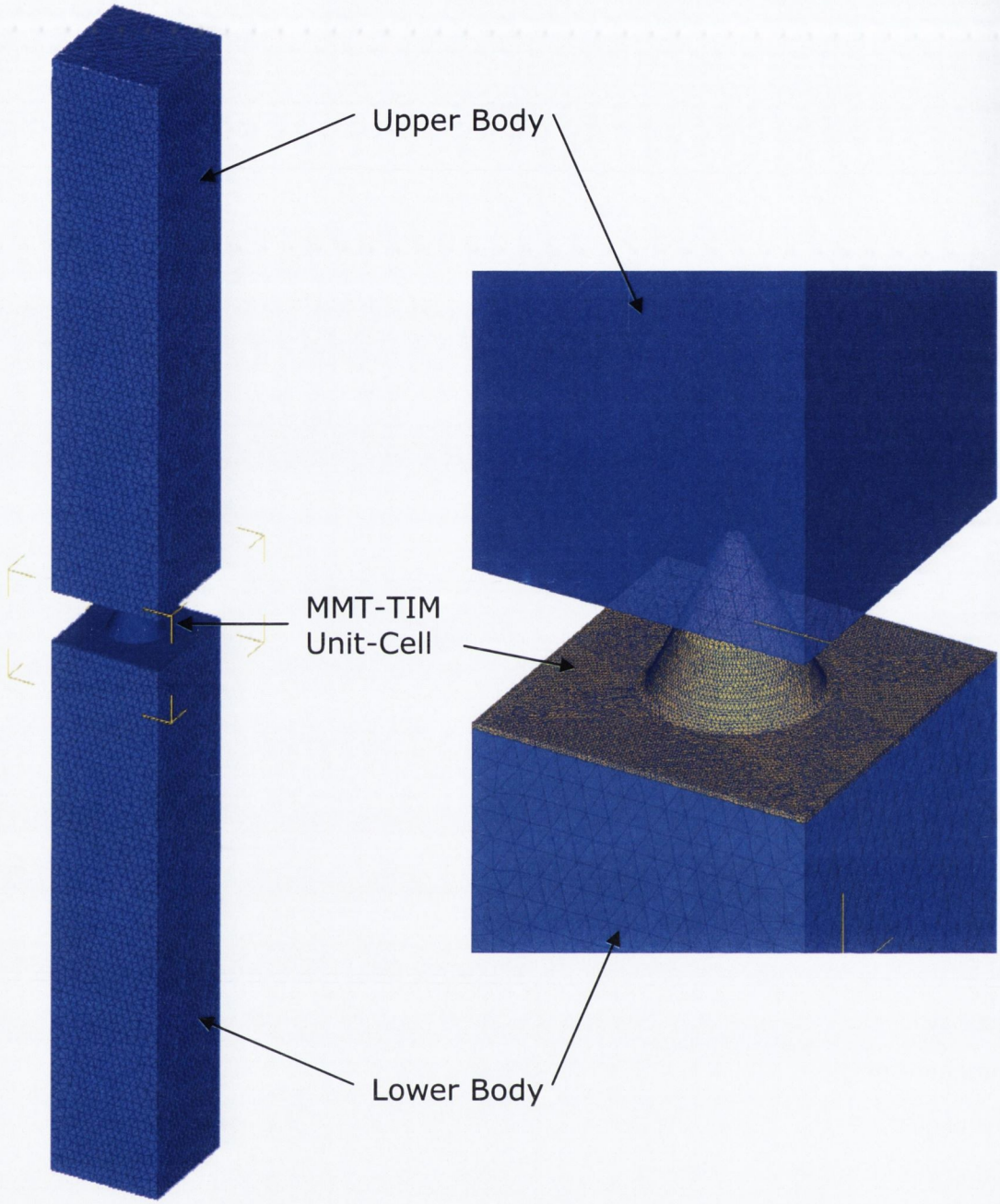


Fig. 3.6: Typical meshed MMT-TIM unit cell showing conical MMT-TIM geometry

From the mechanical-only simulation, information regarding the overall compressive force as well as individual nodal positions and pressures in the MMT-TIM unit-cell were exported to ASCII data files. Thermal results, consisting of the temperature distribution through the MMT-TIM and contacting bodies as calculated by DEFORM were exported to separate ASCII data files. DEFORM is capable of modelling thermal contact resistance by defining either a constant or pressure dependent heat transfer coefficient for the contacting surfaces. However, due to restrictions in transferring contact pressure data between the two simulations, the thermal contact resistance was ignored during the

DEFORM thermal simulation and the effect of contact resistance was modelled subsequently during post-processing in MATLAB. Details regarding thermal contact resistance modelling are discussed further in Sec. 3.4.

MATLAB was used to perform calculations of the MMT-TIM thermal resistance and effective thermal conductivity of the MMT-TIM structure as a function of deformation and pressure by combining the exported mechanical and thermal data from the two DEFORM simulations. A listing of this code is presented in Appendix 2.

3.2.2 Comparison between Numerical and Analytical Models

In order to validate the numerical modelling approach, a direct comparison of the calculated thermal resistance of a solid cylinder was performed between the combined thermal-mechanical numerical model and the analytical thermal model presented in the previous section.

For an initial comparison, the thermal and mechanical response of a solid silver cylinder 1 mm tall and 1 mm in diameter being compressed between two flat bodies having contact areas of 3 mm × 3 mm is presented. The stresses inside the silver cylinder were calculated based on empirical true stress-strain data. A thermal conductivity value of 420 W/m·K for silver was assumed. The contacting bodies were modelled as rigid with a thermal conductivity of 215 W/m·K. A comparison between the analytical and numerical models for a variety of conditions is shown in Fig. 3.7. Here, the thermal resistance of the unit cell is plotted for a variety of conditions. Curve "A" represents the thermal resistance of the cylinder alone as calculated by Eq. 3.2, neglecting any constriction resistance within the contacting bodies or any contact resistances at the contact surfaces. As it is shown the thermal resistance is initially relatively high; however, as the cylinder is compressed, it drops significantly as both the contact area enlarges and the bondline thickness is reduced. The effect of constriction resistance in both the upper and lower contacting bodies is introduced in curve "B" which accounts for the additional resistance due to the change in area at the contacting surfaces. Finally, the added contribution of thermal contact resistance is incorporated in curves "C" and "D". For curve "C" the contact resistance was calculated based on a constant contact heat transfer coefficient, h_c of 1×10^6 W/m^{2}K, whereas the contact resistance calculated for curve "D" was based on a value of contact heat transfer coefficient that varied as a function of interface pressure, which is more likely to be the case in reality. For the purposes of comparison this heat transfer coefficient was arbitrarily defined as

$$h_c = 5\times10^4 \ln(P) + 2\times10^5 \tag{3.11}$$

where h_c is the contact heat transfer coefficient in W/m^2K and P is the contact pressure in MPa.

Clearly, for each case represented in Fig. 3.7, there is excellent agreement between the results predicted by the analytical model and the numerical model for this simple cylindrical geometry. This indicates the numerical model is capturing the necessary physics required to characterize more complex geometries.

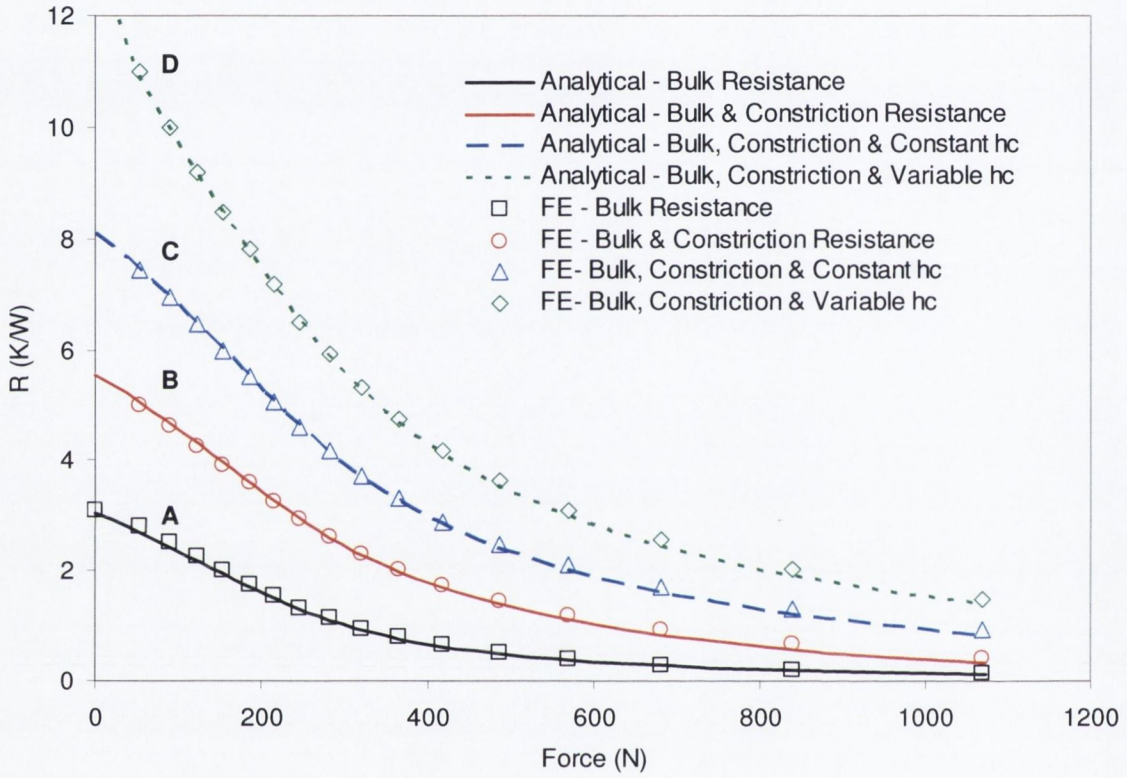


Fig. 3.7: Comparison between the analytical and numerical (FE) models for the variation of thermal resistance for a silver cylinder with force during compression

3.2.3 Initial Comparison to Experimental Results

As discussed in Chapter 2, the embodiment of MMT-TIMs in the present study is textured metal foils consisting of arrays of hollow raised features. These types of geometries represent a significant reduction in the amount of pressure required for significant deformations compared to solid cylindrical or conical features.

An initial investigation into MMT-TIMs with hollow conical geometries was performed by Kempers *et al.* [7]. Here, the geometry under consideration is represented in Fig. 3.8.

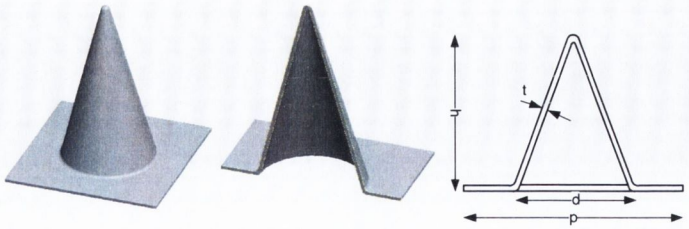


Fig. 3.8: a) 3D view of nominal MMT-TIM geometry, b) 3D cross-section, c) Schematic of cross-section with key dimensions labelled

For this preliminary investigation, the height of the cones was approximately 2.2 mm, the base diameter approximately 1.35 mm, spaced on 2 mm pitch. These cones were assembled into arrays of 20 × 20 features which covered a surface of 40 mm × 40 mm. Deformation of the entire array was conducted simultaneously. Metal thicknesses of 15, 23 and 44 μm were tested and compared to results predicted by the combined numerical model. These overall dimensions were measured using a conventional optical microscope and used to construct 3D solid geometries for use in the numerical model. As mentioned in the preceding section, model results were calculated based on a unit cell containing a single hollow cone element.

A comparison between the effective thermal conductivity measured experimentally and that predicted by the model for the case where t = 23 μm is shown in Fig. 3.9. The experimental results were obtained using a test facility detailed in Kempers *et al.* [7] and will be discussed in detail in Chapter 4.

Generally speaking, all three of the model predictions roughly follow the trend exhibited by the experimental data. This is illustrated in Fig. 3.9 where the results for the 23 μm thickness case are shown. However, there exists a slight offset, which is thought to be due to the relative contributions of the contact resistance. The model prediction using an extremely high heat transfer coefficient (1×10^9 W/m^{2}K) completely negated any contact resistance effects and predicted an effective thermal conductivity for the MMT-TIM somewhat higher than the experimental result. As the HTC was dropped to a constant value of 2.5×10^6 W/m^{2}K, quite good agreement between the model and the experimental results was observed.

From a mechanical response standpoint, the comparison between the pressures predicted by the numerical model and those of the experimental results is shown in Fig. 3.10. A series of corresponding images depicting the predicted deformation of this unit cell are shown in Fig. 3.11.

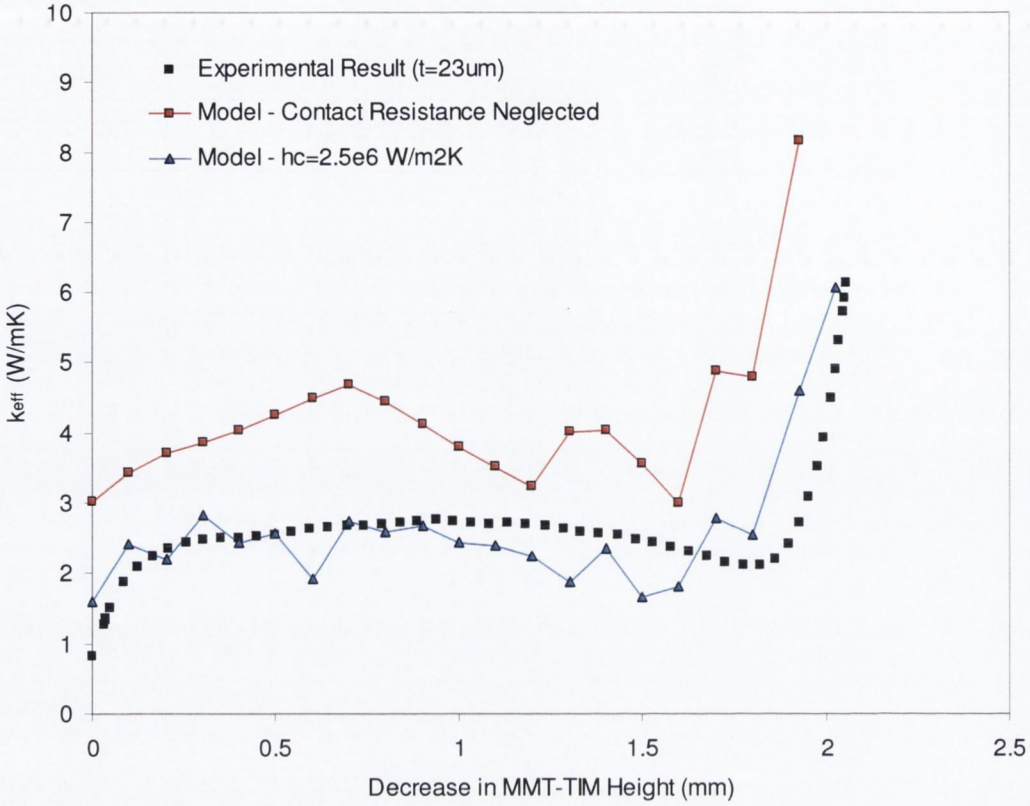


Fig. 3.9: Comparison of effective thermal conductivity of MMT-TIM during compression with initial model results.

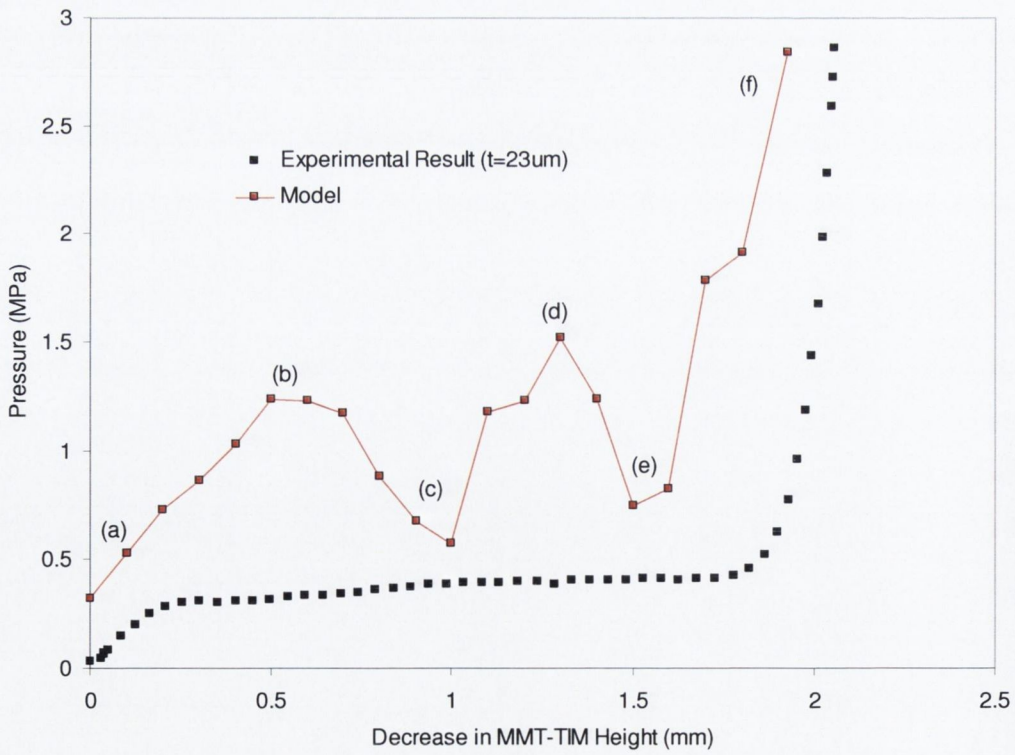


Fig. 3.10: Comparison of applied pressure during MMT-TIM compression with initial model results

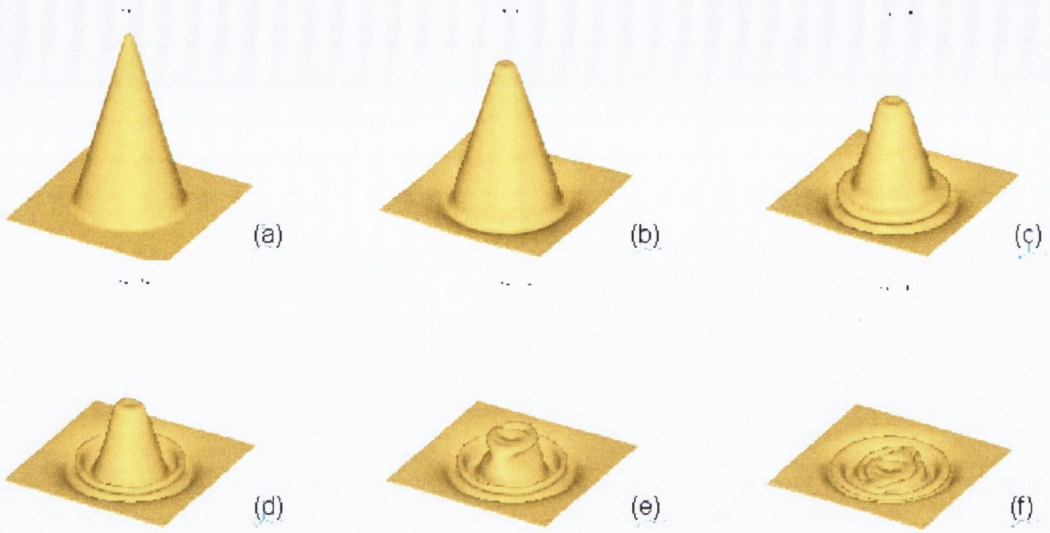
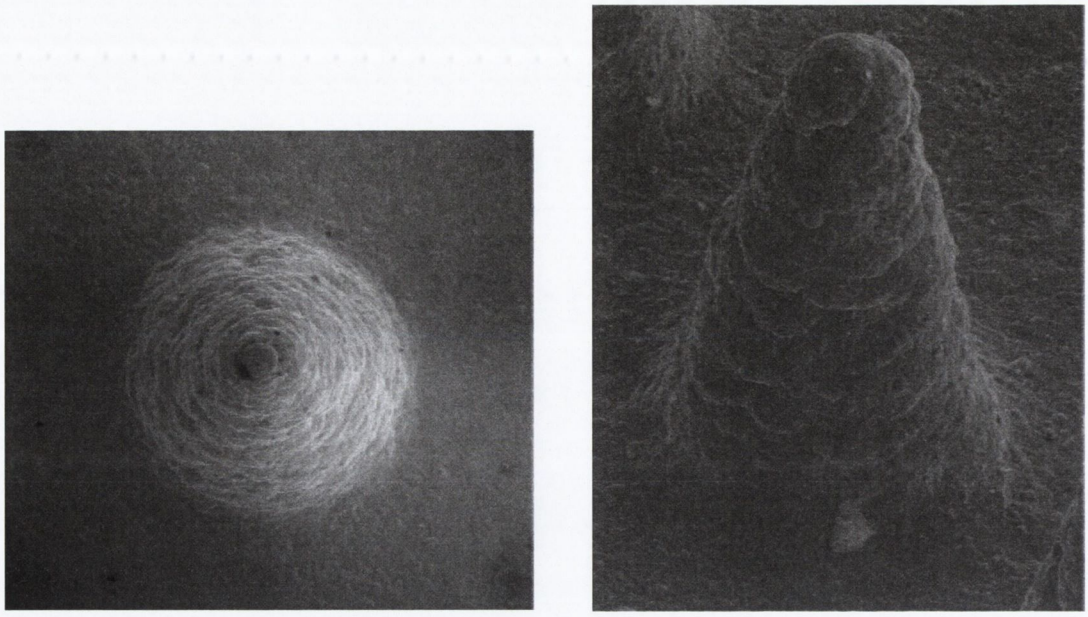


Fig 3.11: Model prediction of MMT-TIM unit cell undergoing deformation corresponding to Fig. 3.10

From Fig. 3.10 it is clear that the pressure required to deform the MMT-TIM to a given height, as predicted by the model, is generally higher than the pressure exhibited experimentally. Furthermore, the model predicts a response that consists of two distinct peaks before the MMT-TIM begins to densify significantly. The images in Fig. 3.11 show the model predicting a relatively uniform azimuthally buckling response where the structure collapses downwards in successive concentric rings. The formation and subsequent collapse of these rings correspond to the peaks and troughs in the model prediction shown in Fig. 3.10.

These MMT-TIMs were manufactured using the method described in Chapter 2. Images obtained using a scanning electron microscope (SEM) of a single conical feature for this MMT-TIM geometry are shown in Fig. 3.12. It is obvious from the pictures that the real structure deviates considerably from the idealized geometry used in the simulation environment shown in Fig. 3.8. In reality the overall conical shape is characterized by a series of bumps and imperfections due to the 3D printing process used to generate the plating template. During plating, these translate into undulations and stress concentrations in the MMT-TIM itself. These stress concentrations would encourage non-uniform buckling and bending in the features, resulting in a structure that would not necessarily deform in the uniform manner predicted by the model in Fig. 3.11. In particular it would be expected that the real structures would deform more easily under applied load which is consistent with what was observed experimentally.



(a) (b)

Fig. 3.12: An SEM images of a single conical MMT-TIM feature from a) above and b) obliquely

To summarize the observations discussed in this section as well as the initial results presented by Kempers *et al.* [7], there are two major modeling challenges to achieve improved prediction of MMT-TIM performance: 1) an improved representation of the MMT-TIM geometry resulting an improved estimation of the mechanical response of the MMT-TIM and 2) estimation of the thermal contact conductance for the MMT-TIMs as they undergo large plastic deformations which would lead to more accurate thermal results. The following sections discuss strategies to address these issues.

3.3 Accurate Characterization of MMT-TIM Geometry

In Sec. 3.2.3, it was hypothesized that the idealization of the MMT-TIM geometries in the numerical model contributed to the lack of agreement between the mechanical response predicted by the model and those realized experimentally. Not only does there exist uncertainty in overall dimensions such as feature diameter or height, but there also exists small-scale variations in surface topography that can contribute to variations in the deformation mechanisms as well.

In order to improve the overall accuracy of the geometrical measurement of MMT-TIM unit cells, as well as capture the necessary details to systematically characterize the various surface imperfections and anomalies, it was decided that a technique known as three-dimensional (3D) stereo microscopy (or stereoscopy) be used to reconstruct the MMT-TIM surface topography using 2D images obtained from a scanning electron microscope (SEM).

This section details the important aspects of this technique as it applies to the present study. Specifically this section will describe the creation of a solid geometry of a single MMT-TIM unit cell that is representative of the larger MMT-TIM array and is readily usable in the FE model outlined in the previous section.

3.3.1 Background & Literature Review

Images obtained via scanning electron microscopy are well suited for subsequent 3D surface reconstruction because the SEM combines high spatial resolution with a large depth of field. Long acquisition times can be used, along with multiple sampling and noise reduction algorithms, to further improve the final image. An SEM is also typically equipped with a precision controllable sample stage which allows for highly repeatable and reproducible movements which are necessary since known tilt angles and working distances are often a prerequisite for the purpose at hand. Finally, the nature of the gathered secondary electron image means the information contained in the electron micrograph has inherent topographical information which can be used to give quantitative height information once the 3D reconstruction process has been completed.

A number of techniques have been developed in order to reconstruct 3D surfaces using 2D SEM imaging data with the major key advancements in this area discussed by Beil & Carlsen [8]. Generally, these approaches can broadly be divided into two groups: The photometric or so-called "shape from shading" approach and the more popular stereoscopic method [8, 9].

Paluszynski & Slwoko [9] discuss the photometric or "shape from shading" approach. This involves the use of multiple detectors placed symmetrically at known angular coordinates around the specimen. By comparing the topographical contrast of secondary and back scattered electrons from opposing detectors, information about the specimen topography can be obtained in terms of both the x and y coordinates through the integration of the normalized differential signals [8, 9]. The advantage of this approach is that it is able to reconstruct relatively smooth objects which are lacking the unique and identifiable surface details required for the stereoscopic method. The accuracy of the resulting surface is critically dependant on the symmetry between detectors and similarity in their sensitivity and subsequent signal amplification [8] making it inherently susceptible to distortion errors [9, 10]. To improve the accuracy of this method, several signal processing techniques have been suggested [10].

The more popular approach towards 3D surface reconstruction is stereoscopy [9] and a number of studies have described this technique in various ways [11-16]. Generally, the principle is based upon using the perspective shift between two images captured at a known angle relative to each other to obtain surface elevations. This involves two steps: First, homologous points representative of corresponding features between images are identified in the stereopair using various pattern matching algorithms [16]. Secondly, the z-coordinates can then be obtained by trigonometry. The heights of the surface features are calculated based on the change in their lateral displacement. The z-coordinate of each pixel is then calculated based upon the parallax movement of each feature [16]. Details regarding the implementation of this technique are discussed in [11, 13, 16] while a discussion of error analysis of this method is presented in [12] and important factors relating to accuracy in [16]. The main drawback of this technique is that, due to the reliance on matching surface topography, it is only applicable to any part of the image showing a uniquely identifiable texture [8]. Another drawback is that the accuracy of the calculated surface depends on the accuracy of the known tilt angle between the two images [11, 13]. However, to address this issue, Danzl *et al.* [14] and Schrottner *et al.* [15] present a method for automatically calibrating the tilt angle by using three images to generate a so-called "stereotriplet" which represents the average of three stereopairs and ultimately improves the overall accuracy of the z-coordinate calculation [16].

In the present study, the application of the stereoscopic 3D surface construction technique is extended by using the 3D surface data generated by the software to create a solid geometry representative of an actual sample for the purposes of subsequent FE modelling. Here, the subject of interest is a single MMT-TIM unit cell. This 3D solid

body is then incorporated directly into the combined mechanical-thermal numerical model, detailed in the previous section, to yield an improved mechanical response compared to idealized geometries based upon conventional spatial measurement techniques.

3.3.2 Image Acquisition

A Carl Zeiss EVO MA-25 Scanning Electron Microscope (SEM) was used to obtain secondary electron images of a particular MMT-TIM unit cell. The system was configured in variable-pressure (VP) mode to allow the imaging of out-gassing samples without the need for sample coating or plasma cleaning, with the aim of preserving subtle surface texturing and avoiding any medication of the sample surface.

An illustration of the setup used to capture the images is shown in Fig. 3.13. The MMT-TIM samples were mounted on a purpose-built 10° wedge-shaped block which was then was mounted to the microscope stage. Since the microscope stage is capable of tilting from -1 to +90 degrees about the *y*-axis, this modifies the tilt range to -11° to +80° from the vertical (normal) position.

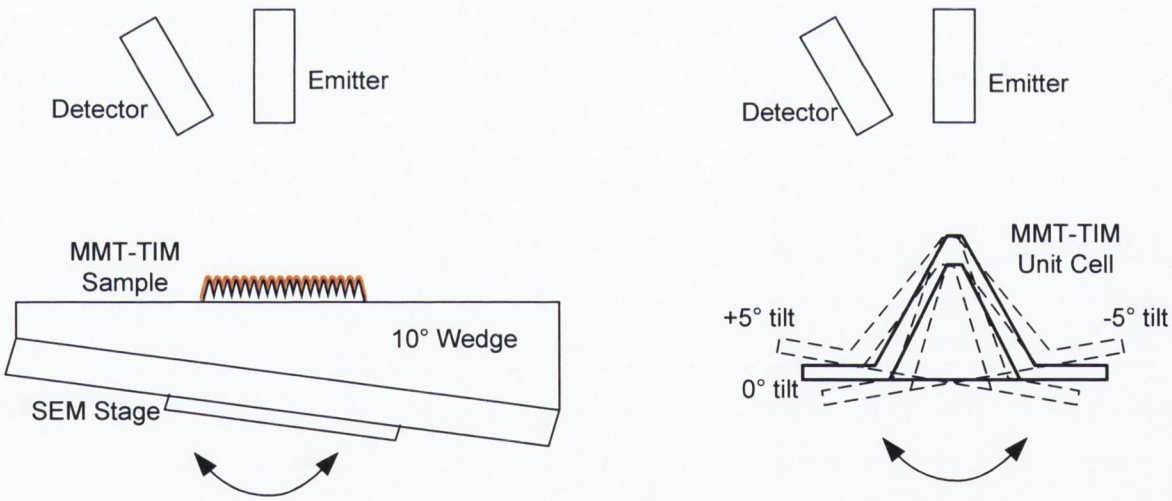


Fig. 3.13: a) Side view of SEM setup for imaging MMT-TIMs for 3D surface reconstruction, b) eucentric tilting of an individual MMT-TIM unit cell

The SEM was set to a pre-defined working distance between the sample surface and the end of the electron column and the sample tilted eucentrically under the electron beam as shown in Fig 3.13b. A series of three images were captured centred about the 0° tilt position (top down). Tilt angles of -5°, 0° and +5° were found to achieve a reasonable representation for the features characterized in the present study.

Since the geometries of interest in this study are relatively large by SEM standards, a magnification range of between 30× and 50× was employed to allow the viewing of one

entire unit cell of the sample. For larger features, it was necessary to focus the SEM on a point midway up the side of the feature in order to maximize the available image depth-of-field. Additionally, since the field of view is reduced somewhat during tilting, it was necessary to capture enough area surrounding the unit-cell such that the reconstructed surface is equal to or greater than the unit-cell size. The capture resolution can be varied from 0.5 to 6 megapixels, however a 1MP image was deemed sufficient to satisfy the necessary pixel spatial resolution for subsequent 3D surface generation while minimizing the computational effort. The resultant spatial resolution was on the order of 3 to 4 μm per pixel, depending on image magnification.

3.3.3 Surface Reconstruction

Stereoscopic 3D surface reconstructions in the present study were obtained using the commercial software package, MeX™ (Alicona Imaging, GmbH) which takes advantage of the aforementioned three-image accuracy improvements [14-16] and carries out pattern matching and subsequent geometric assessment as described above [17]. An example result is shown in Fig. 3.14. The 3D surface data generated is in functional form of z; that is, for a given x-y coordinate, there is only one unique z value. This data is exported from MeX in ASCII format to a text file. To minimize subsequent computation effort while maintaining the necessary spatial accuracy necessary to capture the important nuances of the MMT-TIM geometry, typically the data was down-sampled to a resolution of 4 pixels per data point which was found to be adequate for most cases. This translates to an x-y spatial resolution on the order of approximately 12 μm while the z-coordinate resolution is on the order of the input image resolution (3 to 4 μm).

3.3.4 Data Processing and Generation of Solid Geometry

The 3D surface data generated by MeX was then imported into MATLAB for processing. A listing of the MATLAB code used to accomplish this is presented in Appendix C. What follows is a descriptive summary:

Firstly, the surface data was cropped to the defined unit-cell size based on the centre of the MMT-TIM feature of interest as shown in Fig. 3.15. This was accomplished by first identifying the centre point of the unit-cell and subsequently removing any data that lay outside the unit-cell perimeter. Typically, for the geometries studied in the present work, this was the local maximum of the surface data. However, for more complex geometries, the operator is allowed to define the centre point for cropping of the unit cell.

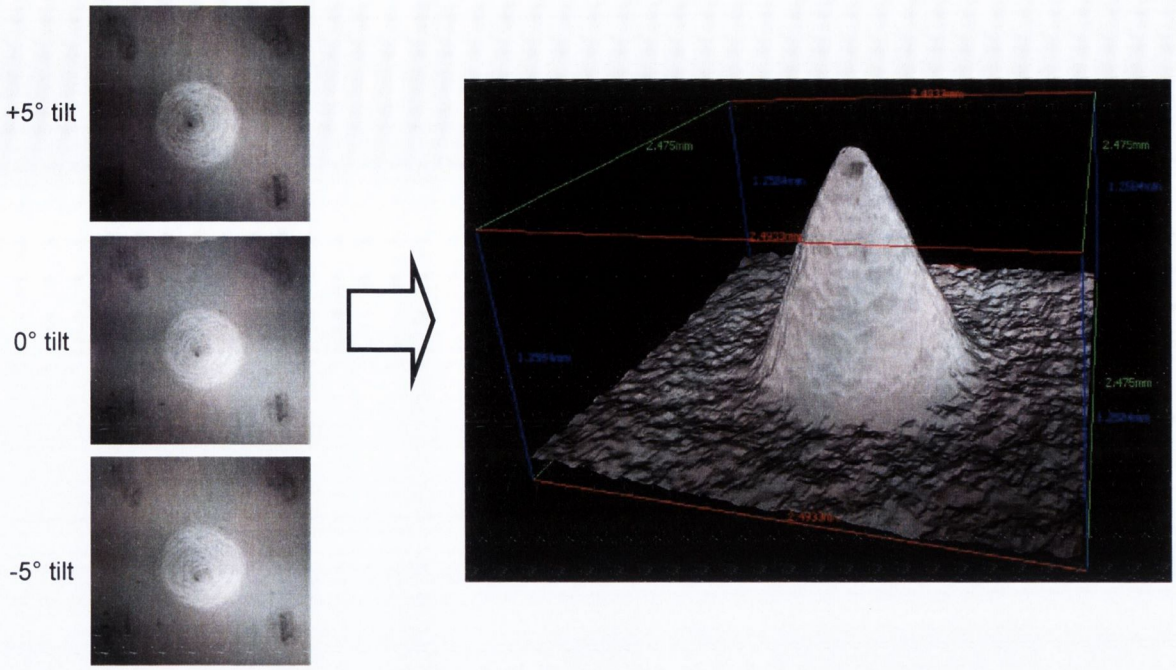
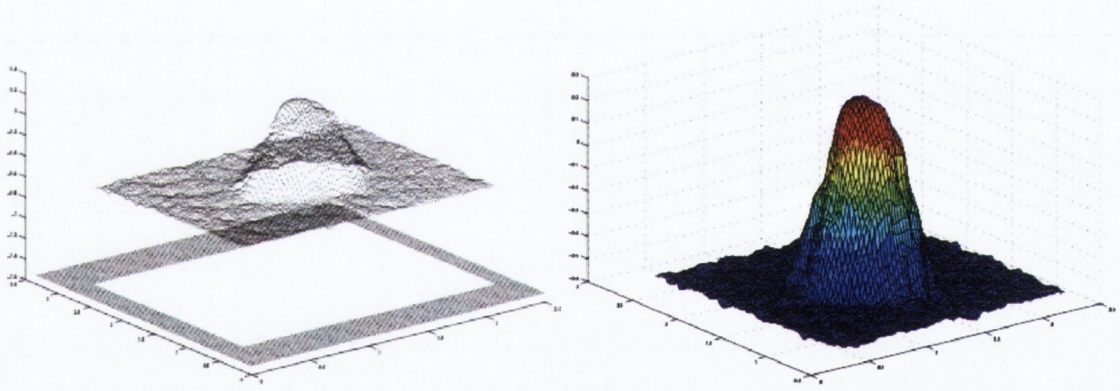


Fig. 3.14: The 3D surface of a MMT-TIM generated using stereoscopic imaging with MeX



(a) (b)

Fig. 3.15: a) Original MeX output data set, b) surface data cropped to the specified unit cell size

Secondly, a mild blurring filter was applied in order to attenuate any high-frequency "noise" in the surface data. The usage of relatively high export spatial resolutions from MeX would sometimes result in the output of physically unrealistic surface aberrations. Upon subsequent thickening, these local maxima and minima would occasionally result in undesirable solid artefacts, impeding the quality of the eventual FE mesh. This filter was applied directly in MATLAB through the 2D matrix convolution function.

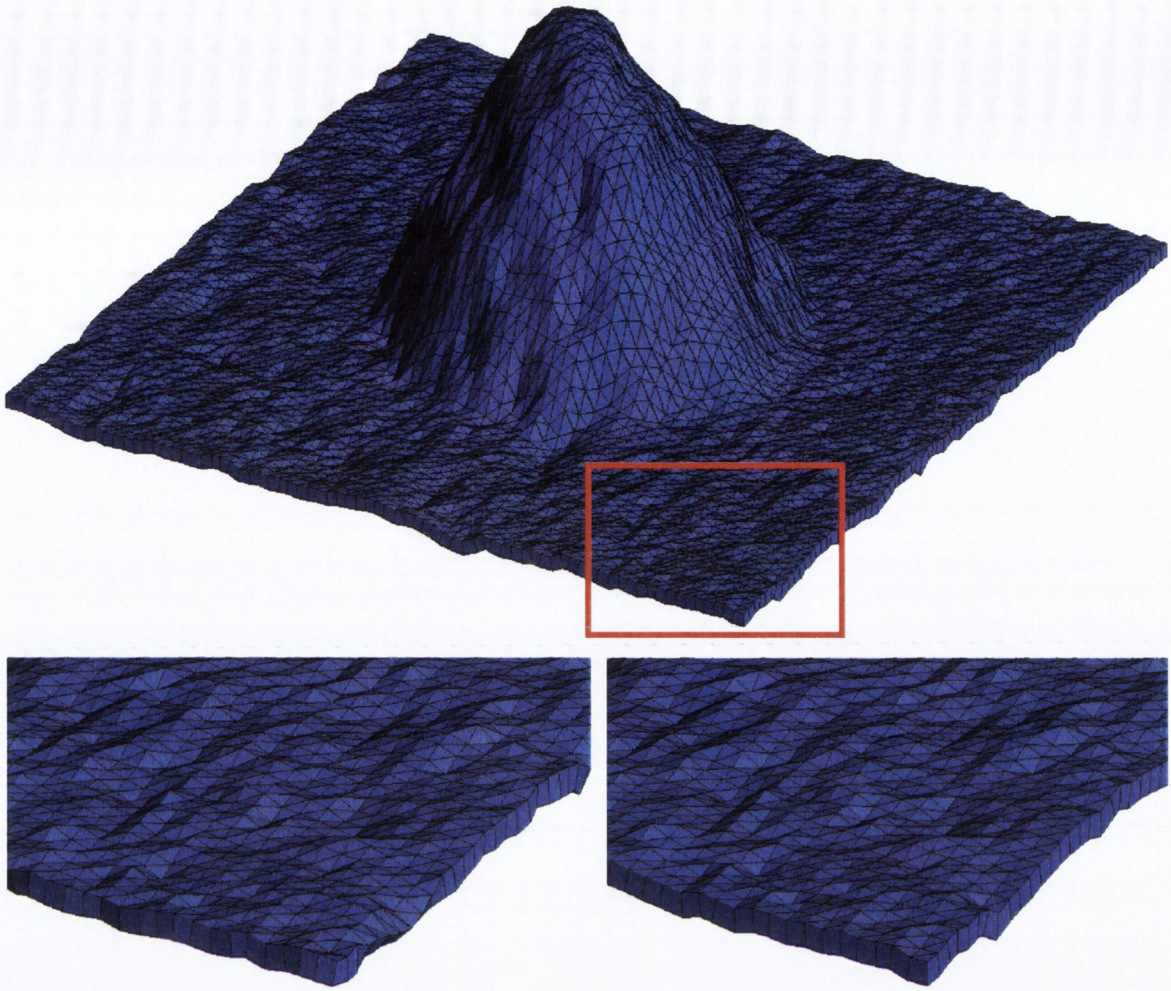
Thirdly, in order to generate surfaces that are amenable to the boundary conditions imposed by the numerical model upon thickening of the 3D surface, the edges of the 3D

surface were made orthogonal to the vertical plane by setting the z-coordinate of the second data point in from the perimeter equal to that of the corresponding perimeter data point. This allows for a more straightforward implementation of the boundary conditions necessary to model this unit cell in DEFORM, in particular the symmetric boundary condition imposed during the deformation simulation.

Finally, the processed 3D surface data was exported as a surface STL file and "thickened" a desired amount in order to create a solid body from the 3D surface data. The commercial 3D modelling software, Form·Z (AutoDesSys, Inc.) was used to generate a surface which is everywhere parallel to the facets of the 3D surface at a desired distance. Fortuitously, this approach is analogous to the reverse of the manufacturing approach for the MMT-TIMs in the present study: Here one begins with the "outer" surface of the MMT-TIM and thickens this surface "inwards" to what would be the geometry of the wax template. The aforementioned technique of equalizing the z-coordinates to one point inside the perimeter serves to create a vertical surface upon thickening, parallel to the sides of rest of the unit cell domain. This effect is illustrated in Fig. 3.16.

While it is hoped that the chosen MMT-TIM unit cell is representative of the larger array, variations in the exact height of the chosen reconstructed unit cell and the average measured MMT-TIM height may be present. These discrepancies can be adjusted in Form·Z by scaling in the z direction. This allows for the reconstructed geometry to better correspond with the experimental data while also maintaining the systematic approach to the geometry reconstruction.

The thickness of the solid feature was determined by weighing the entire MMT-TIM array in an analytical balance and calculating the volume of a single unit cell based upon the density of the metal. From this, the desired thickness could be obtained iteratively by calculating the volume of a thickened geometry (PTC ProEngineer) and adjusting the thickened layer until the correct volume is reached. This approach assumes that the thickness of the MMT-TIM plating is relatively uniform. Indeed cross-sectional micrographs of the initial prototype MMT-TIMs, shown in Fig. 3.17, show this to be a valid assumption despite some smearing that occurred during polishing. Furthermore, measurements of the metal thickness in this cross-section were consistent with the mass estimated value. The final solid geometry was then exported as a solid STL file for importation to DEFORM.



(a) (b)

Fig. 3.16: Effect of edge condition of a thickened surface for, a) raw edge surface data resulting in a non-uniform perimeter surface, b) equalized edge z-coordinates resulting in a uniform vertical surface at the boundary

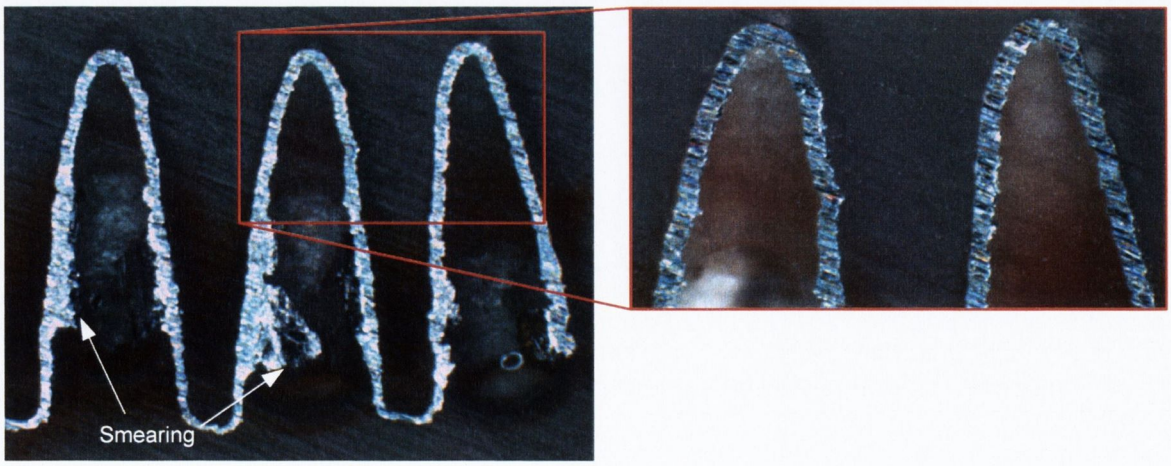


Fig. 3.17: Cross-sectioned prototype plated MMT-TIM demonstrating relatively uniform plating thickness with regions of smearing noted

3.4 Characterization of MMT-TIM Thermal Contact Resistance

As detailed in 3.2, a numerical model was developed that couples the mechanical and thermal properties with the behaviour of MMT-TIMs as they undergo large-plastic deformation during compression. These predict the thermal resistance and effective thermal conductivity of the bulk MMT-TIM as well as its mechanical response. However, to achieve these predictions, an empirical fit parameter was used for the thermal contact resistance [7].

Significant effort has been put forth in order to characterize and model the contact thermal resistance or conductance for a variety of contacting surfaces [18-19]. As discussed in Chapter 2, contact resistance is typically modelled by analytically calculating the thermal constriction resistance of a single contact spot using various geometries and boundary conditions. The number of contact spots, and the mean contact spot radius, are then modelled using statistical surface characterizations and mechanical deformation analysis. These models generally produce reasonable predictions of thermal contact conductance for a range of engineering surfaces; however, they require detailed knowledge of the properties of the contacting surfaces *a priori*. Furthermore, these models typically assume that there is little or no macroscopic plastic deformation of the contact surfaces or significant changes in contact area as pressure is applied. Thus, for the purposes of modelling the contact between MMT-TIMs and rigid surfaces, they are inadequate.

From an experimental standpoint, the challenge in characterizing the thermal resistance of MMT-TIMs is distinguishing the bulk thermal resistance of the MMT-TIM from the contact thermal resistance between the MMT-TIM and the meter bars of the test apparatus. Typically, for conventional, homogeneous TIMs, the contact resistance can be characterized experimentally by measuring several thicknesses of the TIM, plotting the thermal resistance as a function of thickness and extrapolating contact resistance as the y-intercept where the thickness is zero [20]. For MMT-TIMs however, this method cannot be used due to the non-uniform behaviour of the bulk TIM.

The thermal contact resistance and electrical contact resistance are qualitatively similar, as both of these phenomena depend on the ratio of actual, intimate contact area to the apparent contact area [18, 21]. However, whereas thermally the bulk resistances are of similar orders of magnitude as the contact resistances, electrically the resistances of the bulk MMT-TIM are extremely small compared to the resistance at the contact surfaces. For these MMT-TIMs, it has been proposed that a relatively straightforward electrical resistance measurement be employed to characterize the thermal contact resistance [7].

3.4.1 Literature Review

The use of a simple electrical resistance measurement to characterize actual contact area has been considered before, particularly in the areas of mechanical wear and tribological applications [22-24].

Jones *et al.* [22] review a number of experimental methods for determining the real contact area and discuss the use of both thermal and electrical contact resistance measurements. They state that the mechanism for electrical resistance is essentially the constriction resistance to election flow at the contact spot. On the other hand, the mechanism for heat transfer is more complicated since there is not only the analogous constriction resistance, but also conduction through the interstitial gas and the potential for direct radiation across the interspaces which have no electrical analogy. Furthermore, electrically insulating surface oxides can be thermally conducting since they allow a flow of phonons despite the inhibition of electron movement. This can serve to potentially decrease the thermal resistance while simultaneously increasing the electrical resistance [22]. They go on to suggest however that since the electrical measurement can be made relatively easily, it can be used to give qualitative indications of the effects of surface topology on the thermal contact resistance. However, they restrict this use to high-vacuum, cryogenic conditions to eliminate conduction and radiation through the interstitial gaps [22].

Woo & Thomas [23] also reviewed a number of experimental techniques for determining the contact geometry and actual contact area of solids. They discuss electrical and thermal conduction, noting that the total number and size of the contact spots tend to be underestimated by electrical methods since the presence of oxide films between the contacts increase their effective resistance. They also point out that a correction must be made for heat conducted across the interstitial air gaps [23].

Filayev *et al.* [24] employed electrical contact resistance measurements to determine the actual contact area of conducing samples during sliding contact. Here they assume that the electrical contact resistance depends on the sum of the elementary areas of actual contact and behave as conductors in parallel. However, they point out that quantitative values of the actual contact area cannot be obtained using this method due to the lack of a value for the electrical resistance corresponding to a fixed value of actual contact area. This was overcome by testing steel components of varying apparent mating contact areas including one continuous component where the actual contact area was equal to the apparent contact area. Using this method, they examine the change in ratio of actual contact area to apparent contact area as a function of pressure and demonstrate a rapid

increase in contact area at pressures below 0.5 MPa where the actual contact area is approximately 3% of the apparent contact area. Above 0.5 MPa the relationship becomes relatively linear with an actual contact area ratio of 14% at 10.75 MPa [24].

Mizuhara & Ozawa [25] represent the first study to develop direct correlation between thermal and electrical contact resistance for the expressed purpose of estimating thermal contact resistance using a relatively simple electrical measurement. Here they examine the influence of surface roughness and interstitial oil for steel and cast iron contacts for pressures up to 1.53 MPa. As expected, they demonstrate a reduction in both thermal and electrical contact resistance with pressure and attribute this to the increase in actual contact area. Interestingly, they observed a significant increase in electrical contact resistance after repeated loading and unloading cycles. This was attributed to formation of various materials, such as oxides, inhibiting current flow at the interface [25]. From a thermal standpoint, no observable increase in contact resistance was observed for repeated loading cycles. Thermal contact resistance was correlated to electrical contact resistance as a linear relationship on a log-log plot, and asserted to be independent of contact pressure and surface roughness [25]. Despite the data being somewhat scattered, the resulting relationship was calculated to be

$$RA = 0.35R_e^{0.74} \tag{3.12}$$

where RA is specific thermal contact resistance in $m^2K/W \times 10^{-4}$ and R_E is electrical resistance in mΩ. Normalizing the electrical resistance to the area used in this test and converting to standard units, Eq. (3.12) becomes

$$RA = 0.585(R_eA)^{0.74} \tag{3.13}$$

where RA is specific thermal contact resistance in m^2K/W and R_eA is specific electrical resistance in $m^2\Omega$.

3.4.2 Proposed Approach

The objective of the present study is to develop a method to characterize the thermal contact resistance of MMT-TIMs using a simultaneous electrical contact resistance measurement. Tests were carried out using simple deformable metal structures with easily calculated bulk thermal resistances in order to evaluate the effect of pressure and changing apparent contact area as the structure is deformed. Results and discussion of these experiments and their implementation with the model are presented in Chapter 5.

3.5 Summary

Initial thermal models were developed to demonstrate the feasibility of the MMT-TIM concept as an alternative to conventional TIM technologies. To further predict the performance characteristics of MMT-TIMs and serve as a functional design tool, a more complex numerical model was developed and refined to simultaneously characterize the mechanical and thermal response of a MMT-TIM as it undergoes compressive deformation. Two main issues affecting the accuracy of this model were identified and courses of action defined: Firstly, an improved prediction of the mechanical response has been proposed by improving the representation of the MMT-TIM geometry. Here, the technique of 3D surface reconstruction via SEM stereo microscopy as been extended to create reconstructed solid geometries which are more closely representative of the actual MMT-TIMs for implementation into finite element models to.

Secondly, it has been proposed that a straightforward electrical resistance measurement be employed to estimate the thermal contact resistance of MMT-TIMs, thereby allowing an improved model prediction of the overall thermal resistance of the sample as it undergoes deformation.

References

1. Malayappan, S. & Narayanasamy, R., 2005, "Barrelling of aluminium solid cylinders during cold upset forging with constraint at one end", Materials Science and Technology, **19**, pp. 507-511.

2. Li, G., Jinn, J.T., Wu, W.T., Oh, S.I., "Recent development and application of three-dimensional finite element modelling in bulk forming processes", *Journal of Materials Processing Technology*, **113**, pp. 40–45 (2001).

3. Oh, S.I., Wu, W.T., Tang, J.P., Vedhanayagam, A., "Capabilities and applications of FEM code DEFORM: the perspective of the developer", *Journal of Materials Processing Technology*, **27**, pp. 25–42 (1991).

4. Altan, T. & Knoerr, M., "Application of the 2D finite element method to simulation of cold-forging processes", *Journal of Materials Processing Technology*, **35**, pp. 275-302 (1992)

5. Kalpakjian & Schmid, Manufacturing Engineering and Technology: 5th Edition, 2006

6. DEFORM User's Manual, Scientific Form Technologies Corporation

7. Kempers, R., Frizzell, R., Lyons, A. & Robinson, A.J., "Development of a Metal Micro-Textured Thermal Interface Material", ASME InterPACK Conference, IPACK2009-89366, San Francisco, July 8-12, 2009

8. Beil, W. & Carlsen, I.C., "Surface Reconstruction from Stereoscopy and "Shape from Shading" in SEM Images", *Machine Vision and Applications*, **4**, pp. 271-285 (1991)

9. Paluszynski, J. & Slowko, W., "Surface Reconstruction with the Photometric Method in SEM", *Vacuum*, **78**, pp. 533-537 (2005).

10. Drzazga, W., Paluszynski, J. & Slowko, W., "Three-Dimensional Characterization of Microstructures in a SEM", *Measurement Science and Technology*, **17**, pp. 28-31 (2006).

11. Samak, D., Fischer, A. & Rittel, D., "3D Reconstruction and Visualization of Microstructure Surfaces from 2D Images" *Annals of the CIRP*, **56**, pp. 149-152 (2007). doi: 10.1016/j.cirp.2007.05.036.

12. Minnich, B., Leeb, H., Bernroider, E.W.N. & Lametschwandtner, A., "Three-dimensional morphometry in scanning electron microscopy: a technique for accurate dimensional and angular measurements of microstructures using stereopaired digitized images and digital image analysis" *Journal of Microscopy*, **195**, pp. 23-33 (1999)

13. Ostadi, H., Jiang, K. & Prewett, P.D., "Characterisation of FIB milling yield of metals by SEM stereo imaging technique" *Microelectronic Engineering*, **86**, pp. 1021-1024 (2009) doi: 10.1016/j.mee.2009.01.056

14. Danzl, R., Helmli, F. & Scherer, S., "3D Reconstruction of Surfaces with Steep Slopes from Multiple SEM Images" *Microscopy and Microanalysis*, **12**, pp. 1506-1507 (2006) doi: 10.1017/S1431927606063148

15. Schrottner, H., Schmied, M. & Scherer, S., "Robust, dense and accurate 3D surface reconstruction in SEM through automatic calibration data calculation from multiple images" Proceedings EMC, **1**, pp. 441-442, Antwerp, Belgium (2004)

16. Marinello, F., Bariani, P., Savio, E., Horsewell, A. & De Chiffre, L., "Critical Factors in SEM 3D Stereo Microscopy" *Measurement Science and Technology*, **19**, pp. 1-12 (2008) doi: 10.1088/0957-0233/19/6/065705

17. *MeX™ Software* 2005 (Graz, Austria: Alicona Imaging, GmbH)

18. Madhusudana, C.V., Thermal Contact Conductance, Springer-Verlag, New York, (1996).

19. Yovanovich, M.M., 2005, "Four Decades of Research on Thermal Contact, Gap, and Joint Resistance in Microelectronics", IEEE Transactions on Components and Packaging Technologies, **28**, pp. 182-206.

20. Teertstra, P. "Thermal Conductivity and Contact Resistance Measurements for Adhesives". Proceedings of InterPACK 2007, Vancouver, BC, July 8-12, 2007.

21. Braunovic, M., Konchits, V.V. &Myshkin, N.K., Electrical Contacts: Fundamentsl, Aplications and Technology, CRC Press, (2007).

22. Jones, M.H., Howells, R.I.L. & Probert, S.D., "Solids in Static Contact" Wear, **12**, pp. 225-240, (1968).

23. Woo, K.L. & Thomas, T.R., "Contact of Rough Surfaces: A Review of Experimental Work", Wear, **58**, pp. 331-340, (1980).

24. Filayev, A.T., Kornilov, A.V. & Wegrzyn, L., "Determination of the Actual Contact Area During Sliding Contact", Wear, **70**, pp. 259-263, (1981).

25. Mizuhara, K. and Ozawa, N., "Estimation of Thermal Contact Resistance Based on Electrical Contact Resistance Measurements", Int. J. Japan Soc. Prec. Eng., **33**, pp. 59-61, (1999).

Chapter 4

Experimental Apparatus

4.1 Introduction

The objective of the apparatus designed and constructed, as described in this section, was to not only accurately characterize the performance of MMT-TIMs but also to measure the thermal-mechanical properties of existing TIMs with unprecedented precision and accuracy. To work effectively in thermal applications, TIMs must: conform to the mating surfaces under reasonable assembly pressures, have a thin bond line, have low contact resistance with surfaces of interest and exhibit adequate bulk thermal conductivity. As TIM technology evolves, this combination of factors makes accurate quantification of the thermal characteristics of new generation materials difficult, as some of the important quantities that need to be measured are decreasing to levels below the uncertainty floor of conventional measurement methodologies. This poses very serious problems for the electronics packaging community since accurate knowledge of the thermal, mechanical and electrical performance of TIMs, as well as the associated uncertainties in these values, is essential to the proper design of electronic systems and packages [1-4].

A number of physical properties must be known in order to fully characterize TIMs. They include, but are not limited to, thermal conductivity, thermal contact resistance, mechanical strength, compressibility and resilience, thermal stability, coefficient of thermal expansion, dielectric strength and breakdown voltage [5].

Typically, for conventional TIMs, the contact resistance can be obtained experimentally by measuring several thicknesses of TIM, plotting the thermal resistance as a function of thickness and extrapolating the thickness to zero [6]. The contact resistance is determined from the value of the thermal resistance at zero thickness. However, as discussed in Chapter 3, for the MMT-TIMs being investigated in the present study, this method cannot be used due to the non-uniform behaviour of the bulk TIM. Since it is

experimentally difficult to distinguish between the bulk thermal resistance and contact thermal resistances of MMT-TIMs, and since they are highly electrically conductive, it has been proposed that a measurement of electrical contact resistance be used to infer the thermal contact resistance of these TIMs [7].

With regard to thermal resistance and conductivity measurements, the state of the art can be broadly cast into two camps; transient techniques and static techniques, each with its respective niche [1].

Dynamic- or transient-type TIM testers rely on the transient thermal response of a TIM to calculate its thermal resistance. Bosch & Lasance [8] describe a method of characterizing the thermal conductivity of TIMs based on earlier work performed by Lasance & Lacaze [9] using transient techniques. This setup consists of the TIM sample squeezed between an aluminium cooling/heating water jacket and an insulated copper block. The two metal blocks were instrumented with thermocouples. The water supply to the cooling/heating baths was manually selectable between reservoirs at ambient temperature and at an elevated temperature. By introducing a step heat input through switching the water supply, the transient temperature response of the system could be measured. The effective thermal resistance of the sample was obtained by fitting the response data to predictions made with a numerical model of the system using the temperature data as boundary conditions. The authors quote a reproducibility of 0.02 K/W, which corresponds to a specific thermal resistance of 2.51×10^{-5} $m^2 \cdot K/W$ for the sample area employed. Later work by Lasance *et al.* [10] describes this setup as having repeatability in the range from 1×10^{-8} to 1×10^{-7} $m^2 \cdot K/W$ and a reproducibility of 2×10^{-7} $m^2 \cdot K/W$. However, they point out that these accuracies were determined through the procedure used to extract the interface resistance from the experimental results, not taking into account any actual experimental and measurement uncertainties.

Rencz & Székely [11] and Rencz *et al.* [12] further detail the method in which the thermal resistance can be determined through a transient approach. They describe the use of the differential structure function which is calculated by direct transformations from a heating or cooling curve, measured as the thermal response of the system for a step function excitation. Local maxima in these functions yield information about the magnitude of the thermal resistance and capacitance of the different components in the thermal resistance path from the point of excitation and describe the heat flow path based on the geometry and material properties of the structure.

Smith *et al.* [13] and Smith *et al.* [1] discuss a number of difficulties with transient TIM testing. Among them is the inability of the power supply to provide ideally

rectangular power steps, the slow change in heater resistance with temperature change, electrical noise and heat spreading outside the 1-D path. Additionally, there has been little work performed to directly quantify the uncertainty of measurements obtained through these test methods. Still, at the expense of high temporal resolution sampling hardware and advanced data processing software, this technique offers the advantage of rapid testing *in situ* [1].

Another popular transient technique for determining the thermal diffusivity of solid homogeneous materials is the laser flash method, which was originally proposed by Parker *et al.* [14]. Since then, improvements have been made to the technique and data reduction techniques [15-17]. However, the density and heat capacity must be known, and indeed measured independently, in order to calculate the thermal conductivity of the TIM [16]. These additional measurements and sources of error can lead to uncertainties in the thermal conductivity [5, 18]. A recent study employing the laser flash method to measure the performance of thermal interface materials incurred uncertainties up to 25% [17]. Additionally, this method is unsuitable for measuring specimens of non-uniform thickness and has had limited success in characterizing the thermal resistance of a TIM in conjunction with contacting surfaces (or apparent thermal resistance) [17], which is an important consideration for the characterization of TIMs.

Static testing is the second major approach to quantifying TIM thermal performance. Variants of the static test technique following ASTM D5470, "Standard Test Method for Thermal Transmission Properties of Thermally Conductive Electrical Insulation Materials" [19], concern measurement of the effective thermal conductivity or specific thermal resistance of thin conductive materials ranging from liquid compounds to hard solid materials. This technique has emerged as the *de facto* standard for characterizing thermal interface materials by both researchers and manufacturers of TIMs. This standard describes a test procedure wherein heat is conducted between two parallel, isothermal surfaces separated by a test specimen of uniform thickness. The apparent thermal conductivity—the summation of bulk conductivity of the sample and the contact resistance—is calculated based on the temperature difference between the two surfaces and the imposed heat flux. While ASTM D5470 was not originally developed specifically for TIM characterization *per se*, recent revisions of this standard have addressed a number of concerns presented in previous studies [5, 20]. In particular, ASTM D5470-06 includes provisions for force and *in situ* thickness measurements during the application of load [19].

While not the only possible implementation of ASTM D5470, a common experimental approach to obtaining the required data is represented schematically in Fig.

4.1. In this configuration, the sample is squeezed between two meter bars. Heat is supplied at one end and dissipated at the other. Temperature measurements made by sensors arrayed along the length of the meter bars are used to extrapolate the temperature at the contact surfaces. Additionally, with accurate knowledge of the thermal conductivity of the meter bars and adequate insulation, the heat conducted through the sample can be calculated. Alternatively, the structure can be guard heated and the heat flux quantified by the electrical power into the primary heaters. The apparent specific thermal resistance (often referred to as thermal impedance) of the TIM is calculated as

$$RA = \frac{A(T_a - T_b)}{Q} \tag{4.1}$$

where A is the cross-sectional area of the meter bars, T_a and T_b are the extrapolated contact surface temperatures, and Q is the heat transfer rate. The effective thermal conductivity of the joint can then be calculated using

$$k_{eff} = \frac{QL}{A(T_a - T_b)} = \frac{L}{R} \tag{4.2}$$

where L is the thickness of the specimen bond line.

It is also important to point out that the schematic of the approach shown in Fig. 4.1 represents one engineering solution that can be used to impose the required test conditions and accomplish the necessary measurements [19]. Although this design is not a unique implementation of the standard, many previous studies have used variations of this steady-state, heat-flux meter-bar approach [18, 20-25].

Gwinn *et al.* [18] developed an apparatus for testing TIMs capable of measuring specific thermal resistances as low as 6.5×10^{-6} m^2·K/W with a reported uncertainty of 10%. The copper meter bars were 38.1 mm square in cross-section and 45 mm long, instrumented with three 1.59-mm-diameter resistance temperature detectors (RTDs), with the closest RTD located 2 mm from the surface. Here, the RTDs were calibrated to 0.05 K with a thermal resolution of 0.026 K. Heater powers up to 30 W were employed to achieve a measurable temperature difference across the interface. Heat losses were estimated as 30%. A basic error analysis was presented based on these uncertainties to estimate the uncertainty of the thermal resistance. No provisions were included to measure sample thickness *in situ*.

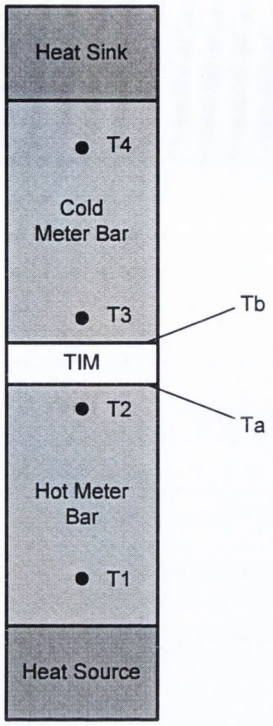


Fig. 4.1: Meter Bar implementation of ASTM D5470-06.

Kearns [20] adapted a commercially available conductivity tester to measure TIM thermal resistance with improved precision. This was due partly through the addition of precision calibrated RTDs and through modification of the apparatus to use meter bars for an improved measurement of surface temperature. This improved test facility measured specific thermal resistances as low as 3×10^{-6} $m^2 \cdot K/W$ with 10% uncertainty. Temperature resolution for this setup was 0.01 K. Heater powers of 25 to 50 W were applied to achieve the necessary temperature difference.

Culham *et al.* [21] detail the design and commissioning of a heat-flux meter-bar TIM tester and examined a number of issues pertaining to heat loss minimization, temperature measurement accuracy and in-situ thickness measurement. In this design, heat loss to the environment was minimized by enclosing the entire apparatus in a bell jar evacuated to a pressure of 1×10^{-4} torr. Aluminium alloy 2024 meter bars instrumented with RTDs were used to both extrapolate the temperature at the TIM surfaces and quantify the heat flux. A laser/detector system was used to measure the distance between the meter bars for an accurate in-situ measurement of the TIM thickness. Savija *et al.* [22] used empirical data obtained using this apparatus in conjunction with an analytical model to predict the thermophysical properties of commercially-available graphite sheets. This study reported relative uncertainty in measured thermal resistances of 2.2 % for the thickest specimens to 13.6 % for the thinnest specimens at the highest contact pressure. This apparatus was modified to measure the thermal conductivity and contact resistance of

adhesives and is one of the few studies to clearly quantify measured uncertainties by plotting error bars on the thermal resistance data [6].

Rao *et al.* [23] developed an apparatus to measure thermal contact resistance between two copper contacts at various atmospheric conditions and temperatures. A similar setup was employed by Misra & Nagaraju [24] to measure both electrical and thermal contact resistance of brass-brass contacts in order to study the stability of electrical contacts due to thermal effects. Temperature measurements were performed using 1.1-mm-diameter T-type thermocouples embedded into 1.2-mm-diameter holes while a digital multi-meter was used to perform electrical contact resistance measurements. This setup was used to validate theoretical models for thermal and electrical contact resistance with good agreement but cannot be used to characterize the performance of thermal interface materials due primarily to the lack of instrumentation to measure bondline thickness.

Singhal *et al.* [25] also developed an apparatus to measure thermal contact resistance between metal-to-metal contacts. As with previous setups, the sensitivity and precision of this apparatus is limited by the elemental thermal uncertainty of the thermocouples being used (0.2 K).

As the next generations of TIMs offer improved thermal performance and thinner bond lines, there is a fundamental necessity for higher precision and more sensitive quantification of TIM performance than what is possible using the reviewed methods. The sensitivity, precision and accuracy of thermal resistance measurements obtained in previous setups are largely dominated by the elemental thermal uncertainties of the sensors used. Additionally, for low thermal resistance measurements, large heater input powers were required to achieve a measureable temperature difference at the interface. This results in a large temperature gradient along the meter-bars and accordingly large heat losses to the ambient which is another major source of uncertainty for these types of apparatus [26]. Furthermore, a detailed and robust uncertainty analysis must also be employed for accurate quantification of the uncertainties associated with the measured quantities and how these uncertainties propagate to the calculated thermal resistance and effective thermal conductivity of the TIM. Previous studies only touch on this issue and present little or no uncertainty data in their results.

The present work addresses these issues and presents an experimental facility designed and built to measure TIM apparent thermal resistance and effective thermal conductivity with unprecedented precision and sensitivity. The underlying approach relies on the proven steady-state technique of using well-characterized meter bars to both extrapolate the temperature at the surfaces in contact with the TIM and measure the heat

flow through the sample as illustrated in Fig. 4.1. It is rooted in setups used in previous studies; in particular the apparatus used by [6, 21-22] which have proven accurate and reliable for many investigations and reflects improvements to the experimental apparatus originally presented by Kempers *et al.* [27].

This particular apparatus is unique primarily because it takes advantage of precision resistance thermometry to measure the axial temperature distribution along the meter bars, similar to the techniques employed by Kolodner *et al.* [28]. This achieves a level of thermal precision an order-of-magnitude higher than previous apparatuses, allows use of low input powers to minimize uncertainties due to heat leakage to the ambient and eliminates any uncertainty arising from variations in meter-bar thermal conductivity due to a large imposed temperature gradient. Provisions were also incorporated to ensure the accuracy of force and thickness measurements. A precision machined sliding and alignment mechanism ensures meter-bar alignment throughout the range of motion. Furthermore, this TIM characterization apparatus is unique in employment of a simultaneous electrical contact resistance measurement to help characterize the electrical conductance and electrical contact resistance of a TIM during compressive loading for the purpose of gaining insight into the relationships between thermal and electrical contact resistance for next-generation MMT-TIMs. Finally, a particularly robust uncertainty analysis has been employed in order to accurately quantify the uncertainties in all measured and calculated quantities.

4.2 Apparatus Design

A detailed scale drawing of the apparatus is shown in Fig. 4.2, while a schematic illustrating the instrumentation is shown in Fig. 4.3. The TIM sample under test is sandwiched between two CuW composite meter bars 120 mm long with contact areas of 40 mm × 40 mm. The lower meter bar (5) is bolted to the water jacket (4), which is cooled by a Julabo model F33 HE constant-temperature circulator. The circulator controller detects the temperature of a Pt100 sensor embedded in the water jacket, keeping its temperature stable to ±0.01 °C. The water jacket is situated atop a 25.4-mm-thick insulating block (3) and is bolted to the 19.05-mm-thick steel lower platen (2).

The upper meter bar (7) is bolted to the copper heater block (8) which contains two cartridge heaters. The heater block is mounted to a load cell (9) through a 12.7 mm steel plate. The load cell is then attached to the upper platen (10) using a similar 12.7 mm steel plate and a series of bolts that allow the upper meter bar to be fixed to the upper platen at a set position relative to the lower meter bar. The upper platen is also constructed from 19.1-mm-thick steel. The distance between the opposing faces of the meter bars is measured using an optical micrometer (6).

The upper and lower platens are fitted with ball bushings and slide on two precision-ground steel shafts, preventing any lateral motion. At the bottom, the shafts are attached to a 25.4-mm-thick steel base plate (1) of lateral dimensions 400 mm X 400 mm. At the top, the shafts are fastened together with a 19.05-mm steel plate (11). A linear actuator (12) is mounted to the top plate with the actuator arm attached to the upper platen. During testing, the meter bars are enclosed in 15 mm of Aspen Aerogel insulation (not shown) to further minimize heat leaks. The manufacturer's specification for the thermal conductivity of this insulation was 0.015 W/m·K. Additional drawings and photographs of the apparatus are presented in Appendix 4.

A typical test procedure consisted of setting the circulator water temperature and input power to the heaters to desired values and incrementing the actuator until the desired displacement and thus starting pressure is realized. The system was allowed to reach steady state, whereupon the measurements were logged, the actuator was incremented a defined amount and the process was repeated. All instrument control and data acquisition was performed using a PC with MATLAB software communicating to the instruments through serial and general purpose interface bus (GPIB) interfaces. The MATLAB code written for all instrument control and data acquisition is presented in Appendix 5.

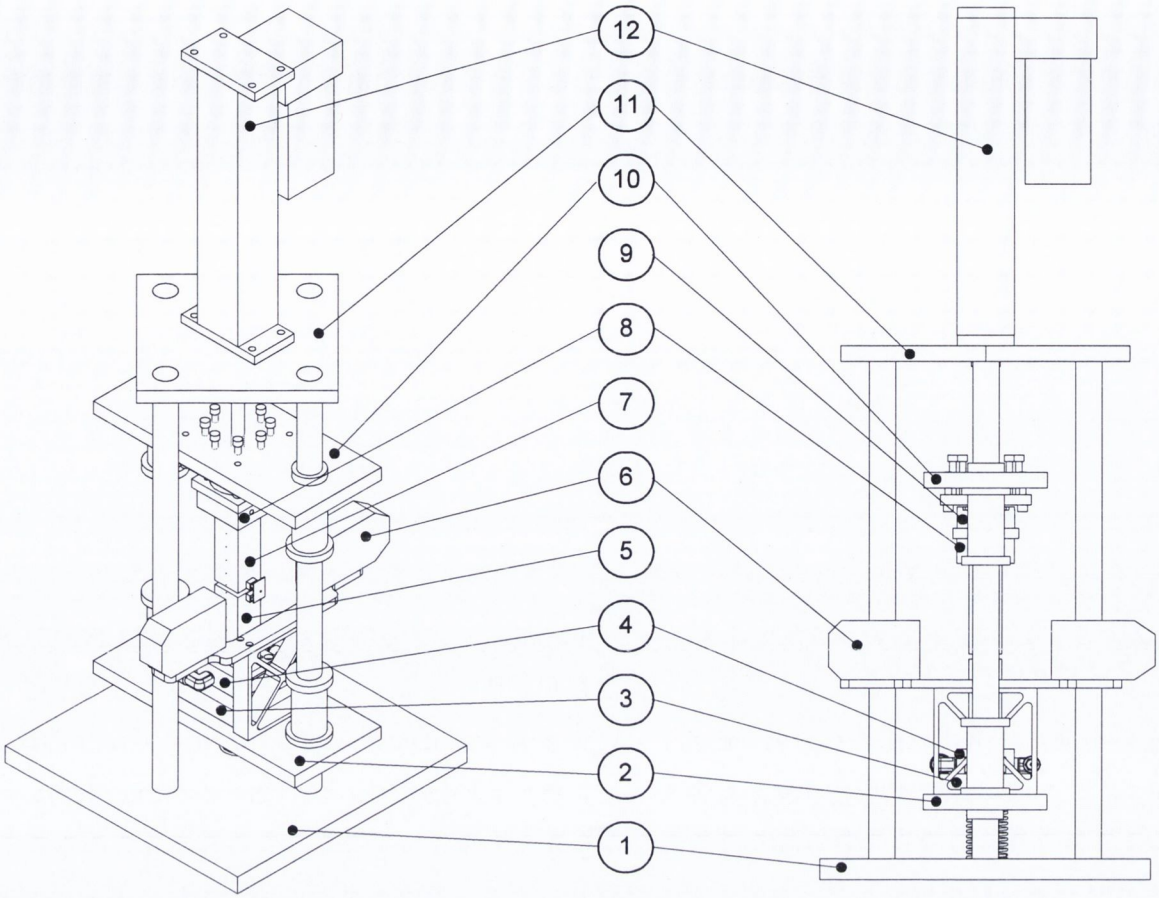


Fig. 4.2: Rendering of experimental facility developed in the present study.

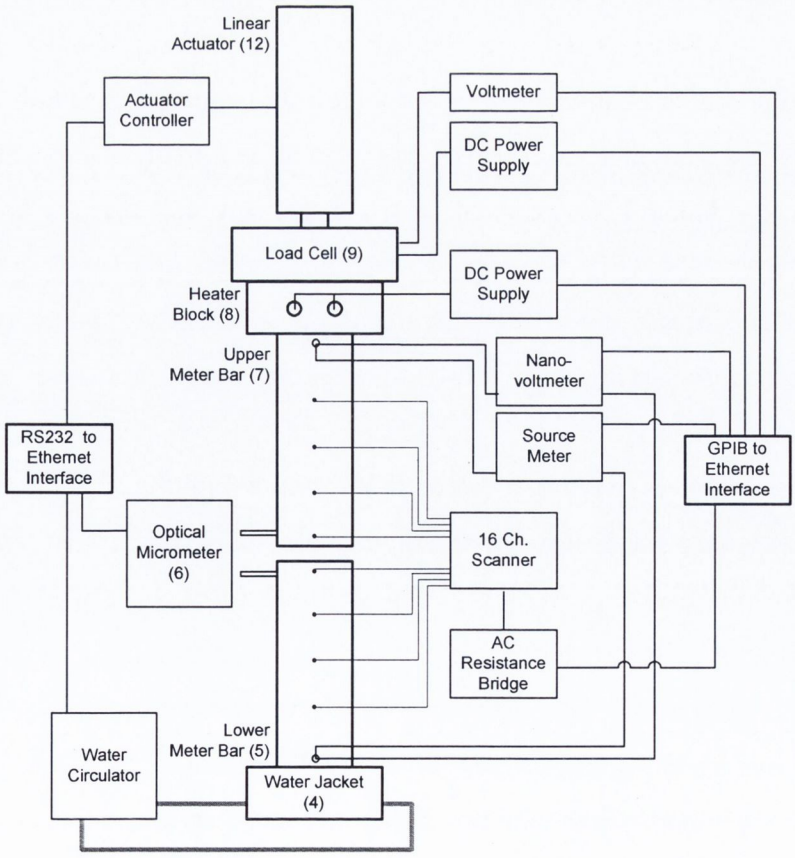


Fig. 4.3: Schematic of instrumentation and control of experimental facility.

4.2.1 Meter Bars, Thermal Instrumentation & Calibration

The meter bars in this apparatus were made from Elkonite Copper-Tungsten alloy 30W3 manufactured by CMW Inc. This alloy consists of 80% W and 20% Cu by weight and consists of micro-sintered W foam filled with Cu, resulting in a hard composite with thermophysical properties that are intermediate between those of the two pure metals and thus a better balance between hardness and thermal conductivity than either pure metal. This reduces the likelihood that the contact surfaces become scratched or worn over time and maintains a low thermal gradient in the meter bars. The hardness of this material was measured before and after final surface finishing and found to have a hardness of 102 Rockwell Hardness B (HRBW). The manufacturer quotes an electrical resistivity of 42.1 nΩ·m.

The surfaces in contact with the specimen were fly-cut and ground in order to achieve a smooth, flat surface. The contact surfaces were characterized using a commercial white-light interferometer at several locations on each meter bar. Over a sample area of 3.7 mm X 5 mm, the lower meter bar had a first-moment of roughness, or average absolute deviation from the mean of 113.7 nm, an RMS roughness of 152.5 nm and a peak-to-trough maximal roughness of 1.79 μm. The upper meter bar had a first-moment of roughness of 78.2 nm, an RMS roughness of 105.5 nm and a maximal peak-to-trough of 1.94 μm. To assess their overall flatness, the polished surfaces were contacted with an optical flat and illuminated with narrow-band green light. The resulting interference fringes were observed visually. The deviation from flatness did not exceed 5 fringes, which corresponds to 2.5 μm. No fall-off was observed at the edges of the polished faces.

Each meter bar was instrumented with four Betatherm thermistors measuring 2 mm long and 0.38 mm in diameter with a nominal resistance of 22 kΩ at 25 °C. Thermistors were chosen for their high temperature sensitivity and small probe size, keeping spatial and thermal uncertainties to a minimum and thereby minimizing the uncertainty of successive calculated quantities of extrapolated temperature and heat flux [29]. The thermistors were inserted into 0.4 mm-diameter holes of 3 mm depth at locations approximately 3, 20, 40 and 60 mm from the contact surfaces. Following machining, the hole positions, hole diameters and contact areas of both meter bars were measured optically using a precisely characterized optico-mechanical measurement & alignment system with a precision of about 1 μm. Average hole diameter was 0.42 mm, thus resulting in a uniform thermistor positioning uncertainty of ± 20 μm.

As in previous investigations [18, 20], numerical simulations were employed to determine the influence of the intruding thermistors on the temperature profile through the meter bars and the associated heat fluxes and the temperature distributions at the contact surface. It was found that the thermistors closest to the contact surface yielded a negligible influence on temperature and heat flux uniformity at the surface. Furthermore, these simulations demonstrated that heat leaks to the ambient had a negligible impact on the energy balance or the linearity of the axial temperature profiles in the meter bars.

The thermistors were held in place using a silicone adhesive. To minimize heat leaks through the thermistor leads, the lead wires were put in thermal contact with the meter bar at the same axial positions before making external connections. For strain relief, the lead wires from each thermistor were soldered to an adhesive-backed soldering strip attached to the side of each meter bar, where connections were made to the external instrumentation via fine CuNb wires to further minimize heat leaks to the environment. Thermistor resistances were measured using a LakeShore model 370 AC resistance bridge equipped with a 16-channel scanner, resulting in accurate and precise 4-wire resistance measurements using AC excitation and low excitation current (3.16 μA) to minimize thermistor self-heating. The temperature resolution of the present setup is approximately 1×10^{-4} °C.

The effect of shot noise and Johnson-Nyquist noise were estimated based on the excitation current and nominal resistance values of the thermistors and found to be on the order of 0.02 Ω, significantly lower than the resolution of the current setup. The noise level was verified experimentally by measuring the resistances of several low-temperature-coefficient resistors in a stable thermal environment continuously over 24 hours and was indeed found be less than the measurement resolution.

Once installed, the thermistors on both meter bars were calibrated simultaneously against a Hart Scientific 5611T secondary reference probe whose absolute calibrated uncertainty was ±0.002 K. The reference probe was mounted inside a copper block bolted tightly to the upper and lower meter bars. The entire assembly was placed inside a 170-mm-diameter, 300-mm-long copper cylinder closed at one end with a removable copper cap at the other end. Copper tubing was densely coiled around the outside of this calibration cylinder and soldered in place. Water, supplied by the constant-temperature circulator with a stability of ±0.01 K, was passed through the copper tubing to control the temperature of the calibration cylinder. The calibration cylinder was insulated with no less than 200 mm of foam insulation to maintain a stable thermal environment. The thermal mass of the calibration cylinder, combined with the imperfect thermal contact with the

assembly inside, reduced these fluctuations to less than 0.001 K at the thermistor locations. The thermistors were calibrated against the secondary reference probe using 6 points over a range from 15 to 40 °C and curve-fit to a generalized Arrhenius form using a 3rd-order polynomial. Between any temperature instabilities in the calibration environment and curve fitting errors, the relative temperature uncertainty measurement between the thermistors was reduced to ±0.001 K with a confidence interval of two standard deviations.

Since the upper and lower meter bars were cast in separate batches and meter-bar thermal conductivity is vital to accurate quantification of heat flux through the sample, their thermal conductivities were carefully measured independently. This was achieved by electrically heating one end and fixing the temperature of the opposite end using the constant temperature circulator and measuring the temperature gradient in the meter-bars using the calibrated thermistors. Ample insulation and low heater powers ensured that negligible heat loss to the ambient air. Estimates using numerical methods further supported this assumption and an uncertainty analysis, similar that presented in the following section, was used to quantify the uncertainty of the measured thermal conductivity. The upper and lower meter bars were found to have conductivities of 214 ± 2 W/m·K and 216 ± 2 W/m·K respectively.

4.2.2 Electrical Contact Resistance Measurement

Electrical connections for the 4-wire resistance measurements were made by drilling a hole approximately 4 mm deep on one side of each meter bar approximately 5 mm from where they connected to water jacket or heater block. The holes were tapped for M3 screws to allow leads to be clamped directly to the meter bars. Care was taken to ensure the meter bars were electrically isolated from the rest of the apparatus. A Keithley model 2400 Sourcemeter was used to provide a constant current of up to 100 mA while a Keithley model 2182A Nanovoltmeter was used to measure the corresponding voltage drop. A current-reversal method was used to minimize thermoelectric voltage offsets [30]. The bulk electrical resistance of each meter bar was calculated to be 2.72 μΩ.

4.2.3. *In-Situ* Sample Thickness Measurement

The sample thickness is measured optically using a Keyence model LS-7030 optical micrometer. Steel gauge pins, 2 mm in diameter and approximately 15 mm long, were mounted normal to the meter-bar surfaces near the contacting surfaces to act as optical trips for the micrometer. Prior to sample insertion, the micrometer was zeroed by bringing the meter bars into contact and measuring the distance between the optical trips.

This setup allowed for the measurement of samples as thick as approximately 20 mm with an uncertainty of ±0.15 μm. This method was favoured over other methods such as a linear variable differential transformer (LVDT) or traditional micrometers due to its non-contact nature and indifference to meter bar thermal expansion or system deflection as loads are applied.

4.2.4 Load Application & Measurement

The upper platen assembly was displaced using an Industrial Devices model EC3 stepper-motor-controlled Acme screw linear actuator, capable of exerting 7200 kN of force. The high-friction characteristics of the Acme screw prevents potential back-driving caused by the weight of the assembly. A controller capable of micro-stepping the stepper motor allowed for sub-micron changes in displacement to the platen.

The force applied to the sample is measured using an AST model KAF-S load cell with a rated load of 5 kN. The accuracy is limited by the load cell to ±0.2% of rated load. Over the meter bar area, this results in a maximum measurable pressure of 3.13 MPa. For lower-pressure testing, the load cell can be replaced with one with a lower rated load to achieve higher accuracies at low pressures.

Due to the employment of a stepper-motor-controlled linear actuator, the applied load is displacement controlled and is adequate for most testing procedures. When testing soft, compliant TIMs, the lower platen and meter bar are held rigidly in place, allowing deflection to occur in the TIM only. When testing rigid specimens or performing self-contact tests, the lower platen floats on an array of springs to allow the pressure to be varied linearly over a range of controlled displacements. Additionally, the apparatus is capable of pressure control and thickness control through a software control system relying on feedback from the load cell or optical micrometer.

4.3 Uncertainty Analysis

A rigorous uncertainty analysis was employed in order to quantify how the uncertainties of every measured quantity propagate to the overall uncertainty of the thermal resistance and effective thermal conductivity of the TIMs under test.

Each measured quantity and its associated uncertainty are listed in Table 4.1.

Measured Quantity	**Uncertainty**
Temperature	± 0.001 K
Thermistor Location	± 20 μm
Force	± 0.2 % of rated load
Meter-Bar Area	$\pm 9 \times 10^{-7}$ m^2 (± 0.056%)
TIM Thickness	± 0.15 μm
ECR Current	± 0.066 % + 20 μA for 100 mA range
ECR Voltage	± .005 % + 40 nV for 10 mV range

Table 4.1: Uncertainty of Measured Quantities

4.3.1 Calculated Quantities

The temperatures at the contact surfaces, T_a and T_b, and the heat flux, Q, for each meter bar were obtained by performing least squares regression of the axial temperature distribution to a straight line and computing the resulting y-intercept and slope at the contact surfaces. As a result, the uncertainty of T_a, T_b and Q depend on both the thermal and spatial uncertainties of each thermistor.

There are a number of statistical approaches to calculating how the measured uncertainty propagates through a least-squares regression. Wald [31] and Bartlett [32] outline methods for fitting a straight line when both variables are subject to error. These methods are mathematically involved and rely on the assumption that the uncertainties are uniform and normally distributed. Press *et al.* [33] attempt to describe an analytical method for calculating the uncertainties of the slope and y-intercept of a straight line model based on the assumption of a normal distribution and the standard deviations in both the x and y data. The resulting expressions are non-linear and unwieldy and best suited to numerical solutions [33]. Kedzierski & Worthington [29] present relatively straightforward expressions for estimates of the uncertainties in wall temperature and gradient as originally obtained by Ku [34]. These expressions demonstrate that the lowest uncertainties are obtained by using a meter bar of high thermal conductivity having a large number of well-spaced, small-diameter holes. They further demonstrate that the calculated

surface temperature can have a greater precision than those of the individual temperature measurements [29].

For the present study, the uncertainty of the y-intercepts and slope are computed numerically using a Monte Carlo simulation. Aside from the relative simplicity of this method, it is also advantageous in its ability to deal with non-uniform uncertainties among the temperature and position measurements as well as differing uncertainty distributions. Here, the temperature uncertainty is assumed to have a normal distribution where the uncertainty listed in Table 4.1 is equal to two standard deviations. Previous studies have suggested that the thermistor location uncertainty also has a normal distribution; however, this implies that it is statistically possible for the thermistor to be located outside the hole [29]. Additionally, there is no physical justification for the location uncertainty to have a normal distribution. Other authors have argued that once the temperature sensors are fixed in place, this error is systematic and thus doesn't have as pronounced an effect. In the present study, we opted for the conservative yet realistic approach of modelling this uncertainty as a flat distribution bounded by difference in radius between the thermistors and the holes. The standard deviation for the slopes and the intercepts are calculated by performing 2000 randomized curve fits to the data constrained by the x and y uncertainty distribution at each point. The uncertainty of the slope and y-intercept are then taken as two standard deviations of this data set.

The heat transfer rate through each meter bar is then computed by

$$Q_{mb} = m_{mb} k_{mb} A \tag{4.3}$$

where m_{mb} is the temperature gradient (or slope) through each meter bar, k_{mb} is the thermal conductivity of each meter bar, and A is the cross-sectional area of the meter bar.

The apparent thermal resistance of the TIM is then calculated as

$$R = \frac{(T_a - T_b)}{Q} \tag{4.4}$$

where Q is the mean heat transfer rate through the meter bars. The effective thermal conductivity of the joint can then be calculated using

$$k_{eff} = \frac{QL}{A(T_a - T_b)} = \frac{L}{AR} \tag{4.5}$$

where L is the thickness of the specimen bond line.

The uncertainty of each quantity calculated in Eqs. 4.3-4.5 was obtained using the method of Kline and McClintock [35]. Here, each measurement is denoted by x_i and the uncertainty in the measurement U_i. The result of a calculation using these measurements is

denoted Z, and the uncertainty in the calculated result is denoted by U_z. The uncertainty U_z is then calculated as

$$U_z = \sqrt{\left(\sum_{i=1}^{n} \left[\frac{\partial Z}{\partial x_i} U_i \right]^2 \right)} \tag{4.6}$$

All calculated quantities and their associated uncertainties are computed in real time by the data acquisition software.

As an adjunct to this automated computation, it is useful to estimate and discuss the magnitudes of the different contributions to the total uncertainty U_R. In order of decreasing importance, they are as follows:

1. At low values of the TIM thermal resistance R and sufficiently high heater powers Q, the dominant uncertainty is incurred in extrapolating the temperature profile from the locations d of the two thermistors closest to the contact surfaces to the surfaces themselves. The correction for each surface is $\Delta T = m_{mb} d$, where m_{mb} is the measured temperature gradient and $d \approx 2.8$ mm is the distance to the contact surface. The dominant uncertainty in ΔT is due to the imprecision $U_d = \pm 20$ μm in the thermistor positions, and this leads to a temperature uncertainty $U_T = \sqrt{2} m_{mb} U_d$, where the factor $\sqrt{2}$ is contributed by the independent extrapolation of the temperature gradients in the two meter bars. Dividing this uncertainty by the temperature difference $T_a - T_b = QR$ across the TIM gives the fractional uncertainty f_{ext} in the TIM resistance:

$$f_{ext} = \sqrt{2} U_d / k_{mb} RA = 1.3 \times 10^{-7} / RA \tag{4.7}$$

with RA in units of $m^2 \cdot K/W$. This result implies that this apparatus can measure specific thermal resistances as low as 2.6×10^{-7} $m^2 \cdot K/W$ with 50% fractional uncertainty. Improving this unprecedented sensitivity would require the use of smaller and more precisely located thermistors.

2. If the TIM specific thermal resistance is increased above 1.4×10^{-5} $m^2 \cdot K/W$, the total uncertainty for sufficiently high heater powers Q is dominated by the uncertainty in the independent measurement of the meter-bar conductivities k_{mb}. This fractional uncertainty is 0.9%. This component of uncertainty is systematic, not random. As such, it does not affect the sensitivity of the apparatus or comparisons between different measurements of thermal resistance.

3. An upper bound on the fractional uncertainty contributed by the temperature dependence of the thermal conductivities of the meter bars can be estimated by multiplying the largest end-to-end temperature difference employed in our experiments by any estimate of temperature derivative of the conductivity. Since the meter bars are a CuW composite and not a true alloy, their conductivities are a concentration-weighted average of those of the pure metals. The larger temperature derivative is that of tungsten: $k^{-1}dk/dT = -7.5 \times 10^{-4}$ K^{-1}. The largest temperature difference in these experiments is about 2 K; thus, a very conservative upper bound for this component of fractional uncertainty is 0.15%.

4. The random noise U_T in the thermistor signals is observed to be about $U_T = \pm 0.2$ mK. These fluctuations dominate the total uncertainty at very low heater powers Q. The contribution of these fluctuations to the total fractional uncertainty in TIM resistance is

$$f_n = k_{mb} A U_T / 2Q\Delta d = 1.7 \times 10^{-3} / Q \tag{4.8}$$

with Q in W. Here, Δd = 20 mm is the spacing between thermistors, and the factor 2 represents the averaging of four thermistor temperatures in computing the temperature gradient in the meter bars. This source of uncertainty becomes unimportant when Q is increased above 0.19 W, a very low power level. The extremely low thermistor noise allows this apparatus to be operated with full precision at very low temperature gradients. This results in minimal perturbation of the apparatus by spatially-nonuniform heat leaks to the environment.

5. The uncertainty U_d in the thermistor positions contributes a negligible fractional uncertainty $f_d = U_d/2\Delta d = 5 \times 10^{-4}$ to the imprecision in the measured temperature gradients.

6. The thermistor calibration uncertainty of $U_{cal} = \pm 2$ mK makes an utterly negligible contribution to the total measurement uncertainty. Because the thermistors are all calibrated together, their readings are all affected identically by any distortions in the true temperature calibration of the reference thermistor. Thus, such distortions have a tiny affect on the measurement of temperature differences, which is the basis of our determination of the temperature gradients in the meter bars. A rough estimate of the fractional uncertainty contributed by this distortion is $f_{cal} = U_{cal} / \Delta T_{cal}$, where $\Delta T_{cal} \approx 20$K is the spacing between the calibration points supplied by the thermistor manufacturer. This estimate gives $f_{cal} = 1 \times 10^{-4}$. Since the total temperature gradient in either meter bar is less than 10K even at the highest power levels, the temperature uncertainty of ± 1 mK used

in our Monte Carlo calculations is considered to be a conservative of the effect of thermistor calibration uncertainty.

4.3.2 Comparison to Previous Apparatuses

Ultimately, the precision and sensitivity of thermal resistance measurements obtained using the steady-state, heat-flux meter-bar approach common to our apparatus and those described in the literature rely primarily on the magnitude of two elemental uncertainties, namely the thermal uncertainties of the sensors employed and the uncertainties in their spatial locations. Direct comparisons between apparatuses are difficult due to the varying geometries, testing conditions and information provided in each study. However, a simple comparison demonstrating the influence of only the thermal precision on the uncertainty of the measured specific thermal resistance, U_{RA}, can be made by applying Eq. (4.6) directly to Eq. (4.1). Here it is assumed the temperature uncertainty at the contacting surfaces is equal to the elemental sensor uncertainty and that all other uncertainties are zero. This results in

$$U_{RA} = \sqrt{\left(\frac{A}{Q}\right)^2 (U_{\Delta T})^2 + \left(\frac{-A\Delta T}{Q^2}\right)^2 (U_Q)^2} \tag{4.9}$$

where

$$U_Q = \sqrt{\left(\frac{kA}{\Delta x}\right)^2 (U_{\Delta T})^2} \tag{4.10}$$

and

$$U_{\Delta T} = \sqrt{U_{Ta}{}^2 + U_{Tb}{}^2} \,. \tag{4.11}$$

Thus, for given values of k, A, Δx and Q, the variation of the uncertainty U_{RA} in the specific thermal resistance (Eq. (4.9)) can be plotted as a function of sensor thermal uncertainty, U_T. Figure 4.4 shows the magnitude of U_{RA} evaluated for a common parameter set typical for our experiment (k=215 W/m·K, A=1600 mm^2, Δx= 20 mm and Q=4 W), using values of the thermal precision, U_T, corresponding to previous studies reported in the literature. The labels on the data points indicate the authors whose studies exhibited the value of U_T used for computing that data point. Due to the increase in thermal precision alone, the apparatus developed in the present study allows for an order-of-magnitude improvement in the sensitivity and uncertainty of measured thermal resistance. To emphasize the practical importance of this improvement, the horizontal line plotted in Fig. 4.4 represents 10% of the theoretical specific thermal resistance of a TIM having a thickness of 50 μm and a

thermal conductivity of 5 W/m·K. Based on the assumptions of this simplified analysis, this demonstrates that, in order to accurately characterize the performance of thin bondline, high-performance TIMs, the instrumentation and techniques presented in the present study are indeed essential.

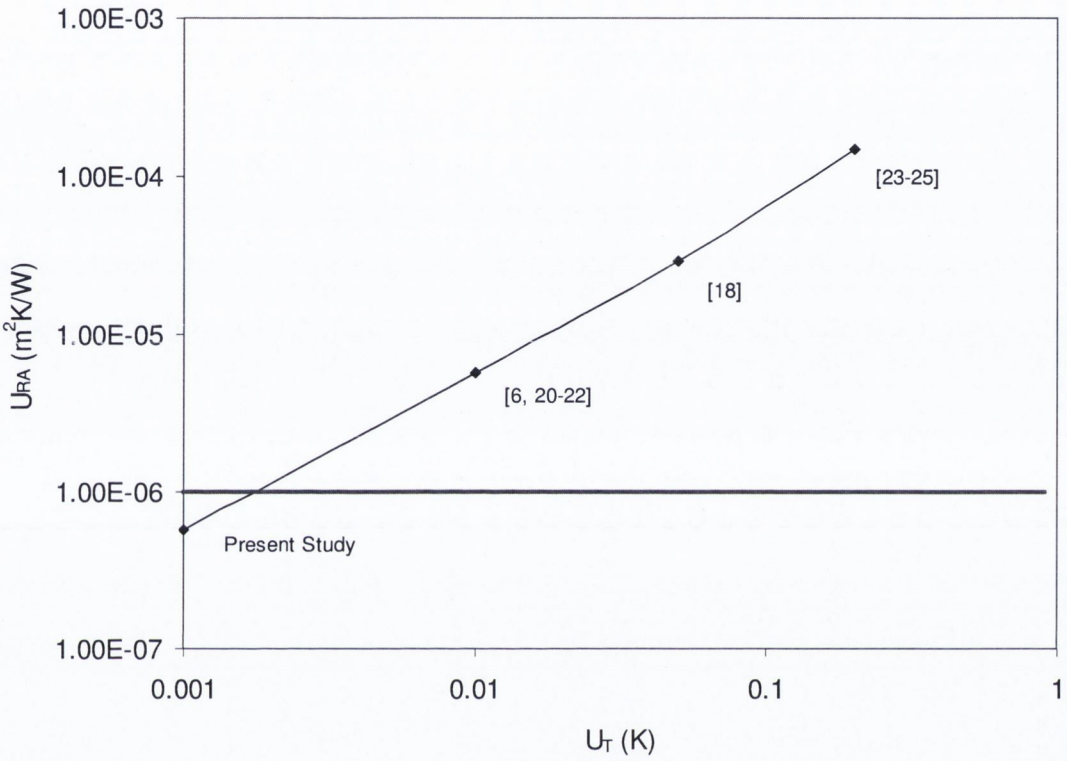


Figure 4.4: Variation of specific thermal resistance uncertainty, U_{RA}, with thermal sensor uncertainty, U_T, for a common set of experimental parameters.

4.4 Results & Discussion

In order to validate the sensitivity and precision of the test facility, self-contact interface tests were performed to characterize system performance for low thermal resistance scenarios, where the specific thermal resistance of the TIM would be on the order of magnitude of the self-contact resistance of the meter bars themselves.

The temperature distribution in the meter bars during self contact is shown in Fig. 4.5. This extremely low-power case (Q = 0.262 ± 0.006 W) demonstrates the linearity of the meter bars and temperature sensitivity of the instrumentation. The linear fits to the data indicate a temperature difference between the contacting surfaces was 0.0089 ± 0.0012 K, while the heat currents in the meter bars agree to within 0.4 %, demonstrating accurate energy balance. As the heater power is increased, these uncertainties drop significantly. Indeed, over a large range of input powers, the calculated heat fluxes between the two meter bars balance within their computed uncertainties, as illustrated in Fig.4.6.

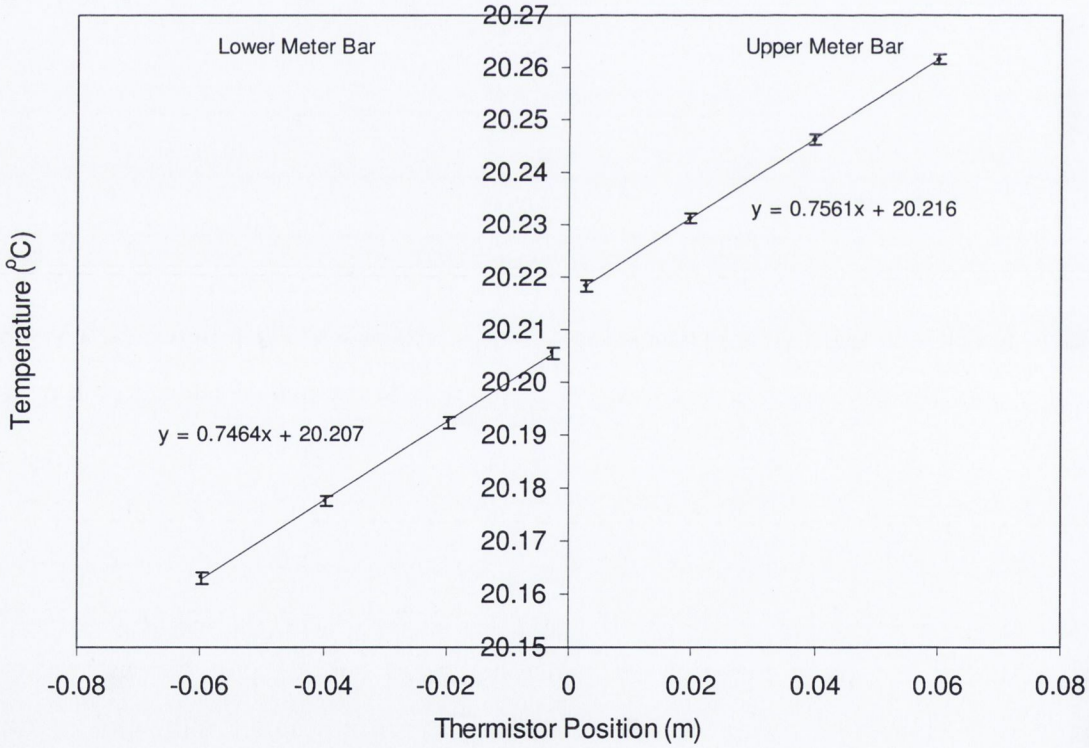


Fig. 4.5: Low-heat-flux meter-bar temperature distribution during self-contact, Q=0.262 ± 0.006 W, P ≈ 0.2 MPa.

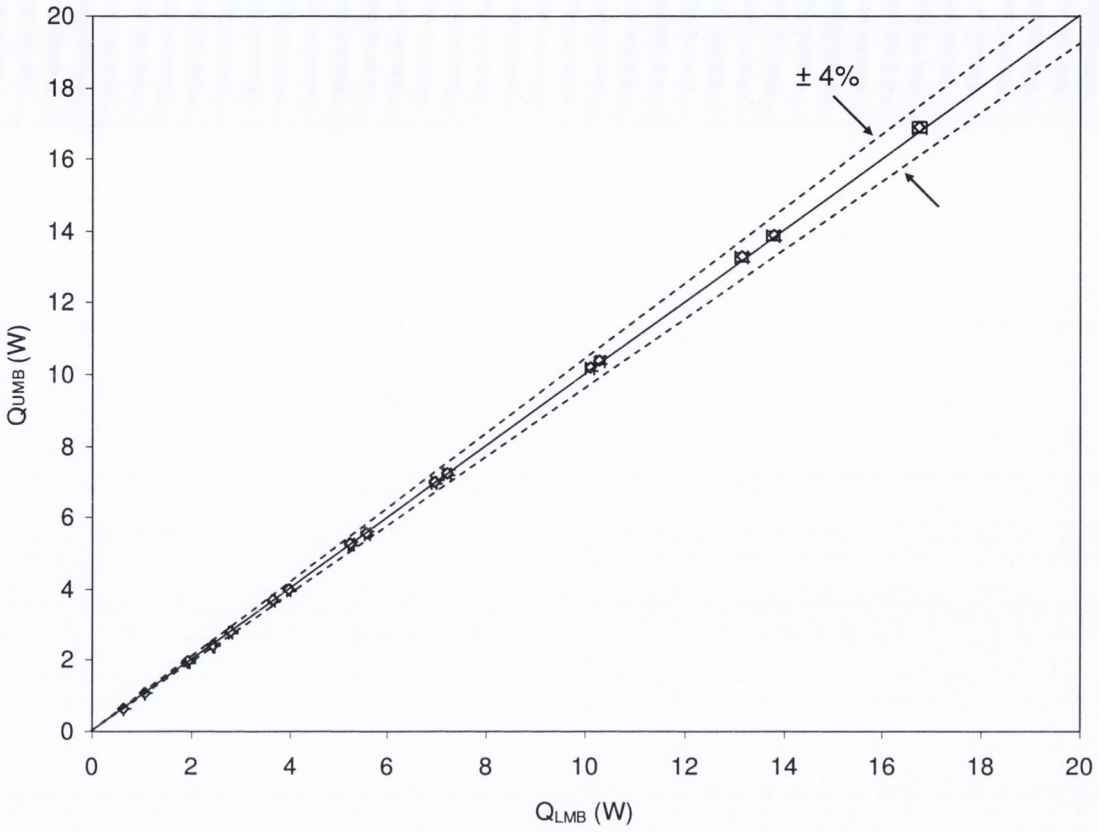


Fig. 4.6: Energy balance between upper and lower meter bars for a range of powers.

The change in specific thermal resistance and electrical contact resistance for the bare, dry meter bars in self-contact is shown as a function of pressure for $Q \approx 4.4$ W in Fig. 4.7. Here one can observe a marked decrease in both resistances initially as the contact pressure is increased. The trend in the change of specific thermal resistance with pressure and the overall magnitude correspond well with the data presented by Yovanovich [36]. A minimum dry-contact resistance of 2.71×10^{-5} m^2K/W was measured with calculated uncertainty of 1.8%. The trend in electrical contact resistance corresponds well with the results of Misra and Nagaraju [24], given the somewhat larger contact area used in the present study. The lowest electrical resistance measured was 320 μΩ, with an uncertainty of 0.15%. Of this, 5.44 μΩ (or 3.4% of this value) can be attributed to the bulk resistance of the CuW meter bars.

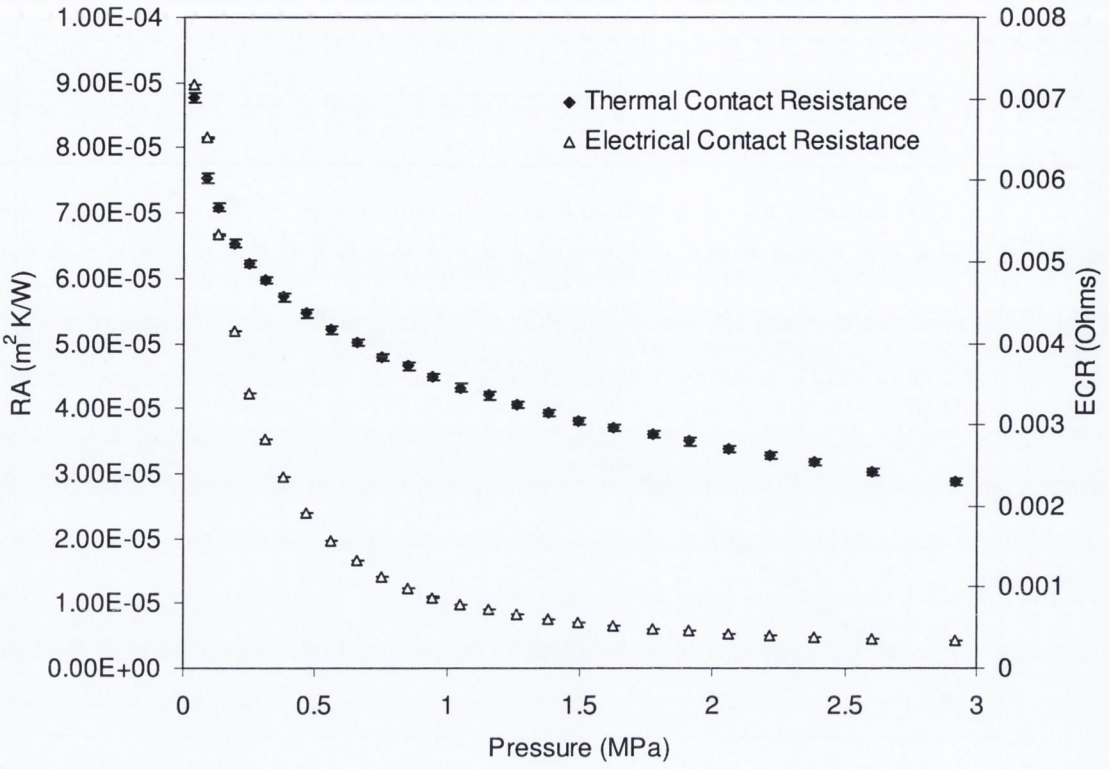


Fig. 4.7: Change in Specific Thermal Resistance and Electrical Contact Resistance with Pressure for Dry Self-Contact, $Q \approx 4.4$ W.

A single drop of mineral oil was compressed between the meter bars at a pressure of approximately 3 MPa to achieve a lower thermal resistance by displacing any air in the microscopic voids of the contact zone. A comparison between the specific thermal contact resistance for the meter bars in dry contact and using oil as a TIM with heat flux is shown in Fig. 4.8. Here, the inclusion of oil as a TIM reduces the thermal contact resistance from approximately 2.75×10^{-5} $m^2\cdot K/W$ to 5×10^{-6} $m^2\cdot K/W$. Also demonstrated in Fig. 4.8 is the reduction in calculated uncertainty with increasing heat flux. The lowest specific thermal resistance measured was of 4.68×10^{-6} $m^2\cdot K/W$ with an uncertainty of 2.7% using a heat transfer rate of 16.8 W. For both the dry contact and wet contact results, the slight decrease in specific thermal resistance with heat flux can be attributed to a small pressure increase due to system thermal expansion as the overall temperatures increase.

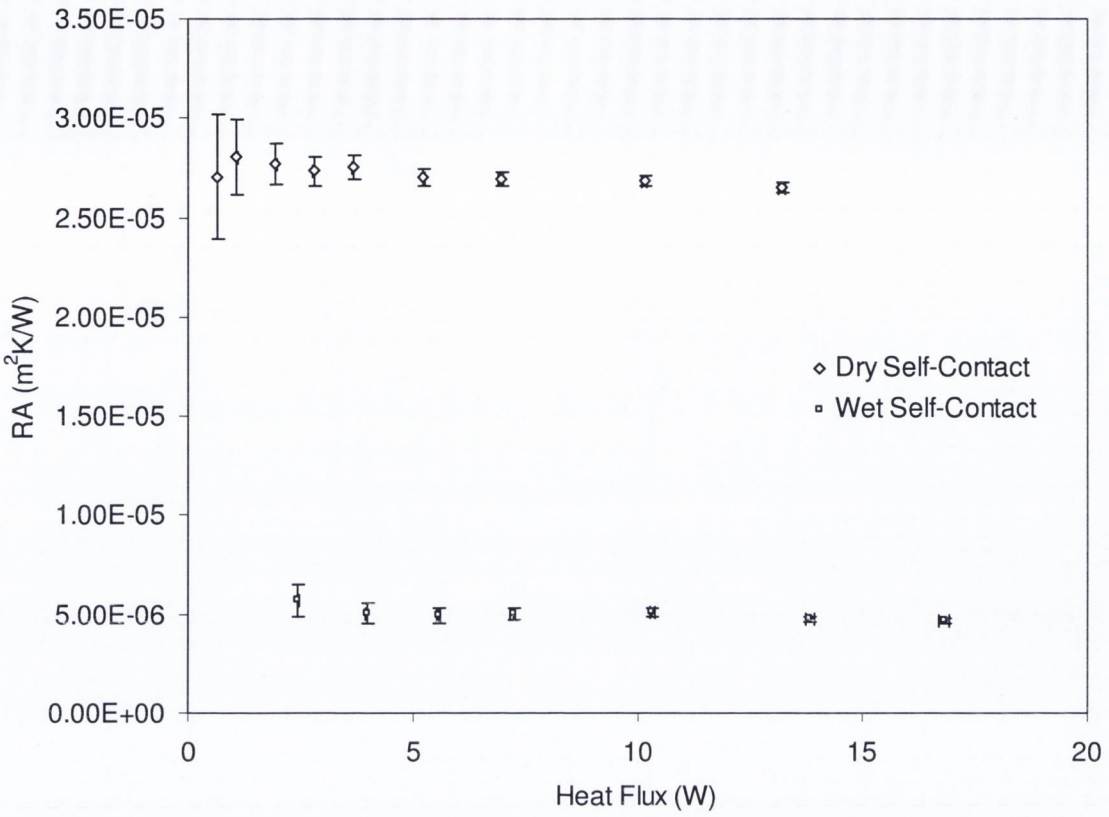


Fig. 4.8: Specific thermal resistance as a function of heat flux for dry and wet self contact ($P \approx 3$ MPa).

A commercially available graphite TIM nominally 0.125 mm thick was characterized using this apparatus. Specific thermal resistance and electrical resistance as function of pressure for this TIM are shown in Fig 4.9. For comparison, the specific thermal resistance and electrical resistances from Fig. 4.8 of the meter bars in dry self-contact are also shown in this figure. These results indicate the specific thermal resistance of the TIM is of the same order of magnitude of the dry contact resistance of the meter bars themselves. This serves to highlight the aforementioned inherent difficulty of discerning the thermal contact resistance between the meter bars and the TIM and the bulk thermal resistance of the TIM itself. Electrically, however, the bulk resistance of the TIM and meter bars can be considered negligible compared to the electrical contact resistances. The bulk electrical resistance for this 0.125 mm graphite pad was calculated as approximately 1 $\mu\Omega$, and, since the electrical resistance measurement with the TIM is considerably higher than that of the dry self-contact, one can infer that the thermal contact resistance between the TIM and the meter bars plays the more important role in the overall measured specific thermal resistance. As discussed in Chapter 3, this ability to simultaneously measure thermal and electrical resistance was developed in order to characterize the thermal contact

resistance of MMT-TIMs. It has been proposed that a correlation relating the electrical and thermal contact resistances as a function of pressure be developed for MMT-TIMs thereby allowing a relatively straightforward electrical conductivity measurement to be used to indirectly distinguish the thermal contact resistance from the bulk thermal resistance of the MMT-TIM or any other electrically conductive material [37].

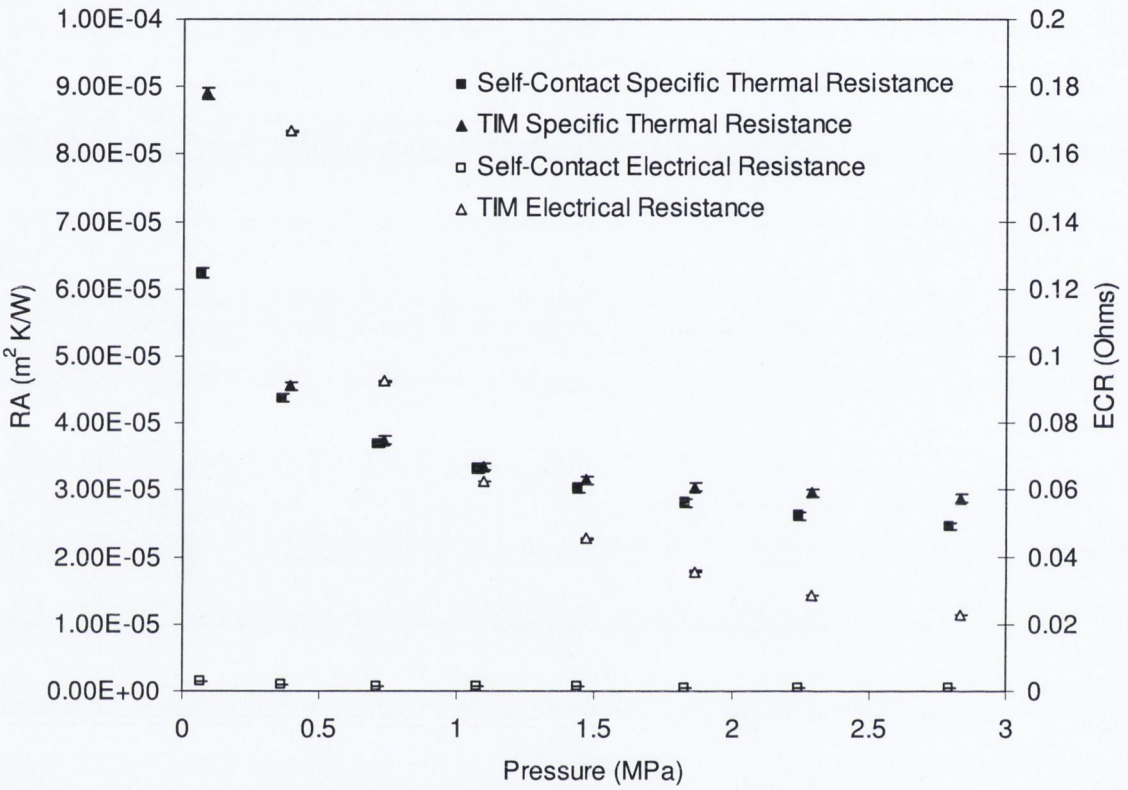


Fig 4.9: Change in specific thermal resistance and electrical contact resistance with applied pressure for a graphite.

The change in apparent thermal conductivity of the graphite TIM as a function of pressure is shown in Fig. 4.10. As the contact resistance between the meter bars and the TIM diminished, the apparent thermal conductivity was seen to asymptotically approach the bulk thermal conductivity value of the TIM, which was approximately 4.5 W/m·K. Results from two subsequent tests are also shown in Fig. 4.10 and demonstrate the repeatability of this measurement. At the highest pressures, the measured effective thermal conductivity the graphite pad exhibited repeatability of approximately 1 %.

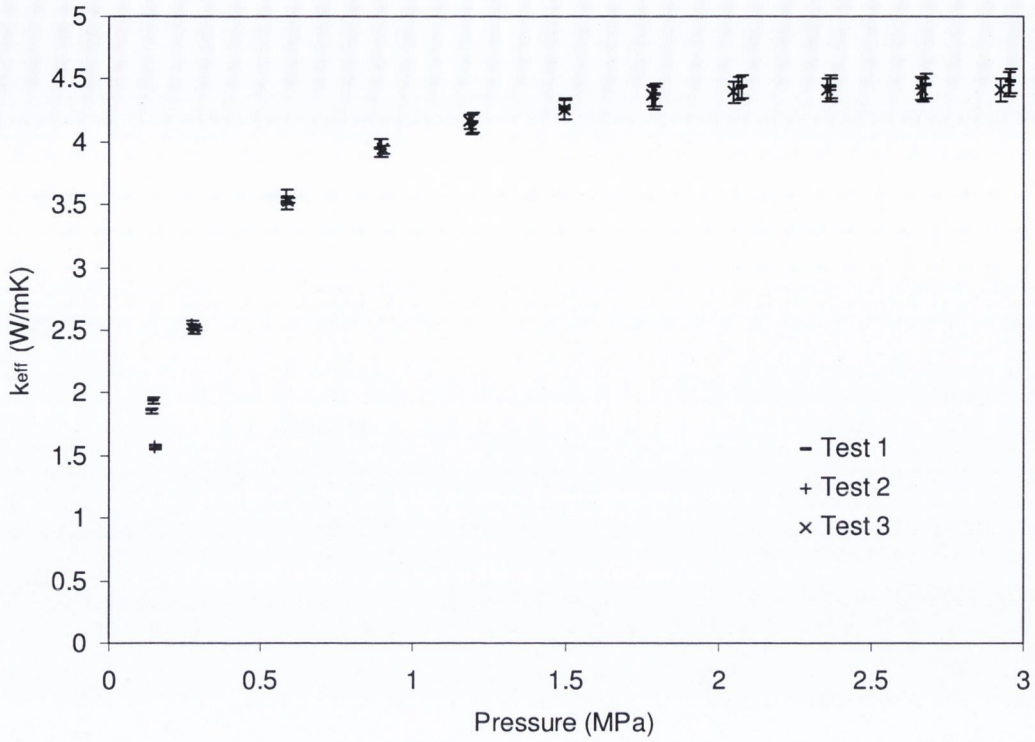


Fig 4.10: Change in effective thermal conductivity with applied pressure for a graphite TIM during three tests.

4.5 Summary

An apparatus with unprecedented precision and sensitivity has been built for the performance characterization of thermal interface materials. This apparatus allows for the precise measurement of specific thermal resistance and apparent thermal conductivity of a TIM under a range of pressures and temperatures simultaneously with electrical resistance measurements.

Thermal and electrical contact resistance measurements of the meter bars in dry and wet self-contact demonstrated the sensitivity and precision for low-level measurements. The lowest specific thermal resistance measured was 4.68×10^{-6} $m^2\cdot K/W$ with an uncertainty of 2.7% at an input power of 16.8 W. It is difficult to make direct, qualitative comparisons against the precisions and uncertainties reported in previous studies due to the paucity of uncertainty analysis presented. However the thermal precision of the current setup alone indicates an order-of-magnitude improvement in precision and sensitivity over any previous investigation. This sensitivity will enable the development and characterization of new, optimized TIM materials with thermal impedance values sufficiently low to meet the demanding requirements of the International Technology Roadmap for Semiconductors [38]. The specific thermal resistance, electrical contact resistance and effective thermal conductivity of a commercially available graphite pad were measured over a range of pressures. The simultaneous measurements of electrical resistance demonstrated a correlation between thermal and electrical contact resistance and will allow for the indirect estimation of thermal contact resistance of the MMT-TIMs investigated in the present study.

References

1. Smith B., Brunschwiler, T., & Michel, B. "Comparison of transient and static test methods for chip-to-sink thermal interface characterization". Microelectron. J., doi:10.1016/j.mejo.2008.06.079 (2008).

2. Linderman, R., Brunschwiler, T., Smith B., and Michel, B. "High performance thermal interface technology overview". Proceedings of the 13th Workshop on Thermal Issues in ICs and Systems (THERMINIC), pp. 129-134 (2007).

3. Ziaei, A. & Demoustier, S., "NANOPACK – Nano Packaging Technology for Interconnect and Heat Dissipation". Proceedings of the 14th Workshop on Thermal Issues in ICs and Systems (THERMINIC), Rome, Italy, September 24-26, 2008.

4. Liu, J., Michel, B., Rencz, M., Tantolin, C., Sarno, C., Miessner, R., Schuett, K. V., Tang, X., Demoustier, S. & Ziaei, A. "Recent Progress of Thermal Interface Material Research – An Overview". Proceedings of the 14th Workshop on Thermal Issues in ICs and Systems (THERMINIC), Rome, Italy, September 24-26, 2008.

5. Tzeeng, J. J. W., Weber, T. W. and Krassowski, D. W. "Technical Review on Thermal Conductivity Measurement Techniques for Thin Thermal Interfaces". Proceedings of the 16th IEEE SEMI-THERM Symposium, pp. 174-181 (2000).

6. Teertstra, P. "Thermal Conductivity and Contact Resistance Measurements for Adhesives". Proceedings of InterPACK 2007, Vancouver, BC, July 8-12, 2007.

7. Kempers, R., Frizzell, R., Lyons, A. & Robinson, A.J., "Development of a Metal Micro-Textured Thermal Interface Material", ASME InterPACK Conference, IPACK2009-89366, San Francisco, July 8-12, 2009

8. Bosch, E. G. T. & Lasance C. J. M. "Accurate Measurement of Interface Thermal Resistance by Means of a Transient Method". Proceedings of the 16th IEEE SEMI-THERM Symposium, pp. 167-173 (2000).

9. Lasance, C. J. M. & Lacaze, C. "A Transient Method for the Accurate Measurement of Interface Thermal Resistance". Proceedings of the 12th IEEE SEMI-THERM Symposium, pp. 43-45 (1996).

10. Lasance, C. J. M., Murray, C. T., Saums, D. L. & Rencz, M., "Challenges in Thermal Interface Material Testing". Proceedings of the 22nd IEEE SEMI-THERM Symposium, pp. 42-49 (2006).

11. Rencz, M. R. & Székely, V., "Measuring Partial Thermal Resistances in a Heat-Flow Path". IEEE Transactions on Components and Packaging Technologies **25**, pp. 547-553. (2002).

12. Rencz, M., Székely, V., Farkas, G. & Courtois, B. "Measuring Interface Thermal Resistance Values by Transient Testing". Proceedings of the IEEE 2002 Inter-Society Conference on Thermal Phenomena, pp. 136-141 (2002).

13. Smith, B., Brunschwiler, T. & Michel, B. "Utility of Transient Testing to Characterize Thermal Interface Materials". Proceedings of the 13th Workshop on Thermal Issues in ICs and Systems (THERMINIC), Budapest, Hungary, September 17-19, 2007.

14. Parker, W. Jenkins, R., Butler, C. & Abbott, G. "Flash Method of Determining Thermal Diffusivity, Heat Capacity, and Thermal Conductivity". Journal of Applied Physics **32**, pp. 1679-1684 (1961).

15. Kehoe, L., Kelly, P. V. & Crean, G. M. "Application of the Laser Flash Diffusivity Method to Think High Thermal Conductivity Materials". Microsystems Technologies **5**, 18-21 (1998).

16. Gaal, P. S., Thermitus, M. A. & Stroe, D. E. "Thermal Conductivity Measurements using the Flash Method". Journal of Thermal Analysis and Calorimetry **78**, pp. 185-189 (2004).

17. Khuu, V., Osterman, M., Bar-Cohen, A. & Pecht, M. "Thermal performance Measurements of Thermal Interface Materials using the Laser Flash Method". Proceedings of InterPACK 2007, Vancouver, Canada (2007).

18. Gwinn, J. P., Saini, M. & Webb, R. L. "Apparatus for Accurate Measurement of Interface Resistance of High Performance Thermal Interface Materials". Proceedings of the 2002 IEEE Inter-Society Conference on Thermal Phenomena, pp. 644-650 (2002).

19. "Standard Test Method for Thermal Transmission Properties of Thermally Conductive Electrical Insulation Materials". ASTM Standard D5470-06, Copyright ASTM International, Conshohocken, PA (2007).

20. Kearns, D. "Improving Accuracy and Flexibility of ASTM D5470 for High Performance Thermal Interface Materials". Proceedings of the 19th IEEE Semi-Therm Symposium, pp. 129-133 (2003).

21. Culham, J. R., Teertstra, P., Savija, I., & Yovanovich, M. M. "Design, Assembly and Commissioning of a Test Apparatus for Characterizing Thermal Interface Materials". Proceedings of the 2002 IEEE Inter-Society Conference on Thermal Phenomena (2002).

22. Savija, I., Culham, J. R. & Yovanovich, M. M. "Effective Thermophysical Properties of Thermal Interface Materials: Part 2 Experiments and Data". Proceedings of InterPACK 2003, Maui, HI, July 6-11, 2003.

23. Rao, V. V., Bapurao, K., Nagaraju, J. & Krishna Murthy, M. V. "Instrumentation to Measure Thermal Contact Resistance". Meas. Sci. Tech. **15**, pp. 275-278 (2004).

24. Misra, P. & Nagaraju, J. "Test Facility for Simultaneous Measurement of Electrical and Thermal Contact Resistance". Review of Scientific Instruments **75,** pp. 2625-2630 (2004).

25. Singhal, V., Litke, P. J., Black, A. F. & Garimella, S. V. "An experimentally validated thermo-mechanical model for the prediction of thermal contact conductance". Int. J. Heat & Mass Transfer **48**, pp. 5446-5459 (2005).

26. Madhusudana, C.V., "Accuracy in Thermal contact Conductance Experiments-The Effect of Heat Losses to the Surroundings" Int. Comm. Heat Mass Transfer **27**, pp. 877-891 (2000).

27. Kempers, R., Kolodner, P., Lyons, A. & Robinson, A. J. "Development of a High-Accuracy Thermal Interface Material Tester". Proceedings of IEEE ITherm 2008, Orlando, FL, pp. 221-226. (2008).

28. Kolodner, P., Hodes, M., Ewes, I., and Holmes, P. "Thermal-Resistance Measurements on Mechanical Gap Fillers". Proceedings of InterPACK 2005, San Francisco, CA, July 17-22, 2005.

29. Kedzierski, M. A. & Worthington, J. L. "Design and Machining of Copper Specimens with Micro Holes for Accurate Heat Transfer Measurements". Experimental Heat Transfer **6**, pp. 329-344 (1993).

30. Keithley, Low Level Measurements Handbook: Precision DC Current, Voltage, and Resistance Measurements, 6th Edition, Keithley Instruments Inc. USA (2004).

31. Wald, A. "The Fitting of Straight Lines if Both Variables are Subject to Error". Ann. Math. Stat. **11,** 284 (1940).

32. Bartlett, M. S. "Fitting a Straight Line When Both Variables Are Subject to Error". Biometrics **5,** pp. 207-212 (1949).

33. Press, W. H., Teukosky, S. A., Vetterling, W. T. & Flannery, B. P., Numerical Recipes in FORTRAN - The Art of Scientific Computing, second edition. Cambridge University Press, Cambridge, chapter 15 (1992).

34. Ku, H. H. "An Introduction to the Statistical Treatment of Measurement Data". NBS Report 8677 (1965).

35. Kline, S. J., and McClintock, F. A. "Describing uncertainties in single sample experiments", Mech. Eng. **75,** pp. 3-8 (1953).

36. Yovanovich, M. M. "Four Decades of Rsearch on Thermal Contact, Gap, and Joint Resistance in Microelectronics". IEEE Transactions on Components and Packaging Technologies **28**, pp 182-206 (2005).

37. Kempers, R., Lyons, A. & Robinson, A.J., "Characterization of Thermal Contact Resistance in Metal Micro-Textured Thermal Interface Materials using Electrical Contact Resistance Measurements" *Accepted to DSL-2009*, June 24-26, Rome, Italy (2009).

38. "The International Technology Roadmap for Semiconductors 2007 Edition: Assembly and Packaging" International Technology Roadmap for Semiconductors (2007).

Chapter 5

Results & Discussion

5.1 Baseline Experimental Results

A relatively simple MMT-TIM design is presented in this section to demonstrate the overall concept of MMT-TIMs and to provide a baseline case for subsequent modelling and experimental comparisons. An illustration of the approximate geometry is shown in Fig. 5.1 while a photograph of the corresponding MMT-TIM is shown in Fig 5.2.



(a) (b) (c)

Fig. 5.1: Nominal feature geometry for baseline MMT-TIM Sample B

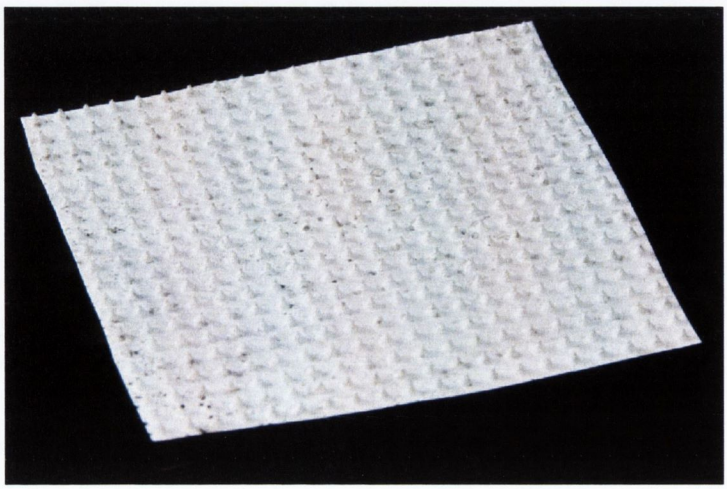


Fig. 5.2: Photograph of MMT-TIM Sample B prior to testing

This design consisted of an array of hollow silver cones approximately 0.95 mm tall and 1 mm in base diameter on a 2 mm pitch and is designated here as Sample "B". To correspond to the experimental test area, an array 40 mm × 40 mm was manufactured using the process outlined in Chapter 2. Two plating thicknesses were tested resulting in the samples having a total mass of 0.781 g and 0.601 g respectively. Upon completion of the surface reconstruction process outlined in Chapter 3, these masses translate to estimates of thickness of approximately 36 μm and 28 μm. A discussion of the uncertainty of these thicknesses is presented in the following section.

The pressure required to deform MMT-TIM Sample B as it is compressed is shown in Fig. 5.3. Here, both sample thicknesses exhibit similar trends: First, the pressure increases linearly as the thickness decreases by 0.2 mm. Next there is a region where the interfacial thickness decreases from 0.8 to 0.4mm yet the pressure remains relatively constant. Finally, the structures begin to densify and the pressure rises steeply after 0.65 mm of compression (<0.35mm of interfacial thickness). Overall, the thicker metal foil requires a correspondingly larger pressure to deform to a given strain (i.e. bondline thickness).

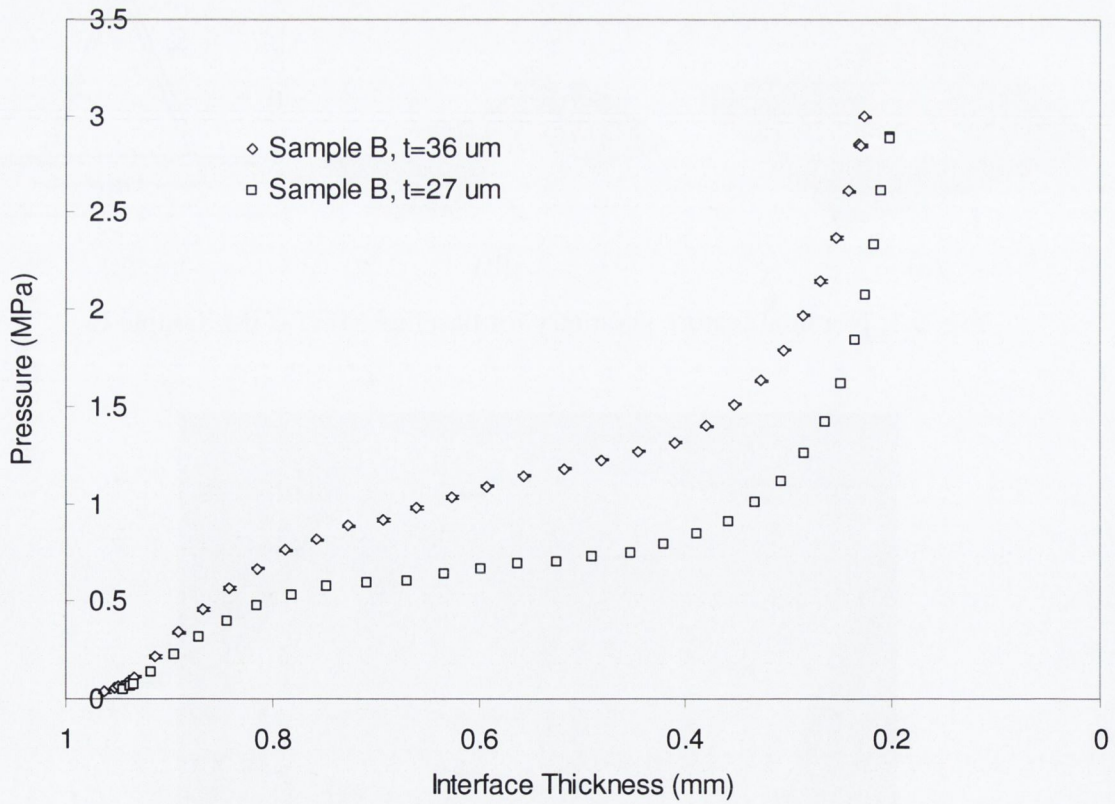


Fig 5.3: Mechanical response of Sample B during compressive deformation

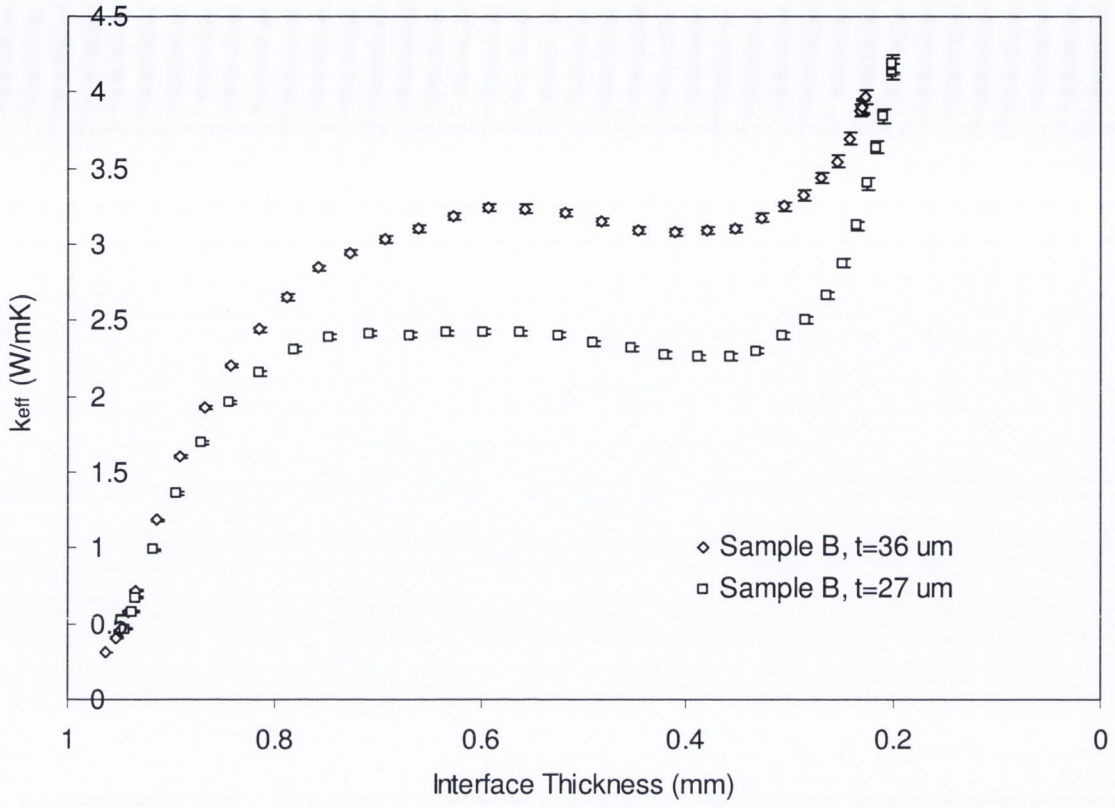


Fig. 5.4: Effective thermal conductivity of Sample B during compressive deformation

The measured effective thermal conductivity for MMT-TIM Sample B during compression is shown in Fig 5.4. Here, an initial increase in effective thermal conductivity is observed as pressure is applied and the contact resistance drops. Similarly to the pressure response, there exists a relatively stable plateau region where the effective thermal conductivity remains relatively constant. Finally, as the structures densify (interfacial thickness <0.35mm), a combination of self-contact within the MMT-TIM and a lower contact resistance due to the increased contact pressure with the meter bars results in a sudden increase in effective thermal conductivity.

The specific thermal resistance of MMT-TIM Sample B having a metal thickness (i.e. plating thickness) of 36 μm as a function of applied pressure is shown in Fig. 5.5. For comparison, the specific thermal resistance measured for a flat silver foil of similar thickness (35 μm) is also plotted. For both structures we see the similar trend of decreasing specific thermal resistance with increasing pressure. For the MMT-TIM, this is due to a combination of decreased contact resistance as the pressure is increased and a decrease in the bulk resistance of the structure as it is deformed. For the flat silver foil however, there is virtually no change in the bulk resistance of the material and the decrease is attributed only to the thermal contact resistance with the meter bars. For the flat silver

foil, with a conductivity of approximately 420 W/m·K, the bulk specific thermal resistance can be readily calculated as 8.33×10^{-8} m^2K/W. Therefore, at the highest pressure, the total specific contact resistance for the flat silver foil amounts to 2.69×10^{-5} m^2K/W or about 99.7% of the total measured thermal resistance. This is further illustrated by the measured effective thermal conductivity of the flat foil as shown in Fig. 5.6. Here the effective thermal conductivity increases roughly linearly with pressure. However it represents only a small fraction of the actual thermal conductivity of silver. Thus, as a thermal interface material, the flat silver foil is limited by its contact resistance at the mating surfaces and not by the bulk conductivity of the material.

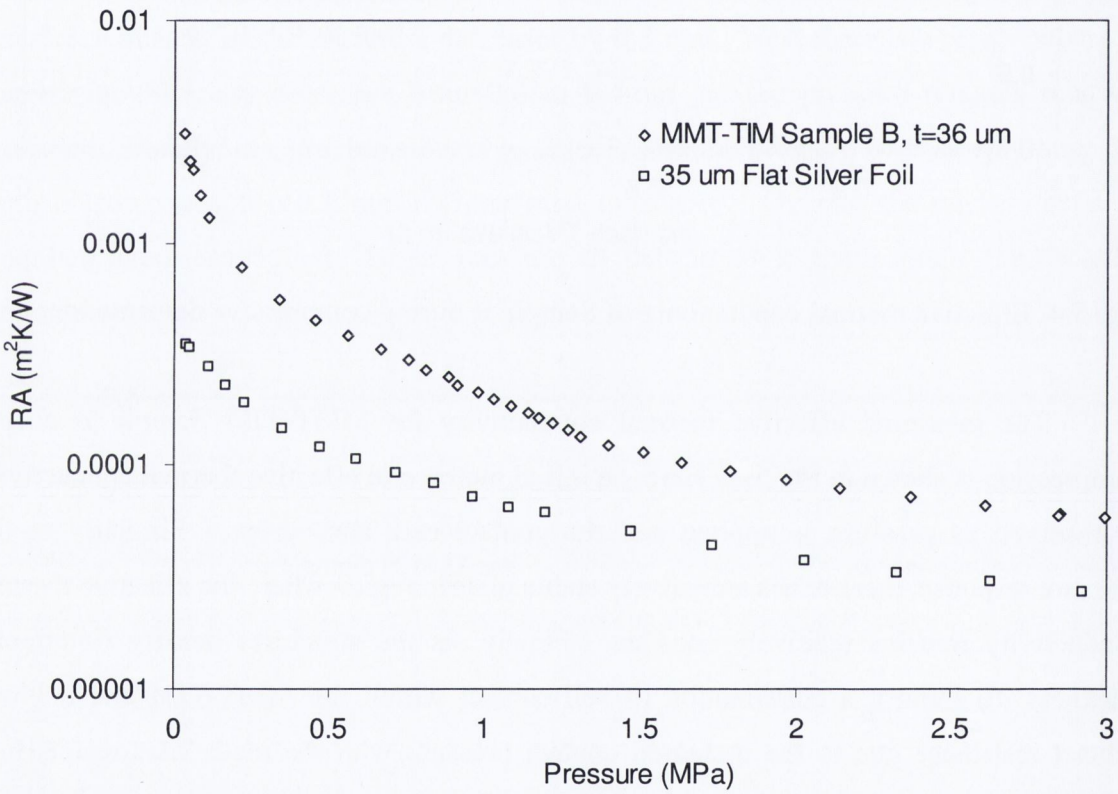


Fig 5.5: Variation of specific thermal resistance with pressure for MMT-TIM Sample B, t=36 μm and a flat silver foil 35 μm thick.

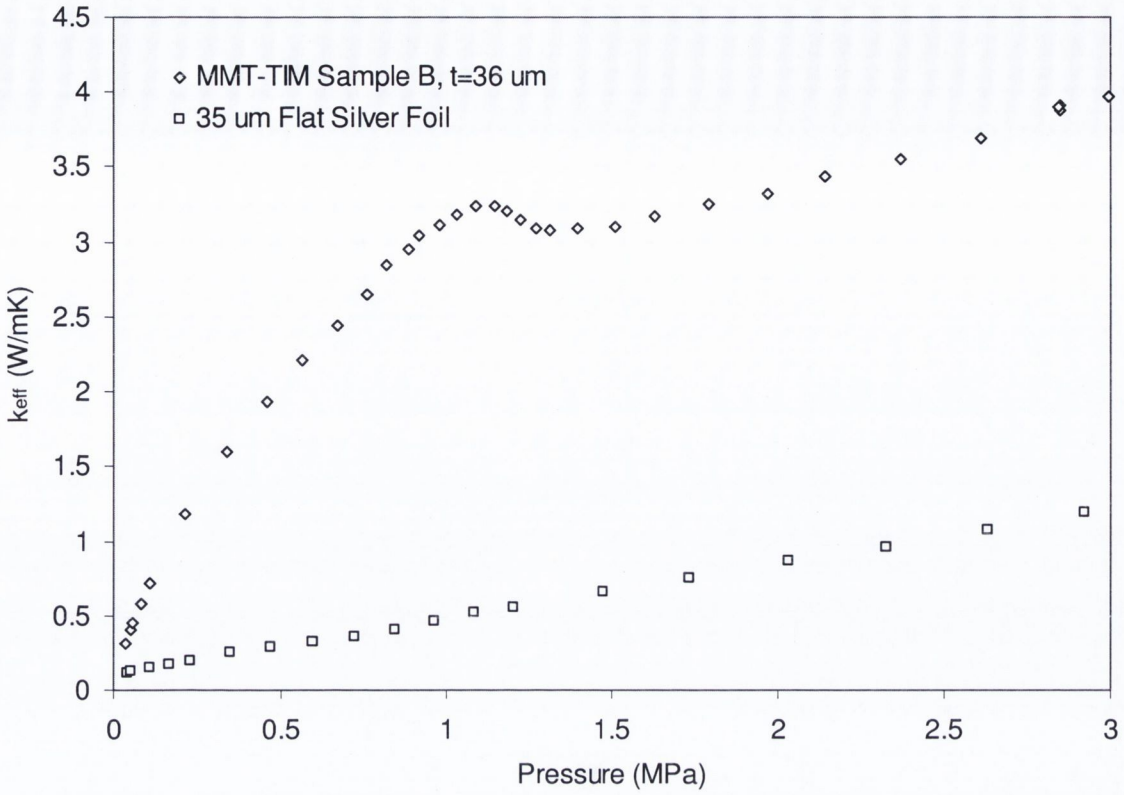


Fig. 5.6: Variation of effective thermal conductivity with pressure for MMT-TIM Sample B, t=36 μm and a flat silver foil 35 μm thick.

The overall specific thermal resistance of the MMT-TIM is significantly higher than that of the flat foil. The resistance of the bulk structure is higher due to the much thicker interface ranging from 1 mm to 0.2 mm as the structure is compressed as well as, presumably, a higher specific bulk resistance since the interface is not filled completely with silver. For now, the bulk thermal resistance of the structure remains unknown. However, in terms of effective thermal conductivity, this structure represents a significant improvement over the flat silver foil, as shown in Fig 5.6. Additionally, the MMT-TIM structure demonstrates a significant ability to strain with a normally applied pressure (up to 80% strain as shown in Fig. 5.4) compared to the flat silver foil which exhibits virtually no compliance (i.e. ability to compress normally with an applied pressure).

In summary, this illustrative example demonstrates the concept of a MMT-TIM: A structure consisting of features that are designed to deform plastically in order to achieve an array of intimate contact mating surfaces whilst maintaining a relatively low bulk resistance and high compliance.

The Sample B design (cone with 1 mm diameter base and 1 mm height) served as a baseline reference geometry from which geometrical variations such as feature height,

diameter or shape were made and have been discussed in detail by Kempers *et al.* [1] and are presented in Appendix 6. However, the remainder of this Chapter will focus on improvements to the numerical model and predictions and comparisons to these baseline results.

5.2 Model Predictions: Mechanical Response

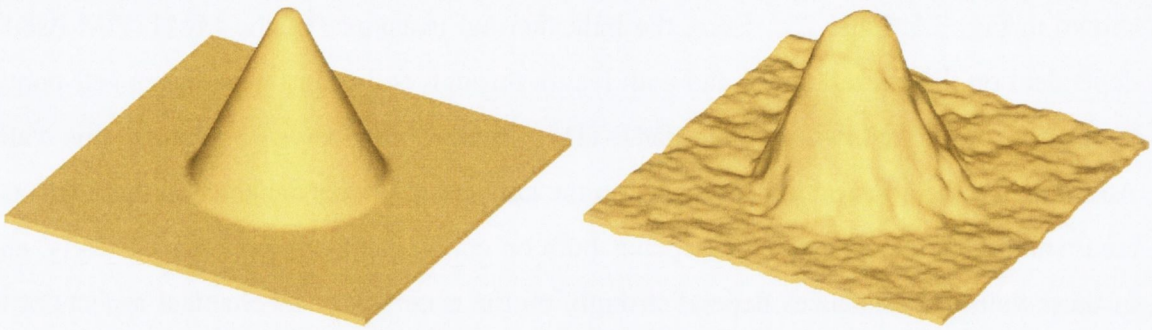
The objective of the combined thermal-mechanical model developed in Chapter 3 is to accurately predict the large plastic deformations and compression forces as these structures are crushed while simultaneously calculating the thermal resistance and effective thermal conductivity of the MMT-TIM. The overall thermal resistance of the MMT-TIM depends on a number of inter-related factors that depend directly on the accuracy of the mechanical result. Consider the diagram of the MMT-TIM thermal resistance network shown in Fig. 3.5, Page 25. Here, the bulk thermal resistance of the MMT-TIM itself is dependent on the overall shape and path length through body. Instances when self-contact is formed or broken within the MMT-TIM structure can serve to change this value. Additionally, the constriction resistance in the contacting bodies depends on the contacting area while the contact resistance depends both on contact area and pressure. Clearly, each of these thermal resistances depend strongly on the accuracy of mechanical aspects of the simulation. The converse, however, is not true: the mechanical response of the MMT-TIM depends largely on the material properties and initial geometrical description of the structure and not on the temperature field. For the purposes of this study, temperature dependence was found to play a negligible role on the material properties and was not included in the model. Thus, in order to achieve accurate results from the model in terms of thermal performance, it is first necessary for the model to accurately capture the mechanical response of the MMT-TIM.

5.2.1 Influence of Geometrical Reconstruction

In Chapter 3, it was hypothesized that a more accurate representation of the MMT-TIM geometry would improve the mechanical response predicted by the numerical model. This was tested by comparing the mechanical responses predicted by the model for both the idealized and reconstructed geometries and comparing them to the experimental results.

The idealized geometry for MMT-TIM Sample B was created by modelling the hollow conical structure of a single unit cell in a 3D solid modeller (PTC ProEngineer). The base diameter of the cones were estimated by imaging the samples beforehand using an SEM image while the feature heights were measured using the initial thickness obtained during testing. The top of the cone and the edges where the cone meets the flat substrate were rounded based on estimates from the SEM images. The thickness of the sample was uniformly defined as 38 μm and 29 μm for the two thicknesses respectively. As disused in Chapter 3, these thicknesses were determined based on the mass of the sample, the density of silver and the geometry volume calculation obtained using the CAD software.

In order to generate a representative reconstructed geometry for MMT-TIM Sample B, a single cone was chosen at random to image. The process described in Chapter 3 was carried out and the reconstructed solid geometry of unit cells representative of MMT-TIM Sample B were generated having resultant thicknesses of 36 μm and 27 μm using the aforementioned procedure. A side-by-side rendering of the final idealized and reconstructed geometries are shown in Fig 5.7 while an SEM image of an actual feature from MMT-TIM Sample B is shown in Fig. 5.8.



(a) (b)

Fig. 5.7: Comparison between a) idealized geometry of MMT-TIM Sample B, t=36 μm unit-cell, b) reconstructed geometry of MMT-TIM Sample B, t=36 μm unit-cell

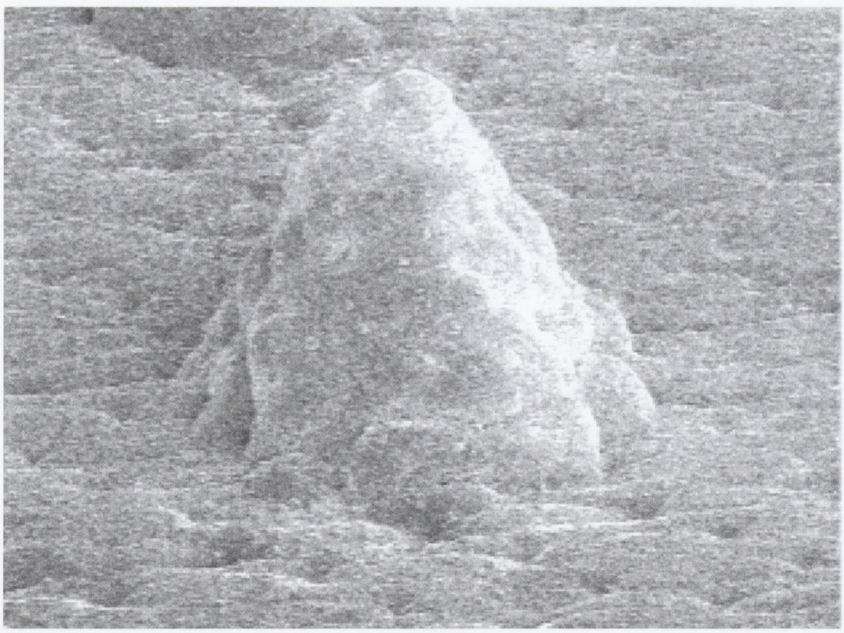


Fig. 5.8: SEM Image of MMT-TIM Sample B, t=36 μm unit-cell

The shapes of the overall geometries were very similar and nominal dimensional measurements were found to agree very well. However, the reconstructed object shown in Fig 5.7b, captures some of the nuances and subtleties present in the actual MMT-TIM structure that remain as artefacts of the manufacturing process. Accurate and systematic

representation of these details in the nominal geometry without this technique would be extremely difficult and time-consuming. The somewhat higher surface area in the reconstructed objects also serves to explain the discrepancy in thickness estimates between the two approaches because the reconstructed surfaces required less material thickness in order to achieve the same overall mass (or volume) as their idealized counterparts (36 μm vs. 38 μm for the thicker sample and 28 μm vs. 29 μm for the thinner sample). A visual comparison to the SEM image of a unit-cell shown in Fig 5.8 clearly shows the reconstructed geometry better agrees with the real features of the actual MMT-TIM.

The two geometries shown Fig 5.7 were employed directly in the numerical model outlined in Chapter 3 to predict the mechanical response of the MMT-TIM Sample B. Sequences of images showing the compressive deformation of the idealized and reconstructed geometries are shown in Fig. 5.9 and Fig. 5.10, respectively.

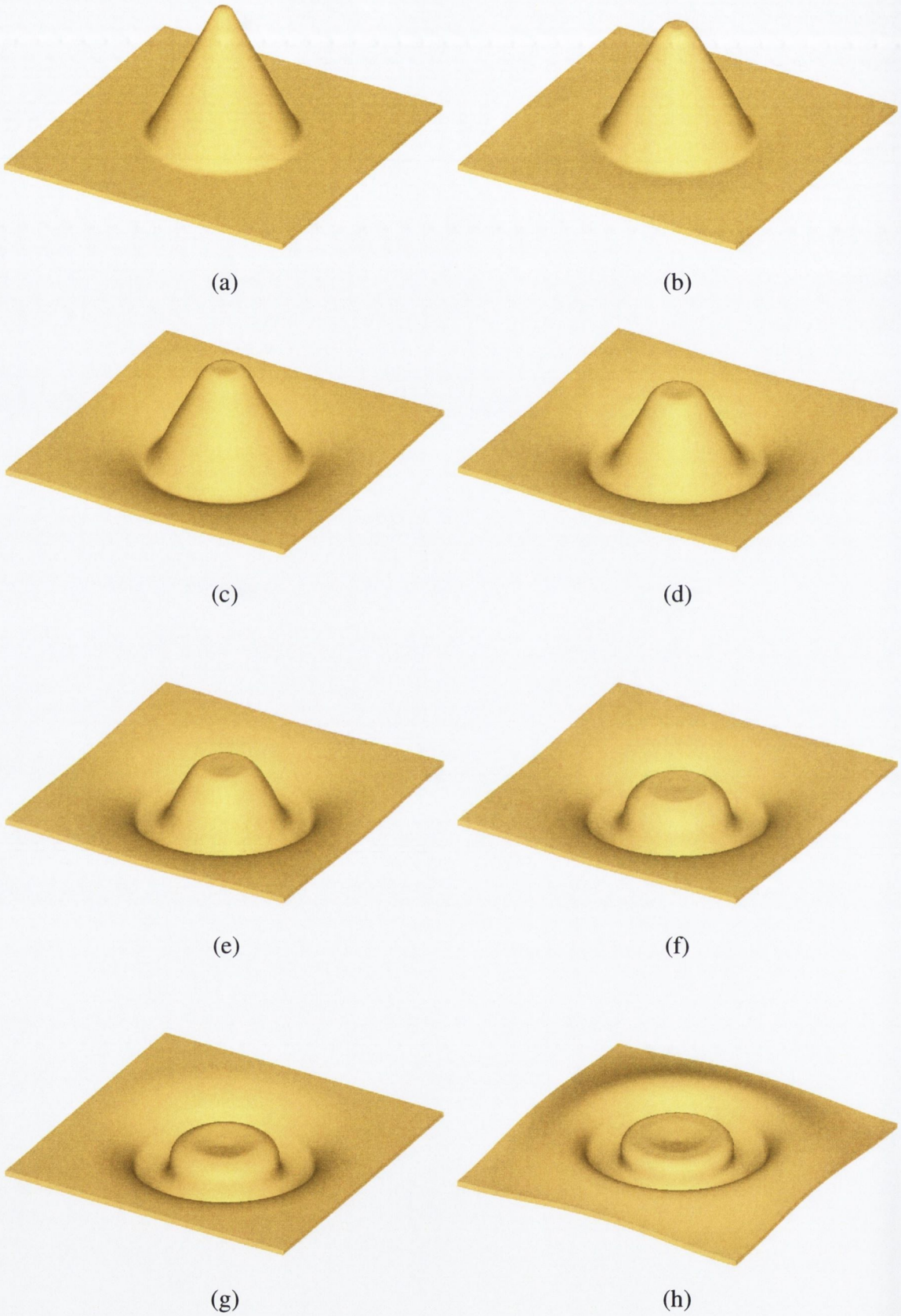


Fig. 5.9: Model prediction of compressive deformation of idealized MMT-TIM Sample B geometry.

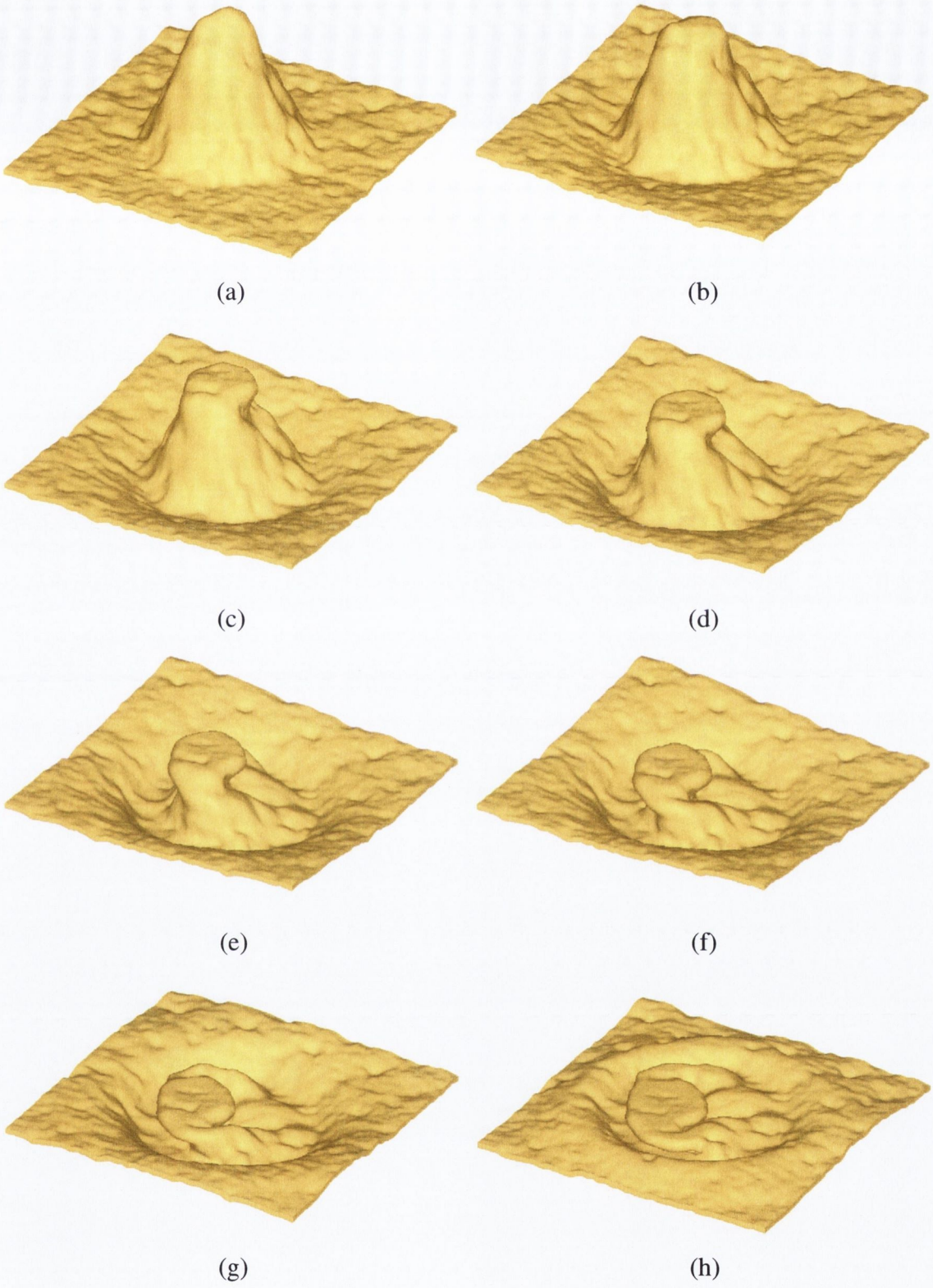


Fig. 5.10: Model prediction of compressive deformation of reconstructed MMT-TIM Sample B geometry.

In Fig. 5.9, one can see the model prediction for the idealized geometry compressed by initially forming a flat region at the peak of the cone shown in Fig. 5.9b. Next, the flat substrate at the bottom was pushed upward as a ring of contact is formed at the base of the cone (Fig. 5.9c-f). Eventually, the peak of the cone deforms downward leaving a ring of contact at the upper surface. The overall deformation was very axisymmetric and indeed symmetry could have been exploited to model this structure with less computational effort. These results are very similar to those reported by Kempers *et al.* [2] and discussed in Chapter 3 where the conical geometries used had a larger aspect ratio.

In comparison, the progressive collapse of the reconstructed MMT-TIM geometry is shown in Fig. 5.10. Here, similar traits such as an initial flattening of the peak of the cone and the upward displacement of the bottom substrate were demonstrated. However in this case, the structure buckled non-uniformly and collapsed in areas where stress concentrations in the geometry existed. This is exemplified by the region just below the peak on the right-hand side shown in Fig. 5.10b-d.

As discussed previously, both pressure and geometry have implications on the eventual calculation of thermal resistance of the MMT-TIM. Thus, the predicted shape of the MMT-TIM during compression is an important aspect in terms of the accuracy the model. An SEM image of the final shape of a single MMT-TIM Sample B feature is shown in Fig. 5.11 while a number of features are shown in Fig. 5.12.

Clearly these particular MMT-TIM structures do not compress in a uniform or symmetric fashion and the final shape predicted in the model using the reconstructed geometry gives a realistic estimation of the final shape of the features. Additionally, the upward bowing of the flat substrate predicted by the model is evident in the experimental case and can be seen clearly in Fig. 5.12.

From a quantitative standpoint, a plot of pressure during compressive deformation for both model geometries and the experimental results for foil thicknesses of 36 μm and 28 μm are shown in Fig. 5.13a and Fig. 5.13b, respectively.

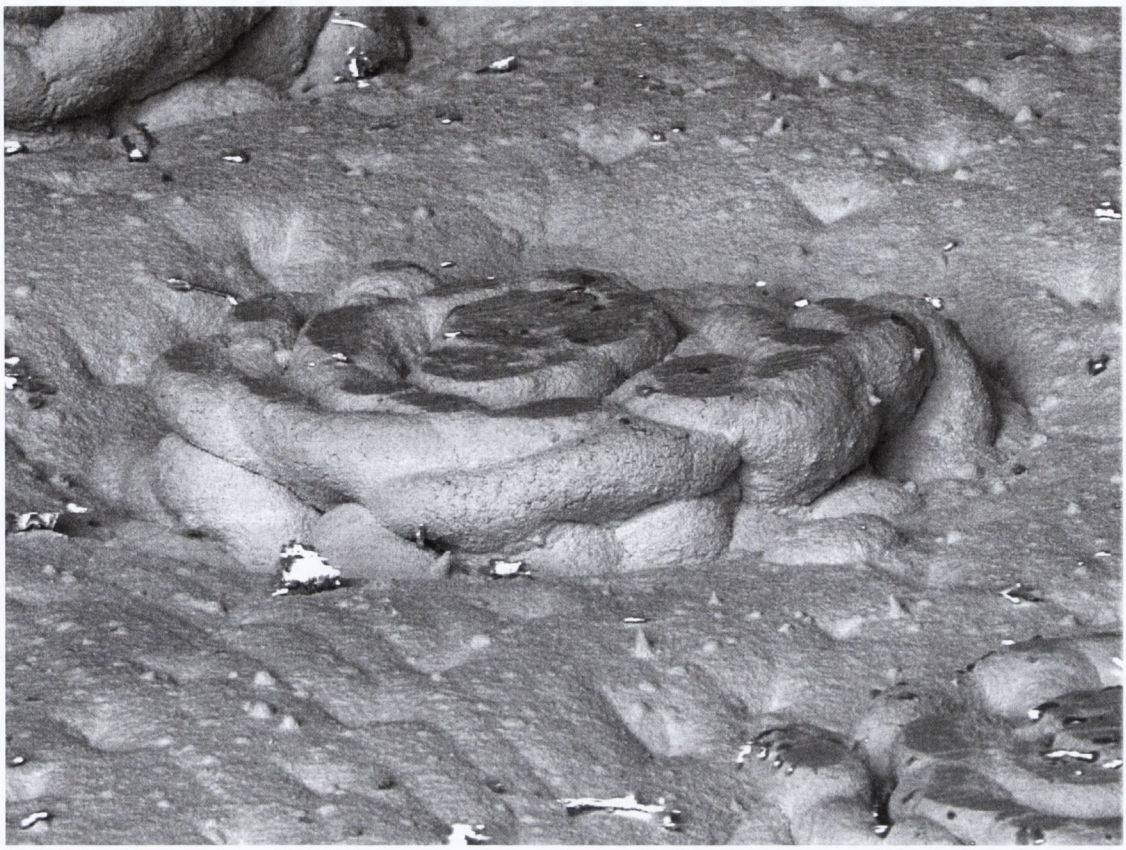


Fig. 5.11: SEM Image of the final shape of a single feature of MMT-TIM Sample B, 36 μm.

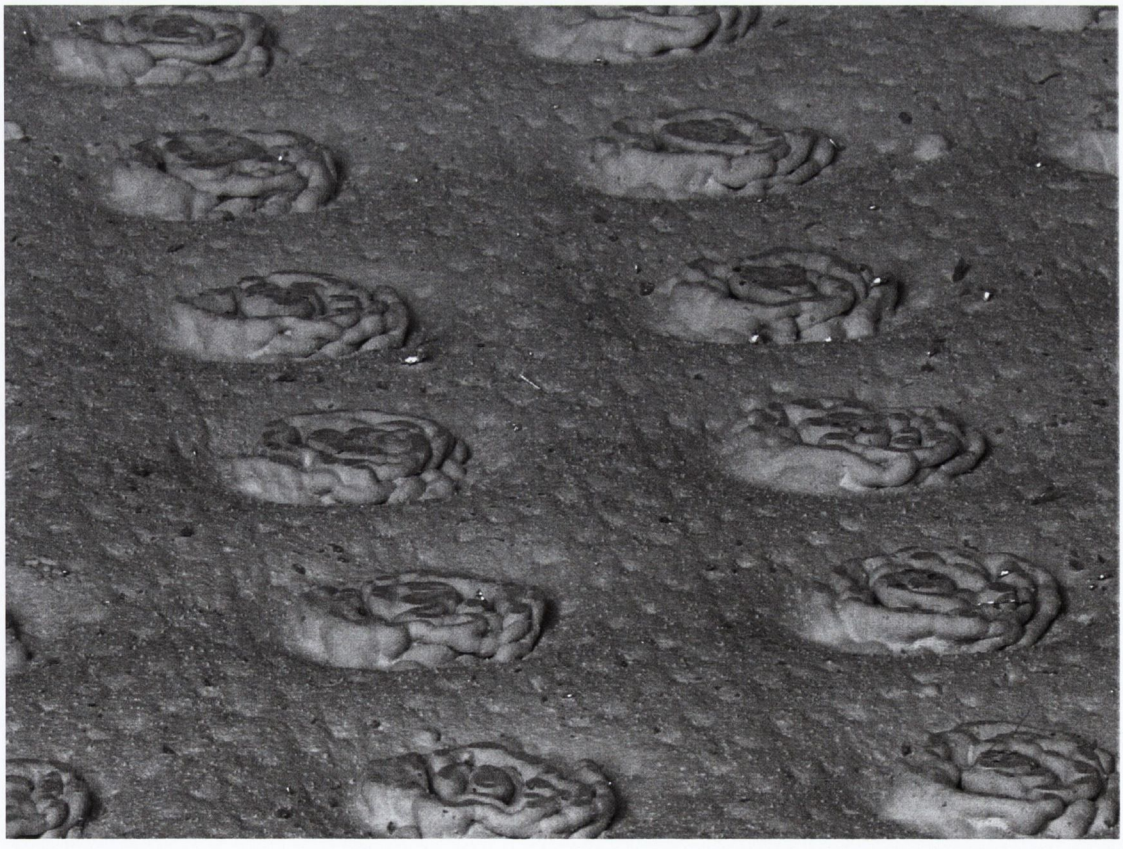


Fig. 5.12: SEM Image of the final shape of a several features of MMT-TIM Sample B, 36 μm.

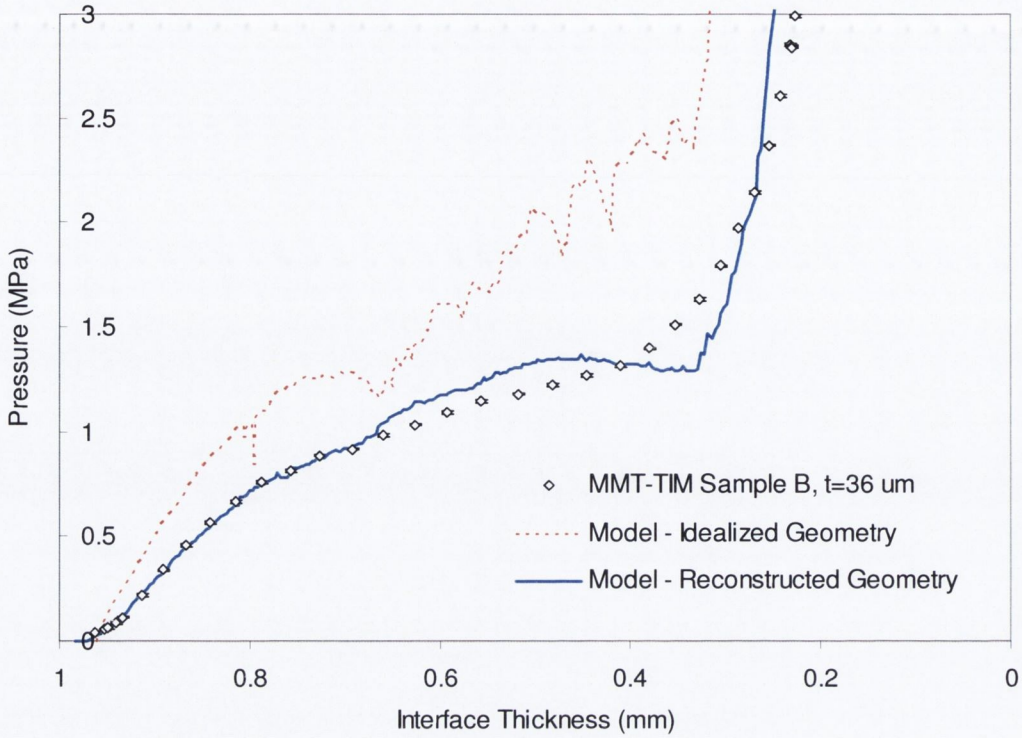


Fig. 5.13a: Comparison between model predictions for compressive pressure based on idealized and reconstructed geometries and the experimental results for MMT-TIM Sample B, t=36 μm.

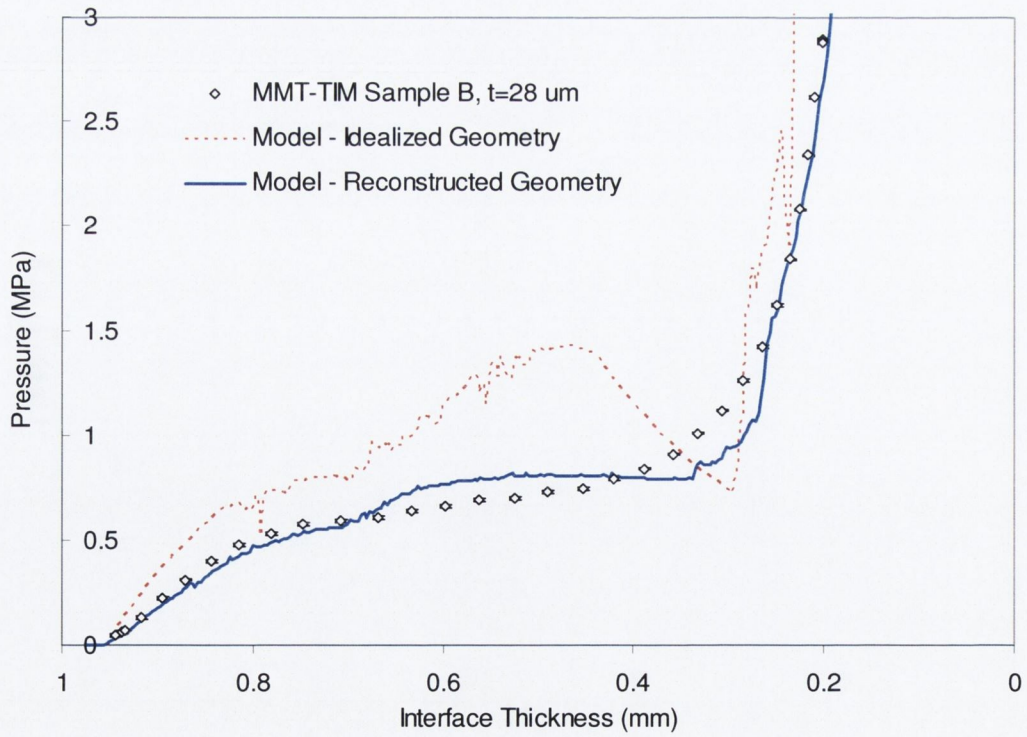


Fig. 5.13b: Comparison between model predictions for compressive pressure based on idealized and reconstructed geometries and the experimental results for MMT-TIM Sample B, t=28 μm.

It is evident that the model results from the reconstructed geometry more accurately predict the pressure required to deform MMT-TIM Sample B for both foil thicknesses as compared to the idealized geometry. Similar to the results discussed in Chapter 3 and reported by Kempers *et al.* [2], the model results based on the idealized, axisymmetric geometry over-predicted the pressure required to deform the MMT-TIM to a given strain because the idealized structure is significantly stiffer. Very accurate predictions were obtained, however, with the model based on the reconstructed geometry. Predicted pressures needed to deform the MMT-TIM to a given interface thickness closely matched the experimental data. Additionally, the mechanical response predicted using this technique results in a much smoother relationship between pressure and MMT-TIM thickness.

The improvement of the model prediction is demonstrated in a more quantitative manner by plotting the model prediction for compressive pressure against the experimentally measured pressure at a given interface thickness in Fig. 5.14.

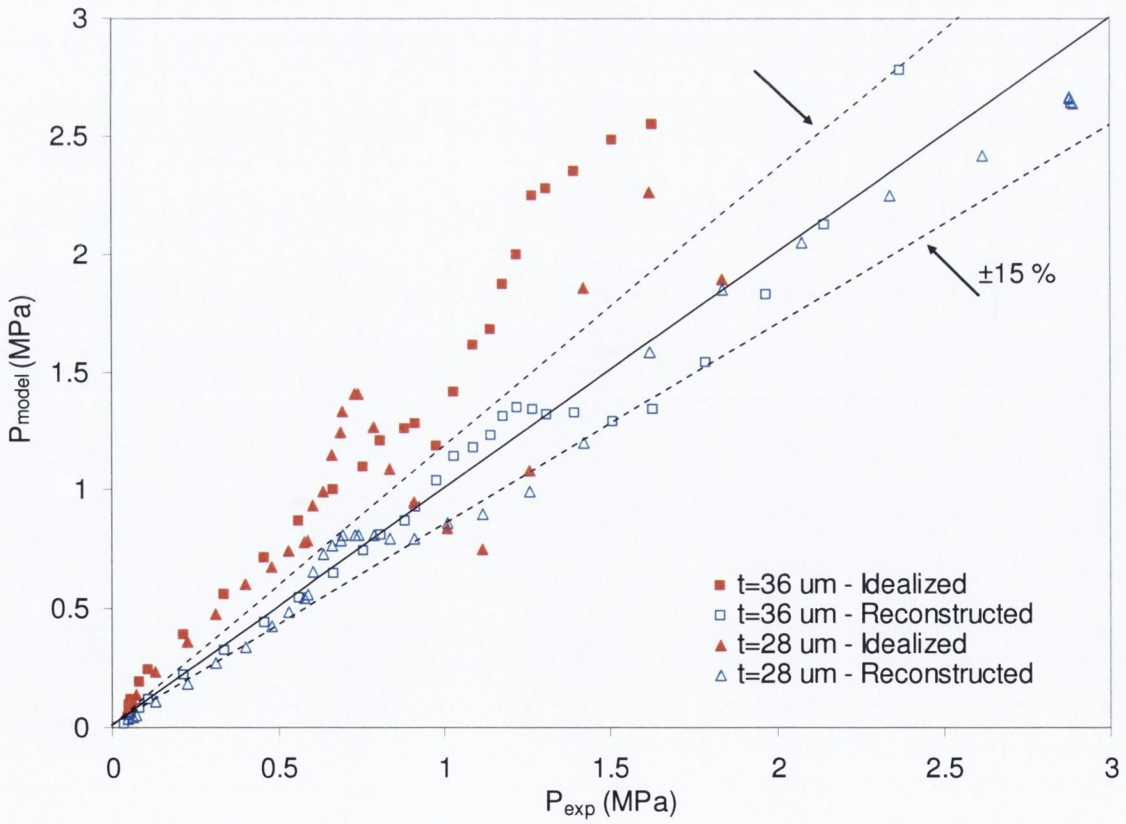


Fig. 5.14: Accuracy comparison between model responses based on idealized and reconstructed geometries for MMT-TIM Sample B

Generally, the model predictions based on reconstructed geometries predict the compressive pressure to within 15% of the measured value while the predictions based on the idealized geometries fall well outside this range.

5.2.2 Sensitivity Analysis of Reconstructed Geometry

Due to the array of repeating features in the actual MMT-TIM, the experimental results represent the mean response of numerous features (400 for the case of MMT-TIM Sample B). However, for modelling purposes, only one unit-cell is considered and is assumed to be representative of the array as a whole. It was demonstrated in the previous section that there exist small-scale defects and non-uniformities in each unit-cell's geometry resulting from the manufacturing process that play a significant role the mechanical response model. Presumably, the location and magnitude of these stress concentrations differ from feature to feature in the larger array. Since the technique of geometry reconstruction is based on a single, arbitrarily chosen unit-cell, additional geometries based on other randomly chosen unit-cells were reconstructed. Models based on these geometries were created in order to determine a rough approximation of the degree which the model results can vary due to this variability.

Two additional unit-cells from MMT-TIM Sample B, t=36 μm were imaged and reconstructed using the same approach. Identical numerical modelling techniques were employed to model their compression and the results for pressure during deformation are shown in Fig. 5.15.

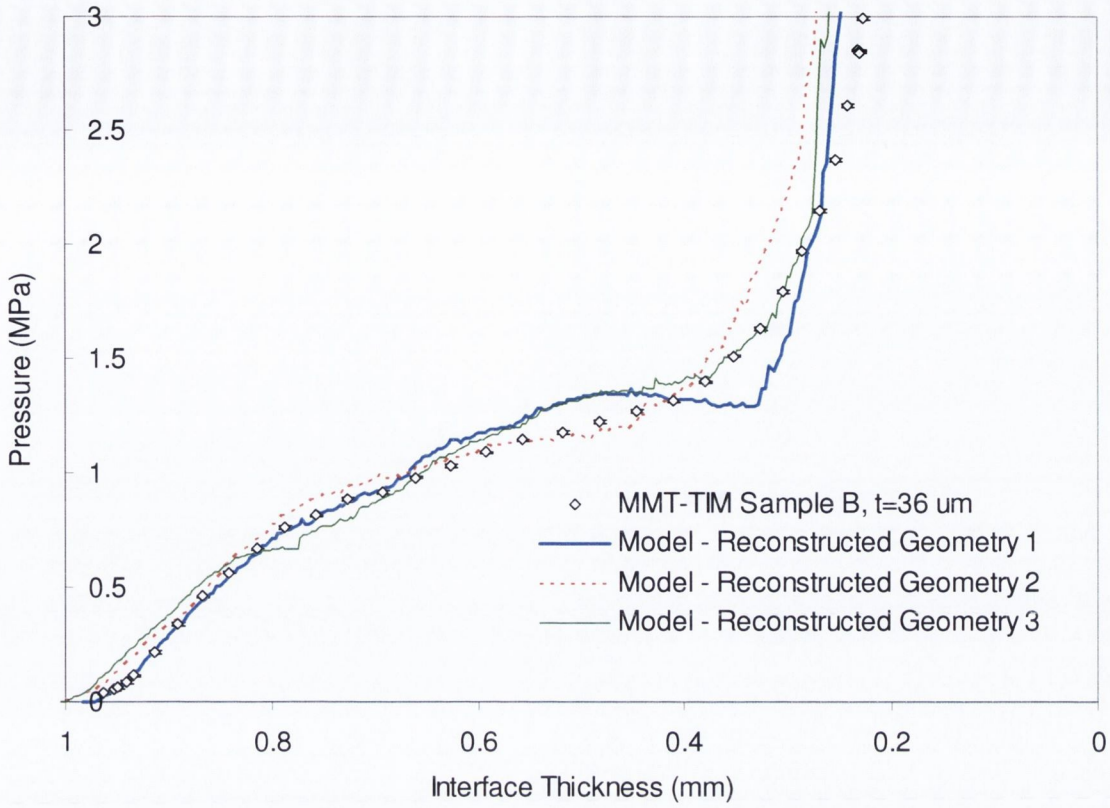


Fig. 5.15: Comparison of model predictions of mechanical response for several independently imaged and reconstructed geometries of MMT-TIM Sample B, t=36 μm.

For these additional cases there is also excellent agreement between the model predictions and the experimental results. Although a very small sample size was used, these results indicate a narrow range of expected uncertainty in the results due to variations between actual feature geometries.

Images showing the initial reconstructed geometries and the model predictions of feature shape at a compressive pressure of approximately 3 MPa for all three reconstruction geometries are shown in Fig. 5.16. While both the initial and final feature shapes vary somewhat between the three cases, qualitatively they are in good agreement with the experimental results shown in Figs. 5.11 and 5.12. This result provides confidence in the efficacy of using models derived from reconstructed SEM images for both the mechanical and thermal characterization of MMT-TIMs.

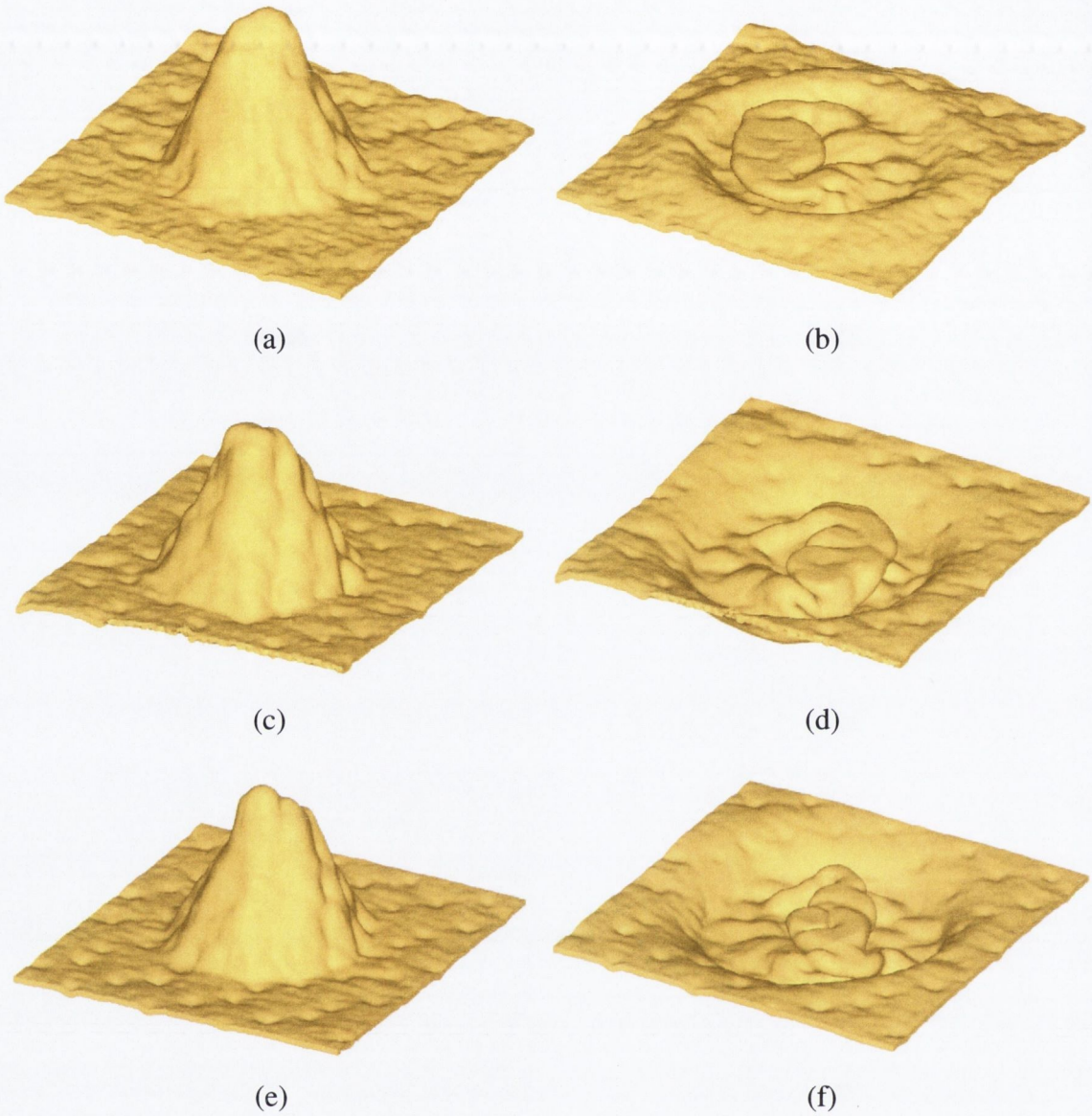


Fig. 5.16: Reconstructed Geometries before and after simulated compression to 3 MPa: a-b) Reconstructed Geometry 1, c-d) Reconstructed Geometry 2, e-f) Reconstructed Geometry 3

5.2.3 Numerical Convergence

Since numerical models inherently represent an approximate solution to a given problem, the numerical convergence of these results was established by comparing the model predictions of pressure during deformation for MMT-TIM Sample B, t=36 μm for a range of mesh densities. The trend in numerical convergence of these results is shown in Fig 5.17.

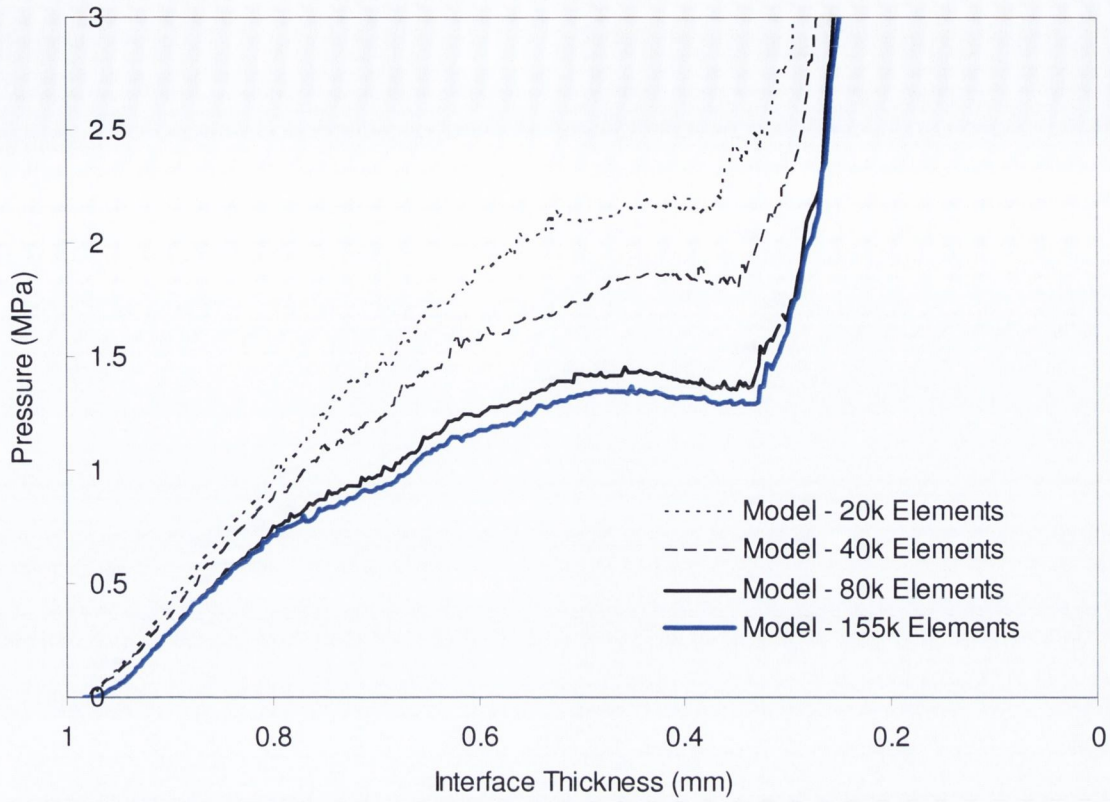


Fig. 5.17: Comparison of model predictions of mechanical response for several simulations with varying numbers of elements demonstrating numerical convergence

Not surprisingly, as the number of elements is increased from 20k to 150k, the predicted solution converges. For a relatively low mesh density where the unit cell was approximated with only 20k elements, the model predicted a relatively stiff structure. Clearly this represents a non-mesh independent solution. As the number of elements was doubled to 40k and again to 80k, the predicted stiffness decreased significantly and the solution begins to converge, indicating mesh independence.

There is a relatively small difference between the pressures predicted by the model employing 80k elements and the model using 150k elements (typically less that 5%). Thus, in order to provide accurate simulations without excessive computational effort, unit-cells were modelled using approximately 150 to 160 thousand elements. Simulations were run on an Intel-based, dual-core computer operating at 3.06 MHz and equipped with 4 GB of RAM. At these mesh densities, typical deformation simulations required approximately 20 to 24 hrs to complete, depending on the range of deformation required. Thermal solutions for the range of deformations were typically obtained in a matter of minutes.

5.2.4 Summary of Mechanical Results

The method for reconstructing MMT-TIM unit cell geometry based on SEM stereoscopic imaging has been shown to yield a more accurate prediction of the mechanical response of the MMT-TIM as it undergoes large-strain plastic deformation. By accurately and systematically representing the various non-uniformities and stress concentrations of the MMT-TIM, the model predictions based on reconstructed geometry yielded both quantitatively more accurate predictions for compressive pressure required to deform the MMT-TIM as well as a qualitatively improved prediction of the shape of the MMT-TIM structured as it is deformed. The influence of the specific geometry chosen for the reconstruction was examined and found to have a small (typically less than 10%) effect on the predicted pressure required to deform the MMT-TIM and little influence on the shape during deformation (typically less than 10%).

With the mechanical aspects of the simulation yielding reasonable predictions for both the shape and pressures required to deform the MMT-TIM, the thermal response of the MMT-TIM can now be addressed.

5.3 Model Predictions: Thermal Response

Upon completion of the mechanical simulation, subsequent thermal simulations were carried out on the MMT-TIM geometries at various stages of deformation, as described in Chapter 3. Initial thermal simulations performed in DEFORM neglect the contact resistance between the MMT-TIMs and the contacting surfaces and only consider the bulk resistance of the MMT-TIM and the constriction resistances occurring in the upper and lower contacting bodies. A plot of specific thermal resistance for both thickness of MMT-TIM Sample B along with these associated model predictions are shown in Fig. 5.18. Here, the predicted specific thermal resistance of both MMT-TIMs is lower than the experimentally measured value at all stages of its deformation. Most of this discrepancy can be attributed to the contact resistance at the upper and lower surfaces, since there is little reason to doubt the veracity of the modelled bulk and constriction resistances.

These results are plotted in terms of effective thermal conductivity in Fig. 5.19. While the model prediction demonstrates a similar shape and captures the effect of the change in foil thicknesses between the two samples, the model predicts higher values for the effective thermal conductivity of the MMT-TIM over the entire range of thickness values. Again, this is attributed to the lack of thermal contact resistance terms in the initial model.

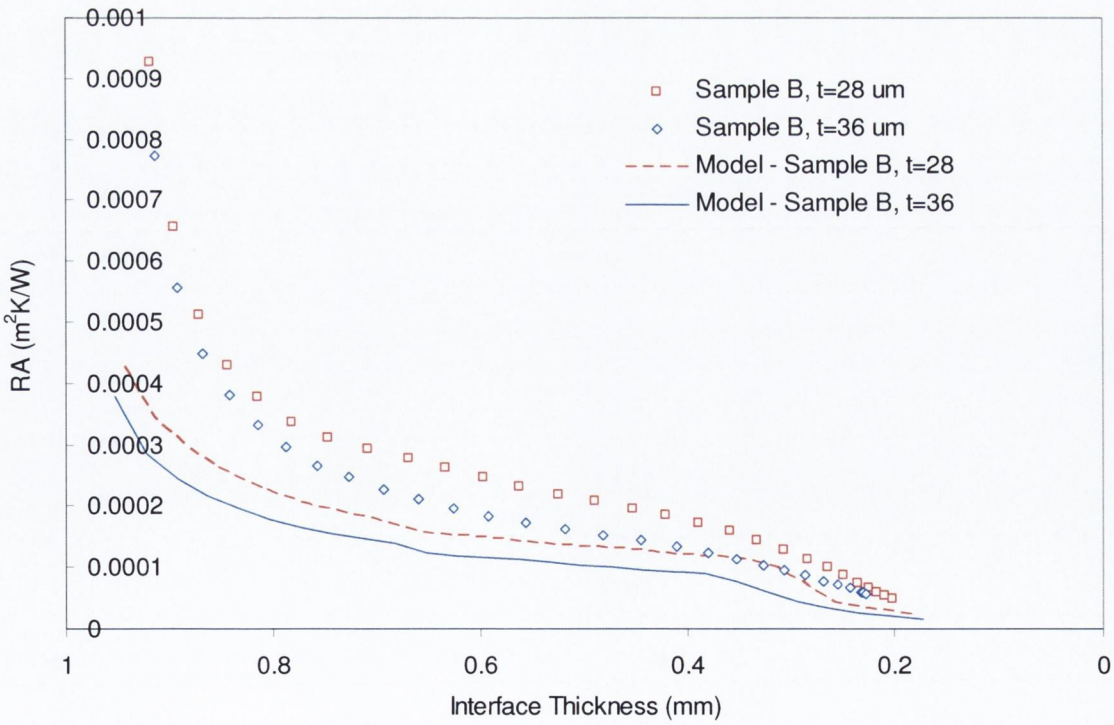


Fig. 5.18: Specific thermal resistance of MMT-TIM Sample B during deformation compared to model predictions neglecting contact resistance

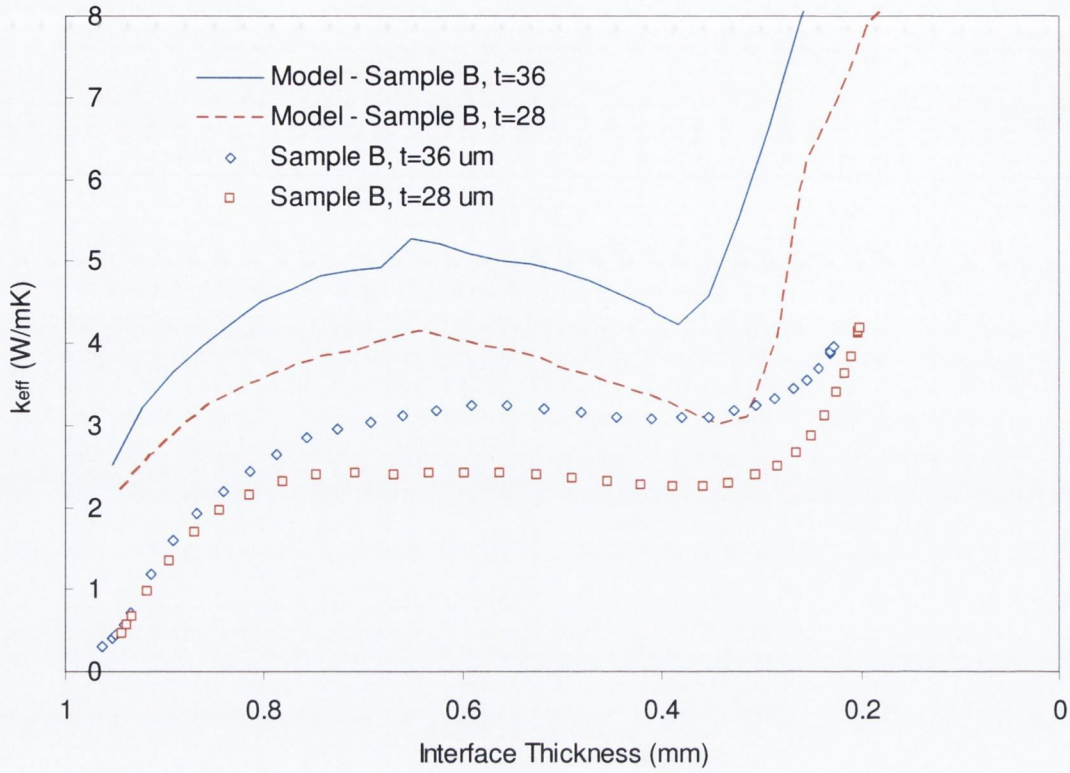


Fig. 5.19: Effective thermal conductivity of MMT-TIM Sample B during deformation compared to model predictions with contact resistance neglected

As with the initial results presented in Chapter 3, the thermal contact resistance of the MMT-TIMs with the contacting surfaces remains an important parameter that needs to be addressed. The rest of this section discusses the first of two approaches used to characterize MMT-TIM contact resistance for the purposes of improving the model prediction of thermal performance. A second approach is discussed in Sec. 5.4.

5.3.1 Thermal Contact Resistance in MMT-TIMs

Consider the diagram of the series of thermal resistances contributing to the measured thermal resistance of the MMT-TIM shown in Fig. 3.5. The thermal contact resistance of the MMT-TIMs with the upper and lower bodies can be defined as

$$R_{c,upper} = \frac{1}{h_{c,upper} A_{c,upper}} \tag{5.1}$$

and

$$R_{c,lower} = \frac{1}{h_{c,lower} A_{c,lower}} \tag{5.2}$$

where R_c is the thermal contact resistance, h_c is the thermal contact conductance and A_c is the contact area. It has been shown experimentally that thermal contact conductance

between two contacting solids depends on, among other things, contact pressure [3-4]. Thus, h_c must be a function of local contact pressure, $h_c = h_c(P_c)$. Quantitative results for contact area and local contact pressures between the MMT-TIMs and meter-bars are difficult to determine experimentally. However, with confidence in the predictions for mechanical deformation, the mechanical model can be employed as an analytical tool to estimate these quantities as the features are compressed.

From the numerical deformation simulation performed in DEFORM, the pressure at each contacting node is computed and exported at each step of the deformation. This result is shown in Fig. 5.20 where the average local contact pressures with the upper and lower contacting bodies are plotted as a function of deformation for MMT-TIM Sample B, t=36 μm. During the initial loading of the structure, both local contact pressures increase significantly before levelling off in the range of 200 to 300 MPa. For the most part, the contact pressure at the upper surface is somewhat higher than at the lower surface due to the pointed geometry of the MMT-TIM at this interface. It is interesting to note that these predictions for local contact pressures are approximately 2 orders-of-magnitude higher than the overall compressive pressure exhibited by the MMT-TIM during its deformation. The apparent "noise" in this result can be attributed to the discrete changes in levels of contact due to resolution limits of the model. This occurs both in the step size between deformation steps as well as spatial resolution limits imposed by the mesh density of the model. In addition, the variability of P_c may be due to changes in contact area resulting from non-uniform plastic deformation of metal at the interface.

The DEFORM simulation independently exports both the total force exerted by the contacting bodies as the MMT-TIM undergoes deformation as well as the overall compressive pressure (e.g. see results presented in the Sec. 5.2). With this information, the local contact area of the upper and lower contact regions can be calculated using

$$A_{c,upper} = \frac{F}{\overline{P}_{c,upper}} \tag{5.3}$$

and

$$A_{c,lower} = \frac{F}{\overline{P}_{c,lower}} \tag{5.4}$$

where A_c is the local contact area, F is the force and $\overline{P}_c$ is the average local contact pressure.

From this, the local contact areas for MMT-TIM Sample B can be estimated based on the deformation simulation results, as shown in Fig. 5.21.

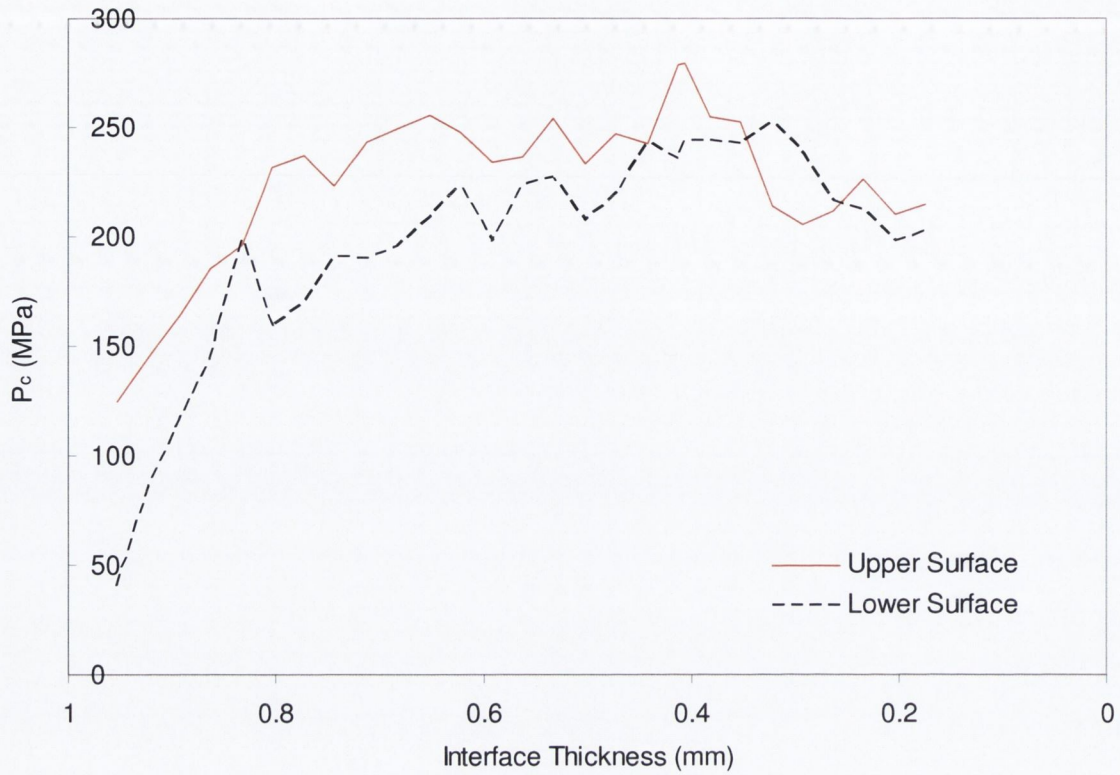


Fig. 5.20: Estimated average local contact pressures for MMT-TIM Sample B, t=36 μm based on model results.

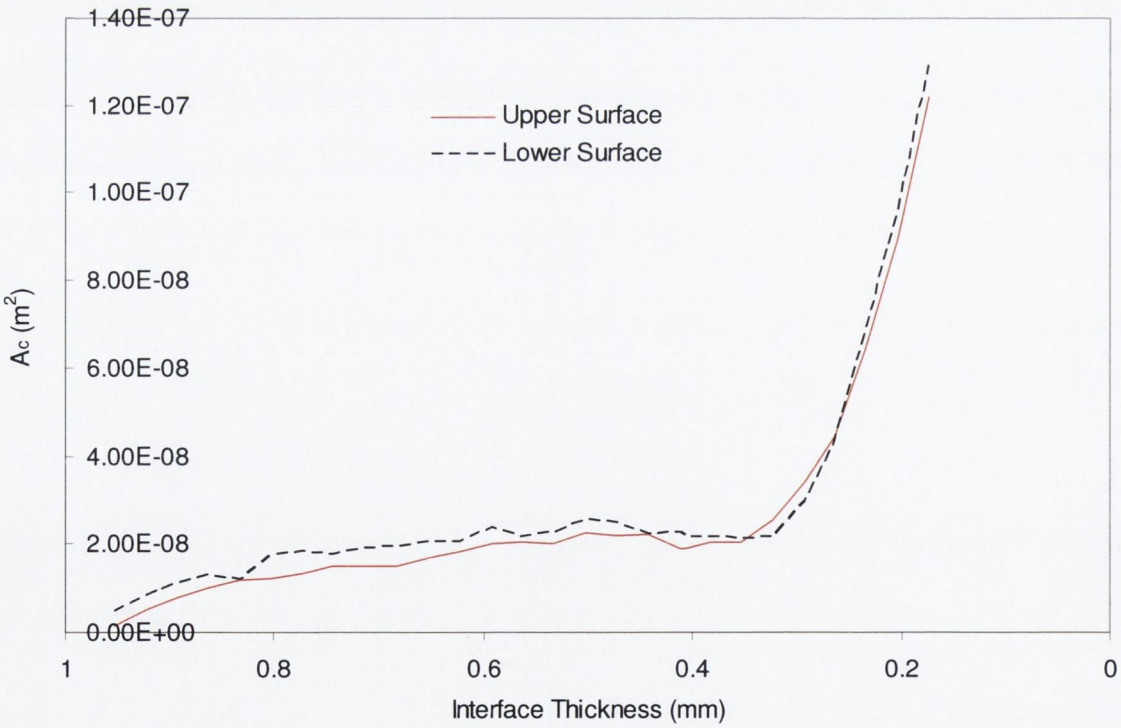


Fig. 5.21: Estimated local contact areas for MMT-TIM Sample B, t=36 μm based on model results.

As pressure is applied to the material, a gradual increase is contact area is observed as the structure deforms. Overall, the contact area of the bottom surface tends to be somewhat higher due the geometry of the specimen. As the MMT-TIM is compressed further, both contact areas are predicted to increase significantly as the structure densifies.

With estimates of local contact pressures and areas for the MMT-TIMs established, a relationship between the thermal contact conductance and pressure can now be defined in terms of modelling the thermal contact resistance of the MMT-TIMs.

If one assumes the model prediction for the bulk thermal resistance of the MMT-TIM and its associated constriction resistances in the upper and lower contacting bodies are reasonably accurate, this quantity can be subtracted from the experimentally measured thermal resistance leaving only the total contact resistance of the MMT-TIM (*i.e.* the sum of the upper and lower thermal contact resistances), $R_{c,total}$. From this, estimates for h_c can be made based on summing Eqs. 5.1 and 5.2 as

$$R_{c,total} = \frac{1}{h_{c,upper} A_{c,upper}} + \frac{1}{h_{c,lower} A_{c,lower}}. \tag{5.5}$$

If one also assumes the thermal contact conductance function, $h_c(P)$, is the same for both contacting surfaces, Eq. 5.5 can expressed as

$$h_c(P) = \frac{1}{R_{c,total}} \left[\frac{1}{A_{c,upper}} + \frac{1}{A_{c,lower}} \right] \tag{5.6}$$

By substituting Eqs.5.3 and 5.4 into Eq. 5.6 it becomes

$$h_c(P_c) = \frac{1}{R_{c,total}} \left[\frac{\overline{P}_{c,upper} + \overline{P}_{c,lower}}{F} \right]. \tag{5.7}$$

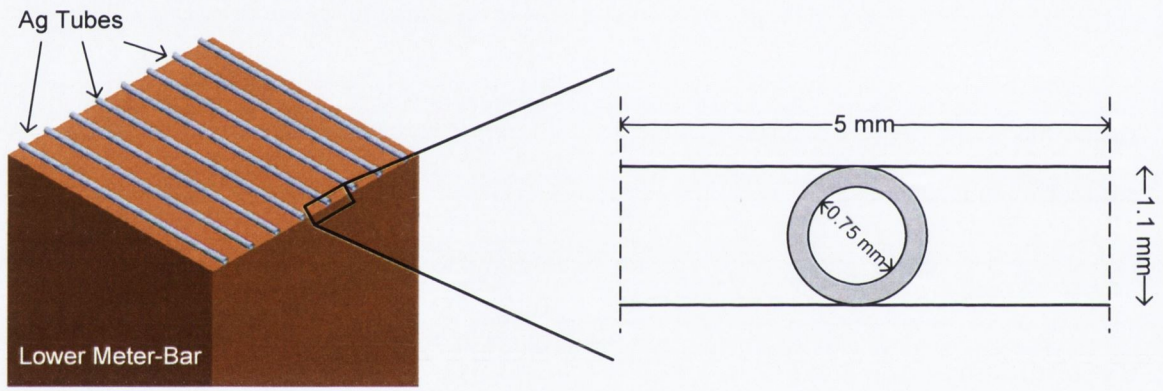
However, from these MMT-TIMs, the thermal contact conductance, $h_c(P)$, cannot be factored from Eq. 5.5 due to the non-symmetric geometry of MMT-TIM Sample B. That is, the non-symmetric nature of this geometry inhibits the explicit development of an expression for h_c as a function of pressure because the contacting pressures on each side of the MMT-TIM differ during compression. Thus, Eqs. 5.6 and 5.7 are applicable only for interfacial structures where the contact pressure is the same on both sides during deformation.

5.3.2 Development of an Expression for $h_c(P)$

To address this issue, experiments were performed using symmetric metal interface structures. Initial experiments, such as those presented in Sec. 5.1, employed flat silver foils to serve as the bulk resistance. The advantage of these specimens was that their bulk

resistance could be easily calculated in order to "back-out" the contact resistances from the measured thermal resistance. However, due to the relatively large apparent contact area (i.e. the area that is in contact macroscopically), the maximum apparent contact pressure that could be achieved experimentally was limited to approximately 3 MPa. As stated previously, estimates of local contact pressures for MMT-TIMs predicted by the model (Fig. 5.20) are approximately 200-250 MPa; this range is approximately 2 orders-of-magnitude higher than can be achieved on the flat foils with the TIM test apparatus. Furthermore, the flat silver foils demonstrated no macroscopic plastic deformation or significant change in contact area making their usefulness as MMT-TIM models questionable.

An experiment was devised that consisted of testing an interface of symmetric silver tubes that would undergo significant macroscopic plastic deformation when compressed. An illustration of the setup is shown in Fig 5.22.



(a) (b)

Fig. 5.22: a) Rendering of Ag tube test (upper meter-bar not shown), b) cross section of Ag tube

Here, eight silver tubes, initially 1.1 mm outer diameter and 0.75 mm inner diameter, were cut to length, annealed in air at 400 °C for 30 minutes and spaced evenly between the contacting surfaces of the upper and lower meter-bars to form an interface of 8 parallel resistances as shown in Fig. 5.22a. Eight tubes spaced evenly along the meter-bar width ensured that constriction resistances in the meter-bars occurred within the first 3 mm from the surface and therefore measured accurately; *i.e.* at the location of the closest thermistor, the temperature profile in the meter-bars was uniform. This was verified through conduction simulations performed using ANSYS. Additionally, the use of eight tubes resulted in an interface that was easily deformable given the range of experimentally available compressive force. Finally, the relatively simple geometry of the silver tubes

allowed much greater certainty in the model predictions of local contact pressure, contact area and bulk thermal resistance as opposed to the more complicated and somewhat more uncertain MMT-TIM geometry; the accuracy of which are essential in characterizing the contact thermal resistance at the interfaces using this methodology.

The overall compressive pressure required to deform the interface of annealed silver tubes is shown in Fig. 5.23 along with the associated model prediction. Here the tubes were modelled using a single unit cell measuring 5 mm × 1.1mm × 0.1 mm with the appropriate symmetric boundary conditions. In order to accurately predict the deformation of the silver tubes, a slightly modified material model for annealed silver was necessary. For the MMT-TIM geometries, localized regions of the model tended to undergo relatively large and therefore more plastic strain. For the tubes on the other hand, initially the strains occurring in the geometry were much more uniform and therefore smaller and occurred in the elastic range of the stress-strain curve. Thus, in order to more accurately predict their deformation, an elastic-plastic model was used in DEFORM.

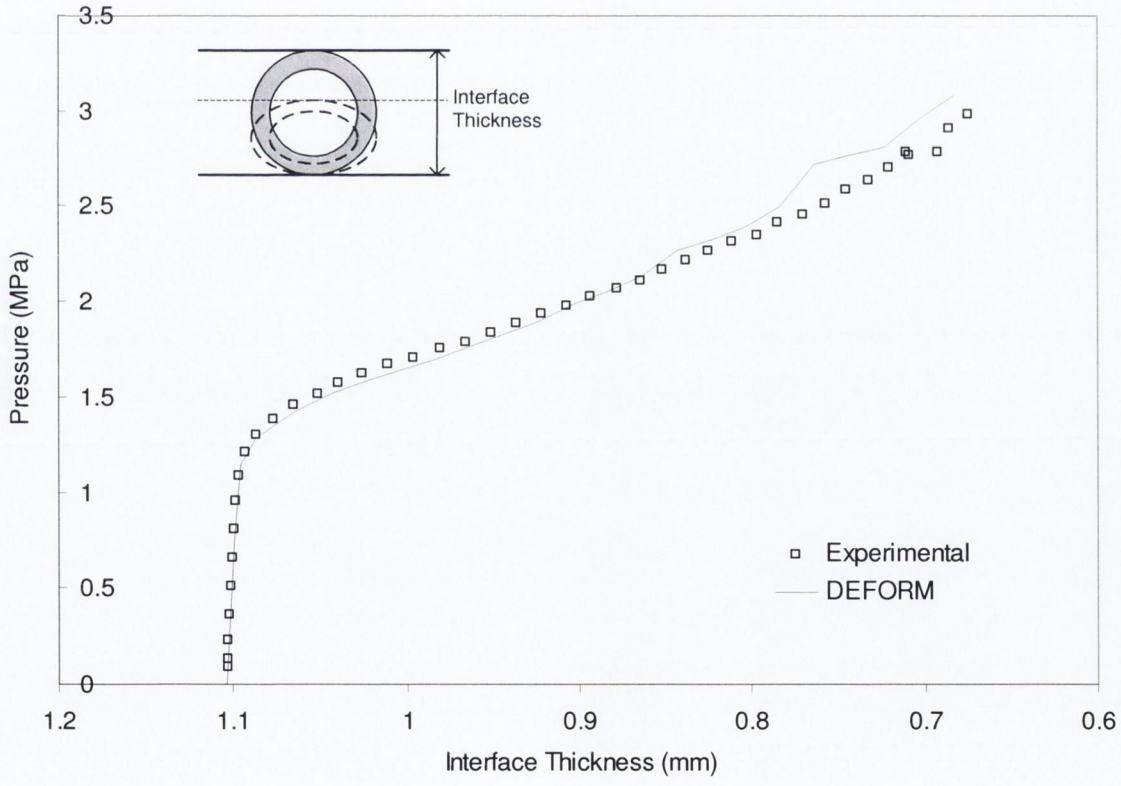


Fig. 5.23: Overall compressive pressure required to deform Ag tubes

Based on the agreement between the model prediction for compressive pressures of the tubes, it is safe to assume that the associated geometry changes predicted by the model are also representative of the experimental result. A series of images showing the model prediction of the cross-sectional shape of the tube is shown in Fig. 5.24.

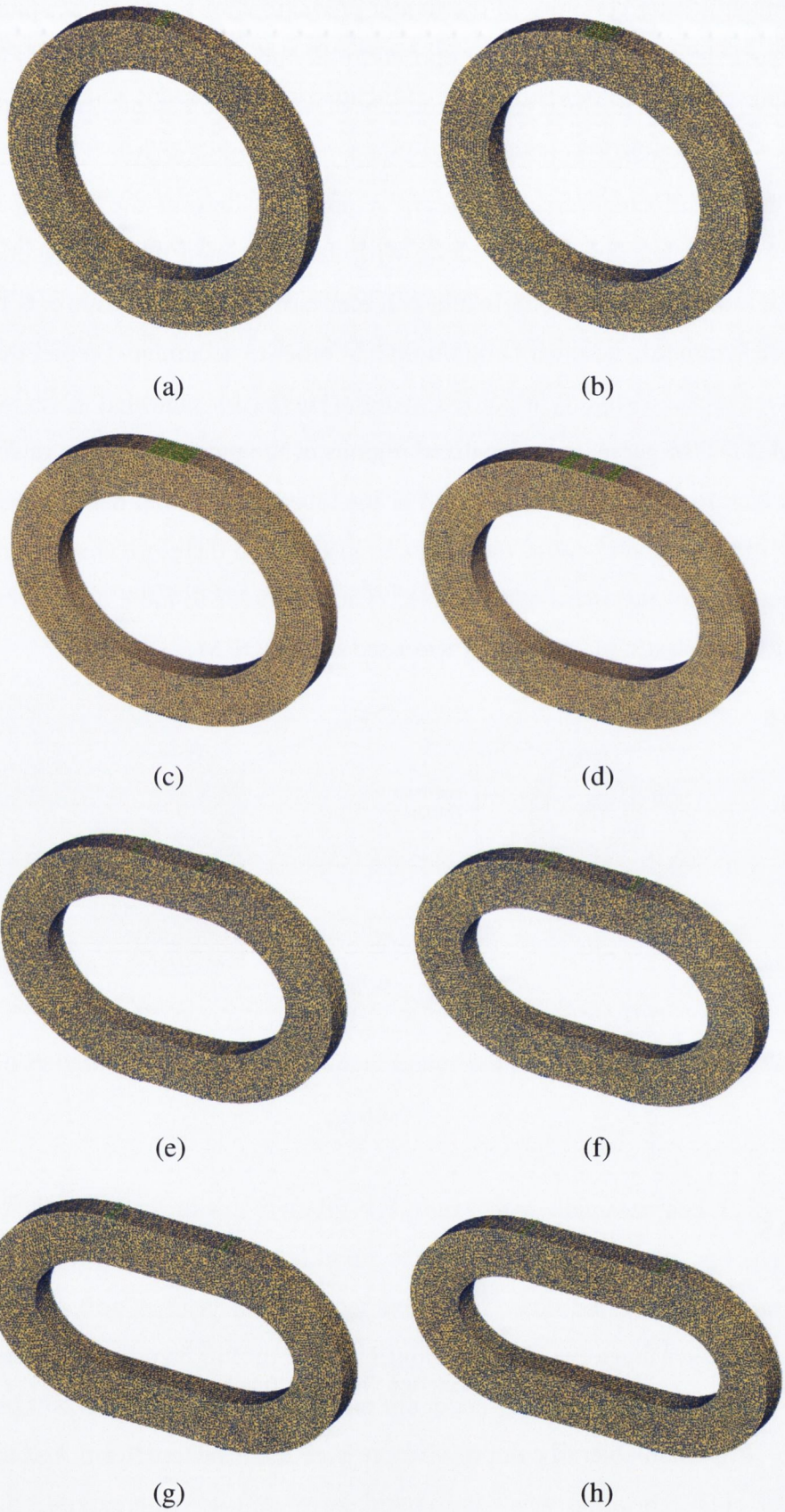


Fig. 5.24: Model prediction of the cross-sectional shape of the Ag tubes, showing apparent contact regions, during compressive deformation

Here, the contacting nodes on at the upper surface are highlighted, indicating how the apparent contact evolved during deformation. Initially, contact occurs in a small region centred at the top of the tube. This region increases until eventually, as the tube deforms, the upper surface begins to bow inward and the contact region is split as shown in Fig. 5.24d-h. This phenomenon was observed experimentally as well, lending further confidence to the efficacy of this simulation result.

Due to the symmetrical nature of this geometry, the mean local contact pressures predicted by the model at both surfaces were essentially identical. The resulting estimate of the mean local contact pressure of the silver tubes as they undergo deformation is plotted in 5.25 while the associated prediction for local contact area is shown in Fig. 5.26.

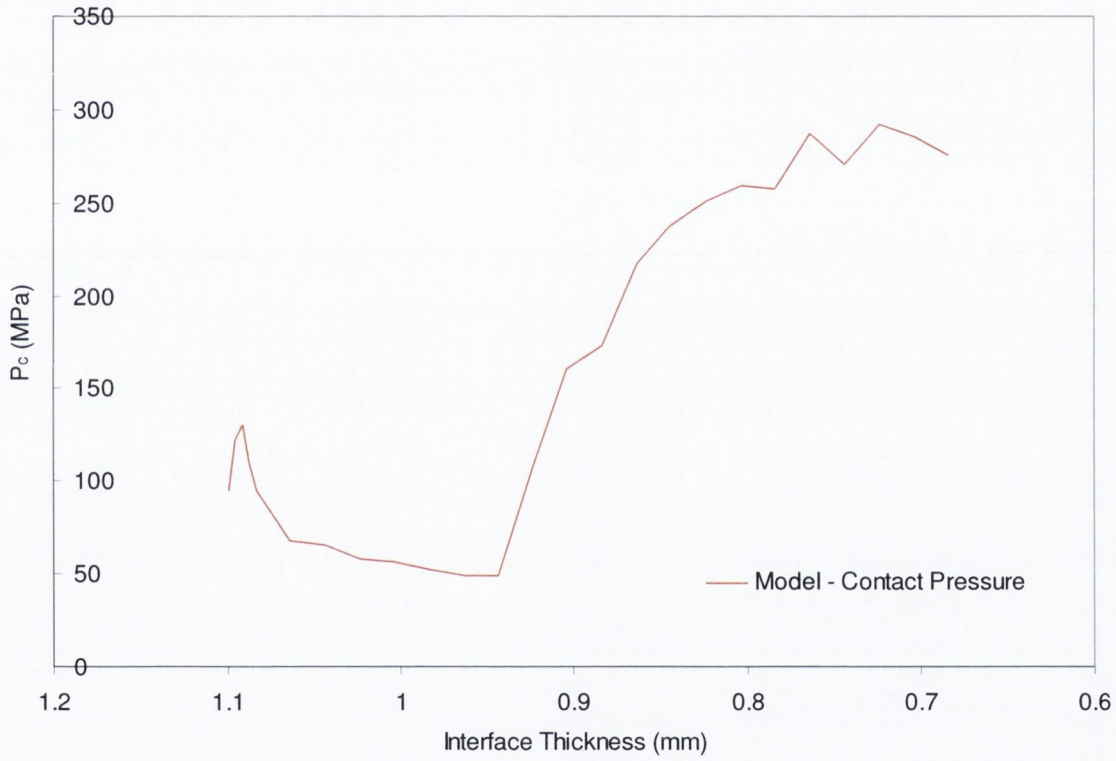


Fig. 5.25: Model prediction local contact pressure of tubes during deformation

The aforementioned "bowing" in the contacting surfaces as predicted by the model, manifests as a sudden decrease in contact area and increase in local contact pressure at an interface thickness of approximately 0.95 to 0.9 mm in Figs. 5.25 and 5.26.

Upon completion of the mechanical simulation, the thermal simulation of the bulk resistance and constriction resistance was carried out using DEFORM. The specific thermal resistance computed by the model during deformation is compared to the experimentally measured specific thermal resistance in Fig. 5.27.

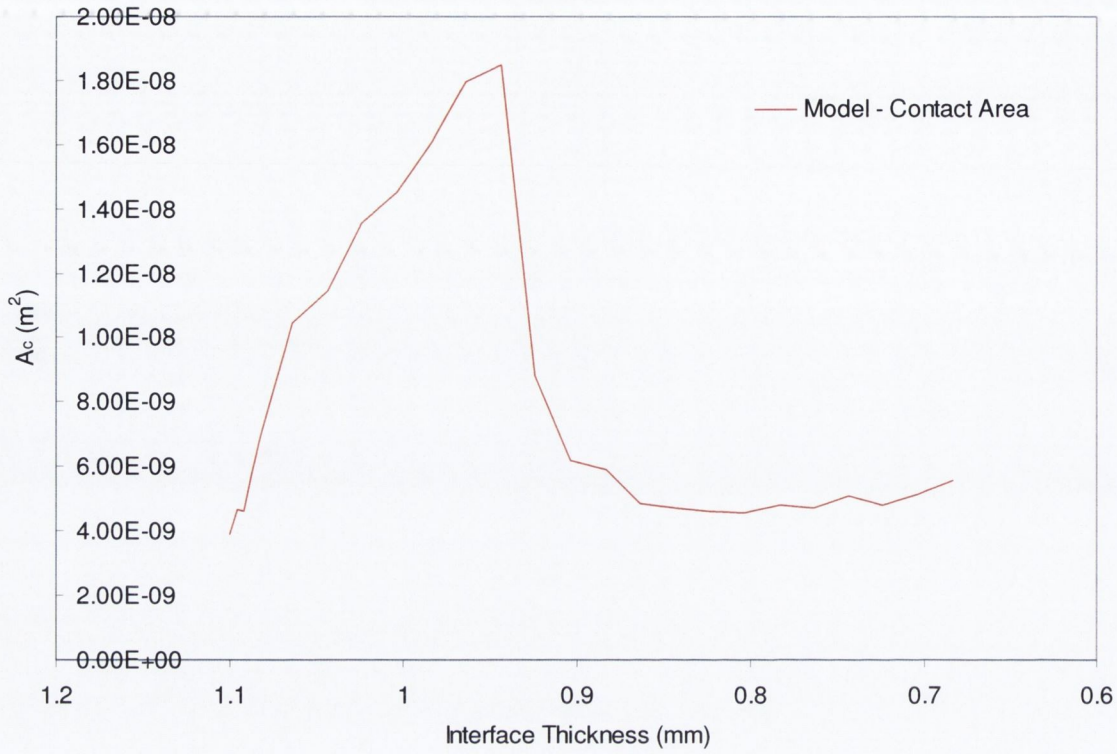


Fig. 5.26: Model prediction of apparent contact area of tubes during deformation

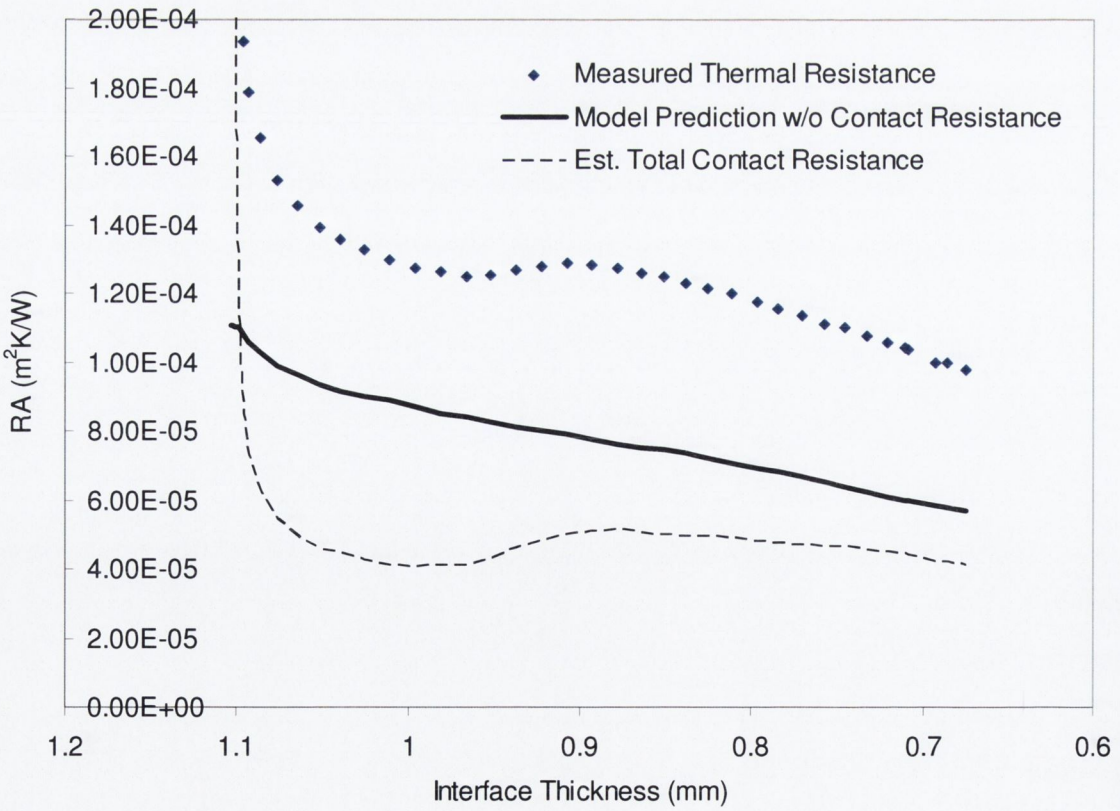


Fig. 5.27: Comparison of between experimentally measured and model-predicted thermal resistance of Ag tubes during deformation

Experimentally, there is a sharp drop as the pressure is initially applied to the tubes. Since there is no apparent deformation during this period, this can be attributed primarily to a drop in thermal contact resistance. As expected, the same drop is not observed in the model result where the thermal contact resistance was ignored (i.e. thermal contact resistance assumed to be zero). The initial inflection in the model result is due to a slight drop in constriction resistance as the contact area initially increases. The total specific thermal contact resistance of the Ag tubes was estimated by subtracting model-predicted specific thermal resistance from the experimentally measured specific thermal resistance, R_cA. This result is plotted as the broken line in Fig. 5.27. Based on this estimate, it is noted that the thermal contact resistance is a major component to the overall thermal resistance of these structures, accounting for approximately 60% of the overall thermal resistance.

By expressing Eq. 5.5 in terms of specific thermal resistance, one can write

$$R_cA = A_{uc}\left[\frac{1}{h_{c,upper}A_{c,upper}} + \frac{1}{h_{c,lower}A_{c,lower}}\right] \tag{5.8}$$

where A_{uc} is the area of the single modelled unit-cell. Due to the symmetrical geometry of this case, Eq. 5.8 can be simplified and rearranged to solve for h_c as

$$h_c = \frac{A_{uc}}{R_cA}\left[\frac{2}{A_c}\right] \tag{5.9}$$

or in terms of mean contact pressure as

$$h_c\left(\overline{P}_c\right) = \frac{A_{uc}}{R_cA}\left[\frac{2\overline{P}_c}{F}\right]. \tag{5.10}$$

The resulting estimate for h_c is plotted against mean local contact pressure in Fig. 5.28. As would be expected, there exists a strong correlation between the h_c and $\overline{P}_c$. Here it was fit using a power law relationship as

$$h_c = 1.24\times10^5\,\overline{P}_c^{\,0.638} \tag{5.11}$$

Also plotted in Fig. 5.28 is the initial, low pressure data set for the aforementioned flat silver foils.

This correlation was then incorporated back into the thermal simulation for the Ag tubes to yield an improved estimate of their thermal response. A plot of the effective thermal conductivity of the Ag tubes during compression is shown in Fig. 5.29.

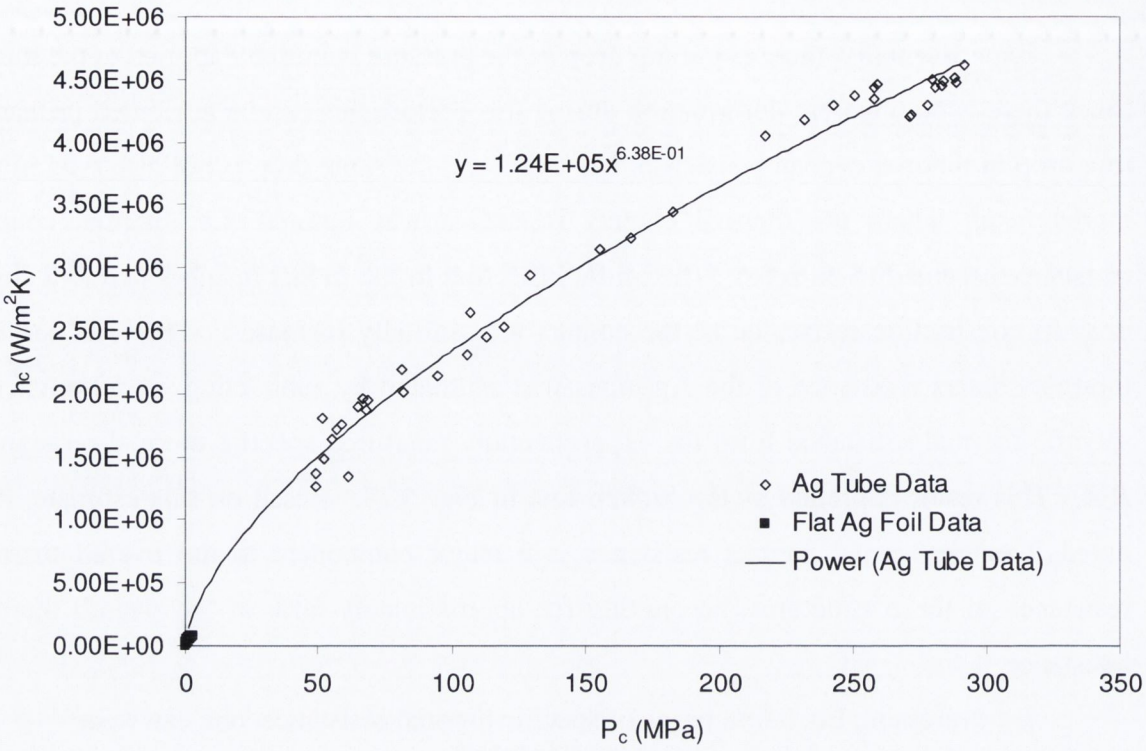


Fig. 5.28: Thermal contact conductance as a function of mean local contact pressure

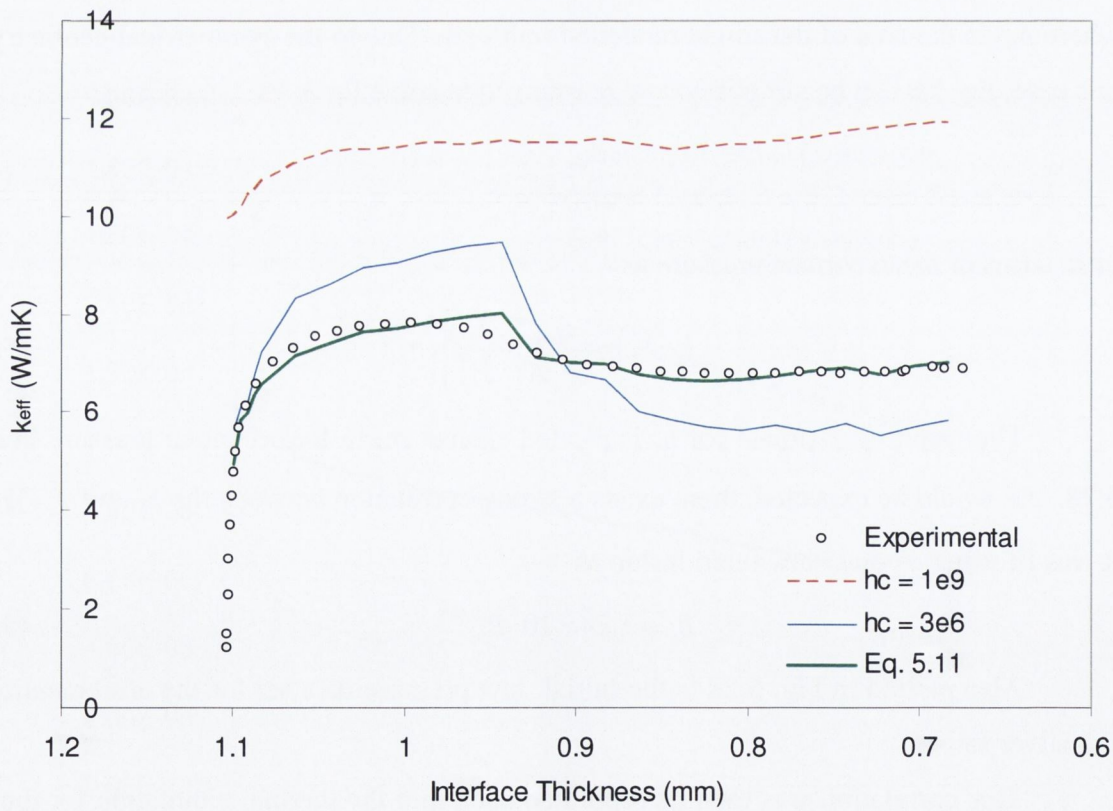


Fig. 5.29: Predicted effective thermal conductivity of Ag tubes based on different values of h_c

For the case where an extremely high thermal contact conductance is used (h_c=1×10^9 W/m^{2}K), the contact resistance is essentially zero and the model over-predicts the effective thermal conductivity of the Ag tubes. By using a constant value of h_c=3×10^6 W/m^{2}K, the model prediction is improved somewhat, however the effective thermal conductivity remains over-predicted during the initial deformation and under-predicted upon further deformation. However, when using the empirically obtained correlation in Eq. 5.11, the model reproduces the experimental result very well. Here, any discrepancies are indicative of the quality of the fit used to obtain this correlation.

5.3.3 Implementation of h_c Correlation

The relationship between thermal contact conductance and mean local contact pressure obtained semi-empirically using compressed Ag tubes and expressed in Eq. 5.11, was then implemented in the thermal model for the MMT-TIMs using Eq. 5.8. The resulting prediction for the effective thermal conductivity of MMT-TIM Sample B, t=36μm is shown in Fig.5.30. Here, incorporating realistic values of thermal contact resistance resulted in predictions of k_{eff} that are seen to more closely match the experimentally measured effective thermal conductivity. At high degrees of compression however, this model tended to over-predict the thermal contact resistance resulting in a somewhat lower effective thermal conductivity. For comparison, the cases of h_c=1×10^9 W/m^{2}K, representing essentially zero contact resistance, and h_c set arbitrarily to the constant yet somewhat reasonable value of 6×10^6 W/m^{2}K, are also plotted in Fig. 5.30.

Model predictions for effective thermal conductivity based on Eq. 5.11 are also shown for MMT-TIM Sample B, t=28 μm in Fig. 5.31. Similarly, the model prediction employing Eq. 5.11, tended to over-predict the thermal resistance of this MMT-TIM resulting in a lower effective thermal conductivity for most of the compression range. For this cases, a constant value of h_c=6×10^6 W/m^{2}K demonstrated an improved estimate of contact resistance and therefore effective thermal conductivity for most of the deformation.

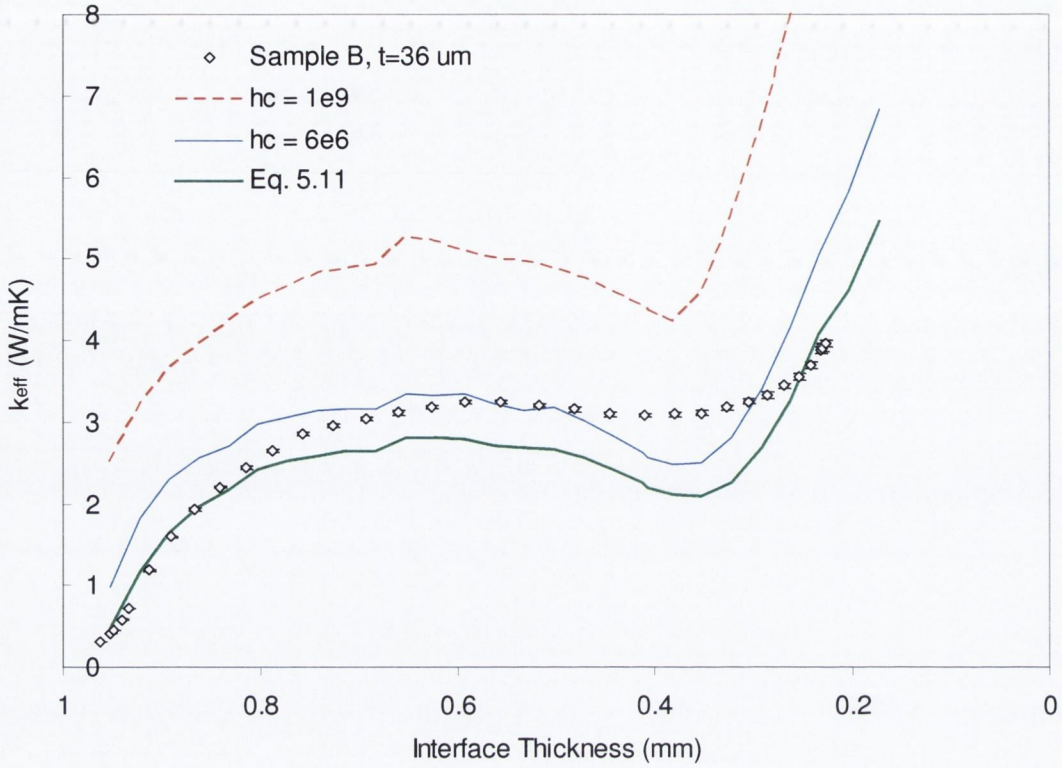


Fig. 5.30: Predicted effective thermal conductivity of MMT-TIM Sample B, t=36 μm based on different values of h_c

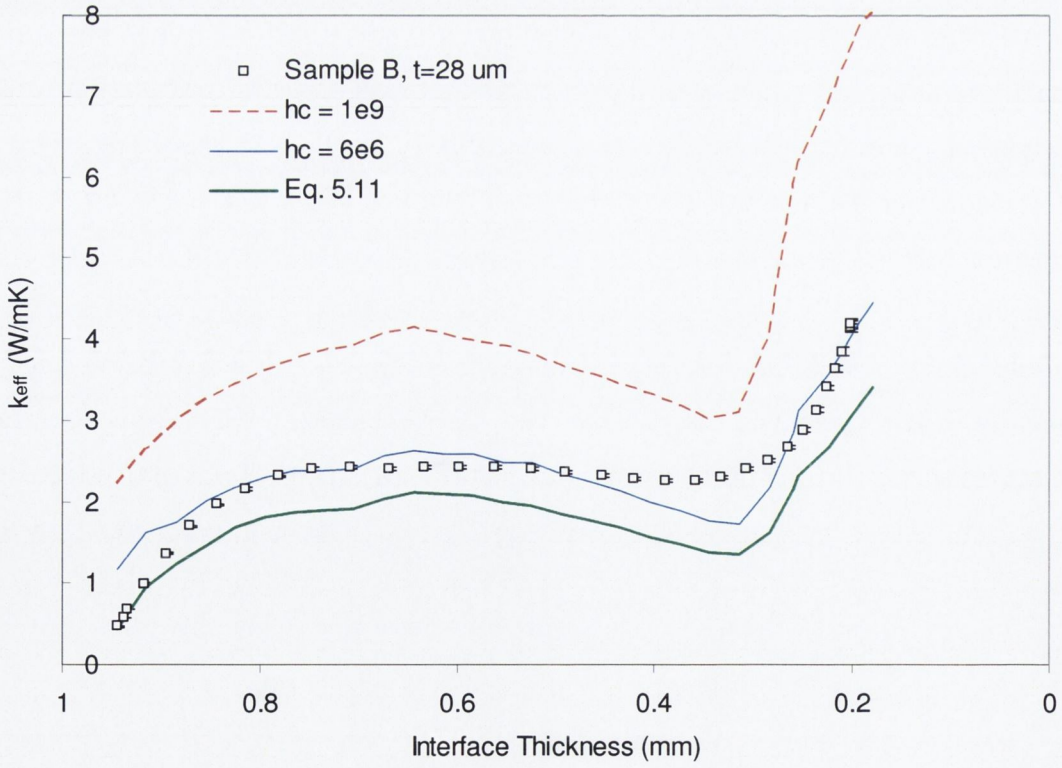


Fig. 5.31: Predicted effective thermal conductivity of MMT-TIM Sample B, t=28 μm based on different values of h_c

It is believed that this discrepancy lies in the application of this semi-empirical correlation developed using a smooth extruded solid to a MMT-TIM structure that was manufactured using an electroplating technique. Not only would the micro-structures of the surfaces be significantly different between the two cases, but also different levels of oxidization on the surface of these samples could complicate the ability to transfer the correlation developed using the Ag tubes to the Ag MMT-TIMs.

Another important factor is the accuracy of the DEFORM model in predicting the local contact pressures and areas. In order to estimate these quantities accurately, the mechanical model must be accurately predicting the overall mechanical response of the MMT-TIM during deformation. Additionally, the mesh density near the contacting regions must be sufficiently high to achieve a reasonable estimate of changes in contact pressure and area.

5.3.4 Summary

A method for characterizing thermal contact resistance in MMT-TIMs was developed in which the numerical model was used to compute the mechanical deformation of the MMT-TIM features. This method was then employed as an analytical tool to estimate the local contact pressures and areas at the contacting surfaces of the MMT-TIM. Baseline experiments employing simple, symmetric geometries (i.e. tubes) demonstrated a strong correlation between thermal contact conductance and local contact pressure for deformable structures at similar contact pressures occurring in the MMT-TIMs. This relationship was correlated using a power law given by Eq. 5.11 and was incorporated into the thermal model for the MMT-TIMs. The resulting prediction for the thermal response of the MMT-TIMs demonstrated a somewhat more realistic estimation of the thermal response of the MMT-TIMs. However, the use of this semi-empirical relationship tended to over-estimate the contact resistance of the silver MMT-TIMs. This approach provides a reasonable estimate of the contact resistance of the MMT-TIMs and improves the overall accuracy and predictive capabilities of the coupled mechanical-thermal model. Then next section describes a second approach, namely electrical resistance, to obtaining a more accurate estimate of thermal contact resistance.

5.4 Thermal and Electrical Contact Resistance Relationship

It was proposed in Chapter 3 that electrical resistance measurements be employed to experimentally characterize the thermal contact resistance between the MMT-TIMs and the contacting bodies due to the similarities between these two phenomena.

The measured specific electrical resistance of the MMT-TIM Sample B during deformation is shown in Fig. 5.32. Here, the specific electrical resistance is based on the overall MMT-TIM sample area (*i.e.* 40 mm × 40 mm). Initially, the electrical resistance drops rapidly as pressure is applied to the MMT-TIMs. Below an interface thickness of 0.8mm (≈20% strain), the resistance levelled-off somewhat before dropping further as the features began to densify. It can readily be shown that the bulk electrical resistance of the silver MMT-TIMs is negligible compared to this measured resistance; thus, this measurement represents the total electrical contact resistance of the MMT-TIMs with the upper and lower meter-bars as it undergoes deformation.

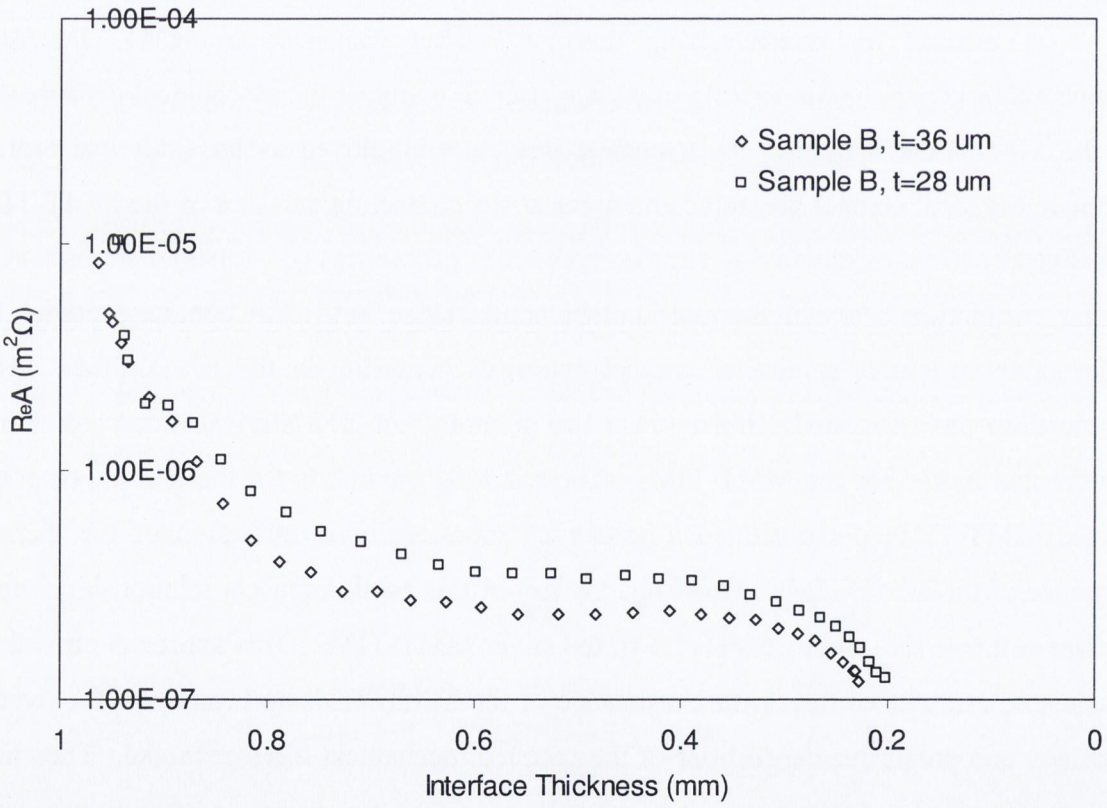


Fig. 5.32: Specific electrical resistance of MMT-TIM Sample B during deformation

Overall, this trend is very similar to the inverse of the mechanical response of this MMT-TIM, presented in Fig. 5.3, indicative of the relationship between pressure and electrical contact resistance. Overall, the thinner sample (t=28 μm) exhibited a slightly higher measured electrical resistance. However, a straightforward calculation

demonstrates that this change in thickness would not result in a significant change in the bulk resistance to affect this measurement. Thus, this provides further evidence of pressure dependence since this thinner sample exerts less reaction force during deformation.

From a practical engineering standpoint, a direct relationship between the electrical and thermal contact resistances would be useful. That is, from a relatively straightforward electrical contact resistance measurement, an estimate of the thermal contact conductance of the MMT-TIMs could be made directly. Several approaches to develop this relationship are described and discussed in the following sections.

5.4.1 Flat Foil Tests

Electrical contact resistance measurements were performed using the flat silver foils from the previous section, in order to determine if a correlation with thermal contact resistance could be established. The results of these initial tests are discussed in detail by Kempers *et al.* [5]. Generally, these tests suffered from the same limitation as their thermal counterpart; namely covering a range of contact pressures far below those that occur in MMT-TIMs. As a result, any correlation between electrical and thermal contact resistance would have limited applicability towards predicting the behaviour of MMT-TIMs.

5.4.2 Silver Tube Tests

Silver tubes offer an improved material from which to derive a useful correlation between electrical and thermal contact resistance. As discussed in Sec. 5.3.2, silver tubes present a deformable, symmetric silver interface structure which can be mechanically modelled to yield unambiguous deformation information over the range of contact pressures exhibited by the MMT-TIMs. The specific electrical resistance of the silver tubes is plotted as a function of deformation in Fig. 5.33. Since it can be shown that the bulk electrical resistance of the tubes is negligible, this measurement represents the total specific electrical contact resistance (*i.e.* $R_eA = R_{ec}A$).

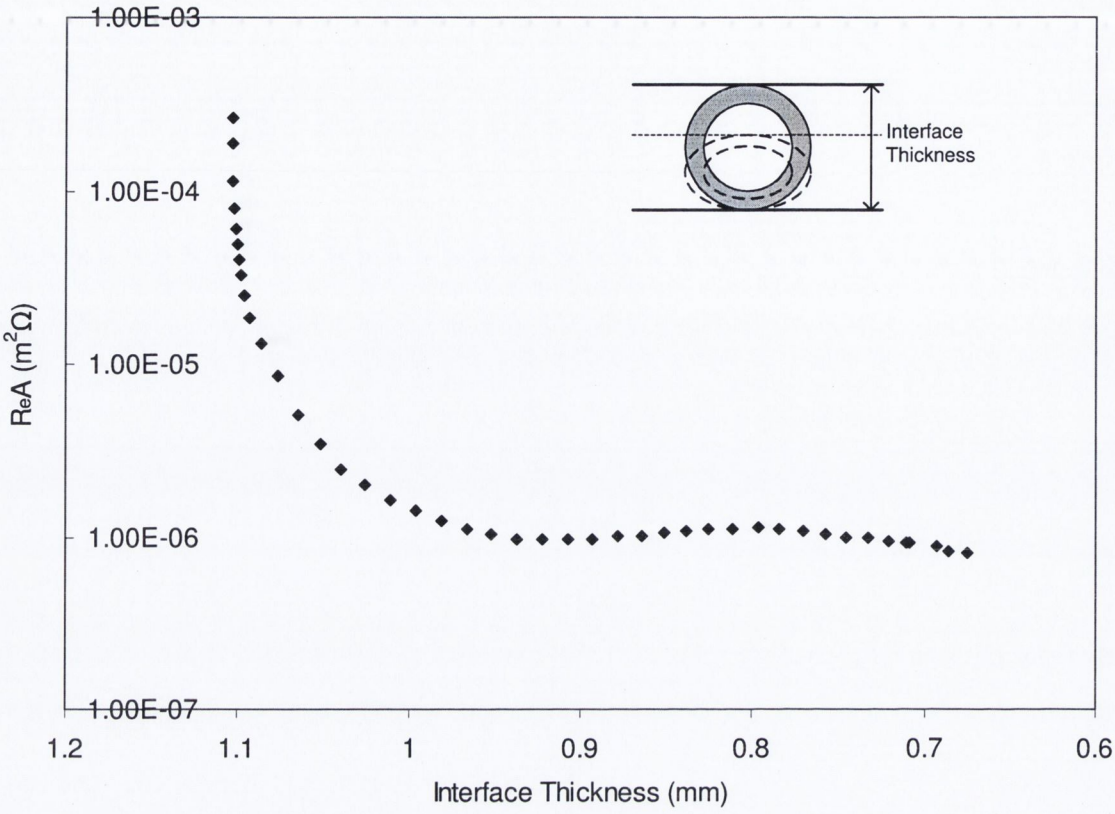


Fig. 5.33: Specific electrical resistance of Ag tubes during deformation

Here, the electrical contact resistance is once again seen to drop significantly during the initial stages of deformation as the contact pressure is increased before levelling off at the later stages of compression.

As was done in Sec. 5.3.2, the specific thermal contact resistance of the silver tubes during deformation was estimated by subtracting the model prediction for its bulk resistance from the experimentally measured value. The estimated specific thermal contact resistance for the silver tubes is plotted against the specific electrical contact resistance in Fig. 5.34. Here one can observe a direct relationship between these two quantities and for this case, this data was well fit by a 2nd order polynomial as

$$R_c A = 1495(R_{ec} A)^2 + 2.64 R_{ec} A + 4\times10^{-5} \tag{5.13}$$

This empirical relationship was demonstrated for the Ag tubes themselves by estimating the specific contact resistance of the tubes using the electrical resistance measurements and Eq. 5.13. This quantity was added to the specific thermal resistance predicted by the DEFORM thermal model (which does not account for contact thermal resistance) to predict the total thermal resistance of the tubes. This corresponding effective thermal conductivity is shown in Fig. 5.35.

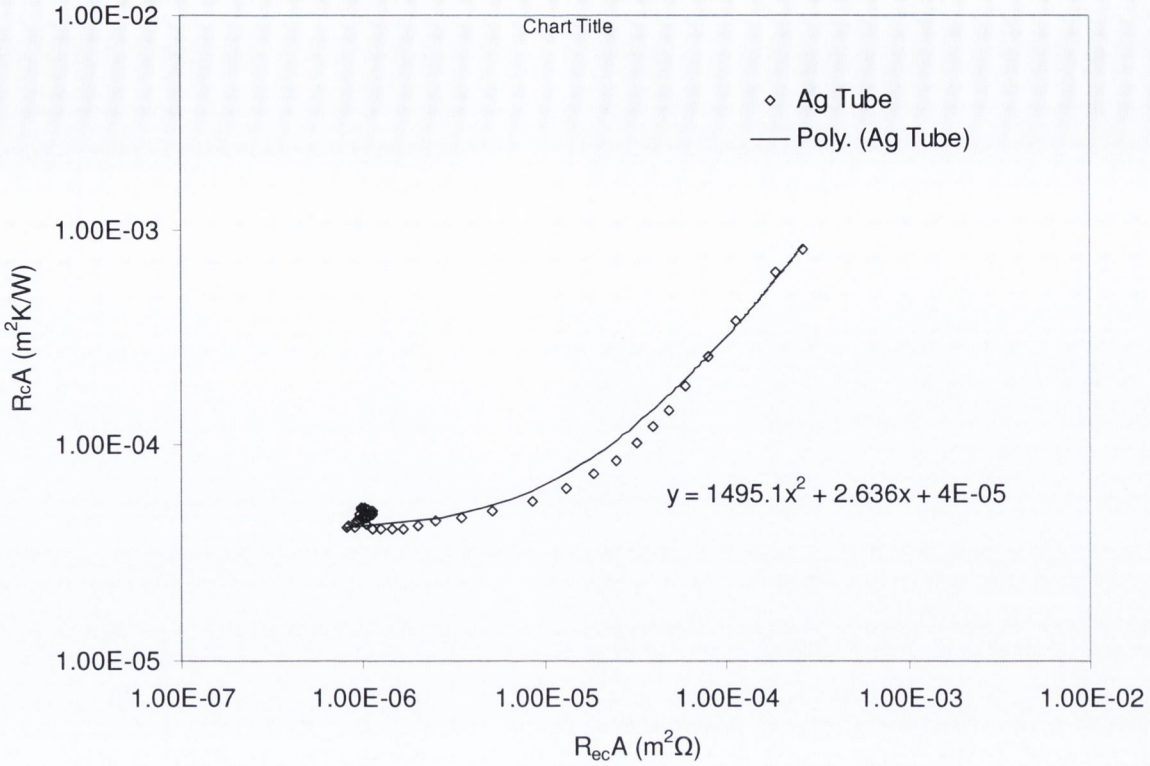


Fig. 5.34: Relationship between estimated specific thermal resistance and measured specific electrical resistance for Ag tubes

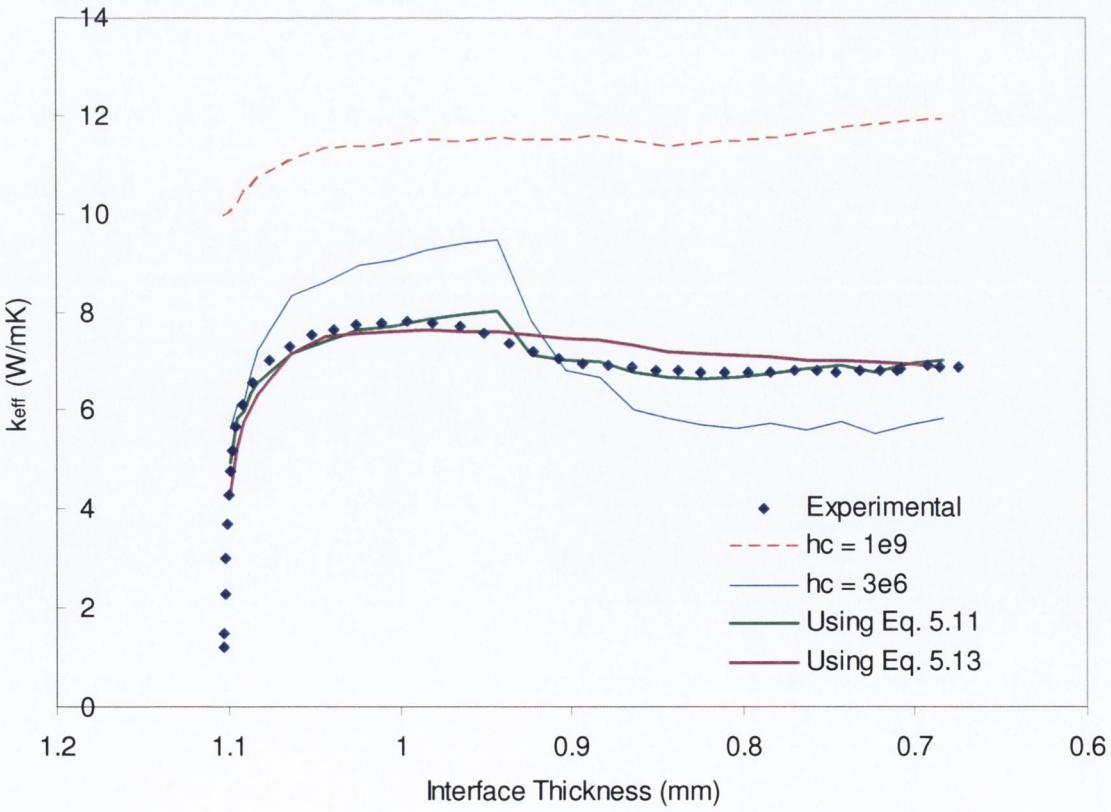


Fig 5.35: Prediction of effective thermal conductivity of Ag tubes based on various contact resistance models

The agreement between the result predicted using Eq. 5.13 and the experimental data is not surprising considering the correlation was generated from this data and serves to illustrate the effect of any discrepancy in the curve fit. The appropriateness of this relationship to estimate the thermal contact resistance of the MMT-TIMs is discussed in the following section.

5.4.3 Correlation derived from Silver MMT-TIMs

Because of the differences between the electro-deposition process and cold drawing process, we also used the MMT-TIMs, themselves to establish a correlation between electrical and thermal contact resistance. This approach is reasonable assuming that the model predictions for the bulk thermal resistance of the MMT-TIMs were reasonably accurate. The same approach was used as for the silver tubes:

a. Measure the value of the thermal resistance of the MMT-TIMs

b. Calculate the total thermal resistance from the model neglecting contact resistance.

c. Subtract b. from a. to estimate the total contact thermal resistance.

d. Plot this estimate of the specific thermal contact resistance against the measured specific electrical resistance, as shown in Fig. 5.36.

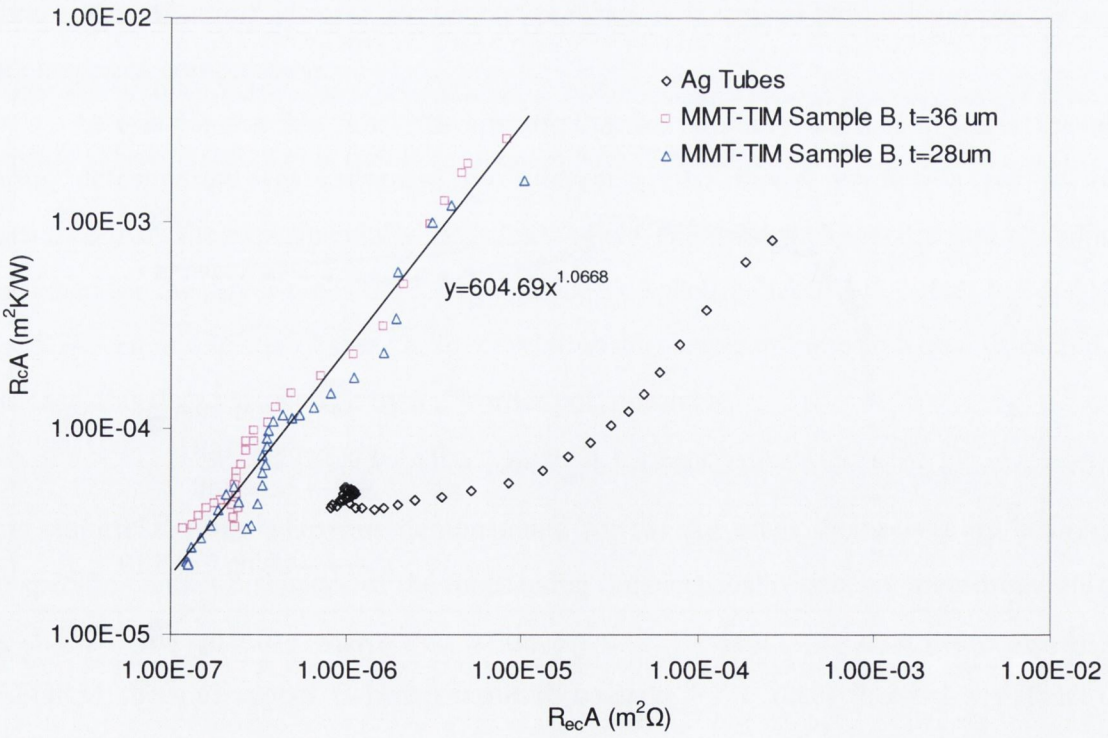


Fig. 5.36: Relationship between estimated specific thermal resistance and measured specific electrical resistance for MMT-TIM Sample B and Ag tubes

Here, the data for both thicknesses of MMT-TIMs follow the same trend which is distinctly different from than that of the silver tubes (plotted again in Fig. 5.36). Generally, for a measured electrical resistance, the total specific thermal contact resistance for the MMT-TIMs is significantly higher. This further illustrates the discrepancy between the material properties. Both MMT-TIM data-sets collapse reasonably well and are well correlated using a power law as

$$R_c A = 605(R_{ec} A)^{1.07} \tag{5.14}$$

Additionally, this relationship makes more physical sense than Eq. 5.13 since it would be expected that if the electrical resistance is either zero or infinite, so too would be the thermal resistance.

This semi-empirical correlation developed using the MMT-TIM data was introduced back into the MMT-TIM thermal model in order to estimate the thermal contact resistance of the MMT-TIMs. The corresponding prediction for effective thermal conductivity was shown in Figs. 5.37 and 5.38.

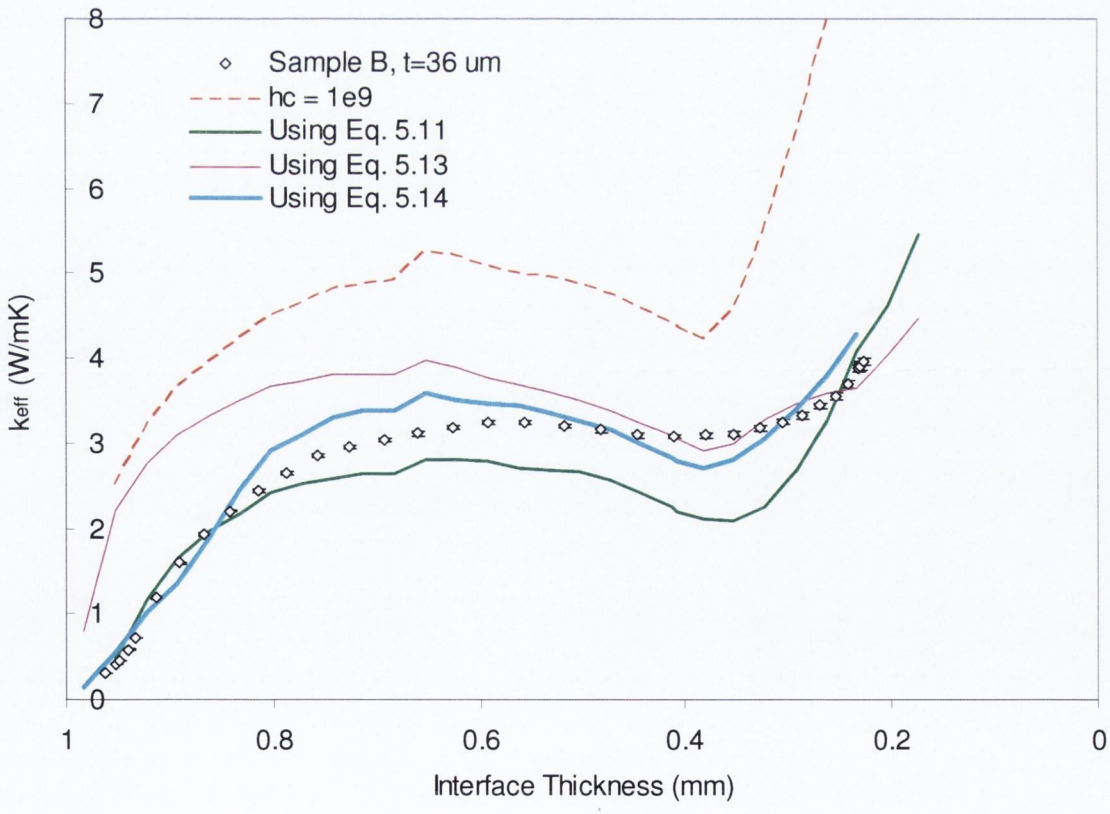


Fig. 5.37: Model predictions of effective thermal conductivity of MMT-TIM Sample B, t=36 μm

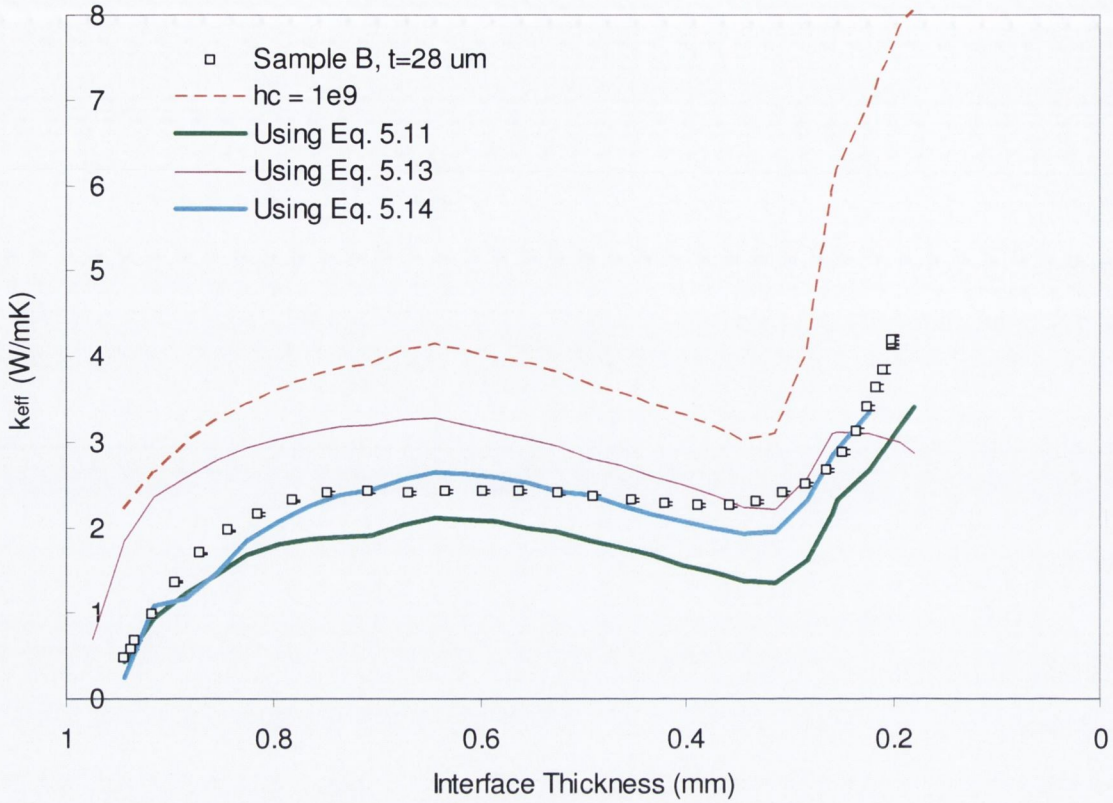


Fig. 5.38: Model predictions of effective thermal conductivity of MMT-TIM Sample B, t=28 μm

As would be expected, the agreement using this approach for these two MMT-TIM samples is very good. Discrepancies here illustrate the effect of the lack of fit between Eq. 5.14 and the empirical data used to generate it. For comparison, model predictions of effective thermal conductivity based on the thermal-electrical relationship generated from the silver tubes (Eq. 5.13) and the thermal-mechanical relationship developed in Sec. 5.3 (Eq. 5.11) are also shown.

5.4.4 Summary

By subtracting the model prediction for the bulk resistance of the interfacial material from the experimentally measured value, a direct relationship between electrical and thermal contact resistance was developed for the silver tubes as they undergo compressive deformation. This relationship was applied to the MMT-TIM data but found not to accurately predict the thermal contact resistance of these materials. This may be accounted for by the difference in material properties between the MMT-TIMs and the extruded silver tubes used to generate it. To overcome this difference, the same approach

was applied using the MMT-TIMs themselves to develop a distinctly different relationship between the specific electrical and thermal contact resistances, given as Eq. 5.14.

The major difference between this electrical contact resistance approach and the semi-empirical relationship developed in Sec. 5.3 (embodied in Eq. 5.11) is that here, accurate estimates of local contact pressures and areas are not required in order to evaluate the thermal contact resistance of the MMT-TIMs. Indeed, even when h_c is assumed to be constant, accurate predictions of contact areas by the model are required.

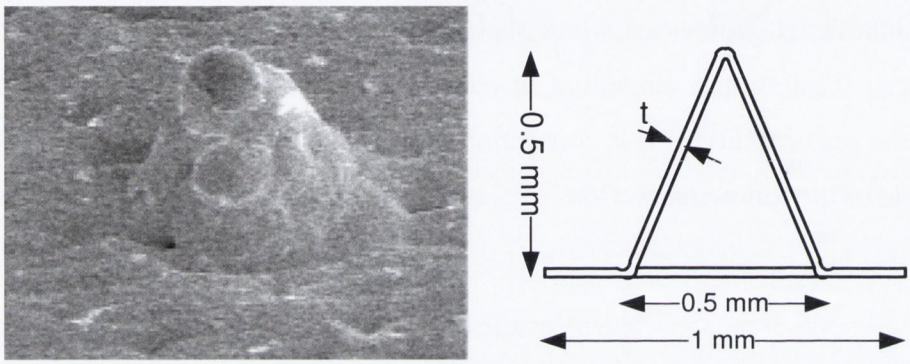
Instead, an additional experimental measurement of electrical resistance is used to directly estimate the thermal contact resistance based on correlations developed using baseline interfacial geometries where their bulk thermal resistance was known with good confidence. Testing and modelling of additional MMT-TIM geometries is necessary to validate the applicability of this correlation to other electroplated silver MMT-TIMs. This is the topic of the following section.

5.5 Additional MMT-TIM Geometries: Results & Model Comparisons

Several additional silver MMT-TIM geometries were tested and modelled in order to evaluate the efficacy of the various methods for predicting the contact thermal resistance of MMT-TIMs presented in the previous sections, and will be discussed in turn.

5.5.1 MMT-TIM Sample F

The first additional geometry examined here is denoted as MMT-TIM Sample F. An SEM image of feature and its nominal outer dimensions are shown in Fig. 5.39.



(a) (b)

Fig. 5.39: SEM Image and nominal outer dimensions of MMT-TIM Sample F

While similar into MMT-TIM Sample B, for this specimen the outer dimensions were scaled down by approximately 50% while the thicknesses tested remained the same, specifically t=36 μm and t=28 μm. Additionally, the spacing of features in the array was also reduced to 1 mm resulting in 1600 features present in the sample area of 40 mm × 40 mm.

Similar to before, the geometry reconstruction process developed in the present study was used to obtain a representative unit-cell geometry. A sequence of images depicting the model-predicted deformation of MMT-TIM Sample F, t=36 μm to an overall compressive pressure of 3 MPa is shown in Fig. 5.40.

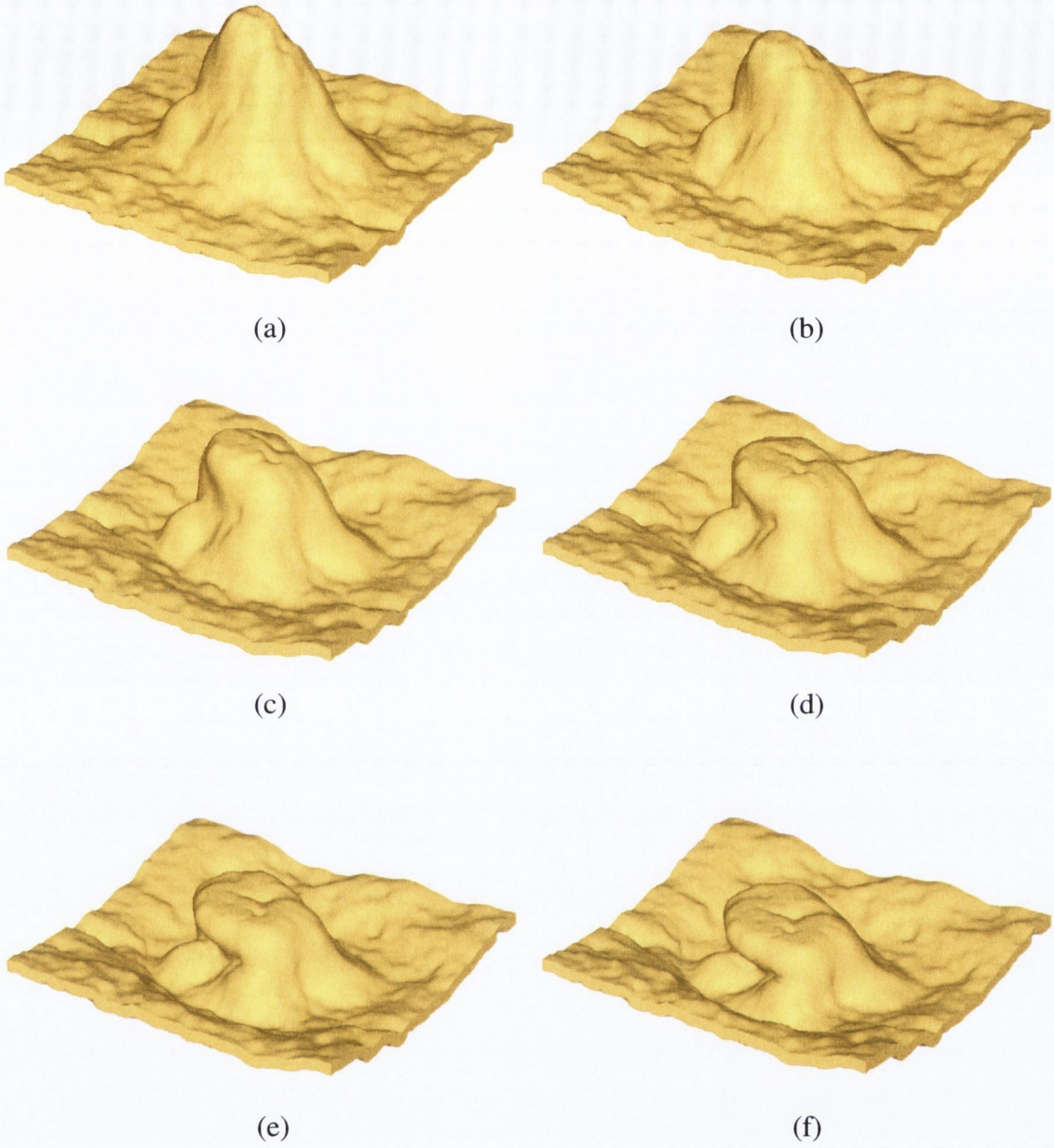


Fig. 5.40: Model prediction of compressive deformation of reconstructed MMT-TIM Sample F, t=36 μm geometry.

Due to the somewhat irregular shape of the initial cone, non-uniform buckling was also predicted in this model result. Additionally, the relative strain to which the feature deformed was significantly less than that predicted for MMT-TIM sample B: At 3 MPa MMT-TIM Sample B, t=36 μm exhibited approximately 76% strain while MMT-TIM Sample F, t=36 μm exhibited only 43% strain. This is due to the significantly higher wall-thicknesses relative to the feature size for Sample F.

The measured compressive pressure and associated model predictions during deformation for MMT-TIM Sample F are shown in Fig. 5.41.

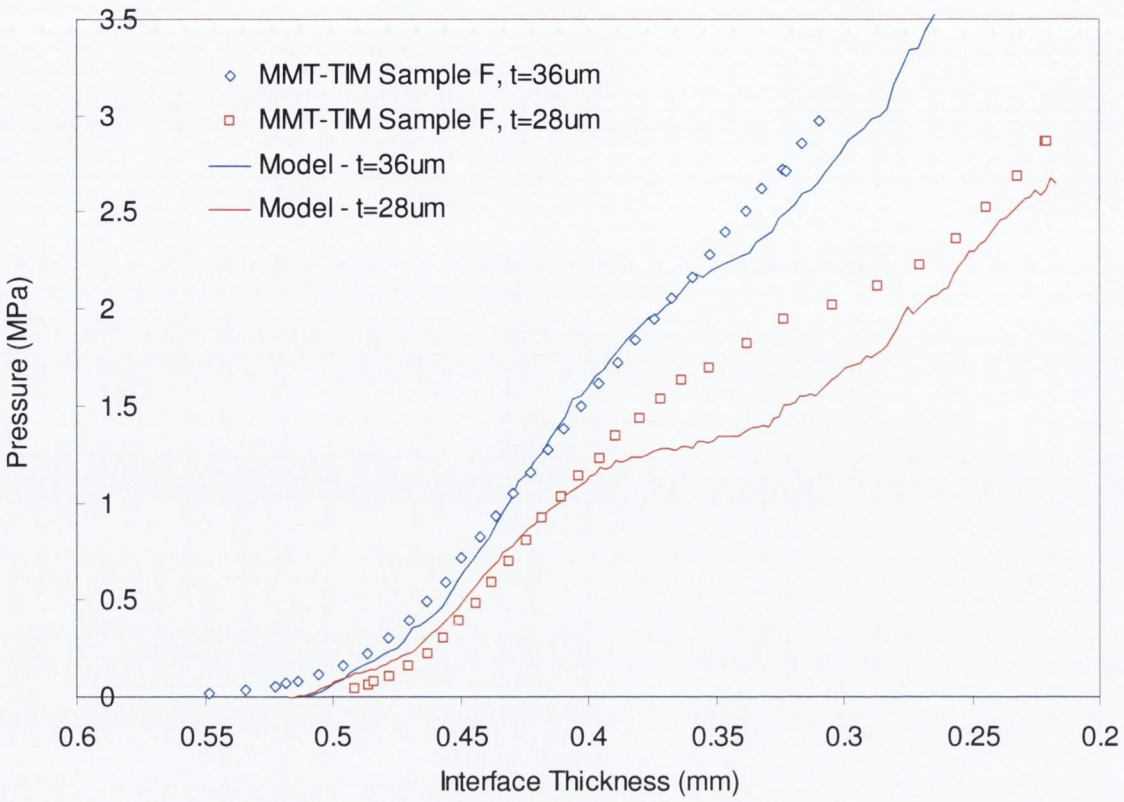


Fig. 5.41: Comparison of model predictions of mechanical response for MMT-TIM Sample F

Here the pressure required to deform this Sample varies nearly linearly as it is compressed with no significant plateau region occurring. Generally, the model predictions of the compressive pressure are quite reasonable although at interfaces thicknesses between 0.4 mm and 0.25 mm, the model prediction for t=28 μm tends to under predict the experimental pressure. This can be attributed to an increased sensitivity of the model to the chosen specific geometry at this length scale. In other words, the size of the features used in MMT-TIM Sample F is closer to the resolution limits of the 3D printer used to manufacture the template. As a result, there tends to be greater variation in feature shape between arbitrarily chosen features resulting in a relatively wider band of unit-cell geometries. The implications of these mechanical discrepancies are discussed below.

Thermal simulations for MMT-TIM Sample F were conducted using the aforementioned models for thermal contact resistance and the results are presented as effective thermal conductivity versus deformation in Figs. 5.42 and 5.43 for t=36 μm and t=28 μm, respectively.

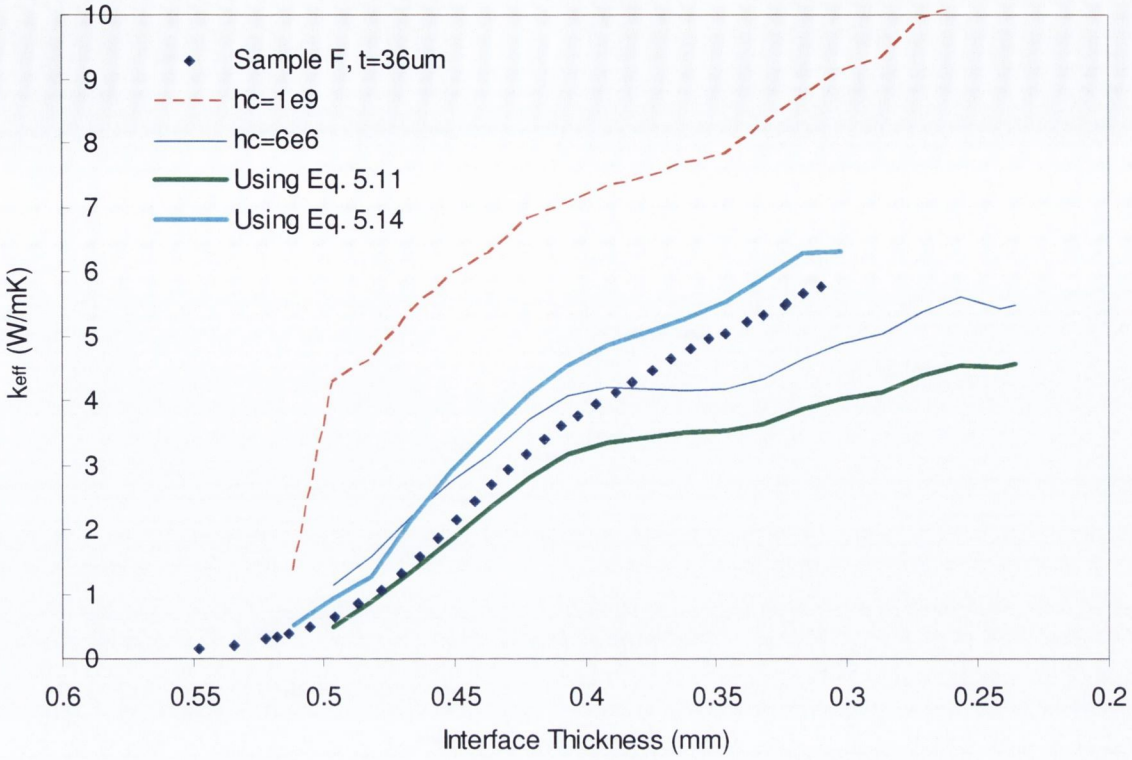


Fig. 5.42: Model predictions of effective thermal conductivity of MMT-TIM Sample F, t=36 μm

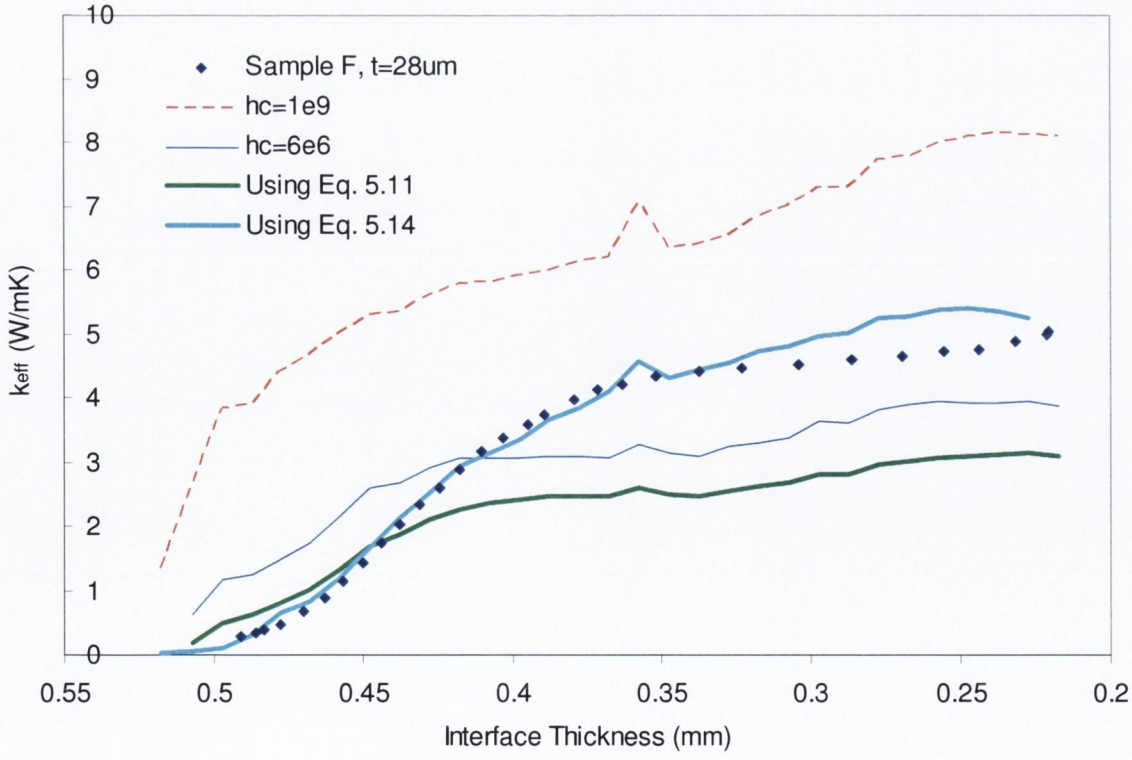


Fig. 5.43: Model predictions of effective thermal conductivity of MMT-TIM Sample F, t=28 μm

For both cases, relatively good agreement is observed between the measured effective thermal conductivity and that predicted by the model employing a constant h_c of 6×10^6 W/m^{2}K. However, for both thicknesses, this approach tended to under-predict the contact resistance at lower compressive pressures and over-predict the contact resistance at higher pressures.

The model prediction based the thermal-mechanical correlation for h_c (Eq. 5.11) initially gave good estimates of the thermal resistance of these samples, however it tended to under predict the effective thermal conductivity at higher deformations, particularly for MMT-TIM Sample F, t=28 μm in shown Fig. 5.43. This discrepancy can be attributed in part to the differences in materials from which this correlation was based as discussed in Sec. 5.3.3. However, this result also serves to highlight another source of uncertainty, namely the reliance of this model on the accuracy of the mechanical deformation prediction. As shown in Fig. 5.41, the model prediction for overall compressive pressure case lies significantly below the experimentally measured value for t=28 μm. As a result, the predicted local contact pressures would presumably be much lower and therefore the corresponding thermal contact conductance given by Eq. 5.11.

The thermal response predicted by the model using the thermal contact resistance calculated from the electrical contact resistance correlation developed in Sec. 5.4 (Eq. 5.14) seems to most accurately predict the effective thermal conductivity over the range of deformations for both thickness, and particularly well for t=28 μm.

Finally, for comparison, the upper limit of the predicted thermal conductivity is represented for the case when $h_c=1\times10^9$ where the contact resistance is essentially zero.

5.5.2 MMT-TIM Sample K

A silver MMT-TIM with raised features on both sides of a mid-plane was manufactured and characterized in order to further evaluate the accuracy of the models developed in the present study and is denoted here as MMT-TIM Sample K. An SEM image of this geometry is shown in Fig. 5.44 while a reconstructed unit-cell is shown in Fig. 5.45. Here, the MMT-TIM consists of alternating upward and downward opening domes resulting in a nearly symmetrical geometry about the horizontal mid-plane. The base diameter of each dome is approximately 1 mm as is the overall initial thickness of this specimen. The silver thickness of this sample was approximately 31 μm.

A series of images depicting the compression of MMT-TIM Sample K to a pressure of 3 MPa is shown in Fig. 5.46

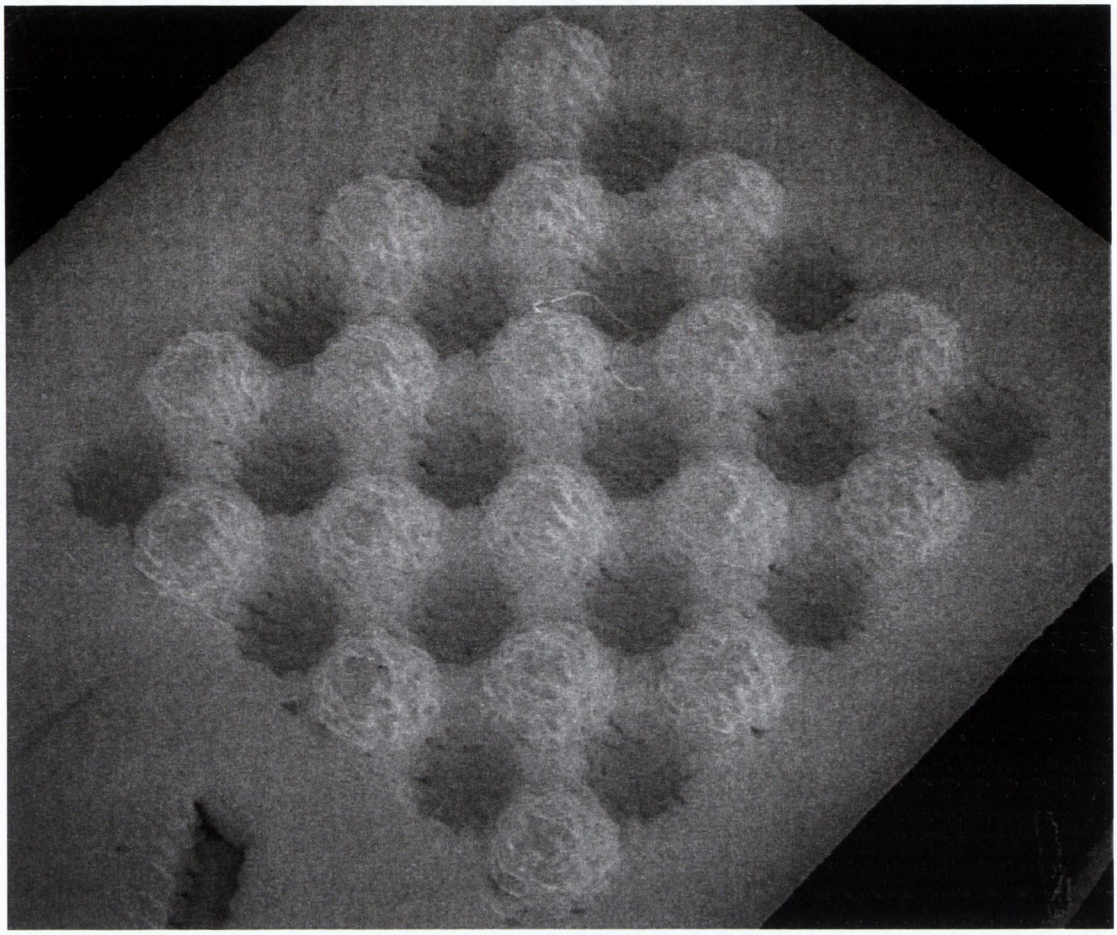


Fig. 5.44: SEM Image of MMT-TIM Sample K

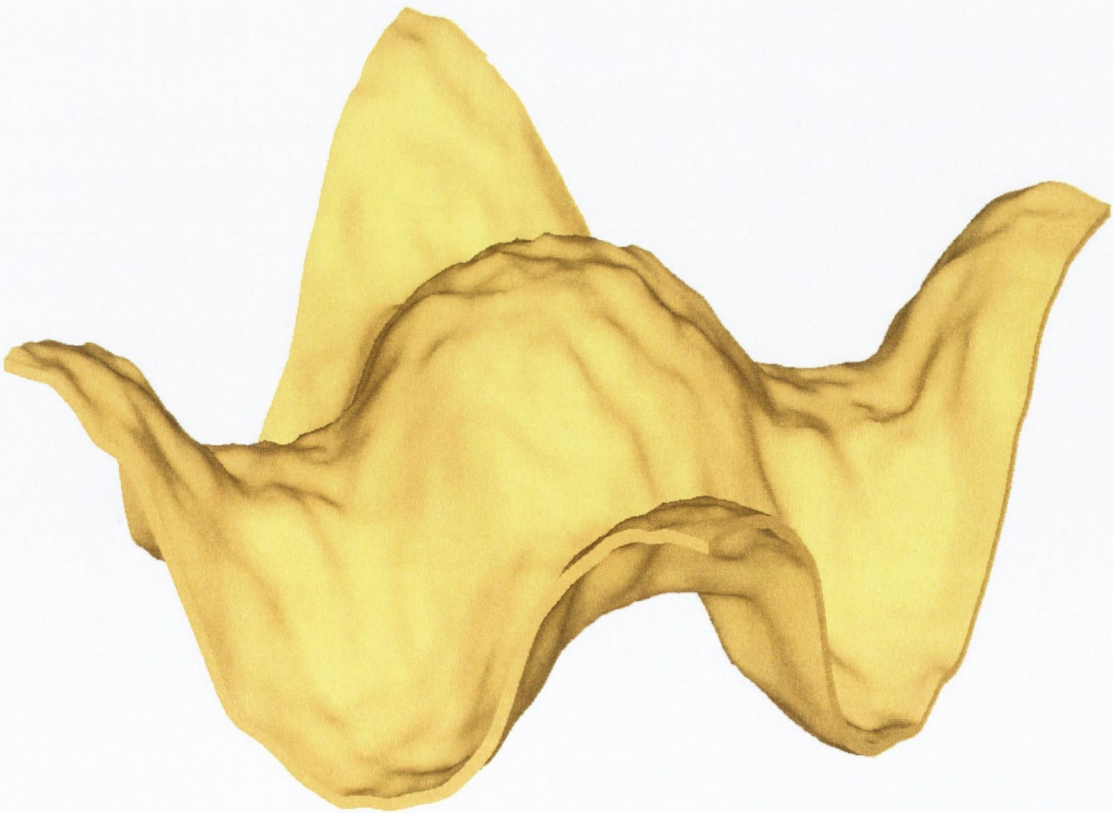


Fig. 5.45: Reconstructed geometry of a unit-cell of MMT-TIM Sample K

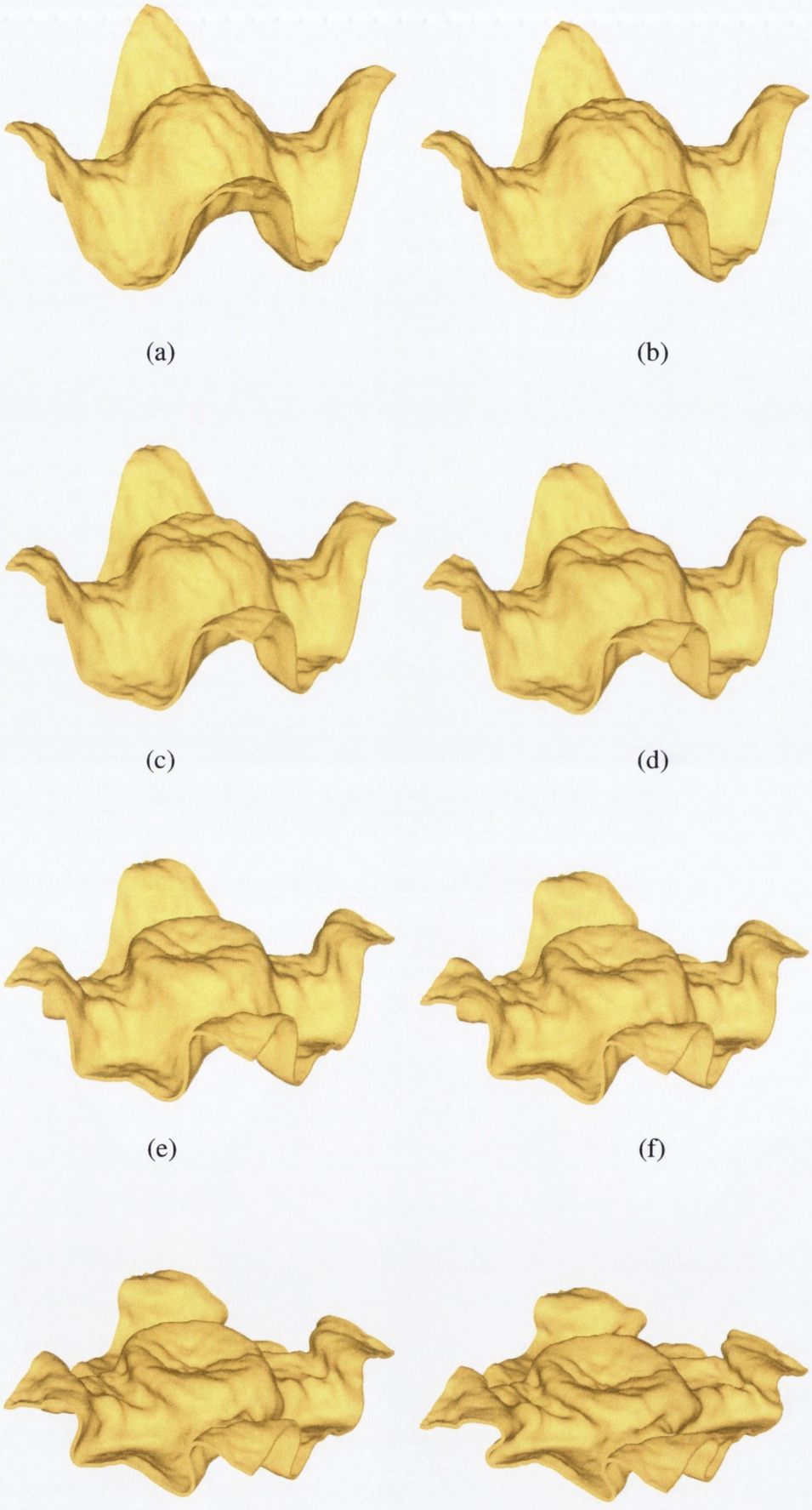


Fig. 5.46: Model prediction of compressive deformation of MMT-TIM Sample K.

This model prediction demonstrates that the features tend to deform on both sides of the horizontal mid-plane simultaneously. Also evident is the inward bowing of the centre of the dome structures as they are compressed.

The corresponding mechanical response of this simulation is shown in Fig 5.47 where the compressive pressure is shown during deformation.

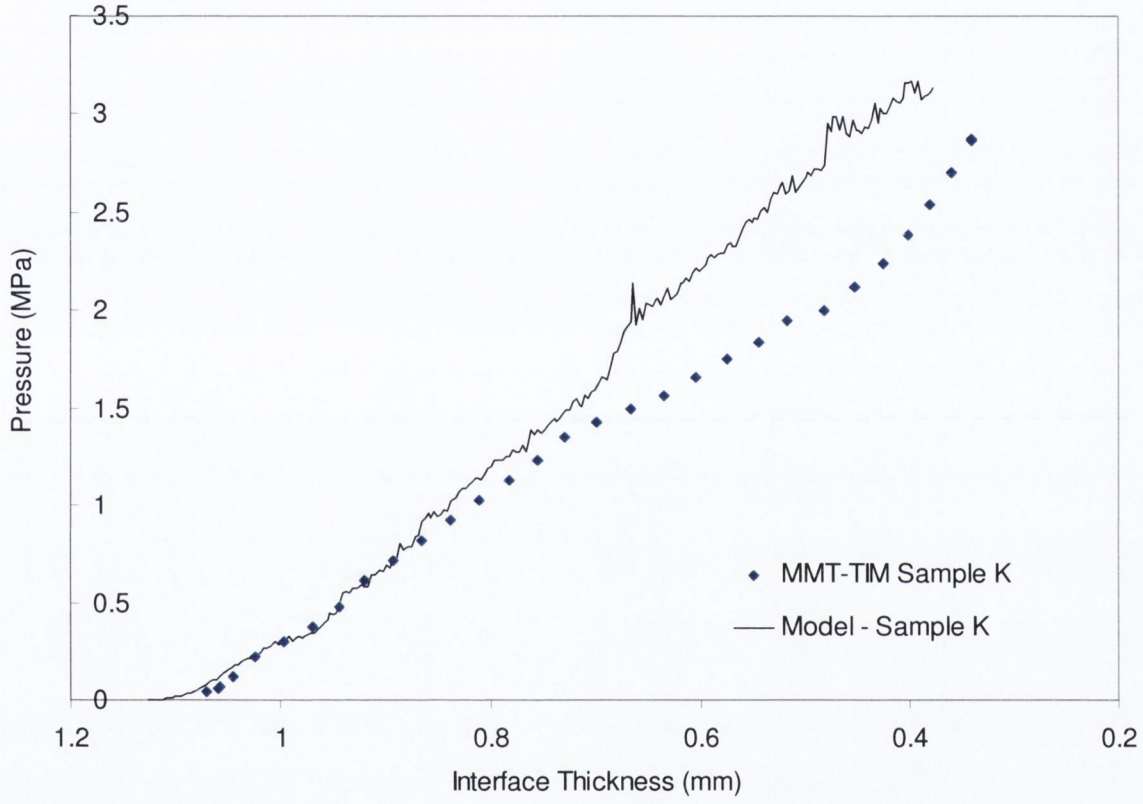


Fig. 5.47: Experimental and model-predicted of mechanical response for MMT-TIM Sample K during deformation

Here, the model prediction of overall compressive pressure is reasonably accurate during the first stages of deformation. However, below an interface thickness of approximately 0.8 mm, the model tends to over-predict the stiffness of this structure somewhat.

The thermal simulation results for MMT-TIM Sample K are shown in Fig. 5.48.

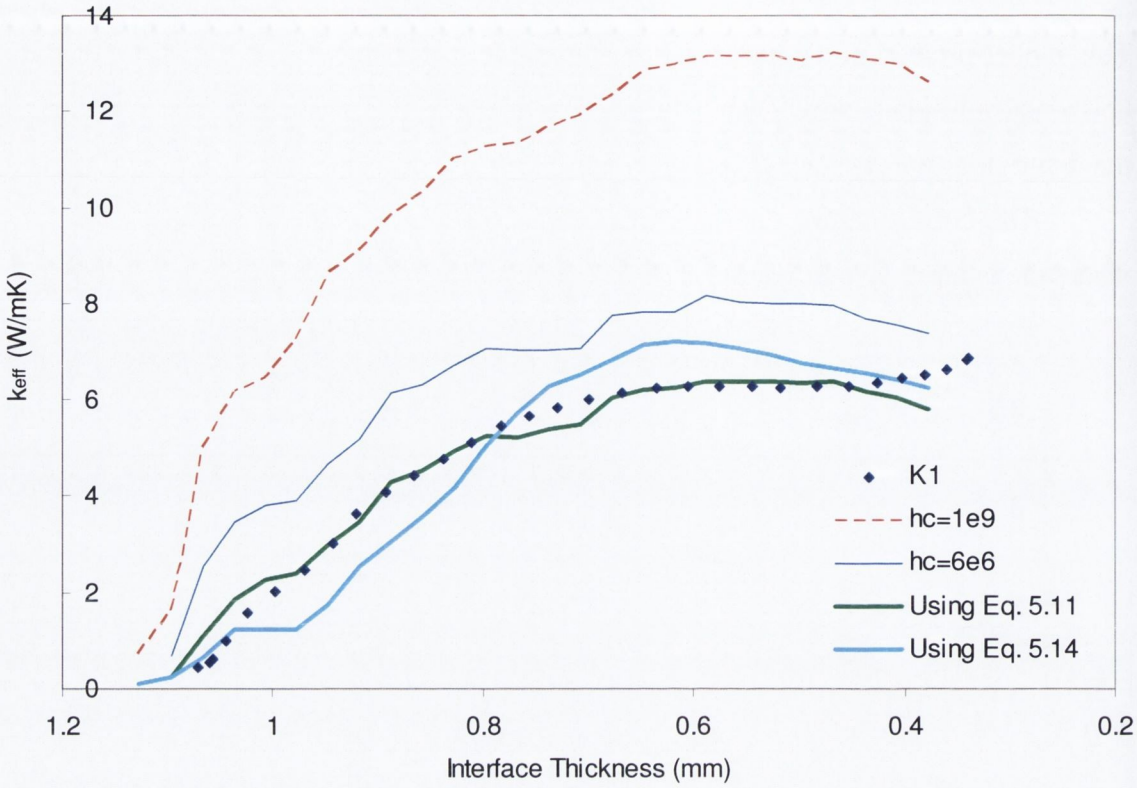


Fig. 5.48: Model predictions of effective thermal conductivity of MMT-TIM Sample K during deformation

Again, the various approaches to modelling the contact thermal resistance of the MMT-TIM are compared:

Overall, the model employing a constant h_c of 6×10^6 W/m^{2}K everywhere under-predicted the thermal resistance of MMT-TIM Sample K, resulting in an overly optimistic prediction of its effective thermal conductivity.

Both the model predictions based on the thermal-mechanical correlation for silver tubes (Eq. 5.11) and the electrical contact resistance correlation (Eq. 5.14) demonstrated good agreement with the measured thermal response. In previous cases, the model prediction using Eq. 5.11 tended to under-predict the effective thermal conductivity of the MMT-TIMs at larger deformations. However, for this example, since the model prediction for the mechanical response was somewhat higher than the measured result, the corresponding prediction for h_c using this model was also higher, resulting in a more realistic prediction of MMT-TIM thermal resistance.

5.5.3 Summary

To summarize and compare the different model predictions for MMT-TIM thermal performance, an aggregate of the predicted effective thermal conductivities for MMT-TIM

Samples F and K, using the various thermal contact resistance models are plotted against their corresponding experimental values during deformation in Fig. 5.49. Generally, all of the models incorporating a reasonable value for the thermal contact resistance, result a more realistic prediction of MMT-TIM thermal response. The model prediction based on the thermal-mechanical correlation using the silver tubes (Eq. 5.11) typically tended to under-predict the effective thermal conductivity of these silver MMT-TIMs. The model employing the contact resistance measurements and associated correlation developed in Sec. 5.4 (Eq. 5.14) tended to most accurately predict the thermal resistance of these three additional MMT-TIMs with over 70% of all data points falling with in ±15% of the measured effective thermal conductivity.

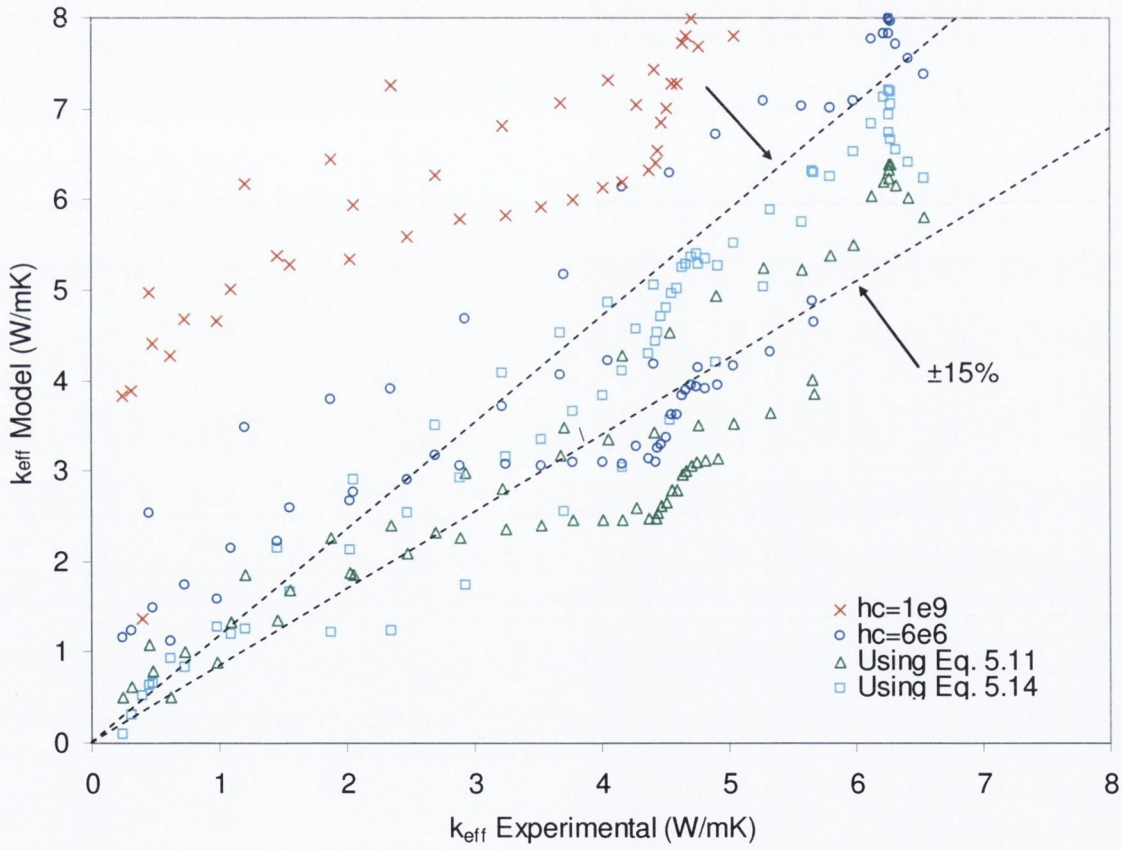


Fig. 5.49: Comparison between various model predictions and measured values of effective thermal conductivity for MMT-TIM Samples F and K

5.6 Summary

Initial results using a relatively simple illustrative geometry served to illustrate the concept of MMT-TIMs and provide a baseline from which model predictions were verified and refined.

By implementing the geometry reconstruction scheme outlined in Chapter 3, significant improvements were made to the mechanical model predictions of both compressive pressures during deformation over the conventional approach using idealized, nominal geometries. This approach also resulted in more realistic deformed geometries at a given strain. Additionally, for the baseline MMT-TIM examined, it was shown that the accuracy of this approach is relatively insensitive to the arbitrarily chosen unit-cell from which the geometry reconstruction takes place.

To improve the accuracy of the thermal model, two methods were developed to address the issue of contact thermal resistance: The first approach predicted the thermal contact conductance, h_c using predictions of local contact pressures and areas calculated by the mechanical model through a semi-empirical correlation developed using a baseline geometry of silver tubes. When applied to MMT-TIMs, this model resulted in a significantly improved estimate of thermal resistance however tended to somewhat over-predict the thermal resistance of the MMT-TIMs at higher strains and pressures.

The second approach developed to model thermal contact resistance in MMT-TIMs required an additional measurement of electrical resistance. Since factors such as contact area and pressure govern both electrical and thermal contact resistance in a similar way, an empirical correlation between the specific electrical contact resistance and specific thermal contact resistance for silver MMT-TIMs was developed. This model tended to provide more accurate estimates of MMT-TIM thermal resistance and effective thermal conductivity in subsequent model and experimental comparisons using additional MMT-TIM geometries.

Based on these developments, the analytical tools are in place for the design of an optimum MMT-TIM for a given application.

References

1. Kempers, R., Robinson A.J. & Lyons, A. "Characterization of Metal Micro-Textured Thermal Interface Materials" Proceedings of the 15th Workshop on Thermal Issues in ICs and Systems (THERMINIC), Leuven, Belgium, Oct 7-9, 2009.

2. Kempers, R., Frizzell, R., Lyons, A. & Robinson, A.J., "Development of a Metal Micro-Textured Thermal Interface Material", ASME InterPACK Conference, IPACK2009-89366, San Francisco, July 8-12, 2009

3. Yovanovich, M.M., 2005, "Four Decades of Research on Thermal Contact, Gap, and Joint Resistance in Microelectronics", IEEE Transactions on Components and Packaging Technologies, **28**, pp. 182-206.

4. Madhusudana, C.V., Thermal Contact Conductance, Springer-Verlag, New York, (1996).

5. Kempers, R., Lyons, A. & Robinson, A.J., "Characterization of Thermal Contact Resistance in Metal Micro-Textured Thermal Interface Materials using Electrical Contact Resistance Measurements" Defect and Diffusion Forum, **297-301**, pp. 1190-1198 (2010). doi:10.4028/www.scientific.net/DDF.297-301.1190

Chapter 6

Conclusions & Recommendations

6.1 Summary & Conclusions

The reduction of thermal contact resistance is an important issue in conduction based heat transport systems. Much effort has gone towards creating high performance TIMs in order to mitigate this resistance. However, there remain many shortcomings in these commercially available solutions. The overall objectives of the present work were to develop and prove the concept of a metal micro-textured thermal interface material (MMT-TIM), develop the required experimental tools for their characterization and develop quantitative and accurate analytical tools to model MMT-TIMs to serve as potential design and optimization tools for future applications. Presented here is a summary of the important findings of this study and major contributions to this area of research.

To address the shortcoming of conventional TIMs, the concept of the MMT-TIM was developed. The embodiment studied in the present work consisted of silver foils with raised, small-scale, hollow features. Upon compression between two solids, these features plastically deform, conforming to the asperities of the contacting surfaces thereby achieving intimate contact in the contact regions and a high conductivity bondline. Additionally, a manufacturing process was developed by which feature size and shape could be varied in order to study the effect of geometry on the thermal and mechanical response of the MMT-TIM.

The ongoing performance improvement in TIMs serves to highlight another challenge that was addressed in this study: namely the accurate and precise measurement of the thermal and mechanical properties of TIMs in general. Previous generations of TIM testers could not achieve the necessary sensitivity to measure thin bondline, high performance materials nor did they provide an explicit and conservative uncertainty analysis of their results. Here, an apparatus with an order-of-magnitude greater precision

has been developed to quantify the thermal and mechanical response of TIMs. Also, a robust and conservative uncertainty analysis provides quantitative assessments of all results. Finally, the simultaneous measurements of thermal and electrical resistance allowed for the indirect estimation of thermal contact resistance of the MMT-TIMs investigated in the present study.

The next issue that was addressed was the mechanical modelling of the large-scale plastic deformations occurring in the MMT-TIMs as they were compressed. It was shown that modelling these structures using idealized geometric representation techniques did not achieve accurate predictions of the mechanical response. To address this deficiency, a technique was developed whereby the surfaces of the MMT-TIMs were reconstructed using SEM images and 3D surface reconstruction software. The 3D surface data was subsequently used to create a more detailed and accurate solid geometry that was employed directly in the numerical model. This resulted in excellent agreement between the experimental and predicted results in terms of both compressive force and deformed geometry shape. This technique could be extended to any other micro-scale finite element modelling applications where accurate geometry representation would be valuable.

A combined thermal-mechanical model was developed in order to simultaneously characterize thermal response of the MMT-TIMs as they underwent large compressive deformations. While it was shown that the thermal contact resistance of the MMT-TIMs is an important factor, its characterization by conventional means was impossible. Two different approaches were developed to characterize the thermal resistance of MMT-TIMs.

The first approach developed to characterize MMT-TIM thermal contact resistance employed a numerical model as an analytical tool to estimate the local contact pressures and areas occurring at the contact surfaces of the MMT-TIM during deformation. By performing tests using symmetrical silver tubes, the predicted bulk thermal resistance was subtracted from the corresponding experimental measurement resulting in an estimate of the contact resistance. From this a semi-empirical relationship was developed relating the thermal contact conductance to the mean local contact pressure for silver structures undergoing large plastic deformations. This correlation was applied to the MMT-TIM thermal models and resulted in more realistic predictions of MMT-TIM thermal performance. Generally, however, this approach tended to over estimate the total thermal resistance of the MMT-TIMs due to material property differences between the electroplated MMT-TIMs and the extruded silver tubes from which the correlation was generated.

Another method for characterizing MMT-TIM thermal contact resistance was developed using electrical contact resistance measurements. Here a correlation was established between the estimated thermal contact resistance and the experimentally measured electrical contact resistance. The thermal contact resistance was estimated by subtracting the bulk thermal resistance of a baseline MMT-TIM (calculated using the initial thermal model) from its experimentally measured value. While the previous method required additional predictions of local contact pressures and areas to calculate the contact thermal resistance, this method requires only an additional measurement of the electrical resistance.

The electrical-thermal contact resistance correlation, based on the baseline Sample B geometry, provides the best results as it accurately predicted the performance of MMT-TIMs with cones of smaller size, as well as novel geometry. The use of this correlation is limited, however, to electroplated silver MMT-TIMs and probably would not be useful in predicting the performance of wrought, embossed, or extruded silver TIMs, or other electroplated metal structures. For pure, fabricated silver, the contact resistance derived from the silver tubes might provide better a better estimate of the thermal performance of such MMT-TIMs. Correlations between electrical and thermal contact resistance for metals other than silver would need to be determined experimentally before model predictions could be made reliably.

The stiffness of the micro-textured feature significantly affects the thermal performance of the TIM. The electroplated conical features perform significantly better than their corresponding idealized cone models as the actual structures incorporate various imperfections that provide numerous stress-concentration sites. This enables the structure to buckle through a series of small, continuous, asymmetric steps rather than the discrete, axisymmetric, buckling rings predicted by the finite element model.

The best thermal performance was achieved by using a novel symmetrical, double-sided dome structure (MMT-TIM Sample K) where cones protruded towards both the top and bottom surfaces. This improved performance may be attributable to several different factors including local contact pressure and compliance. Increased local contact pressure would be expected on the bottom surface at the tips of the cones, relative to the standard MMT-TIM (Samples B and F) where the bottom surface is flat and the pressure would be spread over a large surface area. As discussed previously, the higher local contact pressure is expected to reduce the thermal contact resistance as well as the overall thermal resistance. Additionally, MMT-TIM Sample K demonstrated good compliance compared to MMT-TIM Sample F .

To summarize, the concept of MMT-TIMs has been shown to be feasible from results presented using a baseline MMT-TIM geometry. These measurements were obtained using an experimental apparatus developed for measuring TIM performance with unprecedented precision and accuracy. A numerical model was developed to simultaneously characterize the mechanical and thermal response of MMT-TIMs. Improvements to the mechanical response were obtained by developing a novel method of MMT-TIM geometry reconstruction while the thermal response was improved by developing two unique approaches to quantifying MMT-TIM thermal contact resistance. The veracity of the improved MMT-TIM models were demonstrated through the characterization of additional MMT-TIM geometries: Two additional smaller conical geometries and a more complex double-sided MMT-TIM were also characterized with a good degree of accuracy using the methods developed here. Thus, experimental and analytical tools are in place for the design of an optimum MMT-TIM for a given application.

6.2 Recommendations & Future Outlook

The development of a specific "optimum" MMT-TIM is very much dependent on the specific application due to factors such as the length scale of the contacting surface asperities, desired bondline thickness and assembly pressures available. The shapes of the micro-textured features play a large role in determining the overall thermal conductance of the bond. Only a few structures have been evaluated to date. We plan on using the models developed in this work to evaluate a wide range of other shapes to explore alternative geometries which may yield higher performance.

Successful practical implementation of this technology will rely on the development of cost-effective of manufacturing methods. For example, the geometries examined in the present work lend themselves to potential large-scale stamping or embossing operations. Also, additional research is required in terms of the material choice for the MMT-TIM. For example, while silver has a relatively high thermal conductivity, aluminium is significantly softer and an aluminium MMT-TIM could offset the bulk conductivity difference by designing a MMT-TIM array with a higher feature density. Further research is also required in determining the length scales to which this concept is viable, both in terms of application and manufacturability.

Appendix A

Material Property Testing

Compressive upsetting tests were performed on pure, annealed metals in order to provide DEFORM with the requisite plastic stress-strain data (flow stress) for accurate modelling of MMT-TIMs of the same material. This Appendix details this process and presents a summary of the measured data.

Annealing

Samples of relatively pure metals (typically 99.9+ % purity) were cut from cylindrical rods ranging from 5.5 mm to 7 mm in diameter depending on the metal. These were cut to lengths such that their aspect ratios were 1:1. The outer dimensions of each sample were measured prior to testing.

The samples were then annealed in a Carbolite tube furnace under the conditions listed in Table A.1.

Metal	Annealing Temperature (°C)	Annealing Time (min)	Atmosphere
Silver (Ag)	400	30	Air
Gold (Au)	400	30	Air
Copper (Cu)	600	30	N2
Aluminium (Al)	400	30	Air

Table A.1: Annealing conditions

Upsetting Tests

Compressive upsetting tests were performed using an Instron 5589 Materials Tester shown in Fig. A.1. A photograph of a sample prior to testing is shown in Fig. A.2



Fig. A.1: Instron 5589 Material Tester used for compressive upsetting tests

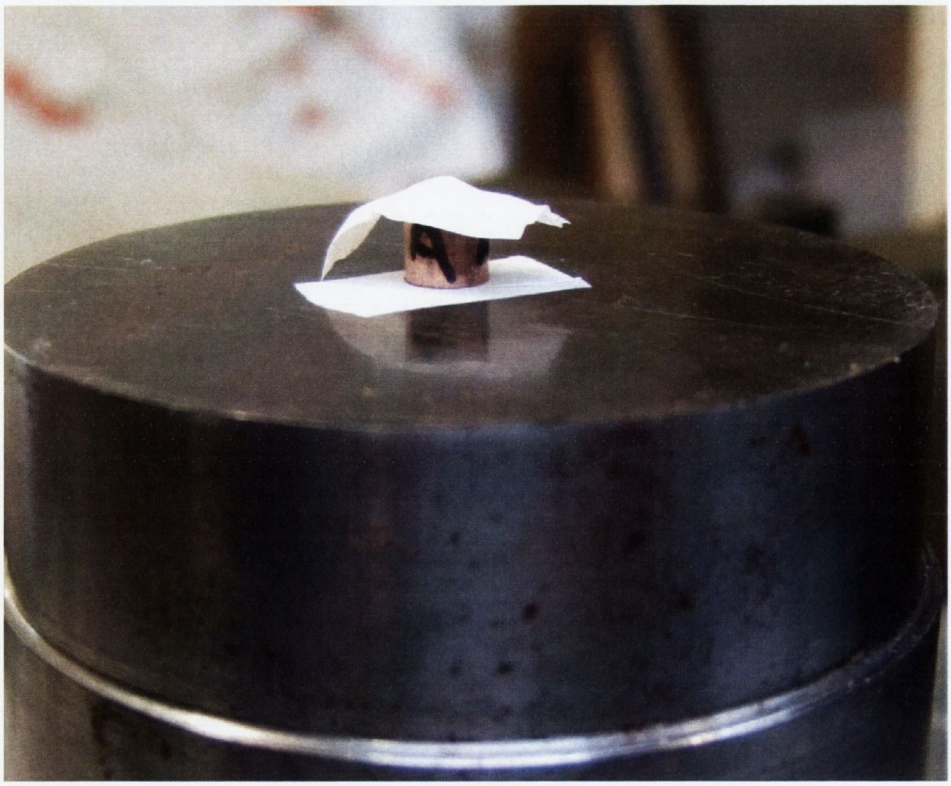


Fig. A.2: Sample setup for upsetting test

The setup in Fig. A.2 shows the samples supported from below upon a smooth steal cylinder. A smooth steel plate attached to the crosshead of the tester provided the upper contacting surface. Thin pieces of Teflon tape were inserted between the contacting surfaces to minimize barrelling during compression. This ensured the stress throughout the specimen at a given strain is uniform as shown in Fig. A.3.

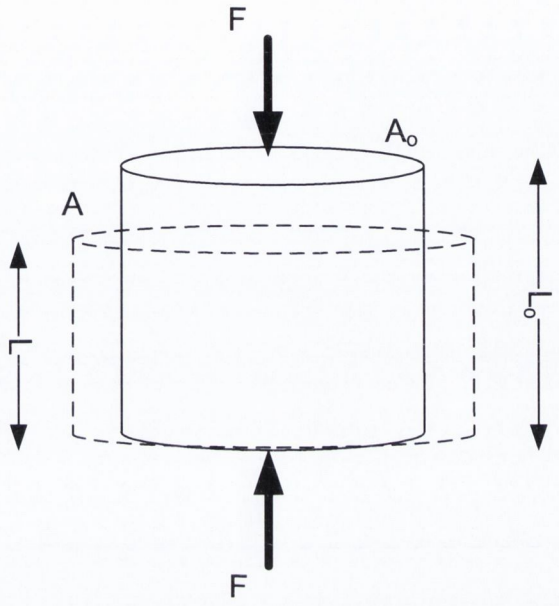


Fig. A.3: Deformation of a cylindrical specimen during compressive upsetting test

The displacement of the Instron crosshead and its load cell measurements were used in conjunction with the sample's initial dimensions to compute the true stress, σ_t, and true strain ε_t, as the material was compressed using

$$\sigma_t = \frac{F}{A} \tag{A.1}$$

and

$$\varepsilon_t = \ln \frac{L}{L_0} \tag{A.2}$$

where F is the applied force, A is the specimen area, L is the specimen thickness and L_0 is the initial specimen thickness. Negligible barrelling was observed during the compression, thus with the assumption of constant volume during deformation, the instantaneous area can be computed based on the displacement of the crosshead.

The MMT-TIMs tested in the apparatus described in Chapter 4 experience extremely low effective strain rates due to the large steady-state wait times between loading steps and relatively small step increments. As a result, in order to achieve

representative stress-strain data, here the cylindrical samples were compressed at a strain rate of 0.1 μm/s.

A summary of the measured data is shown in Fig. A.4.

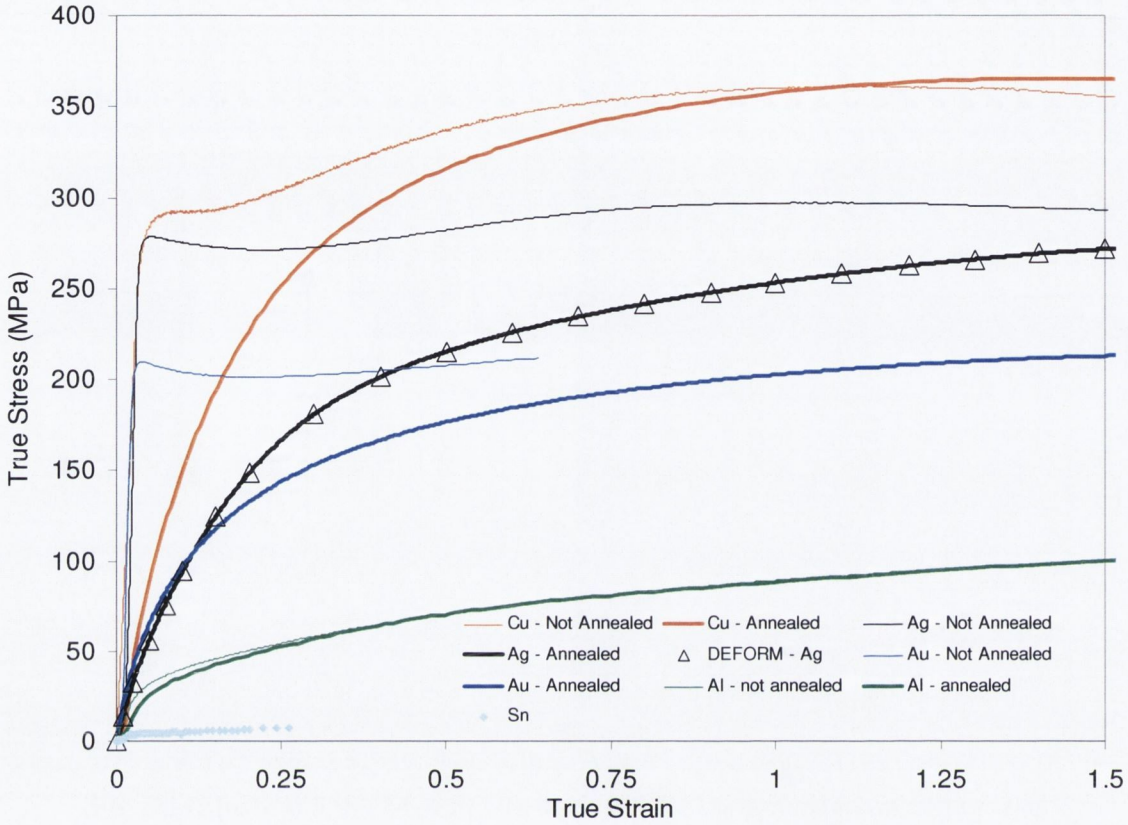


Fig. A.4: Summary of stress-strain data obtained from compressive upsetting tests

Generally, for the un-annealed specimens, there exists a well defined yield. This also serves to demonstrate the importance of annealing in order to soften the material to its softest state. The multi-linear strain hardening model supplied to DEFORM for the models in present study is plotted as a series of triangles in Fig. A.4.

Appendix B

DEFORM Data Extraction and Heat Transfer Calculations

Mechanical and thermal simulation data were exported from DEFORM. MATLAB was used to perform calculations of the MMT-TIM thermal resistance and effective thermal conductivity of the MMT-TIMs as a function of deformation and pressure by combining the exported mechanical and thermal data from the two DEFORM simulations. A listing of this code is presented here.

```
%% DEFORM_CRUNCH
% This script extracts the essential nodal mechanical and thermal data from
% DEFORM's exported data files in order to calculated the thermal
% resistance and effective thermal conductivity of the specimen during
% deformation
%
% REQUIRED DEFORM EXPORTED DATA FILES:
% From the Single Operation Mechanical Simulation:
% Top Die Load-Stroke file
% Workpiece Nodal Coords (RZ) for only +ve steps (except -1)
% Workpiece Calculated Nodal Pressures (PRZB) for all +ve steps and step -1
%
% From Multiple-Operation Heat Transfer Simulation, for the last step of
% each operation:
% Top Die Nodal Coords (RZ)
% Top Die Calculated Nodal Temperature (NDTMP)

clc
clear all

%% BOUNDARY CONDITIONS DEFINED IN DEFORM
Q_flux=1000 %W/m2  [1000 W/m2 = 1 N/mm*s in DEFORM's units]
T_cold = 0.000 %Bottom Die Temperature

k_top_die=215 %Thermal conductivity of Top Die
k_bot_die=215 %Thermal conductivity of Bottom Die

file_prefix=('B3_SO') %Filename prefix using for data files

%% FILENAMES AND INITIALIZATION
% Top Die Files
top_die_RZ_name=strcat(file_prefix, '_DataExtract_RZ.DAT');  % define filename
RZ_FID=fopen(top_die_RZ_name); %open file
fseek(RZ_FID,0,'eof'); % find the end of the file
RZ_size=ftell(RZ_FID); % measure file size
fseek(RZ_FID,0,'bof'); % go to the begining of file

top_die_NDTMP_name=strcat(file_prefix, '_DataExtract_NDTMP.DAT');
NDTMP_FID=fopen(top_die_NDTMP_name);
fseek(NDTMP_FID,0,'eof');
NDTMP_size=ftell(NDTMP_FID);
fseek(NDTMP_FID,0,'bof');

top_die_LS_name=strcat(file_prefix, '_DataExtract_LS.DAT');
LS_FID=fopen(top_die_LS_name);
fseek(LS_FID,0,'eof');
LS_size=ftell(LS_FID);
fseek(LS_FID,0,'bof');

% Workpiece files
```

```
WP_RZ_name=strcat(file_prefix, '_DataExtract_WP_RZ.DAT');
WP_RZ_FID=fopen(WP_RZ_name);
fseek(WP_RZ_FID,0,'eof');
WP_RZ_size=ftell(WP_RZ_FID);
fseek(WP_RZ_FID,0,'bof');

work_piece_PRZB_name=strcat(file_prefix, '_DataExtract_WP_PRZB.DAT');
WP_PRZB_FID=fopen(work_piece_PRZB_name);
fseek(WP_PRZB_FID,0,'eof');
WP_PRZB_size=ftell(WP_PRZB_FID);
fseek(WP_PRZB_FID,0,'bof');

%% READ DATA FROM FILES
i=0;
%Loop going through the steps in the Top Die nodal coords file (RZ) file
while(1) %Obtains unit cell area and displacements at every HEAT TRANSFER step
    i=i+1;  %Index of each step
    while(1) %Reads unitl it finds the next "Step" or reaches EOF
        A=textscan(RZ_FID,'%s',1);
        if isequal(char(A{:}),'Step')==1
            break
        elseif ftell(RZ_FID)==RZ_size
            sprintf('end of RZ file')
            break
        end
    end

    if ftell(RZ_FID)~=RZ_size % If the EOF hasn't been reached yet

        B=textscan(RZ_FID,'%f',1); %Reads the step number
        list_of_steps_RZ(i)=B{:}; %puts it in list of steps

        crap=textscan(RZ_FID,'%s',2); % Ignores next 2

        C=textscan(RZ_FID,'%f',1); %gets the total number of nodes at this step
        total_nodes_RZ(i)=C{:};

        for node=1:total_nodes_RZ(i) %loop going through each node
            D=textscan(RZ_FID,'%f',1); %can ignore this data

            E=textscan(RZ_FID,'%f',1);
            X(node,i)=E{:};

            F=textscan(RZ_FID,'%f',1);
            Y(node,i)=F{:};

            G=textscan(RZ_FID,'%f',1);
            Z(node,i)=G{:};
        end

        width(i)=(max(X(:,i))-min(X(:,i)))/1000; % Unit Cell Width (m)
        depth(i)=(max(Y(:,i))-min(Y(:,i)))/1000; % Unit Cell Depth (m)
        height(i)=(max(Z(:,i))-min(Z(:,i)))/1000; % top die height (m)
        area(i)=width(i)*depth(i); %Unit Cell Area (m2)
        disp(i)=-1*(Z(1,i)-Z(1,1))/1000; %displacement of Node 1 (arbitrarily) (m)

    else %if the EOF has been reached
        i=i-1
        sprintf('end of RZ file')
        break
    end
end

i=0; %Loop going through the steps in the NDTMP file
while(1)%Obtains nodal temperatures and max Temperature (at top) at every step
    i=i+1;  %Index of each step

    while(1) %Breaks after finds the next "Step" or reahes EOF
        A=textscan(NDTMP_FID,'%s',1);
        if isequal(char(A{:}),'Step')==1
            break
        elseif ftell(NDTMP_FID)==NDTMP_size
            sprintf('end of NDTMP file')
            break
        end
    end

    if ftell(NDTMP_FID)~=NDTMP_size % If the EOF hasn't been reached yet
        B=textscan(NDTMP_FID,'%f',1); %Get Step number
        list_of_steps_NDTMP(i)=B{:};
```

```
        crap=textscan(NDTMP_FID,'%s',2); % Ignores these 2

        D=textscan(NDTMP_FID,'%f',1); %gets the total number of nodes
        total_nodes_NDTMP(i)=D{:};

        crap=textscan(NDTMP_FID,'%s',1); % Ignores this one

        for node=1:total_nodes_NDTMP(i) %loop going through each node
            crap=textscan(NDTMP_FID,'%f',1); %can ignore the node number
            E=textscan(NDTMP_FID,'%f',1);
            T(node,i)=E{:};
        end
        T_max_top_die(i)=max(T(:,i));

    else %if the EOF has been reached
        i=i-1
        sprintf('end of NDTMP file')
        break
    end
end

while(1) %prepares to read LS file
    A=textscan(LS_FID,'%s',1);
    if isequal(char(A{:}),'Load_z')==1
        break %Breaks after finds the next "Load_z"
    elseif ftell(LS_FID)==LS_size
        sprintf('end of LS file')
        break %breaks when reahes EOF
    end
end
i=0;
j=1;
while(1)  %Loop going through SINGLE OPERATION Load-Stroke Data File
    i=i+1;
    if ftell(LS_FID)==LS_size || ftell(LS_FID)+1==LS_size || ftell(LS_FID)+2==LS_size %if
the EOF has been reached
        i=i-1
        sprintf('end of LS file')
        break

    else % If the EOF hasn't been reached yet
        B=textscan(LS_FID,'%f',1);
        list_of_steps_LS(i)=B{:};

        C=textscan(LS_FID,'%f',1);
        time(i)=C{:};

        D=textscan(LS_FID,'%f',1);
        stroke(i)=D{:}/1000; % put into m

        E=textscan(LS_FID,'%f',1);
        vel(i)=E{:};

        F=textscan(LS_FID,'%f',1);
        load_x(i)=F{:};

        G=textscan(LS_FID,'%f',1);
        load_y(i)=G{:};

        H=textscan(LS_FID,'%f',1);
        load_z(i)=H{:};

        if j<=length(disp) && abs(stroke(i)-disp(j))<1e-6   %if the disp and stroke match
up
            SO_load_z(j)=load_z(i); %populate the load
            SO_steps(j)=list_of_steps_LS(i); %count the step
            j=j+1;
        end

    end
end

i=0; %Loop going through the WP_RZ file
while(1) %Counts and collects nodes in approximate contact at top and bottom
    i=i+1;  %Index of each step

    while(1) %Reads unitl it finds the next "Step" or reaches EOF
        A=textscan(WP_RZ_FID,'%s',1);
        if isequal(char(A{:}),'Step')==1
```

```
            break
        elseif ftell(WP_RZ_FID)==WP_RZ_size
            sprintf('end of WP_RZ file')
            break
        end
    end

    if ftell(WP_RZ_FID)~=WP_RZ_size % If the EOF hasn't been reached yet

        B=textscan(WP_RZ_FID,'%f',1); %Reads the step number
        list_of_steps_WP_RZ(i)=B{:}; %puts it in list of steps

        crap=textscan(WP_RZ_FID,'%s',2); % Ignores these two fields

        C=textscan(WP_RZ_FID,'%f',1); %gets the total number of nodes at this step
        total_nodes_WP_RZ(i)=C{:};  %This might change due to remeshing

        for node=1:total_nodes_WP_RZ(i) %loop to read position of each node at this step
            D=textscan(WP_RZ_FID,'%f',1); %ignore this data

            E=textscan(WP_RZ_FID,'%f',1);
            WP_X(node,i)=E{:};

            F=textscan(WP_RZ_FID,'%f',1);
            WP_Y(node,i)=F{:};

            G=textscan(WP_RZ_FID,'%f',1);
            WP_Z(node,i)=G{:};  % Z-coord of each node at each step

        end

        WP_top_z(i)=max(WP_Z(1:total_nodes_WP_RZ(i),i)); %Calculate the top-most WP
position for this step, mm
        WP_bot_z(i)=min(WP_Z(1:total_nodes_WP_RZ(i),i)); %Calculate the bottom-most WP
position for this step, mm

        WP_thickness(i)=(WP_top_z(i)-WP_bot_z(i))/1000; %m

        j=1; %index used for list of top contact nodes
        k=1; %index used for list of bottom contact nodes
        z_buffer=0.001; %uncertainty window for nodes that are close, mm
        for node=1:total_nodes_WP_RZ(i) %loop going through every node at this step
            if isinrange(WP_top_z(i)-z_buffer,WP_top_z(i)+z_buffer,WP_Z(node,i))==1 %if the
node's Z-position is in range of the max coord
                top_contact_nodes(j,i)=node; %it gets inserted into the list of top contact
nodes
                total_top_contact_nodes(i)=j; %the total number corresponds to the index
                j=j+1; % increment index
            elseif isinrange(WP_bot_z(i)-z_buffer,WP_bot_z(i)+z_buffer,WP_Z(node,i))==1
                bot_contact_nodes(k,i)=node;
                total_bot_contact_nodes(i)=k;
                k=k+1;
            end
        end

    else %if the EOF has been reached
        i=i-1
        sprintf('end of WP_RZ file')
        break
    end
end

contact_node_errors=0;
i=0; %Loop going through the SINGLE OPERATION WP_PRZB file
while(1)
    i=i+1;  %Index of each step
    while(1) %Reads unitl it finds the next "Step" or reaches EOF
        A=textscan(WP_PRZB_FID,'%s',1);
        if isequal(char(A{:}),'Step')==1
            break
        elseif ftell(WP_PRZB_FID)==WP_PRZB_size
            sprintf('end of WP_PRZB file')
            break
        end
    end

    if ftell(WP_PRZB_FID)~=WP_PRZB_size % If the EOF hasn't been reached yet

        B=textscan(WP_PRZB_FID,'%f',1); %Reads the step number
        list_of_steps_WP_PRZB(i)=B{:}; %puts it in list of steps
```

```
        crap=textscan(WP_PRZB_FID,'%s',2); % Ignores next 2

        C=textscan(WP_PRZB_FID,'%f',1); %gets the total number of contacting nodes at this
step
        total_contact_nodes_WP_PRZB(i)=C{:};

        crap=textscan(WP_PRZB_FID,'%s',1); % Ignores next 1

        j=1; %index for top contact nodes
        k=1; %index for bot contact nodes
        l=1; %index for internal contact nodes
        total_internal_contact_nodes_P=0;
        for node=1:total_contact_nodes_WP_PRZB(i) %loop going through every contacting node
            D=textscan(WP_PRZB_FID,'%f',1);
            WP_contact_nodes(node,i)=D{:}; %This is the list of nodes in contact at this
step

            E=textscan(WP_PRZB_FID,'%f',1);
            P_X(node,i)=E{:};

            F=textscan(WP_PRZB_FID,'%f',1);
            P_Y(node,i)=F{:};

            G=textscan(WP_PRZB_FID,'%f',1);
            P_Z(node,i)=G{:};

            %Determining where contact is occuring
            if max(ismember(top_contact_nodes(:,i),WP_contact_nodes(node,i)))>0
                P_Z_top(j,i)=abs(P_Z(node,i));
                total_top_contact_nodes_P(i)=j;
                j=j+1;
            elseif max(ismember(bot_contact_nodes(:,i),WP_contact_nodes(node,i)))>0
                P_Z_bot(k,i)=abs(P_Z(node,i));
                total_bot_contact_nodes_P(i)=k;
                k=k+1;
            else
                total_internal_contact_nodes_P(i)=l;
                l=l+1;
            end

        end

    else %if the EOF has been reached
        i=i-1
        sprintf('end of WP_PRZB file')
        break
    end

end

%% Save
save temp_data
% load temp_data

%% CALCULATIONS
Q=Q_flux*area(1);
R_top_die=height(1)/(k_top_die*area(1)); %K/W
R_bot_die=R_top_die; %Assume same dimensions & material

for i=1:length(disp)

    %Averaging Top Contact Pressure
    P_avg_top(i)=(sum(P_Z_top(:,i))/total_top_contact_nodes_P(i)); %MPa
    P_avg_bot(i)=(sum(P_Z_bot(:,i))/total_bot_contact_nodes_P(i)); %MPa

    % Estimating Contact Areas
    A_contact_top(i)=abs(SO_load_z(i))/(P_avg_top(i)*1e6); %m2
    A_contact_bot(i)=abs(SO_load_z(i))/(P_avg_bot(i)*1e6); %m2

    A_contact_top_percent(i)=100*A_contact_top(i)/area(1); % percent
    A_contact_bot_percent(i)=100*A_contact_bot(i)/area(1); % percent

    % Various Definitions for hc=========================================
%         h_top(i)=1e9; %W/m2K  really high
%         h_bot(i)=1e9; %W/m2K  really high

        h_top(i)=6e6; %W/m2K  %constant value
        h_bot(i)=6e6; %W/m2K
%
```

```
%     h_top(i)=1.24e5*P_avg_top(i)^0.638;  % W/m2K
%     h_bot(i)=1.24e5*P_avg_bot(i)^0.638;  % W/m2K
    %=====================================================================

    % Calculating contact thermal resistance
    R_contact_top(i)=(h_top(i)*A_contact_top(i))^-1; %K/W
    R_contact_bot(i)=(h_bot(i)*A_contact_bot(i))^-1; %K/W

    R_total(i)=(T_max_top_die(i)-T_cold)/Q; %K/W
    R_bulk(i)=R_total(i) - R_top_die - R_bot_die; %K/W  %Just the resistance of the feature
    RA_bulk(i)=R_bulk(i)*area(1); %m2K/W  %Specific Thermal resistance of features based on
R_bulk
    k_bulk(i)=WP_thickness(i)/RA_bulk(i); %W/mK %Effective k of bulk only

    R_eff(i)=R_bulk(i) + R_contact_top(i) + R_contact_bot(i); %K/W  (R_meas)
    RA_eff(i)=R_eff(i)*area(1); %m2K/W   %Specific thermal resistance of TIM
    k_eff(i)=WP_thickness(i)/RA_eff(i); %W/mK

    pressure(i)=(abs(SO_load_z(i))/area(1))/1e6; %MPa

end

%% EXPORT RESULTS
xls_filename=(['DEFORM Output for ',file_prefix,' - ', datestr(now,30)]);
%Any new headings need to occupy 10 character spaces
headings=['stroke     ';'thickness ';'load_z     ';'pressure  ';'T_max      ';'R_bulk
';'RA_bulk    ';'k_bulk     ';'R_eff      ';'RA_eff     ';'k_eff
';'P_cont_top';'P_cont_bot';'R_cont_top';'R_cont_bot';'A_cont_top';'A_cont_bot';];
headings_list=cellstr(headings)';
xlswrite(xls_filename, headings_list,'Sheet1','A1:Q1');
headings=['m      ';'m      ';'N      ';'MPa    ';'C      ';'K/W    ';'m2K/W ';'W/mK   ';'K/W
';'m2K/W ';'W/mK   ';'MPa    ';'MPa    ';'K/W    ';'K/W    ';'m2     ';'m2     '];
headings_list=cellstr(headings)';
xlswrite(xls_filename, headings_list,'Sheet1','A2:Q2');

xlswrite(xls_filename, disp','Sheet1','A3');
xlswrite(xls_filename, WP_thickness','Sheet1','B3');
xlswrite(xls_filename, abs(SO_load_z'),'Sheet1','C3');
xlswrite(xls_filename, pressure','Sheet1','D3');
xlswrite(xls_filename, T_max_top_die','Sheet1','E3');

xlswrite(xls_filename, R_bulk','Sheet1','F3');
xlswrite(xls_filename, RA_bulk','Sheet1','G3');
xlswrite(xls_filename, k_bulk','Sheet1','H3');

xlswrite(xls_filename, R_eff','Sheet1','I3');
xlswrite(xls_filename, RA_eff','Sheet1','J3')
xlswrite(xls_filename, k_eff','Sheet1','K3');

xlswrite(xls_filename, P_avg_top','Sheet1','L3')
xlswrite(xls_filename, P_avg_bot','Sheet1','M3')

xlswrite(xls_filename, R_contact_top','Sheet1','N3') %K/W
xlswrite(xls_filename, R_contact_bot','Sheet1','O3') %K/W

xlswrite(xls_filename, A_contact_top','Sheet1','P3') %m2
xlswrite(xls_filename, A_contact_bot','Sheet1','Q3') %m2

sprintf('Done writing %s',xls_filename)


%% CLEANUP
fclose('all');
```

Appendix C

3D Surface Data Processing

The 3D surface data generated using MeX was imported into MATLAB for processing as described in Chapter 3. A listing of the MATLAB code used to accomplish this is presented here.

```
% Opens 3D surface data file from MeX
% Performs data smoothing routine
% Allows the User to crop a unit-cell to a given size from a centre point
% Squares off edges of unit-cell to assist in subsequent thickening and BCs
% Writes data to an STL surface file for importing to Form-Z

clear all
clc

%% INITIALIZE FILES
filename=('F3\-8,0,8_grid_4.txt') %ASCII Data file to import

file_FID=fopen(filename)
fseek(file_FID,0,'eof')
file_size=ftell(file_FID)
fseek(file_FID,0,'bof')

%% READ MeX 3D FILE
A=textscan(file_FID,'%s',2);
crap=A{:} %

A=textscan(file_FID,'%f',1); %
number_of_points=A{:} %

A=textscan(file_FID,'%s',2); %R
crap=A{:} %

h=waitbar(0,'Hold on, punk...');
tic

A=textscan(file_FID,'%f',3*number_of_points); %Reads in every coordinate
for i=1:number_of_points

    X(i)=A{1}(3*i-2)*1000; %convert to mm
    Y(i)=A{1}(3*i-1)*1000;
    Z(i)=A{1}(3*i)*1000;

    waitbar((i/number_of_points),h)
end
toc %

close(h);
save test_vars
sprintf('Done reading STL surface!')

% load test_vars

%% CONVERTING TO SURFACE MATRIX
clear
load test_vars
% plot3(X,Y,Z,'k.') %3D plot of orinal data

U_X=unique(X); %creates a vector of unique X-coordinates, mm
U_Y=unique(Y); %vector of unique Y-coordinates, mm
Z_index=1;     %Initializes the index for the Z-coordinates

for i=1:length(U_Y) %Converts the X,Y,Z coordinates to surface matrix in Z
    for j=1:length(U_X)
        Z_surface(i,j)=Z(Z_index);
        Z_index=Z_index+1;
    end
```

```
end

%% SMOOTHING/FILTERING ROUTINE
 F = [.05 .1 .05;
      .1 .4 .1;
      .05 .1 .05]; %Smoothing Matrix

temp_surf=Z_surface;
Z_surface_smoothed = conv2(temp_surf,F,'same');

surf(U_X,U_Y,Z_surface_smoothed)
 keyboard        %Allows the user to select centre point on plot

%% CROPPING OUT UNIT-CELL
unit_cell_size=1.0; %mm --define the unit cell size for cropping
% Using the data cursor, pick values for these two parameters:
% centre_x_pos=
% centre_y_pos=

%Define cropping lines
cut_min_x_pos=centre_x_pos - unit_cell_size/2; %mm
cut_max_x_pos=centre_x_pos + unit_cell_size/2;
cut_min_y_pos=centre_y_pos - unit_cell_size/2;
cut_max_y_pos=centre_y_pos + unit_cell_size/2;

%Initialize x & y indexes for the new cropped Z_surface
i_2=1;
j_2=1;
for i=1:length(U_Y)
    for j=1:length(U_X)

        if U_Y(i) <= cut_min_y_pos || U_Y(i) >= cut_max_y_pos
            i_list(i)=NaN;
        else
            i_list(i)=i;
        end

        if U_X(j) <= cut_min_x_pos || U_X(j) >= cut_max_x_pos
            j_list(j)=NaN;
        else
            j_list(j)=j;
        end
    end
end

Z_surface_cropped=Z_surface(min(i_list):max(i_list),min(j_list):max(j_list));
Z_surface_smoothed_cropped=Z_surface_smoothed(min(i_list):max(i_list),min(j_list):max(j_lis
t));

X_cropped=U_X(min(j_list):max(j_list));
Y_cropped=U_Y(min(i_list):max(i_list));
sprintf('Done cropping Unit Cell')

%% SQUARING OFF EDGES
Z_surface_squared_smoothed=Z_surface_smoothed_cropped;
for i=1:length(X_cropped) %loop that goes along X-direction
    Z_surface_squared_smoothed(1,i)=Z_surface_squared_smoothed(2,i);

Z_surface_squared_smoothed(length(Y_cropped),i)=Z_surface_squared_smoothed(length(Y_cropped
)-1,i);
end
for i=1:length(Y_cropped) %loop going in the Y-direction
    Z_surface_squared_smoothed(i,1)=Z_surface_squared_smoothed(i,2);

Z_surface_squared_smoothed(i,length(X_cropped))=Z_surface_squared_smoothed(i,length(X_cropp
ed)-1);

end
sprintf('Done Squaring-Off Edges')

%% PLOT FINISHED SURFACES

surf(X_cropped,Y_cropped,Z_surface_squared_smoothed)

%% OUTPUT DATA TO STL FILE
surf2stl('F3\mex_output.stl',X_cropped,Y_cropped,Z_surface_squared_smoothed)

%% CLEANUP
fclose('all');
```

Appendix D

Photographs of Experimental Apparatus



Fig. D.1: Experimental Apparatus

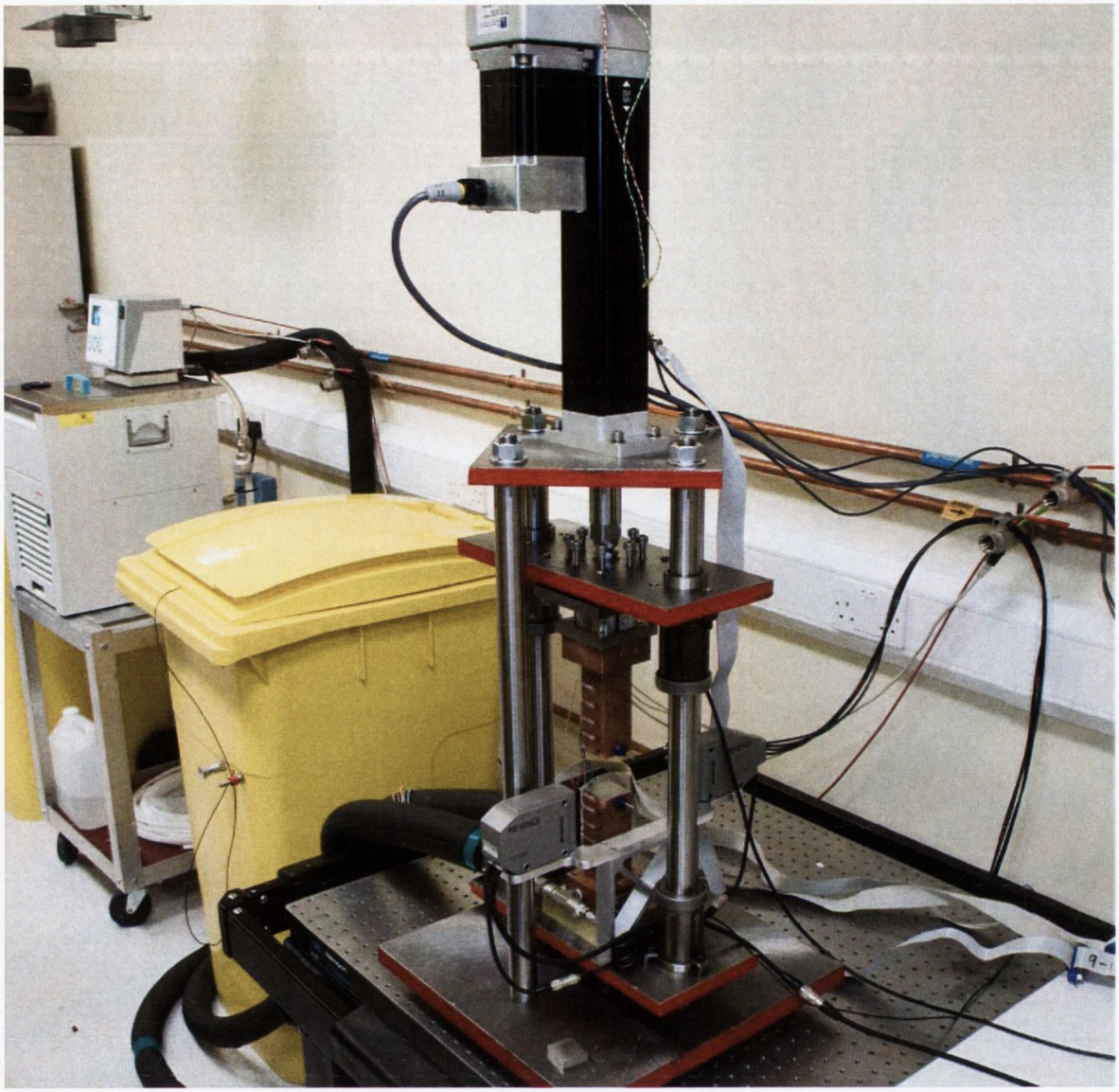


Fig. D.2: Experimental Apparatus

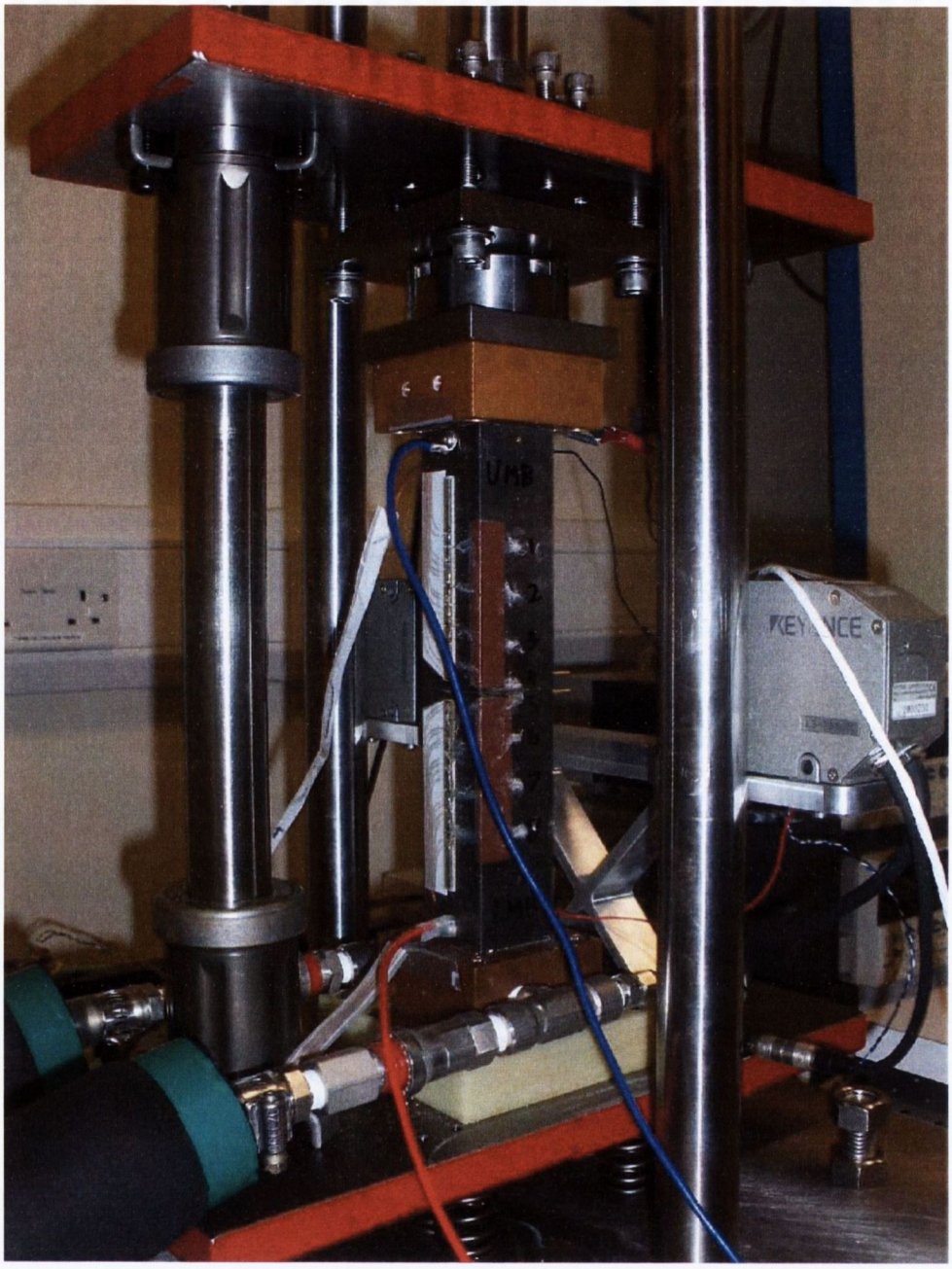


Fig. D.3: Close-up of Meter-Bars

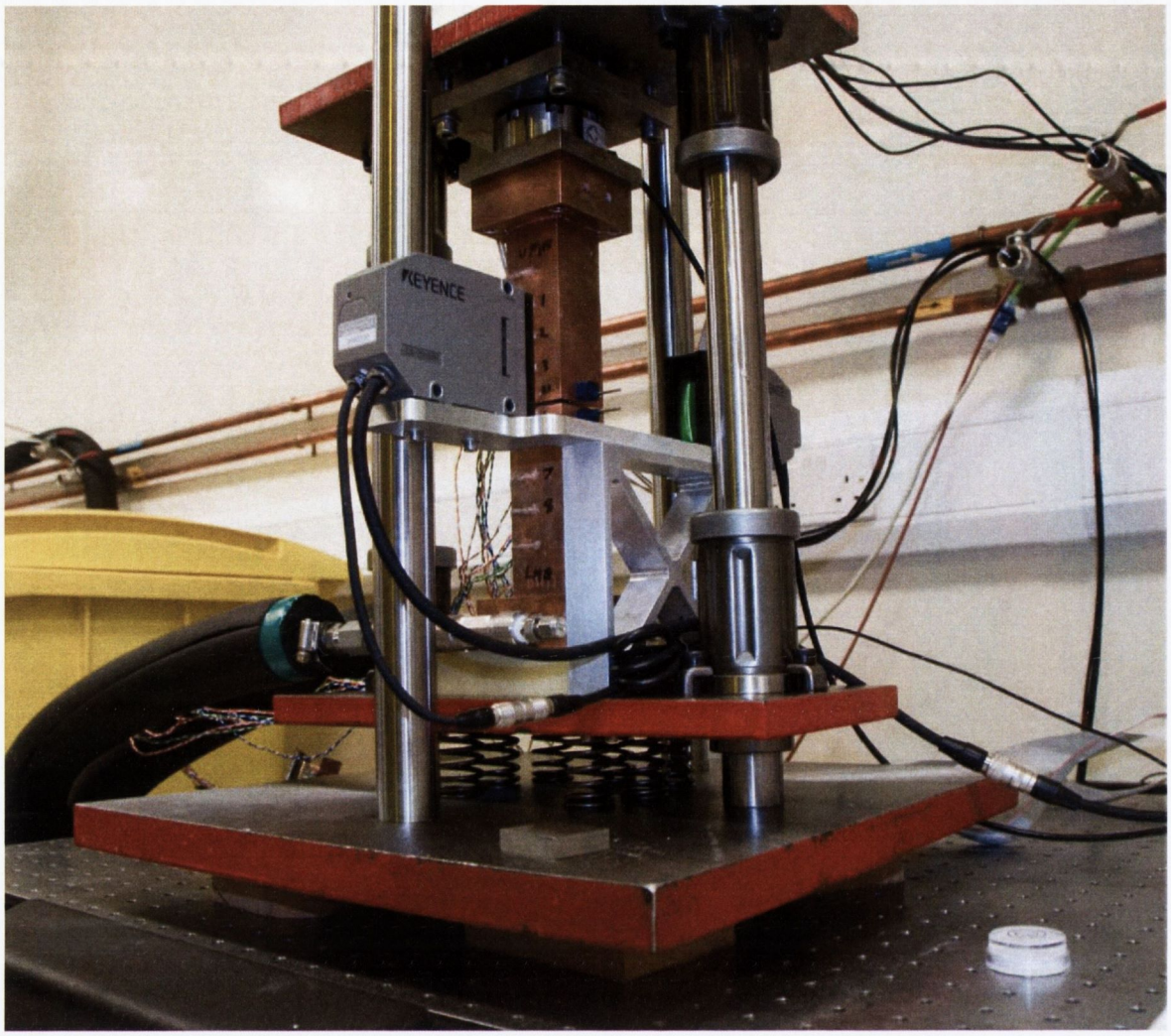


Fig. D.4: Die Set and Lower Platen



Fig. D.5: Meter-bars configured for calibration



Fig. D.6: Meter-bar calibration can

Appendix E

Experimental Apparatus Data Acquisition and Control Software

The MATLAB code used to acquire data from and control the experimental apparatus described in Chapter 4 is presented here.

```
%% TIM TEST RIG DATA AQUISITION - Version 13 ==============================
% Includes uncertainty analysis in the form of [Value Uncty]
% Ambient Temperature Monitoring
% Steady-State Check
% Auto-writes transient & steady-state data
% Auto-Actuator Control (force or displacement control)
% Electrical Contact Resistance Measurements using Keithley
% Global instrument variables for test restart
% Functional instrument reading
% ========================================================================

%% INITIALIZE INSTRUMENTS
f=1 %Use 0 for first time run, 1 for subsequent runs
if f==0
    clear all
    clc
    global actuator julabo keyence keithley2400 keithley2182 agilent6 agilent23 hp ls
agilent21
    f=1;
    tim_test_init_inst(f)
end
clear f
%% CuW METER BAR PARAMETERS & UNCERTAINTIES==============================
k_umb=[214 2]; %W/mK
k_lmb=[216 2]; %W/mK

A_mb=[1.6233e-3 9e-7]; %m2

thermistor_pos=[60.0162 39.7697 19.7144 2.7922 -2.8030 -19.7123 -39.6428 -59.7504]/1000; %m;
U_x=0.020/1000; %Thermistor Position Uncertainty in m

U_T=0.001; %Gloabal Temperature Uncertainty
T_sigma=U_T/2;  %Standard Deviation
T_var=T_sigma^2; %Sigma squared

%% MAIN PROGRAM ==========================================================

heater(4); %Desired Heater Power (W)
julabo_setpoint=chiller(23.00) % Set Chiller

%LINEAR ACTUATOR ADVANCEMENT LOOP
for j=6:20
    j
    %CLEARS UP VARIABLES BASED ON k FOR NEXT STEP
    clear T_axial U_T_axial T_amb power thickness force voltage current power
julabo_probe_temp  ecr ecr_V ecr_p
    clear umb_fit lmb_fit linear_T mb_fit_diff T_a T_b delta_T m_umb m_lmb Q_umb Q_lmb
Q_mean E_bal R RA k_eff P T_TIM
    clear umb_fit_2 lmb_fit_2 linear_T_2 mb_fit_diff_2 T_a_2 T_b_2 delta_T_2 m_umb_2
m_lmb_2 Q_umb_2 Q_lmb_2 Q_mean_2 E_bal_2 R_2 RA_2 k_eff_2 P T_TIM_2
    clear functions
    clf

    k=0;
    while(1) %WAITING FOR STEADY-STATE LOOP
        k=k+1
        for ls_chan=1:9    % LAKESHORE CHANNEL LOOP
```

```
            fprintf(ls, 'SCAN %d,0',ls_chan) %Change channel
            pause(5)     %Wait while LakeShore unit switches channels
            for i=1:10   %Scan Channel for so many seconds (Lakeshore settling time)
                tic
                fprintf(ls, 'RDGR? %d',ls_chan);    %Asks for resistance reading
                res(i,ls_chan)=str2num(fscanf(ls)); %Reads and converts resistance
                T(i,ls_chan)=T_fit_CuW(res(i,ls_chan),ls_chan); %Converts resistance to
Temp
                calc_time=toc;
                pause(1-calc_time)
            end
            T_axial(k,ls_chan)=T(i,ls_chan); %populates axial temperatures with last point
after scan
            U_T_axial(k,ls_chan)=U_T; %Uncertainty set as global temp. uncty
        end
        % OVER TEMPERATURE CHECK=========================
        if T_axial(k,:)>35 %Check for over-temperature
            fprintf(hp, 'VOLT 0')  %Turns heater off if too hot
        end

        %AMBIENT TEMPERATURE MEASUREMENT================
        T_amb(k,1)=T_axial(k,9);
        T_amb(k,2)=U_T;

        %ELECTRICAL CONTACT RESISTANCE==========================
%         ecr(k,1:2)=get_ecr();
                ecr(k,1:2)=NaN;

        %FORCE MEASUREMENT======================================
        force(k,1:2)=get_force();

        %THICKNESS MEASUREMENT==================================
        thickness(k,1:2)=get_thickness();

        %HEATER POWER===========================================
        voltage(1,1:2)=get_voltage(agilent23);
        current(1,1:2)=get_current(agilent6);
        power(k,1)=voltage(1,1)*current(1,1);
        power(k,2)=sqrt(voltage(1,1)^2*current(1,2)^2 + current(1,1)^2*voltage(1,2)^2);
%Calculates Power Uncertainty

        %CHILLER DATA ==========================================
        fprintf(julabo, 'in_pv_02','async'); %Asks for temperature of external probe
        pause(.25);
        julabo_probe_temp(k,1)=str2double(fscanf(julabo,'async')); %gets & converts
external probe temp

        %CALCULATIONS ==========================================
        %Calculate linear fit coeffeicients
        umb_fit(k,1:2)=polyfit(thermistor_pos(1:4),T_axial(k,1:4),1);
        lmb_fit(k,1:2)=polyfit(thermistor_pos(5:8),T_axial(k,5:8),1);
        %Uncertainty in fit coefficients
        for r=1:2000
            MC_umb_fit(r,1:2)=polyfit(random('unif',thermistor_pos(1:4)-
U_x,thermistor_pos(1:4)+U_x), random('norm',T_axial(1:4),T_sigma),1);
            MC_lmb_fit(r,1:2)=polyfit(random('unif',thermistor_pos(5:8)-
U_x,thermistor_pos(5:8)+U_x), random('norm',T_axial(5:8),T_sigma),1);
        end
        %Linear predictions of T
        linear_T(k,1:4)=thermistor_pos(1:4)*umb_fit(k,1) + umb_fit(k,2);
        linear_T(k,5:8)=thermistor_pos(5:8)*lmb_fit(k,1) + lmb_fit(k,2);
        %Calculate residuals
        mb_fit_diff(k,1:8)=T_axial(k,1:8)-linear_T(k,1:8);

        T_a(k,1)=umb_fit(k,2);  %UMB Surface Temperature based on fit y-intercept
        T_a(k,2)= 2*std(MC_umb_fit(:,2)); %based on 2 standard deviations

        T_b(k,2)= 2*std(MC_lmb_fit(:,2));
        T_b(k,1)=lmb_fit(k,2);  %LMB Surface Temperature

        delta_T(k,1)=T_a(k)-T_b(k);
        delta_T(k,2)=sqrt(T_a(k,2)^2 + T_b(k,2)^2);

        m_umb(k,1)=abs(umb_fit(k,1)); %(K/m)
        m_umb(k,2)= 2*std(MC_umb_fit(:,1)); %2 std dev based on MC simulation

        m_lmb(k,1)=abs(lmb_fit(k,1)); %(K/m)
        m_lmb(k,2)= 2*std(MC_lmb_fit(:,1)); %2 std dev based on MC simulation

        Q_umb(k,1)=m_umb(k,1)*A_mb(1,1)*k_umb(1,1); %UMB heat flux based on slope of fit
```

```
        Q_umb(k,2)= sqrt( (k_umb(1,1)*A_mb(1,1))^2*m_umb(k,2)^2 +
(m_umb(k,1)*A_mb(1,1))^2*k_umb(1,2)^2 + (m_umb(k,1)*k_umb(1,1))^2*A_mb(1,2)^2);

        Q_lmb(k,1)=m_lmb(k,1)*A_mb(1,1)*k_lmb(1,1); %LMB heat flux based on slope of fit
        Q_lmb(k,2)= sqrt( (k_lmb(1,1)*A_mb(1,1))^2*m_lmb(k,2)^2 +
(m_lmb(k,1)*A_mb(1,1))^2*k_lmb(1,2)^2 + (m_lmb(k,1)*k_lmb(1,1))^2*A_mb(1,2)^2);

        Q_mean(k,1)=(Q_umb(k) + Q_lmb(k))/2;
        Q_mean(k,2)=sqrt( (1/2)^2*Q_umb(k,2)^2 + (1/2)^2*Q_lmb(k,2)^2 );

        E_bal(k,1)=100-100*(Q_umb(k,1)-Q_lmb(k,1))/Q_mean(k,1);
        E_bal(k,2)= sqrt((100/Q_mean(k,1))^2*Q_umb(k,2)^2 + (-
100/Q_mean(k,1))^2*Q_lmb(k,2)^2 + (-100*(Q_umb(k,1)-
Q_lmb(k,1))/Q_mean(k,1)^2)^2*Q_mean(k,2)^2);

        R(k,1)=delta_T(k,1)/Q_mean(k,1); %K/W
        R(k,2)=sqrt( (1/Q_mean(k,1))^2*delta_T(k,2)^2 + ((-
delta_T(k))/(Q_mean(k,1))^2)^2*Q_mean(k,2)^2 );

        RA(k,1)=R(k,1)*A_mb(1,1); %m2K/W
        RA(k,2)= sqrt( A_mb(1,1)^2*R(k,2)^2 + R(k,1)^2*A_mb(1,2)^2);

        k_eff(k,1)=thickness(k,1)/(A_mb(1,1)*R(k,1));  %W/mK
        k_eff(k,2)= sqrt((1/(A_mb(1,1)*R(k,1)))^2*thickness(k,2)^2 + (-
thickness(k,1)/(A_mb(1,1)^2*R(k,1)))^2*A_mb(1,2)^2 + (-
thickness(k,1)/(A_mb(1,1)*R(k,1)^2))^2*R(k,2)^2);

        P(k,1)=(force(k,1)/A_mb(1,1))/1e6; %Pressure in MPa
        P(k,2)= (sqrt((1/A_mb(1,1))^2*force(k,2)^2 + (-
force(k,1)/A_mb(1,1)^2)^2*A_mb(1,2)^2))/1e6; %Pressure Uncertainty in MPa

        T_TIM(k,1)=(T_a(k,1)+T_b(k,1))/2;
        T_TIM(k,2)= sqrt( (1/2)^2*T_a(k,2)^2 + (1/2)^2*T_b(k,2)^2);

        %PLOTS ================================================
        subplot(2,2,1)
        errorbar(thermistor_pos(1:8),T_axial(k,1:8),U_T_axial(k,1:8),'k.')
        if k > 1
            hold on
            errorbar(thermistor_pos(1:8),T_axial(k-1,1:8),U_T_axial(k-1,1:8),'b.')
            if k > 2
                errorbar(thermistor_pos(1:8),T_axial(k-2,1:8),U_T_axial(k-2,1:8),'c.')
            end
        end
        hold on
        plot(thermistor_pos(1:8),linspace(T_amb(k),T_amb(k),8),'g-')
        xlabel('Thermistor Position (mm)');
        ylabel('Ambient Temp. (oC)');
        title(sprintf('j=%d, k=%d, Tamb=%2.3f',j,k,T_amb(k)))
        hold off

        subplot(4,4,3)
        errorbar(thermistor_pos(1:8),mb_fit_diff(k,1:8),U_T_axial(k,1:8),'.')
        xlabel('Thermistor Position (mm)');
        ylabel('Deviation form Linear Fit (oC)');
        hold off

        subplot(4,4,8)
        errorbar(k,T_amb(k,1),T_amb(k,2),'m.')
        xlabel('Iteration')
        ylabel('Temperature (oC)')
        hold on


        subplot(4,4,9)
        errorbar(k,force(k,1),force(k,2),'k.')
        xlabel('Iteration')
        ylabel('Force (N)')
        hold on

        subplot(4,4,10)
        errorbar(k,Q_umb(k,1),Q_umb(k,2),'r^')
        hold on
        errorbar(k,Q_lmb(k,1),Q_lmb(k,2),'b.')
        xlabel('Iteration')
        ylabel('Q (W)')
        title(sprintf('%2.2f +/- %2.2f',Q_mean(k,1),Q_mean(k,2)))

        subplot(4,4,11)
        errorbar(k,ecr(k,1),ecr(k,2),'c.')
```

```
        xlabel('Iteration')
        ylabel('ECR (Ohms)')
        hold on
        title(sprintf('%2.3d +/- %2.3d',ecr(k,1),ecr(k,2)))

        subplot(4,4,12)
        errorbar(k,E_bal(k,1),E_bal(k,2),'b.')
        hold on
        xlabel('Iteration')
        ylabel('Energy Balance (%)')
        title(sprintf('%3.2f +/- %1.2f',E_bal(k,1),E_bal(k,2)))

        subplot(4,4,13)
        errorbar(k,thickness(k,1)*1e6,thickness(k,2)*1e6,'g*') %Plots in um
        xlabel('Iteration')
        ylabel('Thickness (um)')
        hold on

        subplot(4,4,14)
        errorbar(k,delta_T(k,1),delta_T(k,2),'b.')
        hold on
        xlabel('Iteration')
        ylabel('delta_T (K)')

        subplot(4,4,15)
        errorbar(k,RA(k,1),RA(k,2),'b.')
        hold on
        xlabel('Iteration')
        ylabel('RA (m^2K/W)')

        subplot(4,4,16)
        errorbar(k,k_eff(k,1),k_eff(k,2),'b.')
        hold on
        xlabel('Iteration')
        ylabel('k_eff (W/mK)')

        %CHECK FOR STEADY-STATE=========================================
        steady=tim_test_steady(k,julabo_probe_temp,julabo_setpoint,E_bal,RA,ecr)
        if sum(steady)==5

write_tim_test_data(j,k,T_axial,T_amb,power,thickness,force,julabo_probe_temp,T_a,T_b,delta
_T,Q_umb,Q_lmb,Q_mean,E_bal,R,RA,k_eff,P,mb_fit_diff,ecr)
            break
        end
        pause(0.05)
        clear functions %resets functions for dynamic editing during testing
    end  %END OF STEADY STEAT LOOP

    %INCREMENT LINEAR ACTUATOR ======================================

    %Over Force Check
        check_force(1,1:2)=get_force();
        if check_force(1,1)>4600
            sprintf('Force Limit Reached - actuator not incremented')
            check_force
        else
            %Typically 0.1 mm for thick soft TIMs (no springs), 0.5 for hard TIMS(with
springs)
            %inc_act(0.02,.1) %0.02 gives you about 0.008 mm of disp

            inc_act(0.05,.01) %was 0.04 for B3
            %0.02,.01 for silver tubes
        end
%      step_force(j)
end

sprintf('TIM Test Done')
```

```
function z=tim_test_init_inst(f)
global actuator julabo keyence keithley2400 keithley2182 agilent6 agilent23 hp ls agilent21

%% SERIAL INSTRUMENT INITIALIZATION ===================

%ACTUATOR ================================================
actuator = instrfind('Type', 'serial', 'Port', 'COM6', 'Tag', '','BaudRate', 9600,
'Parity','None','FlowControl','software','DataBits',8,'StopBits',1,'Terminator','CR');
if isempty(actuator)
    actuator = serial('COM6','BaudRate', 9600,
'Parity','None','FlowControl','software','DataBits',8,'StopBits',1,'Terminator','CR');
else
    fclose(actuator);
    actuator = actuator(1);
end
fopen(actuator)

%CHILLER==================================================
julabo = instrfind('Type', 'serial', 'Port', 'COM4', 'Tag', '','BaudRate', 4800,
'Parity','Even','FlowControl','hardware','DataBits',7,'StopBits',1,'Terminator','CR');
if isempty(julabo)
    julabo = serial('COM4','BaudRate', 4800,
'Parity','Even','FlowControl','hardware','DataBits',7,'StopBits',1,'Terminator','CR');
else
    fclose(julabo);
    julabo = julabo(1);
end
fopen(julabo)

%KEYENCE==================================================
keyence = instrfind('Type', 'serial', 'Port', 'COM5', 'Tag', '','BaudRate', 9600,
'Parity','None','FlowControl','none','DataBits',8,'StopBits',1,'Terminator','CR');
if isempty(keyence)
    keyence = serial('COM5','BaudRate', 9600,
'Parity','None','FlowControl','none','DataBits',8,'StopBits',1,'Terminator','CR');
else
    fclose(keyence);
    keyence = keyence(1);
end
fopen(keyence)
keyence_zero=0; %mm
%% GPIB INSTRUMENT INITIALIZATION ===================

%KEITHLEY 2400 SOURCEMETER=============================================
keithley2400 = instrfind('Type', 'gpib', 'BoardIndex', 0, 'PrimaryAddress', 24, 'Tag', '');
if isempty(keithley2400)
    keithley2400 = gpib('ni', 0, 24);
else
    fclose(keithley2400);
    keithley2400 = keithley2400(1);
end
fopen(keithley2400);
idn_24 = query(keithley2400, '*IDN?')

%KEITHLEY 2182A NANOVOLTMETER=========================================
keithley2182 = instrfind('Type', 'gpib', 'BoardIndex', 0, 'PrimaryAddress', 25, 'Tag', '');
if isempty(keithley2182)
    keithley2182 = gpib('ni', 0, 25);
else
    fclose(keithley2182);
    keithley2182 = keithley2182(1);
end
fopen(keithley2182);
idn_25 = query(keithley2182, '*IDN?')

%% ECR INSTRUMENT CONFIGURATION ============================================
fprintf(keithley2400, '*RST')
%Arm-Layer
fprintf(keithley2400, ':ARM:SEQ:LAY:SOUR IMM') % Immediate
fprintf(keithley2400, ':ARM:SEQ:LAY:TCON:ASYN:OLIN 3')
fprintf(keithley2400, ':ARM:SEQ:LAY:TCON:ASYN:OUTP NONE')
fprintf(keithley2400, ':ARM:SEQ:LAY:COUN INF')
%Trig-Layer
fprintf(keithley2400, ':TRIG:SEQ:SOUR TLIN')
fprintf(keithley2400, ':TRIG:SEQ:TCON:ASYN:ILIN 1')
fprintf(keithley2400, ':TRIG:SEQ:TCON:DIR ACC')
fprintf(keithley2400, ':TRIG:SEQ:TCON:ASYN:INP SOUR')
fprintf(keithley2400, ':TRIG:SEQ:TCON:ASYN:OLIN 2')
fprintf(keithley2400, ':TRIG:SEQ:TCON:ASYN:OUTP SOUR')
%Delay & Trigger Count
```

```
fprintf(keithley2400, ':TRIG:SEQ:DEL 0')
fprintf(keithley2400, ':TRIG:SEQ:COUN 2')
%Source Current, Measure Voltage
fprintf(keithley2400, ':SOUR:FUNC:MODE CURR')
fprintf(keithley2400, ':SOUR:CURR:LEV:IMM:AMPL 1')
fprintf(keithley2400, ':SENS:FUNC:ON "VOLT:DC"')
%Configure 2-Point Sweep
fprintf(keithley2400, ':SOUR:SWE:POIN 2')
fprintf(keithley2400, ':SOUR:LIST:CURR .1, -.1')
%Custom Sweep
fprintf(keithley2400, ':SYST:KEY 28') %Config
fprintf(keithley2400, ':SYST:KEY 27') %Sweep
fprintf(keithley2400, ':SYST:KEY 18') %Enter
fprintf(keithley2400, ':SYST:KEY 10') %Right
fprintf(keithley2400, ':SYST:KEY 10') %Right
fprintf(keithley2400, ':SYST:KEY 18') %Enter
fprintf(keithley2400, ':SYST:KEY 11') %Exit
fprintf(keithley2400, ':SYST:KEY 11') %Exit
fprintf(keithley2400, ':SYST:KEY 11') %Exit
%Infinite Sweep Count
fprintf(keithley2400, ':SYST:KEY 28') %Config
fprintf(keithley2400, ':SYST:KEY 27') %Sweep
fprintf(keithley2400, ':SYST:KEY 10') %Right
fprintf(keithley2400, ':SYST:KEY 18') %Enter
fprintf(keithley2400, ':SYST:KEY 10') %Right
fprintf(keithley2400, ':SYST:KEY 18') %Enter
fprintf(keithley2400, ':SYST:KEY 11') %Exit

%NanoVoltmeter
fprintf(keithley2182, ':SENS:VOLT:DELTA ON') %Enable Delta Measurement
fprintf(keithley2182, ':SENS:VOLT:NPLC 5')
fprintf(keithley2182, ':TRIG:SOUR EXT')

%AGILENT AMMETER ==========================================
agilent6 = instrfind('Type', 'gpib', 'BoardIndex', 0, 'PrimaryAddress', 6, 'Tag', '');
if isempty(agilent6)
    agilent6 = gpib('ni', 0, 6);
else
    fclose(agilent6);
    agilent6 = agilent6(1);
end
fopen(agilent6);
IDN_6 = query(agilent6, '*IDN?')
fprintf(agilent6, 'CONF:CURR:DC')
%AGILENT VOLTMETER ==========================================
agilent23 = instrfind('Type', 'gpib', 'BoardIndex', 0, 'PrimaryAddress', 23, 'Tag', '');
if isempty(agilent23)
    agilent23 = gpib('ni', 0, 23);
else
    fclose(agilent23);
    agilent23 = agilent23(1);
end
fopen(agilent23);
IDN_23 = query(agilent23, '*IDN?')
fprintf(agilent23, 'CONF:VOLT:DC')

%HP 6655A SUPPLY ==========================================================
hp = instrfind('Type', 'gpib', 'BoardIndex', 0, 'PrimaryAddress', 8, 'Tag', '');
if isempty(hp)
    hp = gpib('ni', 0, 8);
else
    fclose(hp);
    hp = hp(1);
end
fopen(hp);
IDN_8 = query(hp, '*IDN?')
fprintf(hp, '*RST')     %Resets power suppply
fprintf(hp, 'CURR 3')   %Set maximum current
% fprintf(hp, 'VOLT 0')   %Sets power supply Voltage
fprintf(hp, 'OUTP ON')  %Turns power supply output on

%LAKESHORE=================================================================
ls = instrfind('Type', 'gpib', 'BoardIndex', 0, 'PrimaryAddress', 12, 'Tag', '');
if isempty(ls)
    ls = gpib('ni', 0, 12);
else
    fclose(ls);
    ls = ls(1);
end
fopen(ls);
```

```
IDN_12 = query(ls, '*IDN?')

%LOAD CELL VOLTMETER=====================================================
agilent21 = instrfind('Type', 'gpib', 'BoardIndex', 0, 'PrimaryAddress', 21, 'Tag', '');
if isempty(agilent21)
    agilent21 = gpib('ni', 0, 21);
else
    fclose(agilent21);
    agilent21 = agilent21(1);
end
fopen(agilent21);
IDN_21 = query(agilent21, '*IDN?')
fprintf(agilent21, 'CONF:VOLT:DC')  %Configures for voltage measurement


function z=heater(set_power)
global hp
set_voltage=11.011766*set_power^0.49665068 %Correlation for V
fprintf(hp, 'VOLT %2.2f',set_voltage)  %Sets power supply Voltage



function z=chiller(julabo_setpoint)
global julabo

if julabo_setpoint=='off'
    fprintf(julabo, 'out_mode_05 0','async')    %Turns chiler OFF
    pause(.25)
else
    fprintf(julabo, 'out_mode_05 1','async')    %Turns chiler ON
    pause(.25)
    fprintf(julabo, 'out_sp_00 %2.2f',julabo_setpoint,'async'); %sets the working
temperature
    pause(.25);
    fprintf(julabo, 'out_mode_01 0','async');   %Tells it to use the working temperature
    pause(.25)
end
z=julabo_setpoint; %Returns the requested setpoint
```

```
%Fucntion that converts resistances to temperatures
%Calibrated for CuW meter bars Dec 9, 2008
% RANGE: 15 to 40 deg C
%Specific to CuW metre bars attached to Lakeshore Channels as below

function z=T_fit_CuW(res,ls_chan)

if ls_chan==1
    A=0.00063448137580653300;
    B=0.00026797666398330400;
    C=-0.00000139024110072178;
    D=0.00000016899862416478;

elseif ls_chan==2
    A=0.00068209345003841500;
    B=0.00025158031598608800;
    C=0.00000038583501696726;
    D=0.00000010090664664929;

elseif ls_chan==3
    A=0.00074847934158771700;
    B=0.00023353556327946700;
    C=0.00000219413810376820;
    D=0.00000004842817353129;

elseif ls_chan==4
    A=0.00074285231076724700;
    B=0.00023656120049330300;
    C=0.00000185924286167027;
    D=0.00000005871733512533;

elseif ls_chan==5
    A=0.00073184218543223200;
    B=0.00024460329745779200;
    C=0.00000126070614262459;
    D=0.00000007186618012963;

elseif ls_chan==6
    A=0.00076560021332358600;
    B=0.00023498269822922100;
    C=0.00000209494103775058;
    D=0.00000004742837537651;

elseif ls_chan==7
    A=0.00075021978809439600;
    B=0.00023204426105432700;
    C=0.00000236971087702499;
    D=0.00000004138208892914;

elseif ls_chan==8
    A=0.00075075030329998400;
    B=0.00024861503744466200;
    C=0.00000064879691925385;
    D=0.00000010119008195208;

elseif ls_chan==9  % Ambient or Auxillary Probe
    A=0.00108928147334943000;
    B=0.00025731849423261300;
    C=-0.00000179626600677407;
    D=0.00000013296372185648;

elseif ls_chan==10
    A=0.00110019477752888000;
    B=0.00025140264995002800;
    C=-0.00000131283200187570;
    D=0.00000011909556838675;

elseif ls_chan==11
    A=0.00107819918416073000;
    B=0.00025939388239333500;
    C=-0.00000220110333099759;
    D=0.00000015163697844447;

end
z=(A+B*log(res)+C*log(res)^2+D*log(res)^3)^-1 - 273.15;



function z=get_ecr()
```

```
global keithley2182

% ELECTRICAL CONTACT RESISTANCE SETTINGS=======

ecr_I(1,1)=0.100; %Set this to the source current (A)

if ecr_I(1,1)<=1e-6
    ecr_I(1,2)=.00035*ecr_I(1,1) + 600e-12; %1 uA Range

elseif ecr_I(1,1)<=10e-6 && ecr_I(1,1)>1e-6
    ecr_I(1,2)=.00033*ecr_I(1,1) + 2e-9; %10 uA Range

elseif ecr_I(1,1)<=100e-6 && ecr_I(1,1)>10e-6
    ecr_I(1,2)=.00031*ecr_I(1,1) + 20e-9; %100 uA Range

elseif ecr_I(1,1)<=1e-3 && ecr_I(1,1)>100e-6
    ecr_I(1,2)=.00034*ecr_I(1,1) + 200e-9; %1 mA Range

elseif ecr_I(1,1)<=10e-3 && ecr_I(1,1)>1e-3
    ecr_I(1,2)=.00045*ecr_I(1,1) + 2e-6; %10 mA Range

elseif ecr_I(1,1)<=100e-3 && ecr_I(1,1)>10e-3
    ecr_I(1,2)=.00066*ecr_I(1,1) + 20e-6; %100 mA Range

elseif ecr_I(1,1)<=1 && ecr_I(1,1)>100e-3
    ecr_I(1,2)=.0027*ecr_I(1,1) + 900e-6; %1 A Range

else
    ecr_I(1,2)=NaN;
end

%TAKE VOLTAGE MEASUREMENT=========================
ecr_V(1,1)=str2num(query(keithley2182, ':FETC?'));
ecr_V(1,2)=(50/1e6)*ecr_V(1,1) + (4/1e6)*10e-3; % 10mV range - 1Year Calibration

%CALCULATE RESISTANCE===========
ecr(1,1)=abs(ecr_V(1,1))/ecr_I(1,1);
ecr(1,2)=sqrt( (1/ecr_I(1,1))^2*ecr_V(1,2)^2 + (-ecr_V(1,1)/ecr_I(1,1)^2)^2*ecr_I(1,2)^2 );

ecr_p(1,1)=ecr_I(1,1)^2*ecr(1,1);
%RESISTANCE HEATING CHECK================
if ecr_p(1,1)>.01 %If it is more than 0.01 W
    sprintf('ATTENTION!! Resistance Heating = %d',ecr_p(1,1))
end
z=ecr;


function z=get_force()
global agilent21

% LOAD CELL PARAMETERS=================================================
lc_rated_load=5000;     %rated load in Newtons (N)
lc_sens=2;              %sensitivity (mv/V)
lc_excite_voltage=19.86;   %applied excitation voltage
lc_rated_load_voltage=(lc_excite_voltage*lc_sens)/1000;  %unamplified output voltage at
rated load
lc_slope=lc_rated_load_voltage/lc_rated_load;     %constant for converting voltage to force
lc_accuracy=0.2;         %percent of rated load
lc_offset=86.0; %Newtons

%Take Measurement
force_voltage(1,1:2)=get_voltage(agilent21); %requests voltage & uncertainty
force(1,1)=force_voltage(1,1)/lc_slope -lc_offset;%Force in Newtons
force(1,2)=lc_accuracy*lc_rated_load/100; %Uncertainty of force measurement (N)
z=force;


function z=get_thickness()
global keyence

U_t=0.0010/1000; %Thickness uncertainty in m

fprintf(keyence, 'M1,0','async');
keyence_output=fscanf(keyence,'async');
thickness(1,1)=(str2num(keyence_output(4:12)))/1000; %thickness in m
thickness(1,2)=U_t;   %Thickness uncertainty
z=thickness;


function z=get_voltage(device)
```

```
voltage=str2num(query(device, 'READ?'));
if voltage <= 100e-3 %Voltage Uncertainty calcs from Agilent specs
    U_v=(0.00005*voltage + 0.000035*100e-3);
elseif voltage >100e-3 & voltage <=1
    U_v=(0.00004*voltage + 0.000007*1);
elseif voltage >1 & voltage <=10
    U_v=(0.000035*voltage + 0.000005*10);
elseif voltage >10 & voltage <=100
    U_v=(0.000045*voltage + 0.000006*100);
else
    U_v=(0.000045*voltage + 0.00001*1000);
end
z=[voltage, U_v];


function z=get_current(device)
current=str2num(query(device, 'READ?'));
if current <= 10e-3  %Current Uncertainty calcs from Agilent specs
    U_c=(0.0005*current + 0.0002*10e-3);
elseif current >10e-3 & current <= 100e-3
    U_c=(0.0005*current + 0.00005*100e-3);
elseif current >100e-3 & current <= 1
    U_c=(0.001*current + 0.0001*1);
else
    U_c=(0.0012*current + 0.0002*3);
end
z=[current, U_c];


function z=inc_act(inc,vel)
global actuator
sprintf('Incrementing Actuator %f mm at %f mm/s',inc,vel)
%Sets Acceleration and Velocity
av=sprintf('AC0.3 VE%f',vel);
fprintf(actuator, av,'async');
pause(0.30);
%Increments Actuator
s=sprintf('DI%f GO',inc);
fprintf(actuator, s,'async');

wait_time=abs(inc/vel);
if wait_time>=0.3 %was 0.25
    pause(wait_time);
else
    pause(0.30); %was 0.25
end
z=wait_time; %Returns wait time


function
z=write_tim_test_data(j,k,T_axial,T_amb,power,thickness,force,julabo_probe_temp,T_a,T_b,del
ta_T,Q_umb,Q_lmb,Q_mean,E_bal,R,RA,k_eff,P,mb_fit_diff,ecr)
%XLS Filenames
transient_xls_file=(['transient_data\MMT-TIM Test - T-Flex 780 - Transient -
',datestr(now,30)]);
steady_xls_file=(['MMT-TIM Test - T-Flex 780 - ',datestr(now,29)]);
%XLS Header

%Creating Output Matrix
transient_output_matrix=[(1:k)', T_axial(:,1:8), T_amb(:,1), power, thickness, force,
julabo_probe_temp, T_a, T_b, delta_T, Q_umb, Q_lmb, Q_mean, E_bal, R, RA, k_eff, P, ecr,
mb_fit_diff];
steady_output_matrix=[j, T_axial(k,1:8), T_amb(k,1),
power(k,:),thickness(k,:),force(k,:),julabo_probe_temp(k,1),T_a(k,:),T_b(k,:),delta_T(k,:),
Q_umb(k,:),Q_lmb(k,:),Q_mean(k,:),E_bal(k,:),R(k,:),RA(k,:),k_eff(k,:),P(k,:),ecr(k,:),mb_f
it_diff(k,:)];

%Write Files
row=j+2; %start on third row
xlswrite(transient_xls_file,transient_output_matrix,'Sheet1','A3');
sprintf('Finsihed writing %s',transient_xls_file)
xlswrite(steady_xls_file,steady_output_matrix,'Sheet1',sprintf('A%d', row));
sprintf('Finsihed writing %s',steady_xls_file)
```

Appendix F

Additional MMT-TIM Experimental Results

A description of the specimens tested for the present study is presented in Fig. F.2. Here, the sample name and approximate nominal geometries are shown. Due to resolution limitations of the wax 3D printer, this "idealized" geometry is rarely realized as indicated by the accompanying SEM image of the subsequently plated structures. The dimensions listed correspond to the measured dimensions of the final structures, corresponding to Fig. F.1. Here, approximate values of diameter and pitch were measured using the SEM image and found to correspond well to the designed geometry. Initial feature height was measured using the experimental apparatus outlined previously. Foil thickness was relatively difficult to control due to the plating process with which the metal was deposited. However, having once obtained the outer dimensions, the approximate thickness was estimated by measuring the mass of the sample. The volume of each unit-cell could then be obtained by using the density of silver in conjunction with the representative 3D CAD model. For the present study, feature "B" in Fig. F.2 served as the base-line case for which to make comparisons to other geometries.

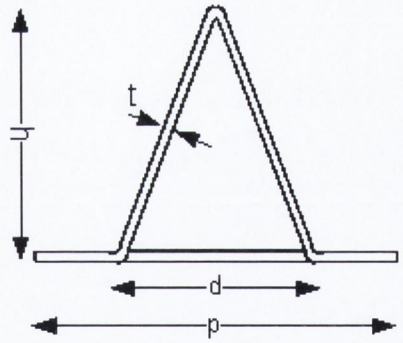


Fig. F.1: Cross-section of hollow conical MMT-TIM geometry

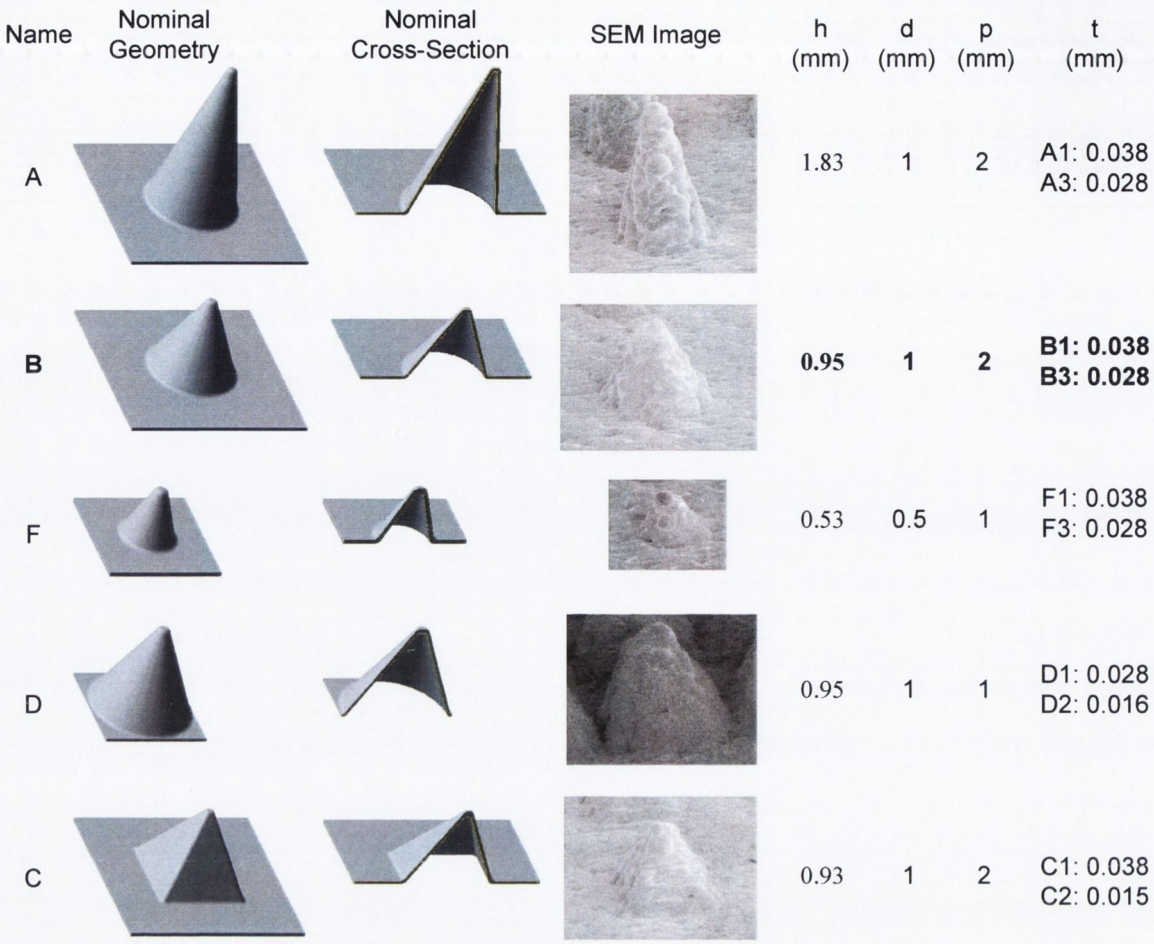


Fig. F.2: Nominal feature geometries and measured dimensions of MMT-TIMs

Effects of Feature Height & Feature Size

The effect of feature height for two metal thicknesses was compared between the nominal case of feature "B" and for a conical structure of similar diameter and approximately twice the height, designated as feature "A" in Fig. F.2. The pressure required to deform these structures is plotted as a function of strain in Fig. F.3. Here, all features exhibit a similar trend: the pressure increases somewhat linearly until approximately 20% strain. Next there is a region of moderate plateau until the structures begin to densify and the pressure rises steeply between 70 and 80% strain. Overall, the thicker metal foil requires a correspondingly larger pressure to deform to a given strain for both feature heights. The trends and magnitudes for the taller structure (feature "A") correspond well to that of a similar geometry investigated in Chapter 3. The taller feature (A) offers greater compliance than "B" as the pressure required to achieve a certain stain (in the 20-70% strain range) is approximately 20-25% lower.

The effect of overall feature size was also compared between the nominal case of feature "B" and for a conical structure half the diameter and approximately half the height, designated as feature "F" from Fig. F.2. From a mechanical standpoint, the trend in

compressive pressure for both thicknesses of the half-sized MMT-TIM is extremely steep, requiring significantly more force to be deformed to a given strain than sample "B". This can be attributed to two reasons: First, ratio of pitch to diameter for both features is the same, resulting in the MMT-TIM array of sample "F" having four times as many features as sample "B". Secondly, while the outer dimensions of sample "F" are approximately 50% of "B", the metal plating thickness remains the same, thereby resulting in an overall stiffer structure.

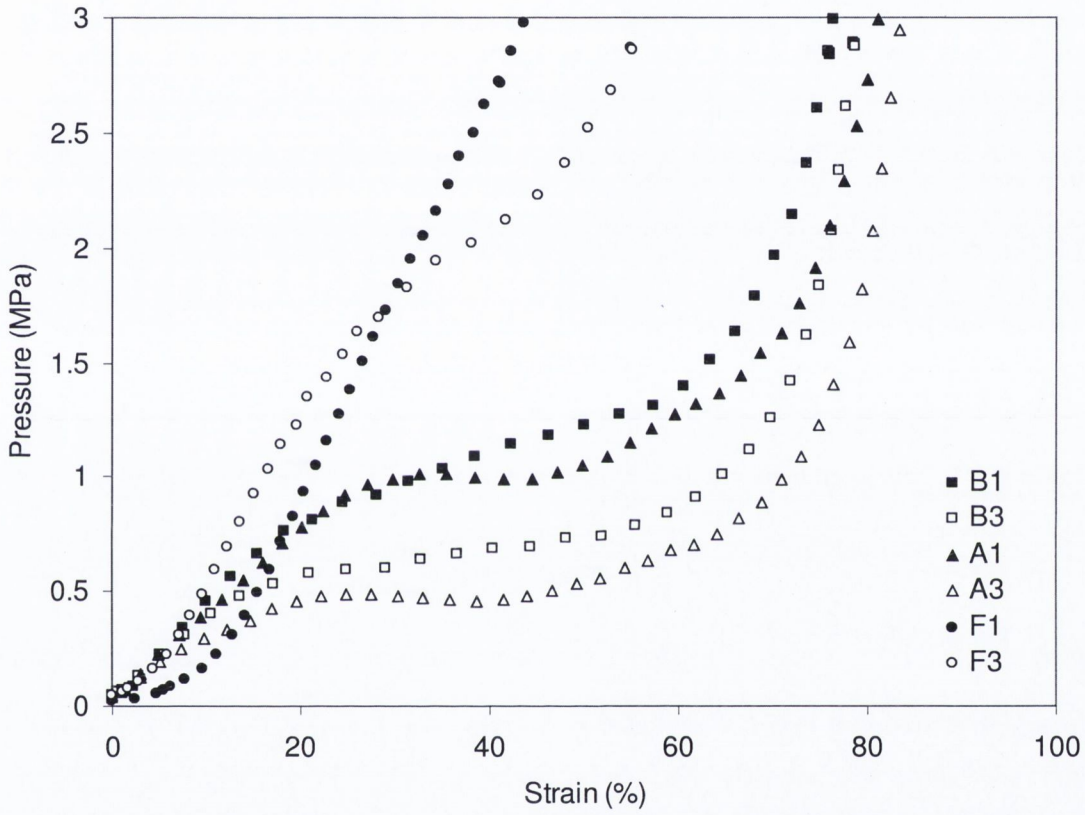


Fig. F.3: Variation of compressive pressure with strain for MMT-TIMs of different heights, outer dimensions and metal thicknesses.

From a thermal standpoint, the variation of effective thermal conductivity with pressure for these MMT-TIMs is plotted in Fig. F.4. At low pressures, the effective thermal conductivity of these structures is relatively low; indicating the role of contact thermal resistance is dominant in this region. However, as the pressure is increased and the structures undergo deformation, the effective thermal conductivity of these structures increases significantly, reaching a maximum of approximately 5.5 W/mK at a pressure of 3 MPa for MMT-TIM "F1". Generally speaking the thicker metal-plated MMT-TIMs exhibited only a slightly higher effective thermal conductivity at pressures in certain

regions of this curve, whereas for the most part, the thinner MMT-TIMs demonstrated similar thermal performance for a given pressure.

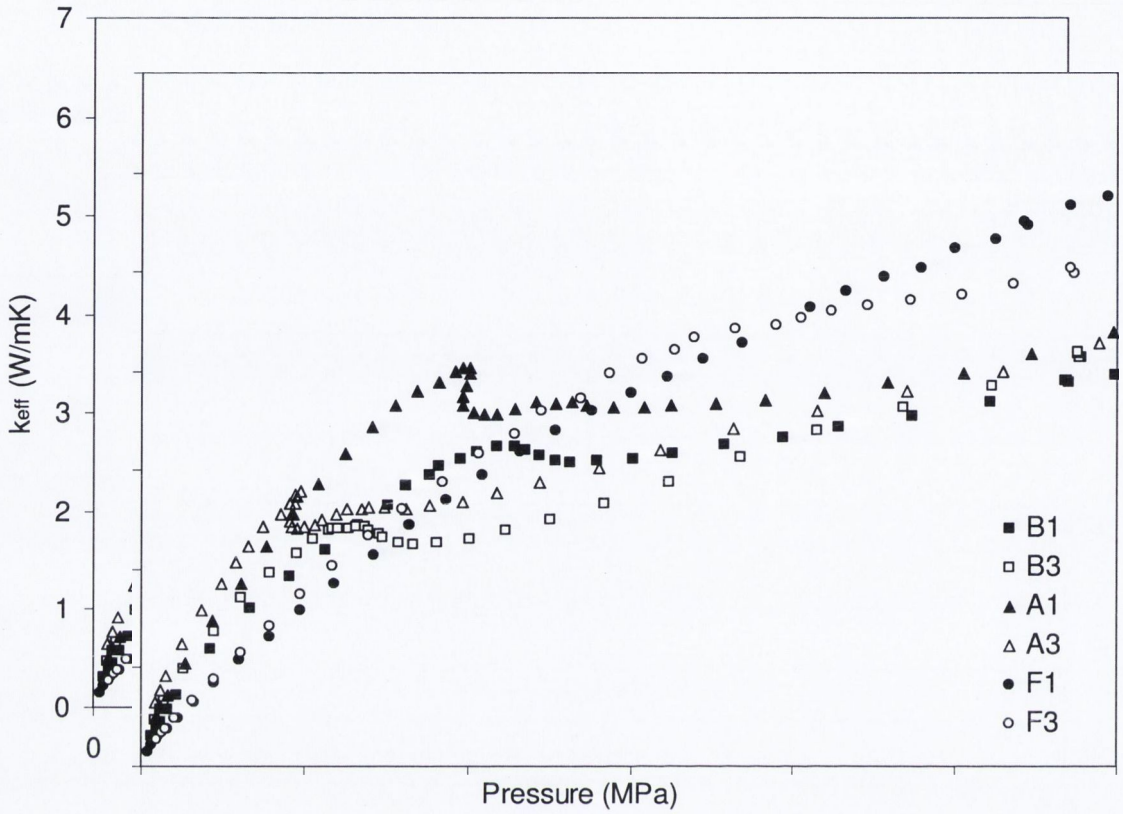


Fig. F.4: Variation of effective thermal conductivity with pressure for MMT-TIMs of different heights, outer dimensions and metal thicknesses.

Effect of Pitch

The effect of feature pitch alone can be established by comparing samples "B" and "D" from Fig. F.2. A plot of their respective stress-strain curves is shown in Fig. F.5. Similar to the result of sample "F" in Fig. F.3, due to the four-fold increase in the number of features being compressed, the amount of pressure required to deform sample "D" to a given strain increases dramatically over the baseline case.

From a thermal standpoint, the effective thermal conductivity and specific thermal resistance are plotted as a function of pressure in Fig. F.6. Here, while the higher feature-density sample "D1" exhibits higher effective thermal conductivity at all pressures, its overall thermal resistance it actually higher in the upper pressure range. This is due to the inability to compress the sample to as thin a bondline as sample "B3" as indicated in Fig. F.5.

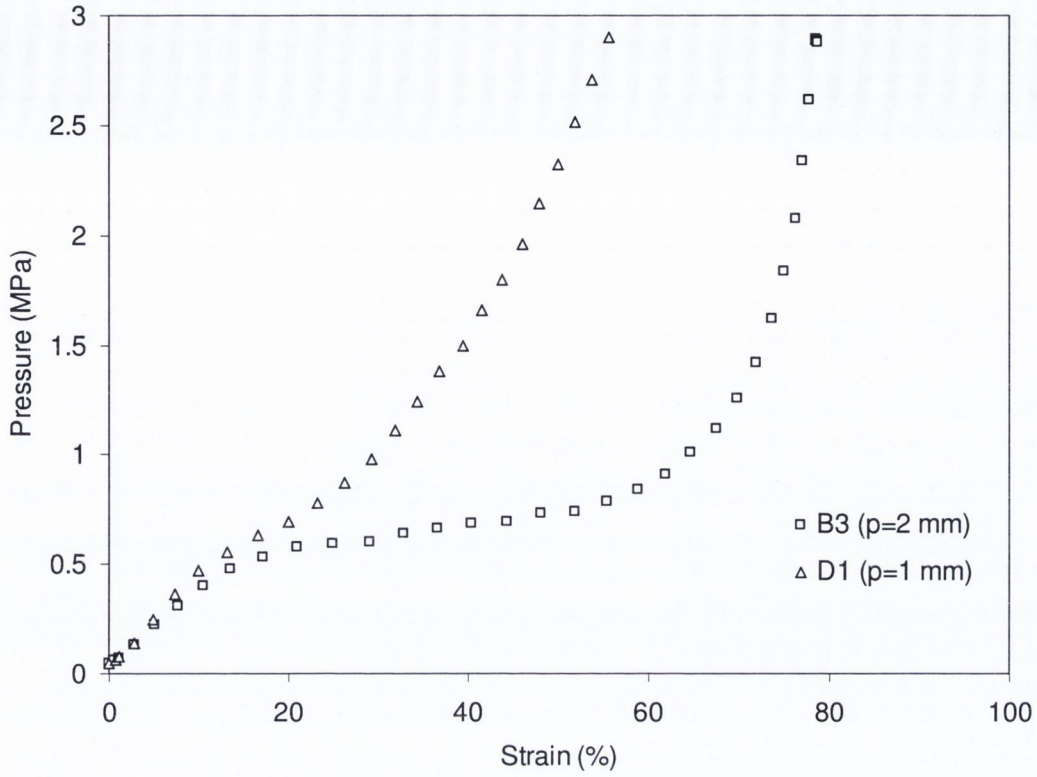


Fig. F.5: Variation of compressive pressure with strain for MMT-TIMs of different pitches

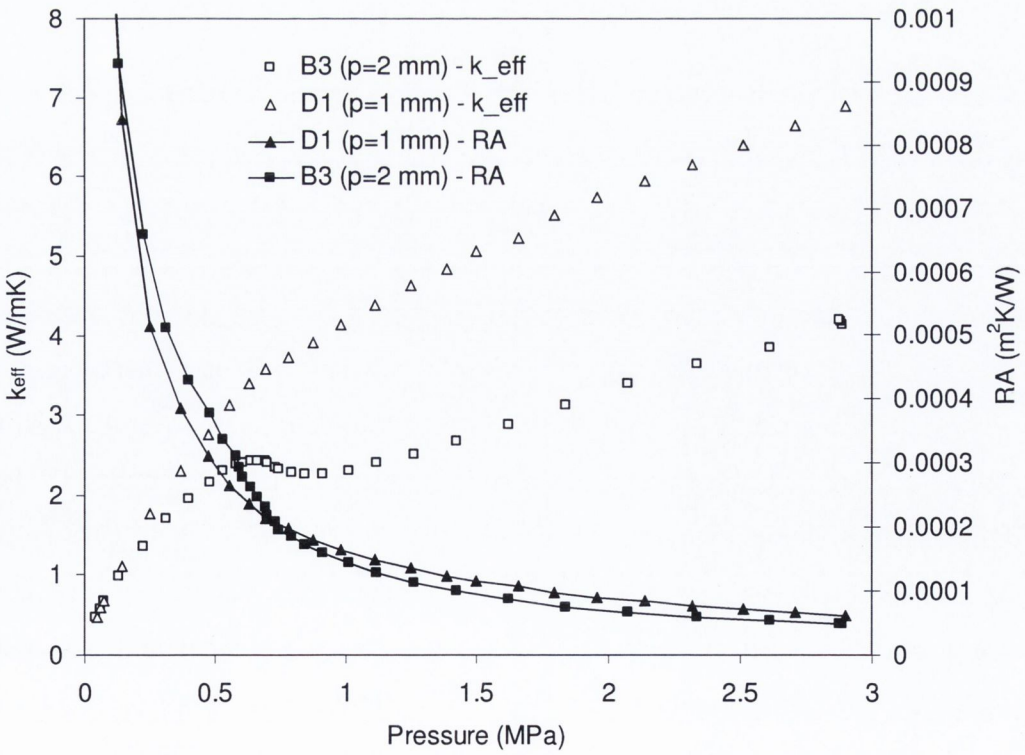


Fig. F.6: Variation of effective thermal conductivity and specific thermal resistance with pressure for MMT-TIMs of two different pitches

Effect of Feature Shape

A direct comparison was made between the baseline case of the circular-based hollow cone (sample "B") and a square-based hollow pyramid of similar outer dimensions and thickness (sample "C"). The variation of pressure as a function strain is presented in Fig F.7. Clearly, the square-based pyramid requires less force to deform to a given strain. It is hypothesized this is due to stress concentrations that exist where the sides of the pyramid meet as opposed to the somewhat stiffer axisymmetric buckling that would occur in the circular hollow cone as predicted by early model results.

From a thermal standpoint, the pyramid structure exhibits a somewhat lower effective thermal conductivity over the range of applied pressure, as illustrated in Fig F.8. In terms of specific thermal resistance, however, at low pressures, the pyramidal MMT-TIM has a lower thermal resistance. At higher pressures, the conical shaped MMT-TIM represents the optimum geometry.

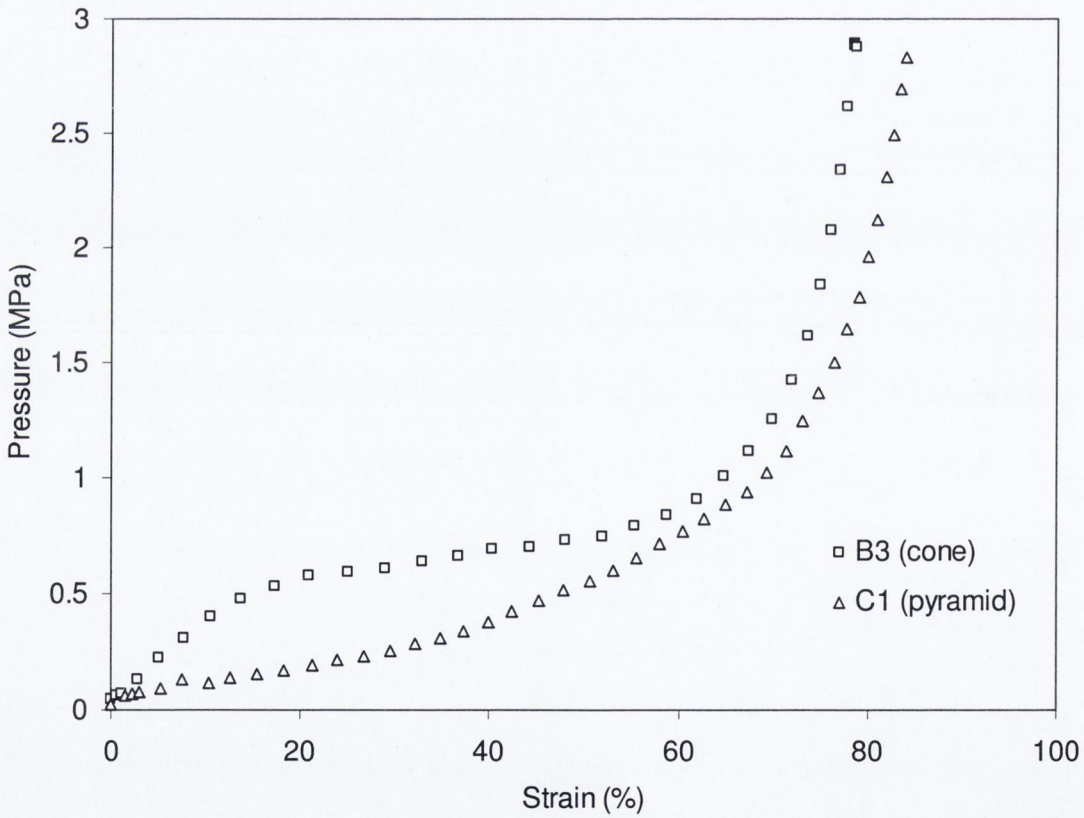


Fig. F.7: Variation of compressive pressure with strain for two conical and pyramidal MMT-TIM geometries of similar dimensions

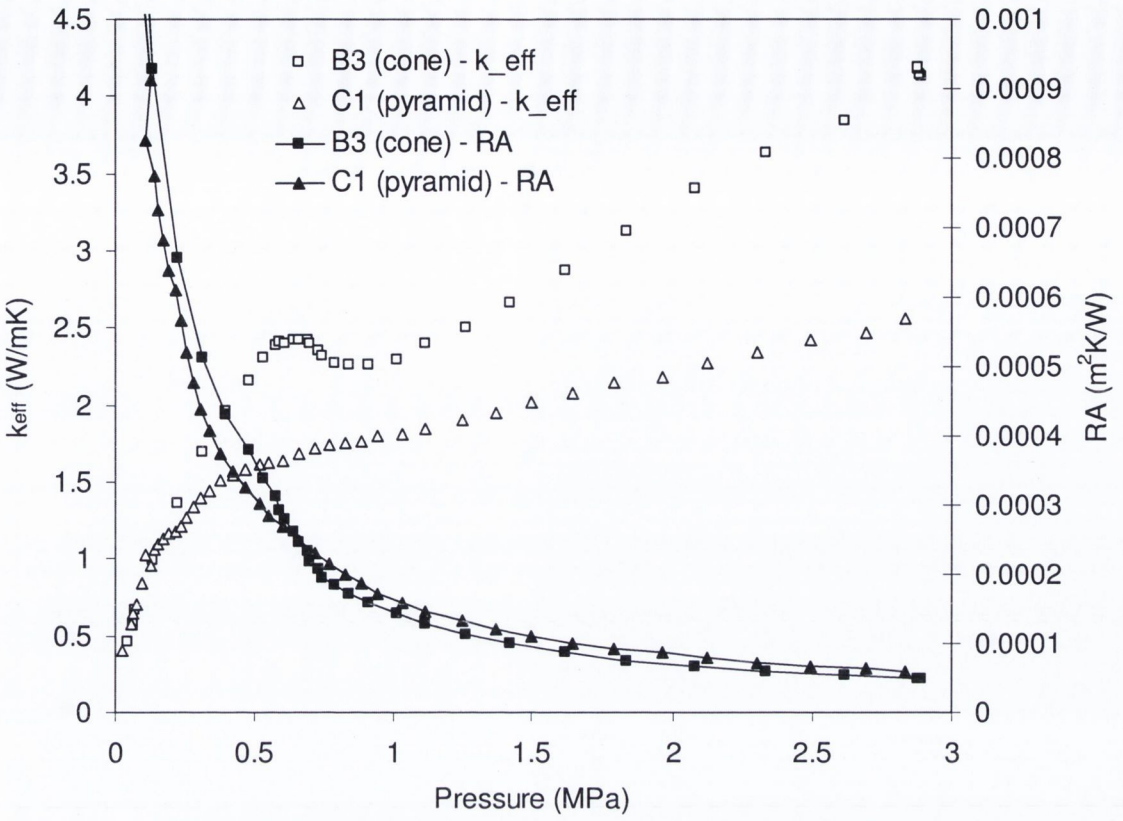


Fig. F.8: Variation of effective thermal conductivity with pressure for conical and pyramidal MMT-TIMs

The specific thermal resistance of each TIM is plotted as a function of pressure at 50% strain in Fig. F.9. Overall, there is a decreasing trend in thermal resistance, which demonstrates that, generally, stiffer structures offer a lower overall thermal resistance. This is indicative of the important role thermal contact resistance plays in the thermal performance of these TIMs. However, compliance is also required of thermal interface materials to avoid exerting excessive stresses on the mating parts. Thus a trade-off between thermal resistance and compressive pressure exists. To this point, sample "D2" exhibits over a 3 fold increase in compliance (i.e. reduction in pressure required to achieve 50% strain) while exhibiting a relatively small increase in thermal resistance (~0.00005 m2k/W)

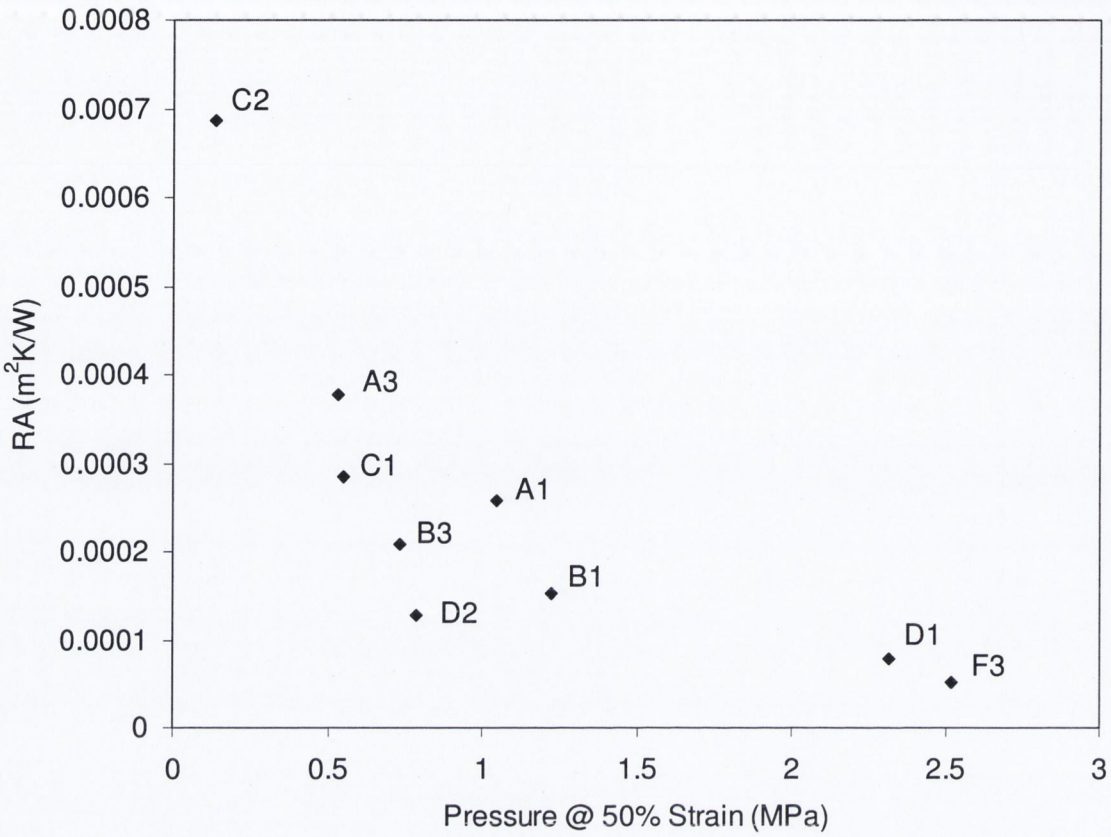


Fig. F.9: Variation of specific thermal resistance with pressure at 50% strain for each MMT-TIM